

Organic Films at the
Electrode-Electrolyte
Interface in CO₂ Reduction

Thesis by
Nicholas B. Watkins

In Partial Fulfillment of the Requirements for
the degree of
Doctor of Philosophy

The logo for the California Institute of Technology (Caltech), featuring the word "Caltech" in a bold, orange, sans-serif font.

CALIFORNIA INSTITUTE OF TECHNOLOGY
Pasadena, California

2024
(Defended September 20, 2023)

© 2023

Nicholas B. Watkins
ORCID: 0000-0001-7251-9387

ACKNOWLEDGEMENTS

In the words of Professor William A. Goddard III, “If you find the right person, marry young and have more time to spend with them” (*Scientist in a Beret*). As such, the first person I would like to thank is the most important person in my life, my wife, Aurland. You have been my biggest supporter, sense of reason, and outlet throughout this degree, and I greatly appreciate all you have done for me.

However, importantly, also in the words of Professor William A. Goddard III, “I am on Zoom” (my, and likely many others’, email inboxes). While the COVID-19 pandemic was an incredibly difficult time, it also marked the beginning of several of my collaborative projects, which ended up being the driving force for my PhD. Accordingly, I am incredibly grateful to every single collaborator I have had here in my time at Caltech.

The first collaborator I gained is Yungchieh (Ty) Lai. I can confidently say my thesis would not be what it is today without him. He has been so excited and motivated at every step of the road and brought so many of our ideas to life with his experiments. Since almost every paper I have is with him, I would argue that this thesis warrants him also receiving this PhD. Now, I will try to list as many people as I can who shaped my scientific career, but cannot possibly fit them all in. Dirk Schild, thank you for being my first mentor of graduate school. Alonso Rosas-Hernandez and Arnaud Thevenon, you shaped the beginning of my PhD by teaching me the ropes of electrochemical CO₂ reduction and how to approach a good Friday afternoon. Graduate students Alex Welch and Éowyn Lucas, thank you for being patient with me in my rotation and becoming incredible resources for me during my PhD. Ian Sullivan, you are the reason why I am able to call myself electrochemist today. Matthias Richter, thank you for being able to fix anything and everything, at any time of day or year. Yueshen Wu, you have provided me with invaluable perspective on the bigger picture of our work. Weixuan Nie, you have been a fountain of knowledge and a great sounding board for idea. Prof. Bill Goddard, you have provided me with never-ending guidance and enthusiasm for science and collaboration in our countless Zoom meetings. Soonho Kwon and Charles B. Musgrave III, thank you for providing Bill the foundation for which he is able to help others and guiding my brief tenure as a computational chemist. Prof. Harry Atwater, thank you for essential support, both on and off the soccer field. Prof. Theo Agapie, thank you for being a

constant source of thoughtful feedback and ideas for new experiments. Gavin Heim, Madeline Hicks, and Matthew Salazar, thank you for our day-to-day discussions, crosswords, and friendship. You all made Jorgensen a home. Undergraduate mentees, Casey, Alex, Matt, Milenia, Pierre, and Virginia, thank you for being patient with me as I grew as a mentor, and I am so proud of you all. Zachary Schiffer, you are the mathematical glue holding together all of my “deep thoughts.” Thank you to all of John Gregoire’s team of research scientists, Yungchieh Lai, Ryan Jones, Lan Zhou, Kevin Kan, and Dan Guevarra, as you have all been pivotal in every single one of my publications. I thank roommates David Cagan, Brian Lee, Robert Anderson, and Tucker Folsom for all of the great times we had together—who knew talking about science almost 24/7 would be so productive? Other friends and coworkers who were essential in my PhD includes but is not limited to Maria Manzanares, Jake Aquilina, Nicholas Miller, Pearl Lee, Martha Oropesa, Guille De La Torre, Leslie Corado Linares, Theodore Donnell, Patricia Nance, Emily Boyd, Florian Grass, Justin Bui, Annette Boehme, Aidan Fenwick, Komron Shayegan, Dr. Heejun Lee, Dr. Matthew Chalkley, Dr. Pablo Garrido-Barros, Dr. Caiyou Chen, Dr. Lucie Nurdin, Dr. Aisulu Aitbekova, Dr. Joel Haber, and Dr. Joeseoph Derosa. I would like to express my appreciation for the rest of the Peters, Atwater, and CX group members not listed for their essential part in surrounding my graduate life with scientific support and joy. I thank my committee members Prof. Kim See, Prof. Sarah Reismann, and Prof. Karthish Manthiram for their valuable time and feedback.

I would like to thank my advisors, Jonas and John. Jonas provided me the opportunity of returning after being a summer undergraduate research student in his lab in 2018 and I could not be more thankful. It has been a privilege to be at Caltech and work with some of the most talented scientists and kindest people I will ever know. Jonas has allowed me to explore projects and ideas freely, which has been essential for my growth as a scientist. John became a co-advisor part way through my journey and has shifted the way I approach experimentation. He has challenged me to think of new ways to use high throughput experimentation to facilitate discovery. I am extremely grateful for both of their guidance and would not be who I am today without their essential influence.

Finally, I cannot thank my family enough for being there for me throughout my 20+ years of education so far (does a postdoc still count as school?).

ABSTRACT

This thesis focuses on the use of high-throughput experimentation and analytical electrochemistry techniques to understand how organic films on (photo)electrode surfaces alter catalyst selectivity. Specifically, the objective has been to deconvolute effects associated with the organic film from the atomic identity of the catalyst, reactant and intermediate concentration polarization effects, and temperature in the context of electrochemical CO₂ reduction. The first chapter provides the motivations behind the transformation of CO₂ into value-added materials using electricity and the challenges that the field faces. The second chapter introduces the data-driven identification of a scaling relationship between the partial current densities of methane and C₂₊ products among 14 bulk copper bimetallic alloys. This strict dependence represents an intrinsic limitation of selectivity tuning through alloying. However, it can be disrupted to favor C₂₊ products by the presence of an organic additive, highlighting the potential of hybrid organic–inorganic catalysts to tune branching ratios in the CO₂R reaction network. The third chapter highlights that with the wide band gap CuGa₃Se₅ chalcopyrite absorber, organic coatings can not only provide dramatic increases in selectivity toward CO₂R products compared to the unmodified system, but also and significantly moderate catalyst corrosion. The fourth chapter unveils a new class of molecular films on polycrystalline copper, derived from aryl diazonium and iodonium salts, that are corrosion resistant even at pH 1 and have the potential for many future electrochemical applications. In the fifth chapter, we demonstrate that increased mass transport at the electrode surface directly resulted in changes to the ethylene and methane Tafel slope values on copper electrodes. These findings emphasize that the apparent Tafel slope reported for any copper system is not necessarily representative of the catalyst's intrinsic kinetics alone, but also contains information about the cell geometry and electrolyte convective transport. The final chapter investigates the combined effect of organic films, mass transport, and electrode heating on electrocatalysis. We find that we can use surface heating to replace bulk heating, but that the complexity of CO₂R prevents predictable behavior. However, the addition of additive films to the electrode surface enables idealized electrochemical CO₂ reduction kinetics, and therefore the calculation of important parameters such as the activation energy for C₂₊ product formation.

PUBLISHED CONTENT AND CONTRIBUTIONS

1. Breaking Scaling Relationships in CO₂ Reduction on Copper Alloys with Organic Additives. Lai, Y.;[†] **Watkins, N. B.**;[†] Rosas-Hernández, A.; Thevenon, A.; Heim, G.P.; Zhou, L.; Wu, Y.; Peters, J.C.; Gregoire, J.M.; Agapie, T. *ACS Cent. Sci.*, **2021**, 1756–1762. DOI: 10.1021/acscentsci.1c00860.
 - ◇ Contribution: Co-first authorship with Yungchieh Lai. Y.L performed the experimentation, while I carried out data analysis and writing of the publication.
2. Molecular Coatings Improve the Selectivity and Durability of CO₂ Reduction Chalcogenide Photocathodes. Lai, Y.; **Watkins, N. B.**; Muzzillo, C.; Richter, M.; Kan, K.; Zhou, L.; Haber, J.A.; Zakutayev, A.; Peters, J.C.; Agapie, T.; Gregoire, J.M. *ACS Energy Lett.*, **2022**, 7, 3, 1195–1201. DOI: 10.1021/acsendergylett.1c02762.
 - ◇ Contribution: As second author, I synthesized molecular additives and carried out data analysis and writing for the publication.
3. In Situ Deposited Polyaromatic Layer Generates Robust Copper Catalyst for Selective Electrochemical CO₂ Reduction at Variable pH **Watkins, N. B.**;[†] Wu, Y.;[†] Nie, W.; Peters, J. C.; Agapie, T. *ACS Energy Lett.* **2022**, 189–195. DOI: 10.1021/acsendergylett.2c02002
 - ◇ Contribution: Co-first authorship with Yueshen Wu. Y.W. initiated the project with diazonium salts and I optimized and expanded the scope of the system using iodonium salts.
4. Hydrodynamics Change Tafel Slopes in Electrochemical CO₂ Reduction on Copper **Watkins, N. B.**;[†] Schiffer, Z. J.;[†] Lai, Y.; Musgrave, C. B. I.; Atwater, H. A.; Goddard, W. A. III.; Agapie, T.; Peters, J. C.; Gregoire, J. M. *ACS Energy Lett.* **2023**, 2185–2192. DOI: 10.1021/acsendergylett.3c00442.
 - ◇ Contribution: Co-first authorship with Zachary Schiffer. I conceptualized the project, performed experimentation, and wrote the publication, while Z.J.S. performed data analysis and COMSOL calculations.
5. Electrode Surface Heating with Organic Films Improves CO₂ Reduction Kinetics on Copper. **Watkins, N. B.**;[†] Lai, Y.;[†] Schiffer, Z. J.; Canestraight, V.M.; Atwater, H. A.; Agapie, T.; Peters, J. C.; Gregoire, J. M. *In preparation*.
 - ◇ Contribution: Co-first authorship with Yungchieh Lai. I conceptualized the project, directed experimentation, and wrote the publication, while Y.L performed the experimentation.

TABLE OF CONTENTS

Acknowledgements.....	iii-iv
Abstract	v
Published Content and Contributions.....	vi
Table of Contents.....	vii-viii
List of Illustrations and/or Tables.....	ix-xvi
Nomenclature.....	xvii-xviii
Chapter 1: Introduction.....	1
1.1 Introduction.....	2
1.2 Results and Discussion.....	3
1.3 Conclusions.....	9
1.4 References.....	11
Chapter 2: Breaking Scaling Relationships in CO₂ Reduction on Copper	
Alloys with Organic Additives	20
1.1 Introduction.....	21
1.2 Results and Discussion.....	23
1.3 Conclusions.....	32
1.4 References.....	33
Chapter 3: Molecular Coatings Improve the Selectivity and Durability	
of CO ₂ Reduction Chalcogenide Photocathodes	42
1.1 Introduction.....	43
1.2 Results and Discussion.....	46
1.3 Conclusions.....	55
1.4 References.....	56
Chapter 4: In Situ Deposited Polyaromatic Layer Generates Robust Copper	
Catalyst for Selective Electrochemical CO ₂ Reduction at Variable pH	64
1.1 Introduction.....	65
1.2 Results and Discussion.....	67
1.3 Conclusions.....	77
1.4 References.....	78
Chapter 5: Hydrodynamics Change Tafel Slopes in Electrochemical CO₂	
Reduction on Copper.....	85
1.1 Introduction.....	86
1.2 Results and Discussion.....	90
1.3 Conclusions.....	101
1.4 References.....	102
Chapter 6: Electrode Surface Heating with Organic Films Improves CO₂	
Reduction Kinetics on Copper.....	108
1.1 Introduction.....	109
1.2 Results and Discussion.....	112
1.3 Conclusions.....	118

1.4 References	119
Appendix 1: Unfinished Work for Future Investigation: Cell Design for Well-Defined Hydrodynamics	125
1.1 Introduction	126
1.2 Cell Design	128
1.3 Evaluation of Cell Design	129
1.4 Conclusions	134
1.5 References	135
Appendix 2: Supplementary Information for Chapter 2.....	138
Appendix 3: Supplementary Information for Chapter 3.....	162
Appendix 4: Supplementary Information for Chapter 4.....	176
Appendix 5: Supplementary Information for Chapter 5.....	218
Appendix 6: Supplementary Information for Chapter 6.....	246

LIST OF ILLUSTRATIONS AND/OR TABLES

Figure 1.1: prototype systems for CO ₂ capture and conversion.	3
Figure 1.2: product profile of electrochemical CO ₂ reduction on copper	5
Figure 1.3: Breadth of potential rate determine steps (RDS) proposed in literature for C ₁ and C ₂ products..	6
Figure 1.4: Two examples of additive coatings that limit the proton concentration at the electrode surface.....	8
Figure 2.1: a) The electrochemical reductive coupling of 1-Br₂ and b) the high throughput catalyst screening system used herein.....	24
Figure 2.2: Illustration of acquired data and correlation analysis.	26
Figure 2.3: a) Possible reaction mechanisms and b) a summary of molar selectivity for reduction of the CO* intermediate... ..	32
Scheme 3.1: Electrochemical dimerization of pyridinium-based molecular additives ...	44
Figure 3.1: Schematic of HT-ANEC and the multilayer structure of the photocathode, and a representative photoelectrocatalysis experiments with and without molecular additive.	46
Figure 3.2. Summary of 32 photoelectrocatalysis experiments.....	48
Figure 3.3. a) Aggregation of the experiments in Figure 3.2 for the no-additive and Add. 2 conditions, b) validation of the screening results with 10 mM Add. 2 using a traditional H-cell, and c) long term electrolysis	50
Figure 3.4. a) Cross section TEM, b) cross section SEM and c) XPS measurements of the Cd-based layer under varying conditions.. ..	53
Figure 4.1: Preparation of hybrid electrodes....	66
Figure 4.2. Enhanced C ₂₊ product selectivity by phenyldiazonium (PD) modification ..	69
Figure 4.3. Comparison of PD- and PI-Cu performance over time during CO ₂ R....	70
Figure 4.4. Comparison of diazonium- and iodonium-based polyaromatic electrode modification via AFM.	71

Figure 4.5. Electrochemical studies of the impact of the organic films.....	74
Figure 4.6. Product distribution and electrolyte pH over 5 hours with PI-Cu at -100 mA cm ⁻² with an initial 1 M H ₃ PO ₄ electrolyte	76
Scheme 5.1: Mechanism for electrochemical reduction of CO ₂ to C ₂₊ products.....	86
Figure 5.1: Graphical representation of the change in concentration of surface species due to electrolyte flow near the electrode surface with a) laminar flow and b) turbulent flow.....	89
Figure 5.2: COMSOL simulations of electrolyte velocity in varying cell designs.....	91
Figure 5.3: Measured partial current densities for CO in each cell geometry with respect to potential	94
Figure 5.4: Tafel analysis of varying cell designs for ethylene.....	95
Scheme 5.2: Schemes describing how transport and films affect CO ₂ delivery to the electrode surface.....	97
Scheme 5.3: Reductive dimerization of 1-Br₂	98
Figure 5.5: The distribution of gaseous products shown with and without 1-Br₂ in two cell designs.	99
Figure 5.6: The distribution of ethylene Tafel slopes with and without 1-Br₂ in two cell designs.	100
Scheme 6.1: Electrochemical pathways for the production of ammonia, ethylene, and hydrogen	109
Figure 6.1: Schematic of the high throughput analytical electrochemistry.....	112
Figure 6.2: OCV measurements at variable electrode temperatures.....	113
Figure 6.3: Electrochemical CO ₂ reduction performance with/without organic films ..	115
Scheme 6.2: Reductive polymerization of diphenyliodonium idonium triflate....	116
Figure 6.4: Probability distributions of the A) activation energy, B) change in applied potential with respect to temperature given a fixed current, and C) change in current with respect to temperature for CO ₂ reduction.....	117

Figure S1.1: Representations of A. rotating cylinder electrode and B. plug flow reactor assemblies with their reactant /product concentration profiles	126
Figure S1.2: Schematic of the parallel plate reactor used in initial experiments	128
Figure S1.3: Qualitative descriptions of how boundary conditions will affect the electrolyte flow velocity	129
Figure S1.4: Comparison of velocity profiles over the width of the cell using fundamental, continuum, and experimental models at varying flow rates....	130
Figure S1.5: Schematic of the finalized reactor used in electrolysis experiments.....	131
Figure S1.6: Comparison of velocity profiles over the width of the original parallel plate reactor with the “new” version.....	132
Figure S1.7: Graph showing the change in concentration boundary layer with respect to flow rate.....	133
Table S2.1: Alloy compositions tested in ANEC cell for performance in CO ₂ R	144
Figure S2.1: Cu alloy product distribution in 0.1M KHCO ₃	145
Figure S2.2: Cu alloy product distribution with 0.1 mM 1-Br₂ in 0.1 M KHCO ₃	146
Figure S2.3: Cu alloy product distribution in 0.25 M KHCO ₃	146
Figure S2.4: a) The data underlying the correlation analysis from 0.25 M KHCO ₃ and b) Comparison for the trends between 0.1 and 0.25 M KHCO ₃	147
Figure S2.5: Pairwise relationships in the current density and FE.....	148
Figure S2.6: 10 pairwise relationships of the partial current densities....	149
Figure S2.7: SEM of catalysts before and catalysis with molecular additives	150
Figure S2.8: SEM of Cu catalyst after catalysis without molecular additives.....	151
Figure S2.9: Pre- and postcatalysis SEM and AFM images of CuMn....	152
Figure S2.10: Pre- and postcatalysis SEM and AFM images of CuIn.....	153
Figure S2.11: CH ₄ vs C ₂₊ at -1.04 V vs RHE at varying timepoints....	154
Figure S2.12: XRD for the as-synthesized alloys investigated	155

Figure S2.13: XRD for alloy CuCo before and after electrolysis.....	156
Figure S2.14: XRD for alloy CuZn before and after electrolysis.....	156
Figure S2.15: XRD for alloy CuMn before and after electrolysis	157
Figure S2.16: XRD for alloy CuIn before and after electrolysis.....	157
Figure S2.17: A complementary figure for Figure 2.3	158
Figure S2.18: Electrochemical current density, CO ₂ consumption (in the headspace) at the end of electrolysis, gas product concentration, and liquid product concentration vs log (C ₂₊ /CH ₄).....	158
Figure S2.19: Product CO concentration vs partial current density of CH ₄ and C ₂ H ₄ ..	159
Figure S3.1: Initial experiments in an electrochemical flow cell.....	168
Figure S3.2: Evaluation of the product distribution with illumination ranging from 617 nm to 385 nm at 0V vs RHE.....	169
Figure S3.3: History of each sample tested and photoelectrochemical CO ₂ reduction performance.....	169
Figure S3.4: GC-MS analyses of ¹³ CO ₂ experiments.....	170
Figure S3.5: Complimentary figure to Figure 3.2	171
Figure S3.6: XPS survey scans of CGS/CdS postcatalysis under varying conditions and subsequent elemental breakdown.....	171
Figure S3.7: Additional TEM data supporting Figure 3.4b.....	172
Figure S3.8: High resolution core level spectra for CGS/CdS postcatalysis under varying conditions.....	173
Table S3.1: The photocurrent, product distribution, as well as XRF and ICP-MS characterization of Cd corrosion.....	174-175
Figure S4.1. Representative gas chromatographs of product stream from CO ₂ R.....	184
Figure S4.2. Representative HPLC trace of catholyte solution after reaction.....	185

Figure S4.3. Representative $^1\text{H-NMR}$ spectrum of the sample prepared from catholyte solution after CO_2 reduction electrolysis by PD-Cu.....	186
Table S4.1. Current density and faradaic efficiency towards different products by PD-Cu during CO_2 reduction at various cathode potentials.....	187
Table S4.2. Current density and faradaic efficiency towards different products by unmodified Cu control during CO_2 reduction	188
Table S4.3. Current density and faradaic efficiency towards different products by PI-Cu during CO_2 reduction using a 5-minute pre-deposition of film.....	189
Figure S4.4: Potential dependent selectivity and activity of bare, PD-, and PI-Cu	190
Figure S4.5. Comparisons of (a) HER and (b) C_{2+} partial current density for PD-Cu and PI-Cu with respect to bare Cu	191
Table S4.4. Current density and FE towards different products in control electrolyses	192
Figure S4.6. LSV measurements of bare Cu, PD-Cu, and PI-Cu under CO_2 and Ar	192
Figure S4.7. AFM images of (a) unmodified polished Cu, (b) PD-Cu, (c) Delaminated PD-Cu post 10 h electrolysis.....	193
Figure S4.8. CV of 5 mM phenyldiazonium tetrafluoroborate in 0.1 M TBABF ₄ in acetonitrile	194
Figure S4.9. CV of 10 mM diphenyliodonium triflate in 0.1 M KHCO ₃	194
Figure S4.10. Long term electrolysis of bare Cu in 0.1 M KHCO ₃ at an applied voltage of -1.1 V vs RHE.....	195
Figure S4.11. FT-IR spectrum of PD-Cu and PI-Cu	196
Table S4.5. Assignment of IR bands in PD-Cu attributed to polyphenylene.....	196
Table S4.6. Assignment of IR bands in PI-Cu attributed to polyphenylene	197
Figure S4.12. FT-IR spectrum of as-synthesized phenyldiazonium tetrafluoroborate ..	198
Figure S4.13. XPS characterization of PD-Cu.....	199
Figure S4.14. XPS characterization of PI-Cu....	200

Figure S4.15. Comparison of XPS for bare Cu, PD-Cu, and PI-Cu	201
Figure S4.16. AFM image of a modified Cu after exposure to the electrodeposition condition for 1 min	202
Table S4.7. Current density and faradaic efficiency towards different CO ₂ reduction products by PD-Cu prepared using different deposition times ..	203
Table S4.8. Current density and faradaic efficiency towards different CO ₂ reduction products by PI-Cu prepared using different deposition times	204
Figure S4.17: Deposition-time dependent performance of a) PD- and b) PI-Cu.....	205
Figure S4.18. A representative current-time profile during electrodeposition of polyphenylene from phenyldiazonium	206
Figure S4.19. CV characterization of ECSA of PD-Cu and Cu control....	207
Table S4.9. Summary of ECSA values of PD-Cu and polished Cu as measured in CO ₂ -saturated 0.1 M KHCO ₃	208
Figure S4.20: Example rotating disk electrode data.....	209
Table S4.10. Summary of RDE values for PD-Cu and PI-Cu as measured in pH ~2.1 0.1 M KClO ₄	210
Figure S4.21: SEM of PD-Cu RDE post measurements.....	211
Figure S4.22: Visual comparison of a (a) post-electrolysis unmodified electrode versus (b) PI-Cu GDE.....	212
Figure S4.23: Average of three multiple 30 minute electrolyses at -100mA/cm ² , either using <i>in-situ</i> deposition or pre-deposition in 1 M KHCO ₃	212
Figure S4.24: 6-hour electrolysis at -100 mA/cm ²	213
Figure S4.25. ¹ H-NMR of as-synthesized phenyldiazonium tetrafluoroborate in d ₃ -acetonitrile....	214
Figure S4.26. ¹ H-NMR of as-synthesized diphenyliodonium triflate in d ₆ -DMSO	215
Figure S5.1: Schematics of cells investigated....	224
Figure S5.2: Concentration boundary layer experiments	225

Table S5.1: Cells and their associated boundary layer thicknesses.....	226
Figure S5.3: The partial current density towards CO ₂ with and without additive films	227
Figure S5.4: The distribution of gaseous products for all cells investigated	228
Figure S5.5: Tafel plots for methane for all cells investigated.....	229
Figure S5.6. Ethylene Bayesian analysis of the data from Kuhl et al....	231
Figure S5.7. Ethylene Bayesian analysis of the data from parallel flow H-cell data.....	231
Figure S5.8. Ethylene Bayesian analysis of the data from angled flow H-cell data.....	232
Figure S5.9. Ethylene Bayesian analysis of the data from ANEC	232
Figure S5.10. Methane Bayesian analysis of the data from Kuhl et al....	233
Figure S5.11. Methane Bayesian analysis of the data from parallel flow H-cell data....	233
Figure S5.12. Methane Bayesian analysis of the data from angled flow H-cell data	234
Figure S5.13 Methane Bayesian analysis of the data from ANEC....	234
Figure S5.14: Tafel plots for a) ethylene and b) methane from ANEC with 0.25 M KHCO ₃ and their Bayesian analysis	235
Figure S5.15: Molecular Dynamics simulation boxes.....	237
Figure S5.16: CO diffusion coefficients calculated at three temperatures with/ without the N,N'-ethylene-phenanthroline dimer.....	237
Table S5.2: All Faradaic efficiencies and currents	238-243
Figure S6.1: Internal and outlet electrolyte temperature profiles according to experiments and simulations.....	252
Table S6.1: Comparison of experimental and COMSOL internal temperatures	253
Figure S6.2: Calibration of OCV versus bulk temperature....	253
Table S6.2: Open Circuit Voltage (OCV) measurements in 0.5 M KCl with 5 mM K ₃ Fe(CN) ₆ and 5 mM K ₄ Fe(CN) ₆	254

Figure S6.3: Zoomed out cyclic voltammograms (CVs) of A) surface heating with fast electrolyte recirculation, B) bulk heating with fast electrolyte recirculation, C) surface heating with slow electrolyte recirculation, and D) surface heating with fast electrolyte recirculation in the presence of a molecular film.....	255
Figure S6.4: Chronoamperometry (CA) at -0.8 V vs Ag/AgCl for 2 minutes of A) surface heating with fast electrolyte recirculation, B) bulk heating with fast electrolyte recirculation, C) surface heating with slow electrolyte recirculation, and D) surface heating with fast electrolyte recirculation in the presence of a molecular film.....	256
Figure S6.5: Concentration boundary layer versus electrolyte recirculation flow rate .	257
Figure S6.6: Calculated concentration boundary layer thickness at a 150 $\mu\text{L/s}$	257
Figure S6.7: Temperature versus resistance plots of surface heated (SH) versus bulk heated (BH) electrolyte using 0.1 M KHCO_3	258
Figure S6.8: Plots of Faradaic efficiencies for polycrystalline Cu CO_2R at variable temperatures in 0.1 M KHCO_3	259
Figure S6.9: Plots of Faradaic efficiencies for organic-modified polycrystalline Cu CO_2R at variable temperatures in 0.1 M KHCO_3	259
Figure S6.10: Fitting of experimental CO_2R data using Butler Volmer kinetics	260
Table S6.3: Potentials, currents, temperatures, and Fes of electrolyses.....	260-262

NOMENCLATURE

CO₂R. CO₂ reduction

NEB. nudge elastic band

RDS. rate-determining step

C_{dl}. double layer capacitance

XRD. X-ray diffraction

FE. Faradaic efficiency

1-Br₂. N,N-phenanthroline dibromide

CA. chronoamperometry

CIGS. Cu(In,Ga)Se₂

PEC. photoelectrochemical

HER. Hydrogen evolution reaction

RHE. reversible hydrogen electrode

HT-ANEC. high throughput analytical electrochemistry screening system

Add. 1. N,N'-ethylene-phenanthroline dibromide

Add. 2. N,N'-(1,4-phenylene)bispyridinium ditriflate

ECMS. electrochemical mass spectrometry

ICP-MS. inductively coupled plasma mass spectrometry

XRF. X-ray fluorescence

MS. mass spectrometry

TEM. transmission electron microscopy

EDS. energy dispersive spectroscopy

SEM. scanning electron microscopy

XPS. x-ray photoelectron spectroscopy

PD-Cu. phenyldiazonium modified copper

PI-Cu. diphenyliodonium modified copper

ECSA. electrochemical active surface area

RDE. rotating disk electrode.

GDE. gas diffusion electrode

RCE. rotating cylinder electrode

ANEC. analytical electrochemistry screening system

LOWESS. locally weighted scatterplot smoothing

PEC. photoelectrochemistry

EDTA. ethylenediaminetetraacetic acid

SH. surface heating

BH. bulk heating

OCV. open circuit voltage

CSTR. continuously stirred tank reactor

PFR. plug flow reactor

Chapter 1

INTRODUCTION

1.1 Opening Remarks

This thesis concerns itself with the influence of reactor design on electrochemical carbon dioxide (CO₂) reduction to evaluate its feasibility as a methodology for combatting climate change. Since anthropogenic climate change is reaching a tipping point of having potentially irreversible and drastic effects on humanity, strategies to mitigate greenhouse gas emissions become ever more pressing.¹ The Paris Agreement marks the international recognition of the effect of CO₂ on the climate and the pledge of 196 countries to limit the warming to less than +1.5 °C.² Given that more than half of the CO₂ released into the atmosphere originates from the energy sectors, the capture and conversion of CO₂ into fuels to replace fossil fuels and other commodity chemicals is necessary to approach a net-carbon negative society.³ However, the current infrastructure for the sequestration and utilization of carbon from the environment is limited.

CO₂ capture and conversion is an energy intensive process that has inspired a number of prototype and pilot-level plants that are attempting to address the issue from different angles, such as dissolving CO₂ in sorbents like water or zeolites, pressurizing it to form minerals or feedstock gasses for electrochemical processes, or fermenting it using bacteria (Fig. 1.1).⁴ Most commonly, the end product of these processes are liquid fuels, which feed back into and close the carbon-based energy cycle. However, this is not necessarily self-defeating. Producing liquid fuels allows for the use of the current energy infrastructure, which prevents significant waste and lowers monetary barriers toward achieving a carbon-neutral energy economy. Furthermore, the hydrocarbons produced via electrolysis can be made using 100% renewable energy and are compatible with the combined-cycle power plants that exist today for liquid natural gasses. These plants are up to 60% efficient, far

carbon coupled products.^{7,8} All other metals produce carbon monoxide (CO) or formate, which are not viable fuels, and often struggle to compete with high rates of the competing hydrogen evolution reaction (HER). The origin of this disparity among metal catalyst selectivities is primarily due to CO binding energies ($*CO$)—if bound too strongly, as in the case of Sn or Ti, the catalyst will mainly produce formic acid, but if bound too weakly, like Ag or Au, the catalyst will mainly produce CO.⁹ Additionally, the relationship between the binding energy of metals and CO scales with the potential applied to the system as well as with subsequent intermediates, forming robust scaling relationships that cannot be broken by changes in morphology or facets exposed.¹⁰ These relationships demonstrate how the CO₂ reduction reaction (CO₂R) follows the Sabatier Principle, which states that the binding of key intermediates can neither be too weak or too strong, as described above, resulting in a volcano plot of reaction rate with respect to binding energy and activity. The disparity among metal catalysts is also explained by the binding energies of $*H$; binding strongly leads to formate and weakly leads to CO.¹¹ Despite copper's privileged nature, it suffers from a lack of selectivity for any one specific product among a multitude of 16+ possible reduced products (Figure 1.2).⁷ Due to the ubiquity of certain products in industrial processes, like ethylene for polymers or ethanol for liquid fuels, the field revolving around electrochemical CO₂R has become a key area of research. Current studies aiming to optimize CO₂ electrolysis focus on a variety of research fronts from increasing total current densities at low overpotentials, to selectively generating one product over all others, to understanding the fundamental science behind the transformation occurring.¹²

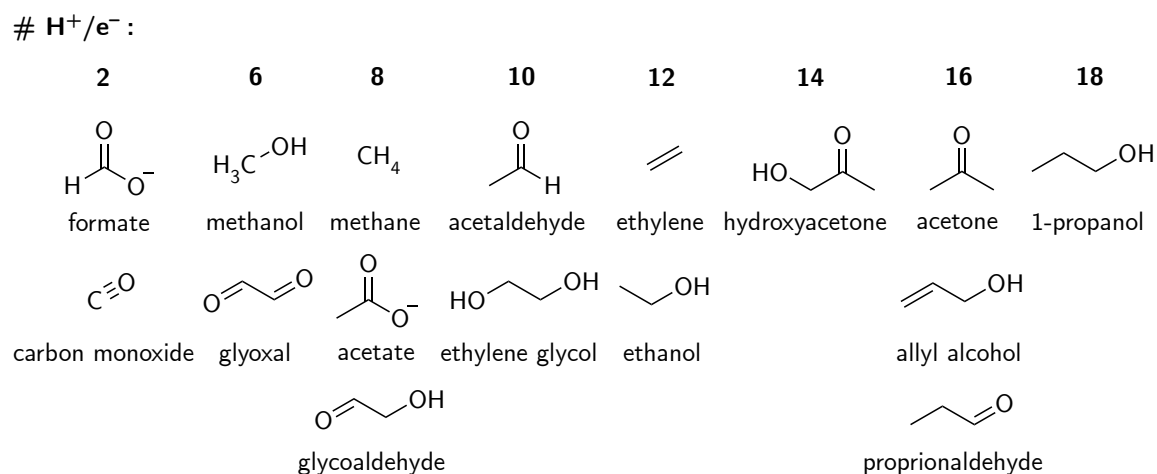


Figure 1.2: Schematic of the product profile of electrochemical CO₂ reduction on copper along with the number of proton/electron transfers associated with each product listed above it.

In order to inform the design of systems that improve the selectivity and activity of electrochemical CO₂R on copper, considerable effort has been made to understand the mechanism of the transformation. Hori and coworkers discovered that the exposed facets of copper altered the product ratio of single carbon products (C₁), like methane, and carbon-coupled products (C₂₊), like ethylene.¹³ This finding suggested that the intermediates along the reaction pathway towards C₁/C₂₊ products interact differently according to the catalyst coordination environment, which motivated the calculation of intermediate binding energies and reaction barriers. Because Cu (100) has one of the highest selectivities towards forming C₂₊ products, early calculations focused on this facet.¹⁴ While studies initially pointed towards metal-carbide like intermediates leading to products like methane and ethylene, analogous to those observed during Fischer-Tropsch, most modern calculations have diverged from this path (though not all).^{15,16} Because CO is the only reaction intermediate to be observed experimentally, the majority of computational models use *CO as branching point for C₁/C₂₊ products. Common pathways investigated include *CO dimerization, *CHO

dimerization, $^*\text{CH}_2\text{O}$ dimerization, and all permutations of heterodimerization.¹⁷ These calculations helped reform the microscopic image of what may be occurring on the catalyst surface. Unfortunately, varying calculation parameters between studies gives drastically different results, and the exact mechanism remains an active area of research (Fig. 1.3).^{18–24}

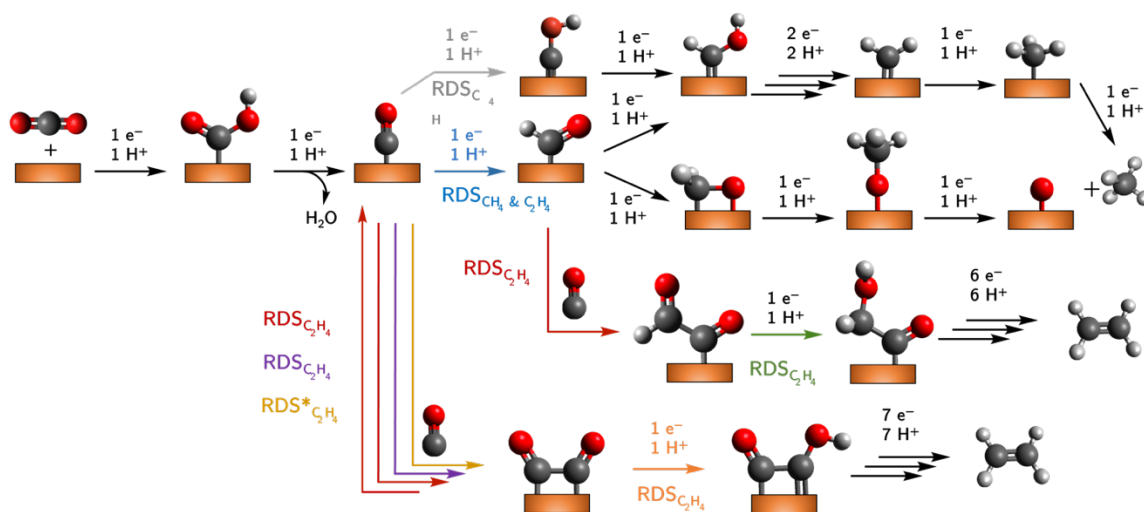


Figure 1.3: Breadth of potential rate determine steps (RDS) proposed in literature for C_1 and C_2 products, with each color corresponding to a different paper (note: this is not a complete picture of all pathways proposed). *Refers to the event being coupled with electron transfer. Colors correspond to the following references: grey [18], blue [19], yellow [20], orange [21], purple [22], green [23], red [24].

Experimental investigations into the chemical mechanism have consisted of Tafel analysis, systematic variation of catalytic conditions, and *in-situ* or *operando* spectroscopy techniques. Tafel analysis is a linearization of the Butler-Volmer equation, which describes the current as a function of applied potential, and it uses the change in current with respect to applied potential to approximate the number of proton/electron transfer steps before the rate-determining step (RDS).²⁵ When this analysis is performed on electrochemical CO reduction, the results suggest that the first electron transfer is the RDS.²⁶ Despite having significant effects on the selectivity of the reaction, altering the pH or cation identity do not

result in a change in Tafel slope.^{27,28} When the facet is varied, a positive shift in onset potential for ethylene is observed for Cu (100) but not Cu (111), which suggests two or more concurrent reaction pathways could exist depending on what facets are exposed and potential is applied.²⁹ Spectroscopic investigations of these systems regularly observe CO, but rarely are capable of identifying other species.^{30–32} Recently, an *OCCO dimer and *CHO were reportedly observed using time-resolved attenuated total reflection-surface enhanced infrared absorption spectroscopy.³³ In this work, they observe independent growth of these two peaks, supporting the hypothesis that *CO is the branching point for C₁/C₂₊ products. However, the difficulties involved in obtaining these results and the infrequency with which these species are observed further support a dynamic mechanism that may change depending on surface composition, morphology, and potential applied, among a variety of other factors. This concept is a main focus and is further explored in **Chapter 2** and **Chapter 5**.

Since pH and cations do not affect the apparent mechanism, but do change the observed selectivity and activity, their effect is most likely attributable to changes in mass transport. Since the hydroxides generated at the electrode surface can react with CO₂ to form bicarbonate, mass transfer plays a pivotal role in maintaining a high concentration of CO₂ at the surface.^{34–36} While the ionic radius of an alkali cation increases going down the group, the resulting hydration shell decrease in size (i.e. hydrated Cs⁺ is smaller than Li⁺).³⁷ Since the effective sizes of the cations change, this results in altered local pH buffering, water concentration, and electric field strength near the electrode surface.^{38,39} In other words, cesium has a greater buffering ability, which increases the local CO₂ concentration and decreases the local H₂O concentration. Due to its smaller size, the effective electric field at the electrode is greater, which increases selectivity, while its effect on the transport of

reactants improves activity.⁴⁰ It is important to note that while increased surface electric field has been associated with higher C₂ selectivity, without limiting the local proton concentration it can instead result in increased HER.^{41,42}

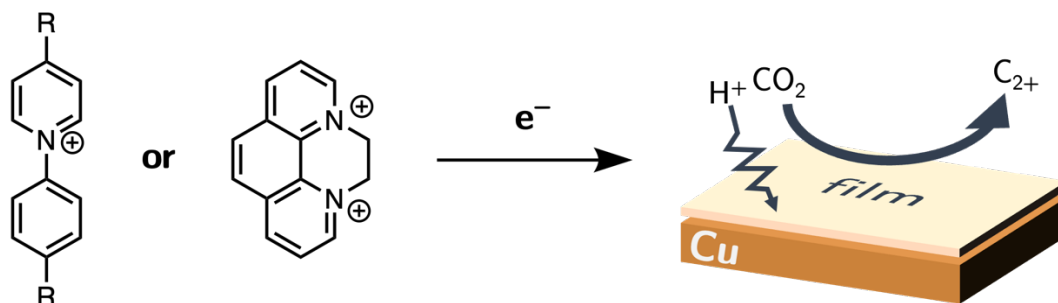


Figure 1.4: Two examples of additive coatings that limit the proton concentration at the electrode surface. Reductive electrochemical synthesis of N-arylpiperidinium and N,N'-phenanthroline molecular additives affords an insoluble film on the electrode surface that suppresses proton transport and facilitates selective CO₂ reduction to multicarbon products.^{43,45}

Because protons are a reactant in any CO₂R reaction, limiting water at the surface has been the subject of a number of recent studies. One common strategy is to use a molecular additive, such as an ionomer or polymeric film, which is proposed to impede proton diffusion without affecting CO₂ transport (Figure 1.4).^{12,43-47} In these studies, HER and C₁ products are greatly suppressed in favor of C₂₊ products. Furthermore, the films are stable over long-term electrolyses, which is essential for their eventual industrial scaling and implementation.^{48,49} The stability of these films is a key subject in **Chapter 3** and **Chapter 4**. However, while the use of molecular additives is a promising strategy for improving performance, many aspects of their influence on the CO₂R mechanisms, such as their interaction with intermediates, interaction with the catalyst, and impact on transport of intermediates, are underinvestigated. This gap in understanding is further explored in **Chapters 2, 5, and 6**.

Overall, this thesis begins with the premise that electrochemical carbon dioxide reduction to multi-carbon products is an essential step in closing the carbon cycle and achieving global sustainability goals. We center around catalyst development and methods for promoting multi-carbon product formation, particularly with respect to the competing hydrogen evolution reaction. We focus in particular on the use of molecular films and their long-term stability as a practical tool for controlling selectivity in electrochemical CO₂ reduction. To finish, we explore the influence of electrolyte hydrodynamics and electrode heating on CO₂R, demonstrating non-traditional methods for controlling reactivity by taking a holistic device-design approach instead of focusing exclusively on the catalyst surface. This work provides new insights into the capabilities of molecular films and techniques for the investigation and control of reaction mechanisms on electrode surfaces.

1.3 Chapter Summaries

In **Chapter 2**, we identify a scaling relationship between the partial current densities of methane and C₂₊ products via high-throughput experimentation on 14 bulk copper bimetallic alloys. With this result, we reveal an intrinsic limitation to the performance of CO₂R on bare copper electrodes. However, we demonstrate that coating the electrodes with a molecular film unilaterally breaks the scaling relationship to promote C₂₊ product formation.

In **Chapter 3**, we demonstrate that for the wide band gap CuGa₃Se₅ chalcopyrite absorber, molecular films provide a 30-fold increase in selectivity toward CO₂R products compared to the unmodified system and lowers Cd corrosion at least 10-fold. This dual

functionality highlights the promise of hybrid solid-state-molecular photocathodes for enabling efficient and durable solar fuel systems.

In **Chapter 4**, we identify polyaromatic layers derived from phenyldiazonium or diphenyliodonium salts are capable of boosting selectivity and activity toward C_{2+} products at variable pHs. We demonstrate the robustness of the films in high-performance testing under acidic conditions to emphasize their potential for use in other electrocatalytic transformations where selectivity or electrode stability remains an issue.

In **Chapter 5**, we find that increased hydrodynamics at the electrode surface results directly in changes to the ethylene and methane Tafel slopes, demonstrating that CO_2R mechanistic work must be considered in the context of the mass transport conditions. We extend our analysis to organic coatings, demonstrating that the films shield the active sites from variability in hydrodynamics and increase the residence time of CO so that it may be further reduced to desirable products.

In **Chapter 6**, we study the impact of local electrode heating on electrochemical CO_2 reduction. We reveal that peak C_{2+} performance can be shifted by 0.1 V compared to ambient conditions by heating the electrode to 60 °C in the presence of an organic film while maintaining an ambient bulk electrolyte. This result highlights a novel approach to thermal management and electrochemical systems design, as well as the opportunity to further probe thermal effects in electrochemical reactions.

1.4 References

- (1) Steffen, W.; Richardson, K.; Rockstrom, J.; Cornell, S. E.; Fetzer, I.; Bennett, E. M.; Biggs, R.; Carpenter, S. R.; de Vries, W.; de Wit, C. A.; Folke, C.; Gerten, D.; Heinke, J.; Mace, G. M.; Persson, L. M.; Ramanathan, V.; Reyers, B.; Sorlin, S. Planetary Boundaries: Guiding Human Development on a Changing Planet. *Science* **2015**, *347* (6223), 1259855–1259855. <https://doi.org/10.1126/science.1259855>.
- (2) United Nations Framework Convention on Climate Change. Adoption of the Paris Agreement. (2015).
- (3) Tong, D.; Zhang, Q.; Zheng, Y.; Caldeira, K.; Shearer, C.; Hong, C.; Qin, Y.; Davis, S. J. Committed Emissions from Existing Energy Infrastructure Jeopardize 1.5 °C Climate Target. *Nature* **2019**, *572* (7769), 373–377. <https://doi.org/10.1038/s41586-019-1364-3>.
- (4) Welch, A. J.; Dunn, E.; DuChene, J. S.; Atwater, H. A. Bicarbonate or Carbonate Processes for Coupling Carbon Dioxide Capture and Electrochemical Conversion. *ACS Energy Lett.* **2020**, *5* (3), 940–945. <https://doi.org/10.1021/acsenergylett.0c00234>.
- (5) Najjar, Y. S. H.; Abu-Shamleh, A. Performance Evaluation of a Large-Scale Thermal Power Plant Based on the Best Industrial Practices. *Sci. Rep.* **2020**, *10* (1), 20661. <https://doi.org/10.1038/s41598-020-77802-8>.
- (6) Hori, Y.; Kikuchi, K.; Murata, A.; Suzuki, S. Production of Methane and Ethylene in Electrochemical Reduction of Carbon Dioxide at Copper Electrode in Aqueous Hydrogencarbonate Solution. *Chem. Lett.* **1986**, *15* (6), 897–898. <https://doi.org/10.1246/cl.1986.897>.

- (7) Kuhl, K. P.; Cave, E. R.; Abram, D. N.; Jaramillo, T. F. New Insights into the Electrochemical Reduction of Carbon Dioxide on Metallic Copper Surfaces. *Energy Environ. Sci.* **2012**, *5* (5), 7050–7059. <https://doi.org/10.1039/C2EE21234J>.
- (8) Kuhl, K. P.; Hatsukade, T.; Cave, E. R.; Abram, D. N.; Kibsgaard, J.; Jaramillo, T. F. Electrocatalytic Conversion of Carbon Dioxide to Methane and Methanol on Transition Metal Surfaces. *J. Am. Chem. Soc.* **2014**, *136* (40), 14107–14113. <https://doi.org/10.1021/ja505791r>.
- (9) Gattrell, M.; Gupta, N.; Co, A. A Review of the Aqueous Electrochemical Reduction of CO₂ to Hydrocarbons at Copper. *J. Electroanal. Chem.* **2006**, *594* (1), 1–19. <https://doi.org/10.1016/j.jelechem.2006.05.013>.
- (10) Peterson, A. A.; Nørskov, J. K. Activity Descriptors for CO₂ Electroreduction to Methane on Transition-Metal Catalysts. *J. Phys. Chem. Lett.* **2012**, *3* (2), 251–258. <https://doi.org/10.1021/jz201461p>.
- (11) Bagger, A.; Ju, W.; Varela, A. S.; Strasser, P.; Rossmeisl, J. Electrochemical CO₂ Reduction: A Classification Problem. *ChemPhysChem* **2017**, *18* (22), 3266–3273. <https://doi.org/10.1002/cphc.201700736>.
- (12) Arquer, F. P. G. de; Dinh, C.-T.; Ozden, A.; Wicks, J.; McCallum, C.; Kirmani, A. R.; Nam, D.-H.; Gabardo, C.; Seifitokaldani, A.; Wang, X.; Li, Y. C.; Li, F.; Edwards, J.; Richter, L. J.; Thorpe, S. J.; Sinton, D.; Sargent, E. H. CO₂ Electrolysis to Multicarbon Products at Activities Greater than 1 A Cm⁻². *Science* **2020**, *367* (6478), 661–666. <https://doi.org/10.1126/science.aay4217>.

- (13) Hori, Y.; Takahashi, I.; Koga, O.; Hoshi, N. Electrochemical Reduction of Carbon Dioxide at Various Series of Copper Single Crystal Electrodes. *J. Mol. Catal. Chem.* **2003**, *199* (1), 39–47. [https://doi.org/10.1016/S1381-1169\(03\)00016-5](https://doi.org/10.1016/S1381-1169(03)00016-5).
- (14) Watanabe, K.; Nagashima, U.; Hosoya, H. An Ab Initio Study of Adsorbed Carbon Monoxide on a Metal Electrode by Cluster Model. *Appl. Surf. Sci.* **1994**, *75* (1), 121–124. [https://doi.org/10.1016/0169-4332\(94\)90147-3](https://doi.org/10.1016/0169-4332(94)90147-3).
- (15) Peng, H.; Tang, M. T.; Liu, X.; Lamoureux, P. S.; Bajdich, M.; Abild-Pedersen, F. The Role of Atomic Carbon in Directing Electrochemical CO(2) Reduction to Multicarbon Products. *Energy Environ. Sci.* **2020**. <https://doi.org/10.1039/D0EE02826F>.
- (16) Peng, H.; Tang, M. T.; Liu, X.; Schlexer Lamoureux, P.; Bajdich, M.; Abild-Pedersen, F. The Role of Atomic Carbon in Directing Electrochemical CO (2) Reduction to Multicarbon Products. *Energy Environ. Sci.* **2021**, *14* (1), 473–482. <https://doi.org/10.1039/D0EE02826F>.
- (17) Montoya, J. H.; Peterson, A. A.; Nørskov, J. K. Insights into C-C Coupling in CO₂ Electroreduction on Copper Electrodes. *ChemCatChem* **2013**, *5* (3), 737–742. <https://doi.org/10.1002/cctc.201200564>.
- (18) Xiao, H.; Cheng, T.; Goddard, W. A. Atomistic Mechanisms Underlying Selectivities in C₁ and C₂ Products from Electrochemical Reduction of CO on Cu(111). *J. Am. Chem. Soc.* **2017**, *139* (1), 130–136. <https://doi.org/10.1021/jacs.6b06846>.
- (19) Cheng, T.; Xiao, H.; Goddard, W. A. Full Atomistic Reaction Mechanism with Kinetics for CO Reduction on Cu(100) from Ab Initio Molecular Dynamics Free-

- Energy Calculations at 298 K. *Proc. Natl. Acad. Sci.* **2017**, *114* (8), 1795–1800.
<https://doi.org/10.1073/pnas.1612106114>.
- (20) Schreier, M.; Yoon, Y.; Jackson, M. N.; Surendranath, Y. Competition between H and CO for Active Sites Governs Copper-Mediated Electrosynthesis of Hydrocarbon Fuels. *Angew. Chem. Int. Ed.* **2018**, *57* (32), 10221–10225.
<https://doi.org/10.1002/anie.201806051>.
- (21) Liu, X.; Schlexer, P.; Xiao, J.; Ji, Y.; Wang, L.; Sandberg, R. B.; Tang, M.; Brown, K. S.; Peng, H.; Ringe, S.; Hahn, C.; Jaramillo, T. F.; Nørskov, J. K.; Chan, K. PH Effects on the Electrochemical Reduction of CO (2) towards C₂ Products on Stepped Copper. *Nat. Commun.* **2019**, *10* (1), 32. <https://doi.org/10.1038/s41467-018-07970-9>.
- (22) Lum, Y.; Cheng, T.; Goddard, W. A.; Ager, J. W. Electrochemical CO Reduction Builds Solvent Water into Oxygenate Products. *J. Am. Chem. Soc.* **2018**, *140* (30), 9337–9340. <https://doi.org/10.1021/jacs.8b03986>.
- (23) Garza, A. J.; Bell, A. T.; Head-Gordon, M. Mechanism of CO₂ Reduction at Copper Surfaces: Pathways to C₂ Products. *ACS Catal.* **2018**, *8* (2), 1490–1499.
<https://doi.org/10.1021/acscatal.7b03477>.
- (24) Goodpaster, J. D.; Bell, A. T.; Head-Gordon, M. Identification of Possible Pathways for C–C Bond Formation during Electrochemical Reduction of CO₂: New Theoretical Insights from an Improved Electrochemical Model. *J. Phys. Chem. Lett.* **2016**, *7* (8), 1471–1477. <https://doi.org/10.1021/acs.jpcllett.6b00358>.
- (25) Bard, A. J.; Faulkner, L. R.; Leddy, J.; Zoski, C. G. *Electrochemical Methods: Fundamentals and Applications*; Wiley, New York, 1980; Vol. 2.

- (26) Li, J.; Chang, X.; Zhang, H.; Malkani, A. S.; Cheng, M.; Xu, B.; Lu, Q. Electrokinetic and in Situ Spectroscopic Investigations of CO Electrochemical Reduction on Copper. *Nat. Commun.* **2021**, *12* (1), 3264. <https://doi.org/10.1038/s41467-021-23582-2>.
- (27) Shin, S.-J.; Choi, H.; Ringe, S.; Won, D. H.; Oh, H.-S.; Kim, D. H.; Lee, T.; Nam, D.-H.; Kim, H.; Choi, C. H. A Unifying Mechanism for Cation Effect Modulating C1 and C2 Productions from CO₂ Electroreduction. *Nat. Commun.* **2022**, *13* (1), 5482. <https://doi.org/10.1038/s41467-022-33199-8>.
- (28) Hori, Y.; Takahashi, R.; Yoshinami, Y.; Murata, A. Electrochemical Reduction of CO at a Copper Electrode. *J. Phys. Chem. B* **1997**, *101* (36), 7075–7081. <https://doi.org/10.1021/jp970284i>.
- (29) Schouten, K. J. P.; Qin, Z.; Pérez Gallent, E.; Koper, M. T. M. Two Pathways for the Formation of Ethylene in CO Reduction on Single-Crystal Copper Electrodes. *J. Am. Chem. Soc.* **2012**, *134* (24), 9864–9867. <https://doi.org/10.1021/ja302668n>.
- (30) Hori, Y.; Koga, O.; Watanabe, Y.; Matsuo, T. FTIR Measurements of Charge Displacement Adsorption of CO on Poly- and Single Crystal (100) of Cu Electrodes. *Electrochimica Acta* **1998**, *44* (8), 1389–1395. [https://doi.org/10.1016/S0013-4686\(98\)00261-8](https://doi.org/10.1016/S0013-4686(98)00261-8).
- (31) Smith, B. D.; Irish, D. E.; Kedzierzawski, P.; Augustynski, J. A Surface Enhanced Raman Scattering Study of the Intermediate and Poisoning Species Formed during the Electrochemical Reduction of CO₂ on Copper. *J. Electrochem. Soc.* **1997**, *144* (12), 4288–4296. <https://doi.org/10.1149/1.1838180>.

- (32) Gao, J.; Zhang, H.; Guo, X.; Luo, J.; Zakeeruddin, S. M.; Ren, D.; Grätzel, M. Selective C–C Coupling in Carbon Dioxide Electroreduction via Efficient Spillover of Intermediates As Supported by Operando Raman Spectroscopy. *J. Am. Chem. Soc.* **2019**, *141* (47), 18704–18714. <https://doi.org/10.1021/jacs.9b07415>.
- (33) Kim, Y.; Park, S.; Shin, S.-J.; Choi, W.; Min, B. K.; Kim, H.; Kim, W.; Hwang, Y. J. Time-Resolved Observation of C–C Coupling Intermediates on Cu Electrodes for Selective Electrochemical CO₂ Reduction. *Energy Environ. Sci.* **2020**, 10.1039/D0EE01690J. <https://doi.org/10.1039/D0EE01690J>.
- (34) Lobaccaro, P.; Singh, M. R.; Clark, E. L.; Kwon, Y.; Bell, A. T.; Ager, J. W. Effects of Temperature and Gas–Liquid Mass Transfer on the Operation of Small Electrochemical Cells for the Quantitative Evaluation of CO₂ Reduction Electrocatalysts. *Phys. Chem. Chem. Phys.* **2016**, *18* (38), 26777–26785. <https://doi.org/10.1039/C6CP05287H>.
- (35) Dunwell, M.; Yang, X.; Setzler, B. P.; Anibal, J.; Yan, Y.; Xu, B. Examination of Near-Electrode Concentration Gradients and Kinetic Impacts on the Electrochemical Reduction of CO₂ Using Surface-Enhanced Infrared Spectroscopy. *ACS Catal.* **2018**, *8* (5), 3999–4008. <https://doi.org/10.1021/acscatal.8b01032>.
- (36) Yang, K.; Kas, R.; Smith, W. A. In Situ Infrared Spectroscopy Reveals Persistent Alkalinity near Electrode Surfaces during CO₂ Electroreduction. *J. Am. Chem. Soc.* **2019**, *141* (40), 15891–15900. <https://doi.org/10.1021/jacs.9b07000>.
- (37) Ringe, S.; Clark, E. L.; Resasco, J.; Walton, A.; Seger, B.; Bell, A. T.; Chan, K. Understanding Cation Effects in Electrochemical CO₂ Reduction. *Energy Environ. Sci.* **2019**, *12* (10), 3001–3014. <https://doi.org/10.1039/C9EE01341E>.

- (38) Singh, M. R.; Kwon, Y.; Lum, Y.; Ager, J. W. I.; Bell, A. T. Hydrolysis of Electrolyte Cations Enhances the Electrochemical Reduction of CO₂ over Ag and Cu. *J. Am. Chem. Soc.* **2016**, *138* (39), 13006–13012. <https://doi.org/10.1021/jacs.6b07612>.
- (39) Ayemoba, O.; Cuesta, A. Spectroscopic Evidence of Size-Dependent Buffering of Interfacial PH by Cation Hydrolysis during CO₂ Electroreduction. *ACS Appl. Mater. Interfaces* **2017**, *9* (33), 27377–27382. <https://doi.org/10.1021/acsami.7b07351>.
- (40) Malkani, A. S.; Li, J.; Oliveira, N. J.; He, M.; Chang, X.; Xu, B.; Lu, Q. Understanding the Electric and Nonelectric Field Components of the Cation Effect on the Electrochemical CO Reduction Reaction. *Sci. Adv.* **2020**, *6* (45), eabd2569. <https://doi.org/10.1126/sciadv.abd2569>.
- (41) Li, J.; Wu, D.; Malkani, A. S.; Chang, X.; Cheng, M.-J.; Xu, B.; Lu, Q. Hydroxide Is Not a Promoter of C₂⁺ Product Formation in the Electrochemical Reduction of CO on Copper. *Angew. Chem.* **2020**, *132* (11), 4494–4499. <https://doi.org/10.1002/ange.201912412>.
- (42) Huang, J. E.; Li, F.; Ozden, A.; Sedighian Rasouli, A.; García de Arquer, F. P.; Liu, S.; Zhang, S.; Luo, M.; Wang, X.; Lum, Y.; Xu, Y.; Bertens, K.; Miao, R. K.; Dinh, C.-T.; Sinton, D.; Sargent, E. H. CO₂ Electrolysis to Multicarbon Products in Strong Acid. *Science* **2021**, *372* (6546), 1074–1078. <https://doi.org/10.1126/science.abg6582>.
- (43) Han, Z.; Kortlever, R.; Chen, H.-Y.; Peters, J. C.; Agapie, T. CO₂ Reduction Selective for C_{≥2} Products on Polycrystalline Copper with N-Substituted Pyridinium

Additives. *ACS Cent. Sci.* **2017**, *3* (8), 853–859.

<https://doi.org/10.1021/acscentsci.7b00180>.

- (44) Banerjee, S.; Han, X.; Thoi, V. S. Modulating the Electrode–Electrolyte Interface with Cationic Surfactants in Carbon Dioxide Reduction. *ACS Catal.* **2019**, *9* (6), 5631–5637. <https://doi.org/10.1021/acscatal.9b00449>.
- (45) Thevenon, A.; Rosas-Hernández, A.; Peters, J. C.; Agapie, T. In-Situ Nanostructuring and Stabilization of Polycrystalline Copper by an Organic Salt Additive Promotes Electrocatalytic CO₂ Reduction to Ethylene. *Angew. Chem. Int. Ed.* **2019**, *58* (47), 16952–16958. <https://doi.org/10.1002/anie.201907935>.
- (46) Nam, D.-H.; De Luna, P.; Rosas-Hernández, A.; Thevenon, A.; Li, F.; Agapie, T.; Peters, J. C.; Shekhah, O.; Eddaoudi, M.; Sargent, E. H. Molecular Enhancement of Heterogeneous CO₂ Reduction. *Nat. Mater.* **2020**, *19* (3), 266–276. <https://doi.org/10.1038/s41563-020-0610-2>.
- (47) Wang, J.; Cheng, T.; Fenwick, A. Q.; Baroud, T. N.; Rosas-Hernández, A.; Ko, J. H.; Gan, Q.; Goddard III, W. A.; Grubbs, R. H. Selective CO₂ Electrochemical Reduction Enabled by a Tricomponent Copolymer Modifier on a Copper Surface. *J. Am. Chem. Soc.* **2021**. <https://doi.org/10.1021/jacs.0c12478>.
- (48) Ozden, A.; Li, F.; García de Arquer, F. P.; Rosas-Hernández, A.; Thevenon, A.; Wang, Y.; Hung, S.-F.; Wang, X.; Chen, B.; Li, J.; Wicks, J.; Luo, M.; Wang, Z.; Agapie, T.; Peters, J. C.; Sargent, E. H.; Sinton, D. High-Rate and Efficient Ethylene Electrosynthesis Using a Catalyst/Promoter/Transport Layer. *ACS Energy Lett.* **2020**, *5* (9), 2811–2818. <https://doi.org/10.1021/acsenenergylett.0c01266>.

- (49) Li, F.; Thevenon, A.; Rosas-Hernández, A.; Wang, Z.; Li, Y.; Gabardo, C. M.; Ozden, A.; Dinh, C. T.; Li, J.; Wang, Y.; Edwards, J. P.; Xu, Y.; McCallum, C.; Tao, L.; Liang, Z.-Q.; Luo, M.; Wang, X.; Li, H.; O'Brien, C. P.; Tan, C.-S.; Nam, D.-H.; Quintero-Bermudez, R.; Zhuang, T.-T.; Li, Y. C.; Han, Z.; Britt, R. D.; Sinton, D.; Agapie, T.; Peters, J. C.; Sargent, E. H. Molecular Tuning of CO₂-to-Ethylene Conversion. *Nature* **2020**, *577* (7791), 509–513. <https://doi.org/10.1038/s41586-019-1782-2>.

*Chapter 2*BREAKING SCALING RELATIONSHIPS IN CO₂ REDUCTION ON
COPPER ALLOYS WITH ORGANIC ADDITIVES

Adapted from:

Lai, Y.; Watkins, N. B.; Rosas-Hernández, A.; Thevenon, A.; Heim, G. P.;
Zhou, L.; Wu, Y.; Peters, J. C.; Gregoire, J. M.; Agapie, T.*ACS Cent. Sci.* **2021**, 7 (10), 1756–1762.

DOI: 10.1021/acscentsci.1c00860

2.1 Introduction

The development of high-performing catalysts for sustainable and economically viable transformations remains a central goal of the chemical industry.¹ Chemical transformations are controlled by thermodynamic and kinetic rate laws that manifest as linear scaling relationships. Such relationships relating structure, activity, and reaction conditions, are established for a range of reactions, including H₂O oxidation and N₂, O₂, CO₂, and H₂O reduction performed on both heterogeneous and homogeneous catalysts.¹⁻⁷ Because they provide theoretical or empirical trends for a particular chemical process, these scaling relationships not only help explain chemical reactivity but also guide the rational design of new and improved catalysts. Determining the underlying connections in chemical processes is particularly desirable toward deconvoluting fundamental selectivity limitations and targeting specific products.^{2,8} Typically, the experimental establishment and breaking of scaling relationships, including mapping of volcano plots, deals with a small set of data points, a limitation that is sometimes compensated for by expansion of data sets through computation. Our development of high throughput electrochemistry coupled to automated product distribution analysis provides new opportunities for identifying scaling relationships.^{9,10} Herein, we demonstrate a combination of catalyst design, high throughput experimentation, and data science as a paradigm shift in both the identification of scaling relationships and the discovery of strategies for breaking them. We focus on applying this approach to CO₂ reduction (CO₂R) on Cu-based electrodes, an area where mechanistic complexity has obscured identification of scaling relationships, hindered catalyst optimization, and warrants further investigation.¹¹

As strategies to transform CO₂ at scale are considered for a more sustainable carbon economy, exploiting the unique ability of Cu to reduce CO₂ to C₂₊ hydrocarbons and oxygenates makes it an attractive catalyst for optimization. The complex pathways towards a myriad reduced products of CO₂R on Cu stymie efforts for producing carbon-coupled products with high selectivity and has prompted investigation into the mechanism of the transformation.¹¹ Systematic trends affecting selectivity have been shown with respect to adsorption energy scaling relationships and pH variation at the electrode surface.^{7,12–15} Promising strategies for improving CO₂R selectivity for C₂₊ products include changing catalyst morphology^{16–19} and electrolyte composition,^{14,20} employing bimetallic systems and alloys,^{21–23} and adding organic modifiers.^{24–29} While these techniques may facilitate altered product distributions, they are not amenable to identifying empirical scaling relationships due to substantial variation in catalyst preparation and electrochemical testing conditions across independent studies. It is consequently pertinent to conduct studies that systematically and broadly vary select parameters. We have identified bulk alloying of Cu as an underdeveloped, though promising strategy for catalyst optimization, with a large parameter space available based on the metal identity and composition,^{30,31} well suited for investigation using our high throughput screening system.^{9,10} Additionally, organic additives represent an attractive orthogonal parameter of catalyst design. They can impact performance in a manner that has seldom been achieved by tailoring inorganic electrocatalyst composition or morphology alone.³²

Inspired by recent success using molecular films to enhance the selectivity of catalysts for CO₂R,^{29,33–35} herein we describe the generation of a uniquely broad and systematic CO₂R catalyst database by combining a Cu bimetallic alloying strategy with the

use of organic additives. Selectivity analysis highlights the impact of integrating high throughput experimentation and data science to discover a power-low scaling relationship between partial current densities of CH₄ and C₂₊ that is broken upon coating with an organic additive, demonstrating a fundamental limitation of CO₂R on Cu and a strategy to overcome it through hybrid inorganic-organic interfaces.

2.2 Results and Discussion

To elucidate correlations in CO₂R, experiments were designed to observe a large dynamic range of catalyst properties while mitigating conflation with experiment parameters such as electrolyte composition and mass transport conditions. For the present work, we varied catalyst composition, applied potential, and molecular additive presence. The choice of Cu alloys was guided by our previous discovery that the alloying elements In, Co, Mn, and Zn alter the activity and selectivity of Cu in different ways, although that study was limited to detection of H₂, CH₄, and C₂H₄.¹⁰ Studying Cu alloys with each of these elements and with different concentrations that span face-centered cubic (fcc) alloys and intermetallic phases (XRD of homogeneous alloys shown in Figs. S2.12-16), we sought to obtain a more comprehensive map of the reactivity of Cu-based alloy catalysts and to identify any systematic trends. The molecular additive, N,N'-ethylene-phenanthroline dibromide (**1-Br₂**), was selected based on its ability to enhance Faradaic Efficiency (FE) and geometric partial current densities for C₂₊ products upon forming a well-defined film on polycrystalline Cu, primarily composed of a *para,para* isomer of the one-electron reduced and dimerized phenanthroline (Equation 1).³³

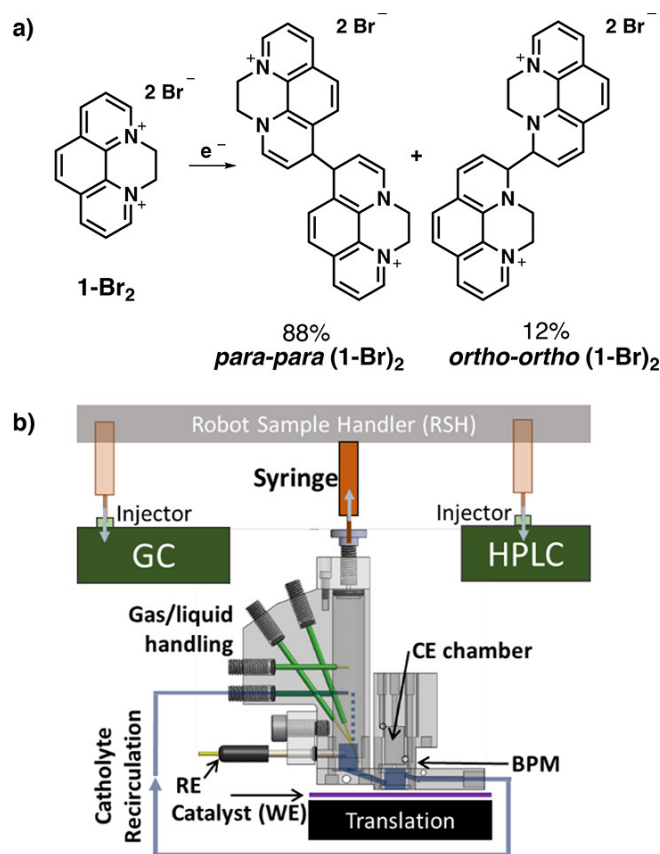


Figure 2.1: a) The electrochemical reductive coupling of two 1-Br_2 molecules results in a mixture of two products; b) The high throughput catalyst screening system where a select catalyst is positioned under a recirculating electrochemical batch reactor. After electrocatalyst operation, a robot sample handler (RSH) uses a syringe (orange) to extract aliquots from the headspace and then catholyte, with each aliquot injected into the respective analytical instrument (green, syringe positions in translucent orange) for gas or high-pressure liquid chromatography (GC, HPLC). The reference electrode (RE) is placed in the electrolyte inlet to the working electrode (WE) chamber, which is separated from the counter electrode (CE) chamber by a bipolar membrane (BPM).

Catalyst performance with or without the additive was evaluated by chronoamperometry (CA) at a series of up to 6 potentials with subsequent product analysis using the batch reactor flow system illustrated in Fig. 2.1. This system uses rapid electrolyte flow, as opposed to vigorous CO_2 bubbling, to generate suitable and reproducible mass transport conditions. The rapid concentration of reaction products enhances measurement throughput by enabling shorter electrolysis and faster chromatography compared to

traditional methods. Hybrid metal-organic electrodes were prepared via electrodeposition of organic films on the polycrystalline metal electrode from an aqueous 0.1 M KHCO_3 buffered electrolyte containing 0.1 mM **1-Br₂**. In total, experiments with 14 alloy catalysts and pure Cu provide electrochemical and partial current densities for 137 unique combinations of catalyst composition, additive presence, and applied potential, as shown for select Mn-doped catalysts in Figs. 2.2a, 2.2b and for all catalysts in Figs. S2.1-2.2.

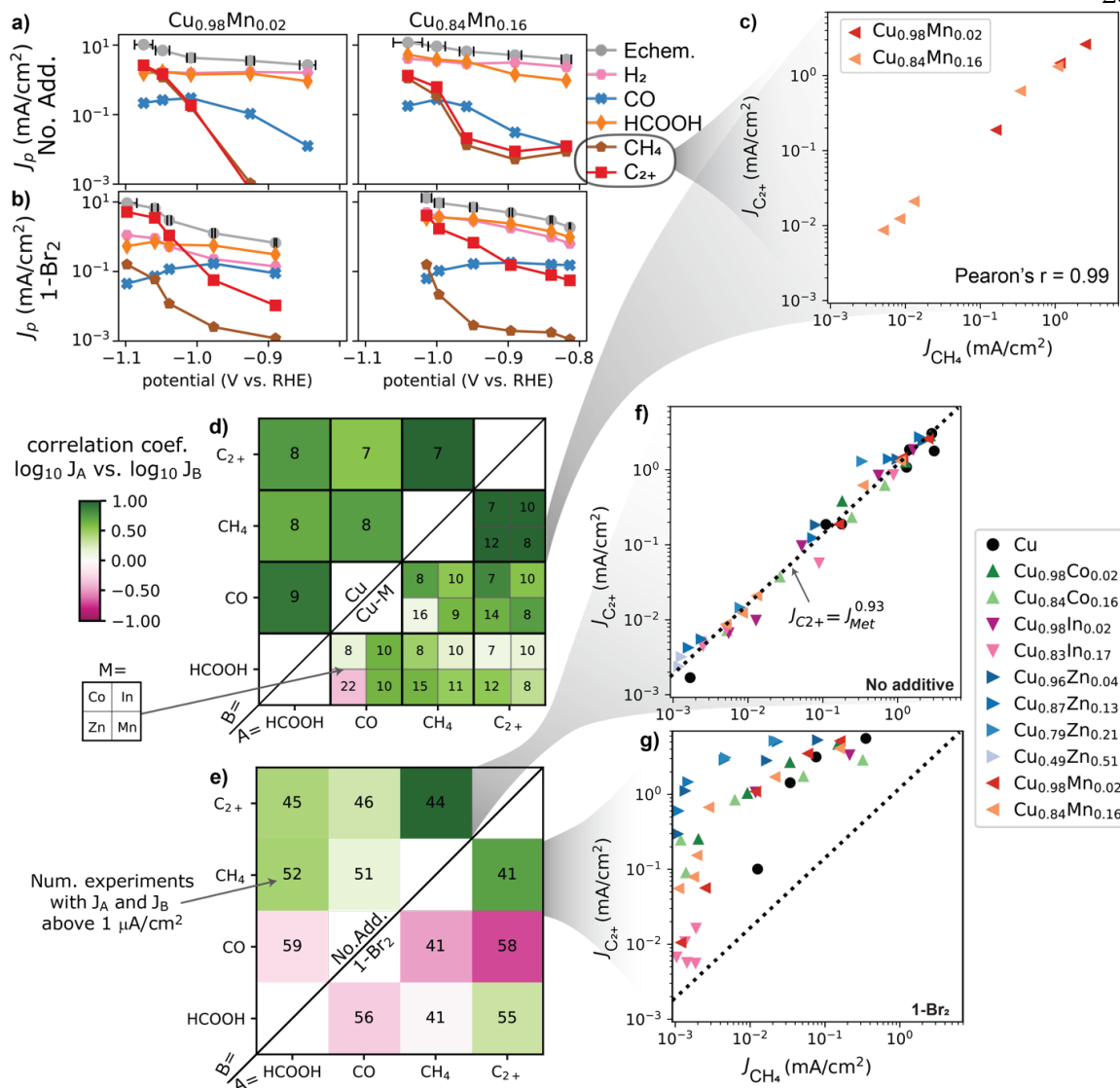


Figure 2.2: Illustration of acquired data and correlation analysis. The electrochemical and geometric partial current densities are shown for 5 electrolysis experiments with $\text{Cu}_{0.98}\text{Mn}_{0.02}$ and 6 electrolysis experiments with $\text{Cu}_{0.84}\text{Mn}_{0.16}$ catalysts, both a) without additive and b) with **1-Br₂**. Select products or product categories were considered for correlation analysis. For A = CH₄ and B = C₂₊, a) contains 8 electrolysis experiments with geometric partial current densities for both A and B above 1 $\mu\text{A}/\text{cm}^2$. The corresponding 8 points are shown in c) and used to calculate the Pearson correlation coefficient to represent additive-free Cu-Mn alloys. This analysis was applied to all 6 pairwise combinations of the products HCOOH, CO, CH₄, and C₂₊ and repeated for pure Cu and each Cu-M alloy system. The resulting set of correlation coefficients is shown in d). The printed numbers in each cell indicate the number of electrolysis experiments used in the calculation, for example 8 for the A = C₂₊, B = CH₄, M = Mn cell corresponding to the plot in c). This analysis was also applied to electrolysis experiments from all compositions, first with and then without **1-Br₂** additive,

to assess the impact of the additive on the 6 pairwise correlation coefficients, as shown in e). For $A = C_{2+}$ and $B = CH_4$ in e), the data underlying the correlation analysis is shown in f) without additive and in g) with $1-Br_2$, where points are colored according to their composition. The data in f) follow the power-law relationship indicated by the dashed line, which is also depicted in g) to show the extent by which the data with $1-Br_2$ deviate from this power-law relationship. The horizontal error bars in a) estimate the variation in potential in each electrolysis, and the quantified uncertainty for each partial current density is smaller than the point size (see experimental uncertainty section in SI).

Pairwise relationships of the geometric partial current density and the FE for representative products (Fig. S2.5) highlight the effect of the combined strategy of alloying and organic films. The intrinsic modification of catalyst selectivity can be detected through analysis of the Pearson correlation coefficient of the logarithm of partial current densities. A close-to-unity positive correlation indicates that selectivity between the two products cannot be tuned with the parameters under consideration, which is indicative of a free-energy scaling relationship. A substantially negative correlation indicates a trade-off in selectivity, wherein enhanced formation of one product occurs at the expense of the other, which is indicative of kinetic competition for a shared reaction intermediate.

The large dataset provided here via high throughput experimentation enables study of correlation coefficients and their modification (Fig. 2.2). Previous work on polycrystalline Cu indicates that the kinetic regimes that govern the CO_2R product distribution differ with applied potential due to modulation of energy landscape as a function of overpotential as well as second-order effects such as CO_2 mass transport and changes to the pH at the catalyst surface.^{36,37} To facilitate observation of how the catalyst itself affects selectivity, we aim to mitigate the influences from the extrinsic effects by limiting the overpotential range (-0.84 to -1.1 V vs RHE) and using rapid electrolyte flow over flat catalyst films with a maximum current density of 15 mA cm^{-2} , which promotes uniform mass transport and limits pH

gradients in the electrochemical reactor. This potential range includes the onset of substantial partial current density for highly reduced products, making alteration of correlation coefficients in this range a prime target for controlling product selectivity with catalyst modification. We first demonstrate Pearson correlation analysis to ascertain the extent by which high correlation coefficients can be lowered via variation in catalyst composition. For example, the box in Fig. 2.2d with A = CH₄ and B = C₂₊ shows a high correlation coefficient of 0.99 for these products when considering a series of 7 electrolysis experiments with a polycrystalline Cu catalyst in which partial current densities for both CH₄ and C₂₊ products varied from approximately 1 μA cm⁻² to 3 mA cm⁻². The analogous analysis for polycrystalline Cu-M alloys is summarized by the boxes with A = C₂₊ and B = CH₄, where the correlation coefficient was calculated for each alloying element using various combinations of alloy composition and applied potential. The source data and its utilization of correlation analysis are illustrated for the Cu-Mn system in Figs. 2.2a and 2.2c.

The total number of electrolysis conditions and range of alloy compositions (x in Cu_{1-x}M_x) are as follows: 7 conditions with M = Co and $x = 0.02$ or 0.16 ; 10 conditions with M = In and $x = 0.02$ or 0.17 ; 16 conditions with M = Zn and $x = 0.04, 0.13, 0.21,$ or 0.51 ; 8 conditions with M = Mn and $x = 0.02$ or 0.16 . Despite the variation in composition and potential within each of these Cu-M systems, each correlation coefficient remains in excess of 0.98, and in total the correlation coefficient for all Cu-M alloys is not meaningfully changed from that observed with pure Cu. Fig. 2.2f shows the aggregation of data for Cu and its alloys, demonstrating that a power-law relationship is closely followed over a broad range of composition and applied potential. This striking relationship, over three orders of

magnitude, in partial current densities, strongly suggests that on these bulk alloy catalysts there is a common branching point, or combination of branching points, that consistently partition between and CH_4 and C_{2+} products (Fig. 2.3a). Preservation of the $\text{CH}_4/\text{C}_{2+}$ ratio as observed here represents a newly discovered fundamental limitation for efforts to improve selectivity through bulk bimetallic alloying alone.

A simple rationale for the near 1:1 ratio observed for CH_4 and C_{2+} products is challenged by the complexity of the mechanism of CO_2R .³⁸ Under different reaction conditions, such as using an alternate bicarbonate concentration, a similar power-law trend is observed, but with a slightly different slope (Fig. S2.4). The up-shifted CH_4 to C_{2+} ratio agrees with the influence of KHCO_3 concentration where 0.1 M was considered to be the optimal environment for C_{2+} products.^{13,14,39,40} The preservation of the scaling relationship is therefore supportive of an intrinsic mechanistic limitation for the production of methane and C_{2+} products for the set of experimental conditions used herein. Also, the alloying elements substantially alter other aspects of the product distribution, making this collection of catalyst electrodes particularly well-suited for inferring intrinsic reactivity trends; the catalyst morphology is kept relatively constant with respect to the compendium of results in the literature.^{11,14,16,17,20–22,24–26,30,41} For example, through study of well-defined Cu surfaces, Hori and others identified that the relative production of CH_4 and C_2H_4 is highly facet-dependent.¹⁵ The distribution of exposed facets of a polycrystalline fcc-phase metal electrode could be altered via alloying due to changes in growth kinetics and/or relative surface energies upon addition of the alloying element, which would in principle provide a method to break the $\text{CH}_4/\text{C}_{2+}$ scaling relationship by tuning catalyst composition. However, the observation that the scaling relationship holds over a broad range of alloy compositions with

distinct product distributions indicates that facet selectivity is not the main contributor in the observed product selectivity.

CO₂R to highly-reduced products such as CH₄ and C₂₊ products proceeds via a common *CO intermediate.^{42,43} Methane synthesis is proposed to proceed via a Langmuir-Hinshelwood pathway, where a surface *H couples with *CO to form a *CHO or *COH intermediate that is further hydrogenated towards methane.^{42,44,45} Meanwhile, the production of C₂₊ products occurs via the coupling of two precursor *CO molecules, potentially involving intermediate *CHO or *COH adsorbates.^{42,43} The absence of CO-CH₄ or CO-C₂₊ power law relationships without the additive and the observation of a negative correlation coefficient between CO-ethylene in the presence of the additive are consistent with kinetic competition for a common intermediate (Fig S2.5). Despite variation in free CO produced (Fig S2.19), for the conditions tested, the assumed variation of CO concentration near the surface of the electrode is inconsequential with respect to the CH₄-C₂₊ relationship. Therefore, although the specific mechanism or mechanisms remain debated and may involve multiple pathways depending on morphology or crystal facet, the observed scaling relationship between CH₄ and C₂₊ indicates that the relative kinetics at the branching point(s), remarkably, remain rigorously locked at the same ratio over the many catalysts and applied potentials tested herein. Breaking this dependence is highly desirable for improved selectivity for C₂₊ products.

The Pearson correlation analysis was extended to the impact of the **1-Br₂** additive (Fig. 2.2e), where the correlation coefficient for each set of conditions includes the aggregation of all catalyst compositions and potentials. Coating the catalysts using **1-Br₂** lowers the correlation coefficient for CH₄ and C₂₊ from 0.99 to 0.74, a striking alteration

whose implication is that, within the range of catalyst compositions considered in the present work, tuning the selectivity between CH₄ and C₂₊ is only achieved in the presence of the additive, underscoring the importance of multi-modal catalyst development.⁴⁶

The basis by which the additive disrupts the scaling relationship between CH₄/C₂₊ (Fig. 2.2f) by increasing C₂₊ production and suppressing CH₄ formation (Fig 2.2g) is of particular interest. Fig. 2.3a illustrates the portion of the CO₂R reaction network wherein branching ratios dictate whether the common CO* intermediate results in the generation of CO, CH₄, or C₂₊ products. Fig. 2.3b highlights how catalyst modification with the organic additive moves product distribution almost completely away from CH₄, to the CO-C₂₊ vector of the graph. While accessing the CO-rich portion of the graph is commonplace in CO₂R electrocatalysis, the C₂₊-rich portion of the graph is only accessed in the presence of **1-Br₂**.¹¹ The maximal selectivity was obtained with a Cu_{0.85}Zn_{0.15} catalyst where 96% of the CO* intermediate was reduced to carbon-coupled products.

The breaking of the scaling relationship in the presence of **1-Br₂** cannot be explained by morphological changes or alloy segregation, as no nanostructuring was observed (Figs. S2.7-10, XRD in Figs. S2.12-16), therefore suggesting that the molecular additive improves selectivity via changes in the microkinetic pathway/s in this system. The organic additive may affect CH₄ - C₂₊ branching point(s) by i) alleviating a rate limitation of the formation of the bound *CHO/*COH intermediate and lowering the barrier towards C–C coupling or ii) promoting dimerization of the bound *CO relative to hydrogenation toward CH₄. In either case, kinetic competition for the *CO would be enhanced in the presence of the additive, which is consistent with the observation of a large and negative Pearson correlation between C₂₊ and CO (Fig. 2.2e). We additionally note that neither of these explanations for the

mechanism underlying the scaling law disruption has implications for the selectivity within the set of C_{2+} products. As shown in Fig. S2.6, additional correlations among these products are observed both in the absence and in the presence of the molecular additive, motivating future tuning of the catalyst system to tackle other branching points in the reaction network for enhanced control over product selectivity.

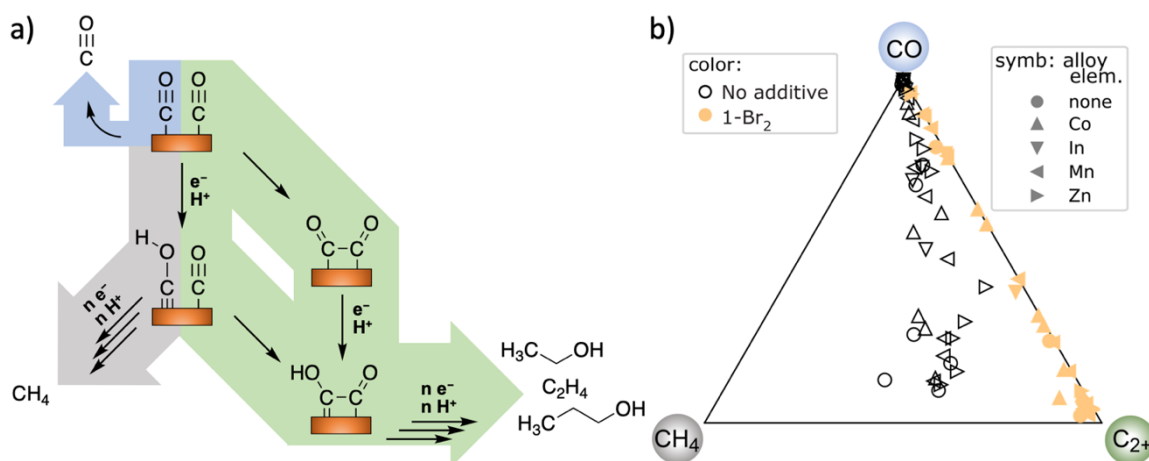


Figure 2.3: a) Possible reaction mechanisms, (selected from a multitude of variations previously proposed),¹¹ where pathways are highlighted in color with respect to their products in Fig. 2.3b. There are two branching points between CH₄ and C₂₊ products that could be responsible for the relationship observed in Fig. 2.2. The strong relationship between the grey and green pathways is broken with the addition of molecular additives, implying a potential change in mechanism. b) Summary of molar selectivity for reduction of the CO* intermediate. Measured partial current densities for CO, CH₄, and C₂₊ products are converted to molar flux of CO* required to produce the respective products, whose normalization provides the ternary composition for inclusion in this figure. Each electrolysis experiment produces 1 data point that indicates the catalyst's selectivity with respect to the three reaction pathways highlighted in part a) that start from the common CO* intermediate.

2.3 Conclusions

High throughput screening of the CO₂R activity and selectivity of Cu alloys with Co, In, Mn, and Zn revealed the propensity of organic additive **1-Br₂** to enable development of hybrid electrocatalysts that can reduce CO₂ to high order products with improved activity

and selectivity. The large data set led to the observation of a CH₄-C₂₊ scaling relationship that demonstrates a particularly robust link between these products over a large range of conditions. The CH₄-C₂₊ relationship represents an intrinsic limitation of selectivity tuning through alloying. However, it can be disrupted to favor C₂₊ products by the presence of the organic additive, highlighting the potential of hybrid organic-inorganic catalysts to tune branching ratios in the CO₂R reaction network. These observations highlight the importance of data-driven identification of relationships that provide mechanistic insights to guide study of complex reactions and catalyst development. Disentangling the possible explanations of the combined mechanistic influence of the additive and alloying elements will require substantial further investigation that will be guided by the observed data relationships elucidated in this study.

2.4 References

- (1) Seh, Z. W.; Kibsgaard, J.; Dickens, C. F.; Chorkendorff, I.; Nørskov, J. K.; Jaramillo, T. F. Combining Theory and Experiment in Electrocatalysis: Insights into Materials Design. *Science* **2017**, *355* (6321), eaad4998. <https://doi.org/10.1126/science.aad4998>.
- (2) Pérez-Ramírez, J.; López, N. Strategies to Break Linear Scaling Relationships. *Nat. Catal.* **2019**, *2* (11), 971–976. <https://doi.org/10.1038/s41929-019-0376-6>.
- (3) Greeley, J. Theoretical Heterogeneous Catalysis: Scaling Relationships and Computational Catalyst Design. *Annu. Rev. Chem. Biomol. Eng.* **2016**, *7* (1), 605–635. <https://doi.org/10.1146/annurev-chembioeng-080615-034413>.

- (4) Liu, X.; Xiao, J.; Peng, H.; Hong, X.; Chan, K.; Nørskov, J. K. Understanding Trends in Electrochemical Carbon Dioxide Reduction Rates. *Nat. Commun.* **2017**, *8* (1), 15438. <https://doi.org/10.1038/ncomms15438>.
- (5) Waldie, K. M.; Ostericher, A. L.; Reineke, M. H.; Sasayama, A. F.; Kubiak, C. P. Hydricity of Transition-Metal Hydrides: Thermodynamic Considerations for CO₂ Reduction. *ACS Catal.* **2018**, *8* (2), 1313–1324. <https://doi.org/10.1021/acscatal.7b03396>.
- (6) Ostericher, A. L.; Waldie, K. M.; Kubiak, C. P. Utilization of Thermodynamic Scaling Relationships in Hydricity To Develop Nickel Hydrogen Evolution Reaction Electrocatalysts with Weak Acids and Low Overpotentials. *ACS Catal.* **2018**, *8* (10), 9596–9603. <https://doi.org/10.1021/acscatal.8b02922>.
- (7) Martin, D. J.; Wise, C. F.; Pegis, M. L.; Mayer, J. M. Developing Scaling Relationships for Molecular Electrocatalysis through Studies of Fe-Porphyrin-Catalyzed O₂ Reduction. *Acc. Chem. Res.* **2020**, *53* (5), 1056–1065. <https://doi.org/10.1021/acs.accounts.0c00044>.
- (8) Vojvodic, A.; Nørskov, J. K. New Design Paradigm for Heterogeneous Catalysts. *Natl. Sci. Rev.* **2015**, *2* (2), 140–143. <https://doi.org/10.1093/nsr/nwv023>.
- (9) Jones, R. J. R.; Wang, Y.; Lai, Y.; Shinde, A.; Gregoire, J. M. Reactor Design and Integration with Product Detection to Accelerate Screening of Electrocatalysts for Carbon Dioxide Reduction. *Rev. Sci. Instrum.* **2018**, *89* (12), 124102. <https://doi.org/10.1063/1.5049704>.
- (10) Lai, Y.; Jones, R. J. R.; Wang, Y.; Zhou, L.; Richter, M. H.; Gregoire, J. The Sensitivity of Cu for Electrochemical Carbon Dioxide Reduction to Hydrocarbons as

- Revealed by High Throughput Experiments. *J. Mater. Chem. A* **2019**, *7* (47), 26785–26790. <https://doi.org/10.1039/C9TA10111J>.
- (11) Nitopi, S.; Bertheussen, E.; Scott, S. B.; Liu, X.; Engstfeld, A. K.; Horch, S.; Seger, B.; Stephens, I. E. L.; Chan, K.; Hahn, C.; Nørskov, J. K.; Jaramillo, T. F.; Chorkendorff, I. Progress and Perspectives of Electrochemical CO₂ Reduction on Copper in Aqueous Electrolyte. *Chem. Rev.* **2019**, *119* (12), 7610–7672. <https://doi.org/10.1021/acs.chemrev.8b00705>.
- (12) Peterson, A. A.; Nørskov, J. K. Activity Descriptors for CO₂ Electroreduction to Methane on Transition-Metal Catalysts. *J. Phys. Chem. Lett.* **2012**, *3* (2), 251–258. <https://doi.org/10.1021/jz201461p>.
- (13) Liu, X.; Schlexer, P.; Xiao, J.; Ji, Y.; Wang, L.; Sandberg, R. B.; Tang, M.; Brown, K. S.; Peng, H.; Ringe, S.; Hahn, C.; Jaramillo, T. F.; Nørskov, J. K.; Chan, K. PH Effects on the Electrochemical Reduction of CO(2) towards C₂ Products on Stepped Copper. *Nat. Commun.* **2019**, *10* (1), 32. <https://doi.org/10.1038/s41467-018-07970-9>.
- (14) Resasco, J.; Chen, L. D.; Clark, E.; Tsai, C.; Hahn, C.; Jaramillo, T. F.; Chan, K.; Bell, A. T. Promoter Effects of Alkali Metal Cations on the Electrochemical Reduction of Carbon Dioxide. *J. Am. Chem. Soc.* **2017**, *139* (32), 11277–11287. <https://doi.org/10.1021/jacs.7b06765>.
- (15) Hori, Y.; Takahashi, I.; Koga, O.; Hoshi, N. Electrochemical Reduction of Carbon Dioxide at Various Series of Copper Single Crystal Electrodes. *J. Mol. Catal. Chem.* **2003**, *199* (1), 39–47. [https://doi.org/10.1016/S1381-1169\(03\)00016-5](https://doi.org/10.1016/S1381-1169(03)00016-5).

- (16) Jeon, H. S.; Kunze, S.; Scholten, F.; Roldan Cuenya, B. Prism-Shaped Cu Nanocatalysts for Electrochemical CO₂ Reduction to Ethylene. *ACS Catal.* **2018**, *8* (1), 531–535. <https://doi.org/10.1021/acscatal.7b02959>.
- (17) Hahn, C.; Hatsukade, T.; Kim, Y.-G.; Vailionis, A.; Baricuatro, J. H.; Higgins, D. C.; Nitopi, S. A.; Soriaga, M. P.; Jaramillo, T. F. Engineering Cu Surfaces for the Electrocatalytic Conversion of CO₂: Controlling Selectivity toward Oxygenates and Hydrocarbons. *Proc. Natl. Acad. Sci.* **2017**, *114* (23), 5918–5923. <https://doi.org/10.1073/pnas.1618935114>.
- (18) Zhang, B.; Zhang, J.; Hua, M.; Wan, Q.; Su, Z.; Tan, X.; Liu, L.; Zhang, F.; Chen, G.; Tan, D.; Cheng, X.; Han, B.; Zheng, L.; Mo, G. Highly Electrocatalytic Ethylene Production from CO₂ on Nanodeficient Cu Nanosheets. *J. Am. Chem. Soc.* **2020**, *142* (31), 13606–13613. <https://doi.org/10.1021/jacs.0c06420>.
- (19) Wang, Y.; Wang, Z.; Dinh, C.-T.; Li, J.; Ozden, A.; Golam Kibria, M.; Seifitokaldani, A.; Tan, C.-S.; Gabardo, C. M.; Luo, M.; Zhou, H.; Li, F.; Lum, Y.; McCallum, C.; Xu, Y.; Liu, M.; Proppe, A.; Johnston, A.; Todorovic, P.; Zhuang, T.-T.; Sinton, D.; Kelley, S. O.; Sargent, E. H. Catalyst Synthesis under CO₂ Electroreduction Favours Faceting and Promotes Renewable Fuels Electrosynthesis. *Nat. Catal.* **2020**, *3* (2), 98–106. <https://doi.org/10.1038/s41929-019-0397-1>.
- (20) Singh, M. R.; Kwon, Y.; Lum, Y.; Ager, J. W.; Bell, A. T. Hydrolysis of Electrolyte Cations Enhances the Electrochemical Reduction of CO₂ over Ag and Cu. *J. Am. Chem. Soc.* **2016**, *138* (39), 13006–13012. <https://doi.org/10.1021/jacs.6b07612>.

- (21) Lum, Y.; Ager, J. W. Sequential Catalysis Controls Selectivity in Electrochemical CO₂ Reduction on Cu. *Energy Environ. Sci.* **2018**, *11* (10), 2935–2944. <https://doi.org/10.1039/C8EE01501E>.
- (22) Morales-Guio, C. G.; Cave, E. R.; Nitopi, S. A.; Feaster, J. T.; Wang, L.; Kuhl, K. P.; Jackson, A.; Johnson, N. C.; Abram, D. N.; Hatsukade, T.; Hahn, C.; Jaramillo, T. F. Improved CO₂ Reduction Activity towards C₂+ Alcohols on a Tandem Gold on Copper Electrocatalyst. *Nat. Catal.* **2018**, *1* (10), 764–771. <https://doi.org/10.1038/s41929-018-0139-9>.
- (23) Zhong, M.; Tran, K.; Min, Y.; Wang, C.; Wang, Z.; Dinh, C.-T.; De Luna, P.; Yu, Z.; Rasouli, A. S.; Brodersen, P.; Sun, S.; Voznyy, O.; Tan, C.-S.; Askerka, M.; Che, F.; Liu, M.; Seifitokaldani, A.; Pang, Y.; Lo, S.-C.; Ip, A.; Ulissi, Z.; Sargent, E. H. Accelerated Discovery of CO₂ Electrocatalysts Using Active Machine Learning. *Nature* **2020**, *581* (7807), 178–183. <https://doi.org/10.1038/s41586-020-2242-8>.
- (24) Wang, J.; Cheng, T.; Fenwick, A. Q.; Baroud, T. N.; Rosas-Hernández, A.; Ko, J. H.; Gan, Q.; Goddard III, W. A.; Grubbs, R. H. Selective CO₂ Electrochemical Reduction Enabled by a Tricomponent Copolymer Modifier on a Copper Surface. *J. Am. Chem. Soc.* **2021**, *143* (7), 2857–2865. <https://doi.org/10.1021/jacs.0c12478>.
- (25) Wei, X.; Yin, Z.; Lyu, K.; Li, Z.; Gong, J.; Wang, G.; Xiao, L.; Lu, J.; Zhuang, L. Highly Selective Reduction of CO₂ to C₂+ Hydrocarbons at Copper/Polyaniline Interfaces. *ACS Catal.* **2020**, *10* (7), 4103–4111. <https://doi.org/10.1021/acscatal.0c00049>.
- (26) Chen, X.; Chen, J.; Alghoraibi, N. M.; Henckel, D. A.; Zhang, R.; Nwabara, U. O.; Madsen, K. E.; Kenis, P. J. A.; Zimmerman, S. C.; Gewirth, A. A. Electrochemical

- CO₂-to-Ethylene Conversion on Polyamine-Incorporated Cu Electrodes. *Nat. Catal.* **2021**, *4* (1), 20–27. <https://doi.org/10.1038/s41929-020-00547-0>.
- (27) Buckley, A. K.; Lee, M.; Cheng, T.; Kazantsev, R. V.; Larson, D. M.; Goddard III, W. A.; Toste, F. D.; Toma, F. M. Electrocatalysis at Organic–Metal Interfaces: Identification of Structure–Reactivity Relationships for CO₂ Reduction at Modified Cu Surfaces. *J. Am. Chem. Soc.* **2019**, *141* (18), 7355–7364. <https://doi.org/10.1021/jacs.8b13655>.
- (28) Banerjee, S.; Han, X.; Thoi, V. S. Modulating the Electrode–Electrolyte Interface with Cationic Surfactants in Carbon Dioxide Reduction. *ACS Catal.* **2019**, *9* (6), 5631–5637. <https://doi.org/10.1021/acscatal.9b00449>.
- (29) Han, Z.; Kortlever, R.; Chen, H.-Y.; Peters, J. C.; Agapie, T. CO₂ Reduction Selective for C_{≥2} Products on Polycrystalline Copper with N-Substituted Pyridinium Additives. *ACS Cent. Sci.* **2017**, *3* (8), 853–859. <https://doi.org/10.1021/acscentsci.7b00180>.
- (30) Gao, D.; Arán-Ais, R. M.; Jeon, H. S.; Roldan Cuenya, B. Rational Catalyst and Electrolyte Design for CO₂ Electroreduction towards Multicarbon Products. *Nat. Catal.* **2019**, *2* (3), 198–210. <https://doi.org/10.1038/s41929-019-0235-5>.
- (31) He, J.; Dettelbach, K. E.; Salvatore, D. A.; Li, T.; Berlinguette, C. P. High-Throughput Synthesis of Mixed-Metal Electrocatalysts for CO₂ Reduction. *Angew. Chem. Int. Ed.* **2017**, *56* (22), 6068–6072. <https://doi.org/10.1002/anie.201612038>.
- (32) Nam, D.-H.; De Luna, P.; Rosas-Hernández, A.; Thevenon, A.; Li, F.; Agapie, T.; Peters, J. C.; Shekhah, O.; Eddaoudi, M.; Sargent, E. H. Molecular Enhancement of

Heterogeneous CO₂ Reduction. *Nat. Mater.* **2020**, *19* (3), 266–276.

<https://doi.org/10.1038/s41563-020-0610-2>.

- (33) Thevenon, A.; Rosas-Hernández, A.; Peters, J. C.; Agapie, T. In-Situ Nanostructuring and Stabilization of Polycrystalline Copper by an Organic Salt Additive Promotes Electrocatalytic CO₂ Reduction to Ethylene. *Angew. Chem. Int. Ed.* **2019**, *58* (47), 16952–16958. <https://doi.org/10.1002/anie.201907935>.
- (34) Li, F.; Thevenon, A.; Rosas-Hernández, A.; Wang, Z.; Li, Y.; Gabardo, C. M.; Ozden, A.; Dinh, C. T.; Li, J.; Wang, Y.; Edwards, J. P.; Xu, Y.; McCallum, C.; Tao, L.; Liang, Z.-Q.; Luo, M.; Wang, X.; Li, H.; O'Brien, C. P.; Tan, C.-S.; Nam, D.-H.; Quintero-Bermudez, R.; Zhuang, T.-T.; Li, Y. C.; Han, Z.; Britt, R. D.; Sinton, D.; Agapie, T.; Peters, J. C.; Sargent, E. H. Molecular Tuning of CO₂ -to-Ethylene Conversion. *Nature* **2020**, *577* (7791), 509–513. <https://doi.org/10.1038/s41586-019-1782-2>.
- (35) Thevenon, A.; Rosas-Hernández, A.; Fontani Herreros, A. M.; Agapie, T.; Peters, J. C. Dramatic HER Suppression on Ag Electrodes via Molecular Films for Highly Selective CO₂ to CO Reduction. *ACS Catal.* **2021**, *11* (8), 4530–4537. <https://doi.org/10.1021/acscatal.1c00338>.
- (36) Ren, D.; Fong, J.; Yeo, B. S. The Effects of Currents and Potentials on the Selectivities of Copper toward Carbon Dioxide Electroreduction. *Nat. Commun.* **2018**, *9* (1), 925. <https://doi.org/10.1038/s41467-018-03286-w>.
- (37) Hori, Y. Electrochemical CO₂ Reduction on Metal Electrodes. In *Modern Aspects of Electrochemistry*; Vayenas, C. G., White, R. E., Gamboa-Aldeco, M. E., Eds.; Springer: New York, 2008; Vol. 42, pp 89–189.

- (38) Kortlever, R.; Shen, J.; Schouten, K. J. P.; Calle-Vallejo, F.; Koper, M. T. M. Catalysts and Reaction Pathways for the Electrochemical Reduction of Carbon Dioxide. *J. Phys. Chem. Lett.* **2015**, *6* (20), 4073–4082. <https://doi.org/10.1021/acs.jpcllett.5b01559>.
- (39) Hori, Y.; Murata, A.; Takahashi, R. Formation of Hydrocarbons in the Electrochemical Reduction of Carbon Dioxide at a Copper Electrode in Aqueous Solution. *J. Chem. Soc. Faraday Trans. 1 Phys. Chem. Condens. Phases* **1989**, *85* (8), 2309. <https://doi.org/10.1039/f19898502309>.
- (40) Murata, A.; Hori, Y. Product Selectivity Affected by Cationic Species in Electrochemical Reduction of CO₂ and CO at a Cu Electrode. *Bull. Chem. Soc. Jpn.* **1991**, *64* (1), 123–127. <https://doi.org/10.1246/bcsj.64.123>.
- (41) Saberi Safaei, T.; Mepham, A.; Zheng, X.; Pang, Y.; Dinh, C.-T.; Liu, M.; Sinton, D.; Kelley, S. O.; Sargent, E. H. High-Density Nanosharp Microstructures Enable Efficient CO₂ Electroreduction. *Nano Lett.* **2016**, *16* (11), 7224–7228. <https://doi.org/10.1021/acs.nanolett.6b03615>.
- (42) Cheng, T.; Xiao, H.; Goddard, W. A. Full Atomistic Reaction Mechanism with Kinetics for CO Reduction on Cu(100) from Ab Initio Molecular Dynamics Free-Energy Calculations at 298 K. *Proc. Natl. Acad. Sci.* **2017**, *114* (8), 1795–1800. <https://doi.org/10.1073/pnas.1612106114>.
- (43) Garza, A. J.; Bell, A. T.; Head-Gordon, M. Mechanism of CO₂ Reduction at Copper Surfaces: Pathways to C₂ Products. *ACS Catal.* **2018**, *8* (2), 1490–1499. <https://doi.org/10.1021/acscatal.7b03477>.

- (44) Schreier, M.; Yoon, Y.; Jackson, M. N.; Surendranath, Y. Competition between H and CO for Active Sites Governs Copper-Mediated Electrosynthesis of Hydrocarbon Fuels. *Angew. Chem. Int. Ed.* **2018**, *57* (32), 10221–10225. <https://doi.org/10.1002/anie.201806051>.
- (45) Xiao, H.; Cheng, T.; Goddard, W. A. Atomistic Mechanisms Underlying Selectivities in C₁ and C₂ Products from Electrochemical Reduction of CO on Cu(111). *J. Am. Chem. Soc.* **2017**, *139* (1), 130–136. <https://doi.org/10.1021/jacs.6b06846>.
- (46) Other potential ways to disrupt the scaling relationship observed here include nanostructuring,^{16–18} higher overpotentials and current densities resulting in pH gradients,^{12–15,20} and bimetallic system engineering.^{21–23}

*Chapter 3***MOLECULAR COATINGS IMPROVE THE SELECTIVITY AND
DURABILITY OF CO₂ REDUCTION CHALCOGENIDE
PHOTOCATHODES**

Adapted from:

Lai, Y.; Watkins, N. B.; Muzzillo, C.; Richter, M.; Kan, K.; Zhou, L.;
Haber, J. A.; Zakutayev, A.; Peters, J. C.; Agapie, T.; Gregoire, J. M.
ACS Energy Lett. 2022, 7 (3), 1195–1201.
10.1021/acseenergylett.1c02762.

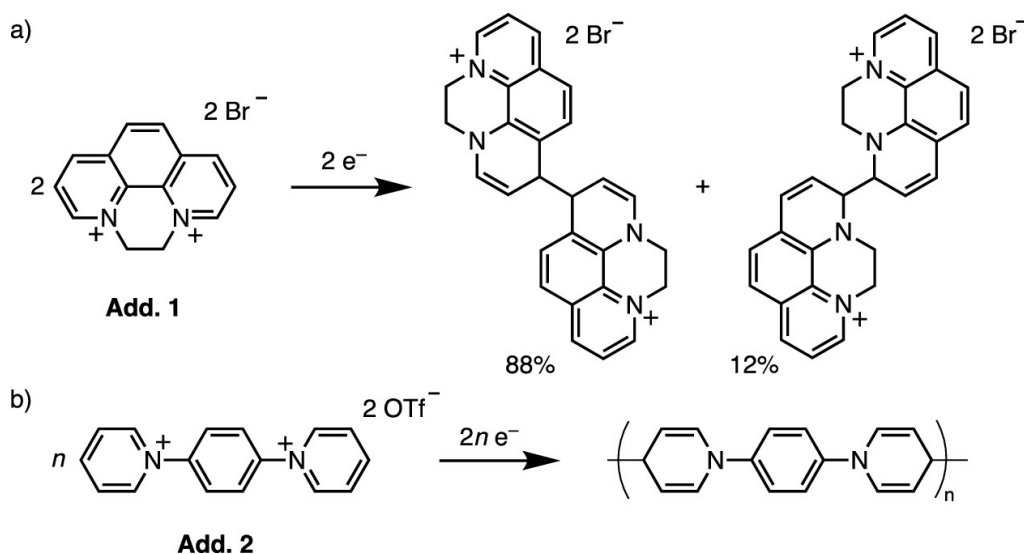
3.1 Introduction

The chalcopyrite family of semiconductors, exemplified by Cu(In,Ga)Se₂ (CIGS), is one of the most important for thin film photovoltaic applications,¹ with >23% solar energy conversion efficiency demonstrated in the lab and >19% efficiency as a solar module.² While the standard CIGS absorbers have been studied as photocathodes in photoelectrochemical (PEC) water splitting applications,^{3–5} to increase the photovoltage, a CdS layer is usually deposited to form a p-n heterojunction with the CIGS. However, due to the instability of the CdS during PEC catalysis,^{6,7} the surface is typically protected with a metal oxide (e.g., TiO₂ or ZnO) and activated with a hydrogen evolution reaction (HER) catalyst. Additionally, the 1.2–1.3 eV band gap of the most common CIGS absorber, CuIn_{0.7}Ga_{0.3}Se₂, is lower than ideal for most photoelectrochemical architectures. More recently, the wider band gap CuGaSe₂,^{8–11} Cu(In,Ga)(S,Se)₂,^{12,13} and (Ag,Cu)-GaSe₂^{14,15} chalcopyrite photocathodes have shown promise for PEC water splitting. Recent work has also expanded the use of CIGS-based photocathodes to CO₂ reduction (CO₂R).^{16–19}

Among chalcopyrite absorbers, one promising CO₂R photocathode is CuGa₃Se₅, an ordered-vacancy compound derived from CuGaSe₂,²⁰ due to its wider bandgap of 1.8 eV and suitable conduction band alignment for HER and CO₂R.²¹ CuGa₃Se₅ with ZnS or CdS adlayers and platinum cocatalysts has reached photocurrent densities of 8–9 mA cm⁻² at an applied bias of 0 V vs RHE^{22,23} and having been pretreated in Cd²⁺ solution with a Mg_xZn_{1-x}O capping layer demonstrates close to 1 V of photovoltage vs RHE.²⁴ In terms of stability, a bare CuGa₃Se₅ photocathode demonstrated 17 days of a continuous water splitting operation,²⁵ and a WO₃-protected CuGa₃Se₅ photocathode with a Pt catalyst layer sustained solar hydrogen evolution for 6 weeks.²⁶ These reports demonstrate the photoelectrochemical

stability of CuGa_3Se_5 , and durable surface modification of this material is one avenue to realize highly efficient and long-lasting fuel-forming PEC cells.

The performance of semiconductor photoelectrodes has long been modified using organic surface coatings of electrically conducting polymers to provide corrosion protection, passivate surface recombination sites, alter band edge positions by introducing dipoles at the surface, and accelerate interfacial charge separation.^{6,7,27,28} Notably, conducting polypyrrole coatings on CdS photoanodes has been shown to channel photogenerated holes to metal catalysts embedded in the polymer matrix, while preventing Cd leaching.^{6,7} Additionally, using methyl viologen as a protective conducting overlayer enhanced charge separation between $\text{Cu}_2\text{ZnSnS}_4$ photocathodes with inorganic buffer layers (CdS, CdSe, or ZnSe), which favorably shifts the flat band potential and improves electron transfer rates across the interface.²⁹



Scheme 3.1: Electrochemical dimerization of pyridinium-based molecular additives a) **Add. 1** and b) **Add. 2** results in an insoluble, nonconductive film on electrode surfaces.

An open question is whether nonconductive molecular films can improve selectivity of CO₂R photocathodes while also addressing the stability issues of the CdS coating. In prior work, two N-substituted pyridinium-derived molecular additives, N,N'-ethylene-phenanthroline dibromide (**Add. 1**) and N,N'-(1,4-phenylene)bipyridinium ditriflate (**Add. 2**), have been used with Cu and/or Ag electrodes for electrochemical CO₂R. Upon in situ reduction and dimerization/ oligomerization of the one-electron reduced additive into a nonconductive layer on the electrode surface (Scheme 1), the metal electrocatalyst exhibits a significant decrease in activity toward hydrogen evolution in favor of CO₂ reduction.³⁰⁻³⁴ Mechanisms proposed to account for the change in selectivity by these and other nonconductive organic films include slow diffusion of proton carriers to the electrode, lower H₂O and increased CO₂ concentration within the films, nanostructuring of the electrode, and interactions of intermediates of CO₂ reduction on the electrode with the film.³⁰⁻³⁶

3.2 Results and Discussion

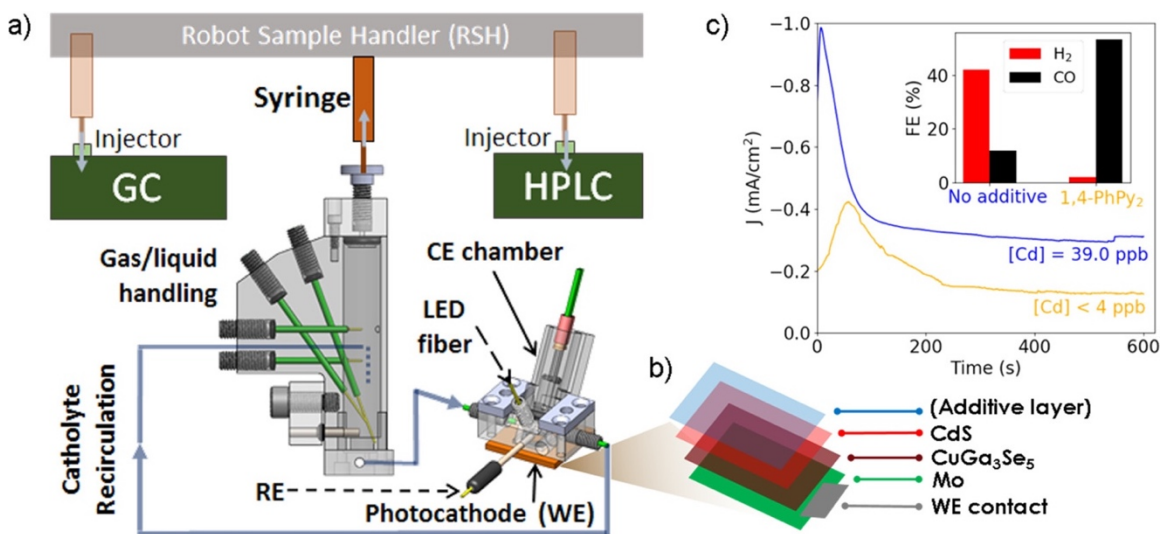


Figure 3.1. a) The HT-ANEC system with front-side electrode illumination includes an electrochemical reactor with fiber-coupled LED illumination, a CuGa₃Se₅/CdS working electrode (WE), a Ag/AgCl reference electrode (RE), and a bipolar membrane-separated chamber with a Pt counter electrode (CE). The electrolyte is recirculated through the reactor and a cell with 1 atm CO₂ headspace where the reactant CO₂ as well as reaction products are equilibrated with the headspace. After electrolysis, gas and liquid aliquots are robotically sampled for product analysis. b) The multilayer structure of the photocathode is illustrated, where the additive layer is generated *in situ* where applicable. c) Representative photoelectrocatalysis experiments at 0 V vs RHE both with and without molecular additive. Each photocurrent signal is averaged and compared to partial current densities of H₂ and CO from postelectrochemical product analysis to determine Faradaic efficiencies. The Cd concentration in the electrolyte from a postelectrolysis aliquot is also shown for each experiment.

Herein, we show that an organic coating derived from **Add. 1** or **Add. 2** improves both CO₂R selectivity and durability of a CdS-coated CuGa₃Se₅ photocathode. Cd corrosion and concomitant restructuring of the surface coating, as well as a H₂-rich product stream, are identified as primary shortcomings of additive-free photocathodes. Coatings formed during photoelectrochemistry in the presence of either additive address these issues, while the conformal coating formed in the presence of **Add. 2** offers the best performance, with more

than a 10-fold decrease in Cd corrosion and a 30-fold increase in CO:H₂. Exploration of this new class of hybrid molecular-inorganic photocathodes was facilitated by the high throughput analytical electrochemistry (HT-ANEC, Figure 3.1a) screening system reported previously,³⁷ adapted in the present work to include front-side illumination for accelerated screening of CO₂R photocathodes (Figure 3.1b). Initial experiments conducted on a high throughput instrument (electrochemical mass spectrometry: ECMS)³⁸ revealed that CuGa₃Se₅ with a CdS coating exhibits a higher photocurrent, diminished dark current, and lower FE for H₂ than the bare CuGa₃Se₅ surface (Figure S3.1). The observation of a negligible dark current in these initial experiments down to -0.4 V vs RHE informed the choice of subsequent operating potentials between 0.2 and -0.4 V vs RHE, such that the only current measured under illumination can be assumed to be the photocurrent. Continued catalyst optimization on the HT-ANEC system (Figure 3.1a) involved varying the illumination source, spanning from 2.1 eV (617 nm) to 3.2 eV (385 nm) at zero applied bias (Figure S3.2). While the 3.2-eV illumination showed a higher FE toward CO, the desire to use visible illumination for solar fuel applications and the consistency in product distribution at all lower photon energies led to the choice of 2.7-eV (455 nm) illumination for further studies.

Even upon incorporation of molecular films, CO and H₂ were the only products observed in this study, making the relative partial current densities toward these products the primary results for each photoelectrolysis experiment (representative data shown in Figure 3.1c). Over the course of each 10- min photoelectrolysis experiment, an initial peak in photocurrent was typically observed followed by a decay to a steadystate photocurrent. We quantify the average product distribution and corrosion through characterization of the

headspace and electrolyte upon conclusion of each photoelectrolysis experiment, producing results such as those indicated in the inset of Figure 3.1c. Inductively coupled plasma mass spectrometry (ICP-MS) was performed on postreaction electrolytes to quantify the corrosion of Cd from the electrode into solution. X-ray fluorescence (XRF) measurements on the electrode surface were performed to confirm the changes in elemental molar loadings of the electrode (see Table S3.1).

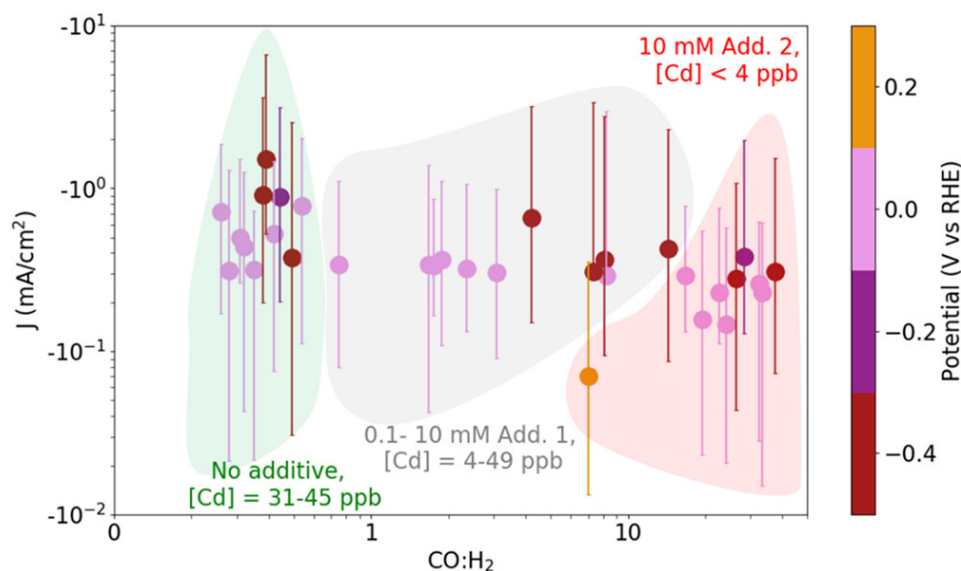


Figure 3.2. Summary of 32 photoelectrocatalysis experiments. For the indicated range of the applied electrochemical potential, the three conditions of no additive, **Add. 1**, and **Add. 2** form clusters indicated by shaded regions, where each additive offers improved CO₂R selectivity at the expense of the lowered photocurrent. The point for a given electrolysis experiment indicates the median photocurrent density with error bars extending from the minimum to maximum photocurrent density during the 10-min photoelectrolysis. The label for each cluster shows the range of Cd concentration in the electrolyte observed for each condition.

The experiments performed can be delineated using the CO:H₂ product ratio and the median photocurrent density from each photoelectrolysis experiment (Figure 3.2). The maximum and minimum of the photocurrent density are shown as vertical error bars. As

expected, changing the applied bias resulted in variation in the photocurrent and product ratio; however, these variations are relatively small compared to those observed when including a molecular additive in the electrolyte. With no additive, CO:H₂ remained below 1 for all experiments. Electrodes modified with **Add. 1** routinely produced CO:H₂ in excess of 1, and electrodes modified with **Add. 2** achieved CO:H₂ in excess of 30. As a result, these electrolysis experiments are cleanly clustered into three distinct groups, with each cluster labeled by the additive as well as the range of the observed concentration of Cd in the electrolyte. Notably, the presence of **Add. 2** lowers Cd levels in the electrolyte from 31 to 45 ppb observed in the absence of a molecular additive to below the noise level of 4 ppb. A range of concentrations of **Add. 1** was evaluated to assess any impact on product selectivity (see Table S3.1), and the concentration was found to be less important than the presence and choice of additive.

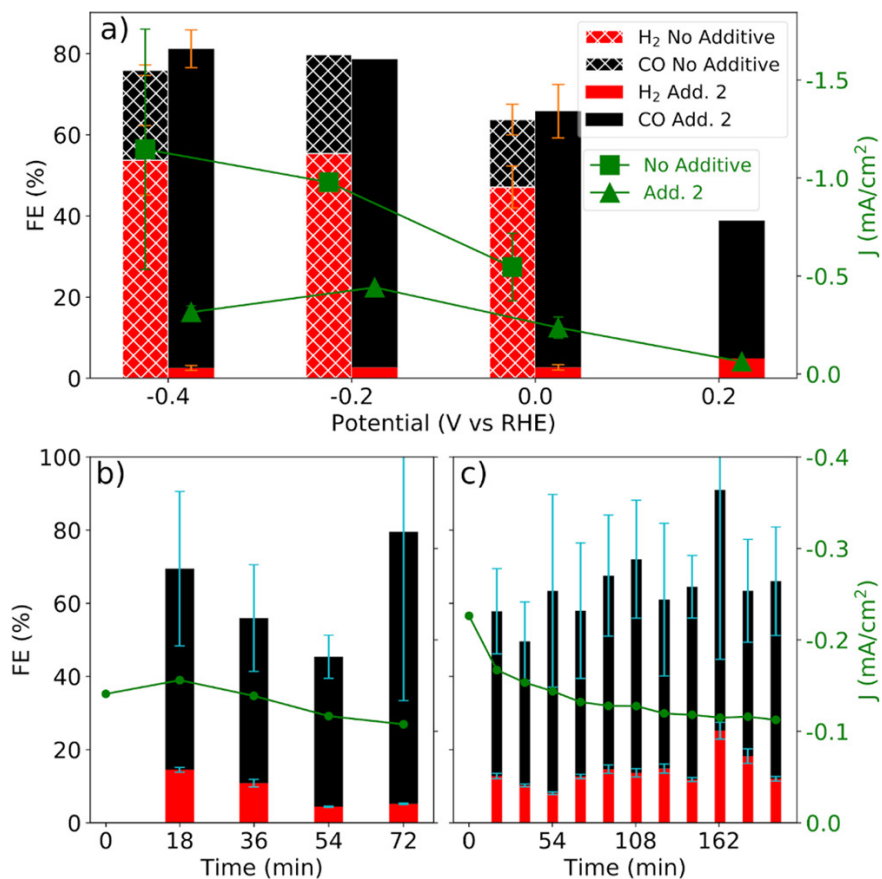


Figure 3.3. a) Aggregation of the experiments in Figure 3.2 for the no-additive and **Add. 2** conditions, showing that the presence of the additive provides high selectivity toward CO. The error bars for both FE and J at -0.4 and 0 V vs RHE represent the standard deviation of the respective measurements over several photoelectrocatalysis experiments shown in Figure 3.2. The shift of the green data points from the labeled potentials groups them with the barplot at the same conditions (with or without **Add. 2**) and does not indicate that the potential is shifted. b) Validation of the high throughput screening results with 10 mM **Add. 2** using a traditional H-cell at 0 V vs RHE with periodic headspace measurements. c) Continued operation of the H-cell with the same electrode at the same potential but starting with the additive-free electrolyte. The continued high CO selectivity and photocurrent demonstrate that the organic coating formed from the initial operation persists and remains effective at suppressing HER in favor of CO₂R to CO. The error bars in b) and c) represent the uncertainty of product quantification by the analytical instruments, and the photocurrent density (green) in these panels corresponds to the right axis.

The potential-dependent selectivity and activity of CuGa₃Se₅/CdS with and without the **Add. 2** additive demonstrate how the organic film causes an increase in selectivity for

CO vs H₂ by more than 30-fold at the expense of a 2–4-fold reduction in the photocurrent (Figure 3.3a). While suppression of HER appears to be a primary contributor to the decrease in the photocurrent (Figure S3.3), the additives may also attenuate the intensity of the incident light and contribute to the observed lower photocurrent. The partial current density for CO at 0 V vs RHE increases with **Add. 1** and even more so with **Add. 2** compared to the no-additive baseline, which may be due to retention of the Cd coating that facilitates carrier extraction from CuGa₃Se₅ as discussed further below. In dark electrolysis experiments with cathodic current densities between 0.5 and 15 mA cm⁻², the total FE of measured products can routinely be as low as 80% due to imperfect product extraction from the headspace from the HT-ANEC system.³⁷ As shown in Figure 3.3a, measurements at -0.2 and -0.4 V vs RHE both with and without an additive result in total FE near 80%. At higher potentials, lower total FE is observed, although this may be due to the lower photocurrent densities causing lower product concentrations and thus increased systematic error in FE quantification. These results can neither confirm nor deny the presence of photoelectrochemical reactions beyond the HER and CO₂R. Possible side reactions include Cd corrosion and electrodeposition of the molecular additive, and a more quantitative evaluation of FE will be pursued in future work.

To validate the primary result of the high throughput screening, a pair of CuGa₃Se₅/CdS electrodes was tested in a traditional H-cell using 10 mM of **Add. 2** and 0 V vs RHE. One experiment involved isotopic labeling in which the cell was operated with a sealed headspace of ¹³CO₂ for 2 h, after which the photoelectrochemical operation was paused and the headspace was changed to flowing ¹³CO₂. After acquiring a background mass spectroscopy (MS) signal, photoelectrochemistry was resumed, resulting in the subsequent

detection of ^{13}CO in the headspace (Figure S3.4) and thereby confirming photoelectrochemical reduction of $^{13}\text{CO}_2$ to ^{13}CO . The second experiment focused on stability and involved a total of 4.5 h of photoelectrolysis at 0 V vs RHE. The first 1.2 h were conducted in the presence of 10 mM **Add. 2**, followed by 3.3 h with the additive-free electrolyte to ascertain whether a stable photocurrent and product distribution could be obtained with the already-deposited molecular coating. The photocurrent and product distribution are shown in Figure 3.3, which has a large uncertainty for FE of CO due to the detection mechanism on this instrument. The results confirm that the high selectivity toward CO in the presence of the additive is maintained upon replacement with the fresh electrolyte. While a higher cathodic photocurrent is initially observed, the subsequent steady-state photocurrent is comparable to that observed with the additive present in the electrolyte. Furthermore, ICP-MS characterization of the additive-free electrolyte after 3.3 h of operation did not show any Cd in the solution (Table S3.1). These results collectively show that **Add. 2** may be applied as a final step of the electrode synthesis, resulting in an electrode that may be operated with no requirements of the additive's presence in the electrolyte, although the stability and possible regeneration requirements for device-scale operation remain under investigation.

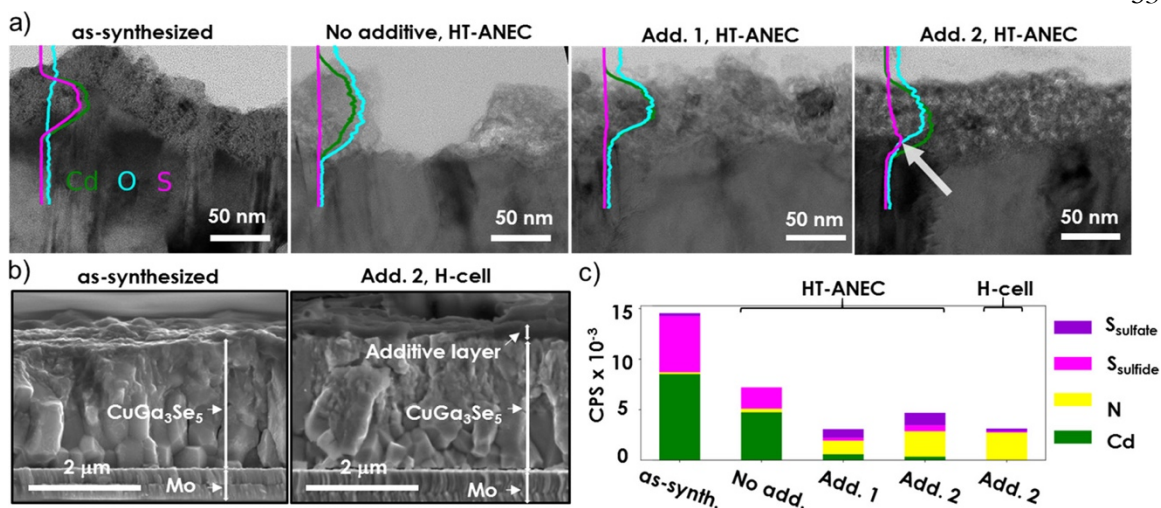


Figure 3.4. a) Cross section TEM measurements of the Cd-based layer and its interface to the CuGa_3Se_5 absorber layer for as-synthesized electrodes and electrodes operated at 0 V vs RHE in the HT-ANEC system with no additive and with each of the molecular additives. The overlay composition plot in each image shows the measured depth profile of Cd, S, and O concentrations from EDS line-scan imaging (see Figure S3.7 for additional composition data), and an arrow points to the retention of S due to the presence of **Add. 2**. Note that the lack of additives seen on TEM images is due to their low contrast to the capping agent used for preparing TEM samples. b) Cross section SEM images of an as-synthesized $\text{CuGa}_3\text{Se}_5/\text{CdS}$ electrode and the electrode with organic coating after the conclusion of the Figure 3c experiment. The coating appears conformal with an approximately 200-nm thickness (see Figure S3.5 for more information). c) XPS characterization of the five conditions from a) and b) for the near-surface compositions. Other detected species can be found in Figure S3.6b. Note that the H-cell data in b) and c) were acquired on the electrode after both the 1.2-h operation with and the 3.3-h operation without **Add. 2**.

Characterization of the postcatalysis electrode surfaces lends insight into the mechanism by which the catalyst performance is enhanced. Tunneling electron microscopy (TEM) with energy dispersive spectroscopy (EDS) mapping was performed to compare the ca. 50 nm CdS capping layer of the as synthesized electrode with electrodes tested by HT-ANEC at 0 V vs RHE with no additive, 0.1 mM **Add. 1**, and 10 mM **Add. 2** (Figures 3.4a and S3.7). Images and compositions of the electrode surfaces postcatalysis show that without an organic coating, the CdS layer is greatly depleted of sulfur in favor of oxygen. These

observations are consistent with an electrochemical reaction that results in partial corrosion and coarsening of the adlayer, which is evident in top-down SEM and TEM images with a larger field of view that show a nanocube morphology (Figures S3.5a and S3.5c). The same phenomena are observed with **Add. 1** but to a lesser extent, which combined with our observation of variable Cd leaching concentrations (Figure 3.2, Table S3.1), suggest that this additive only partially protects the Cd-based layer. With **Add. 2**, the Cd-based coating remains compact, with a 30-nm sulfur containing layer near the interface with the CuGa_3Se_5 absorber that is not observed in the other samples (Figures 3.4a and S3.7). This remaining CdS-like layer is key to preserving the photoactivity of CuGa_3Se_5 and other chalcogenide absorbers.²⁴

To understand the role of **Add. 2** in protecting the CuGa_3Se_5 photoabsorber and preserving the CdS layer, scanning electron microscopy (SEM) and X-ray photoelectron spectroscopy (XPS) measurements were performed. Analysis of the film created by **Add. 2** by cross-sectional SEM revealed that after 4.5 h of operation, a near 200-nm conformal coating is observed with some larger features (Figures 3.4b and S3.5). This result is commensurate with the reported thicknesses of electrodeposited films derived from analogous pyridinium salt precursors on copper and silver electrodes and is on average thicker than the ~30-nm film afforded by **Add. 1**.^{31,34} The **Add. 2** coating results in lower coarsening and improved retention of the CdS layer than in the other experiments, which we attribute to improved protection from its high conformality and greater thickness. XPS near-surface characterization supports the findings that the Cd and S in the as-synthesized electrode are observed to a lesser extent after operation with no additive due to corrosion and

oxidation of the CdS layer (Figures 3.4c and S3.8). The Cd signal is increasingly suppressed with **Add. 1** and **Add. 2**, as the molecular coatings attenuate the signals from the Cd-based layers observed in Figure 3.4a. While the relative impact on product selectivity and corrosion mitigation between the two additives is commensurate with the observed differences in the morphology of the generated coatings, the chemical mechanism for the absolute and relative performance enhancements will be investigated in future work.

3.3 Conclusions

Given the importance of CdS in passivation of surface defects for improved carrier extraction efficiency,²⁴ the ability of **Add. 2** to inhibit coarsening in the Cd-based layer, and thereby maintain sulfur in CdS at the CuGa₃Se₅ absorber interface, is an important observation. Furthermore, due to the lack of Cu, Ga, or Se leaching and the persistence of a compact Cd-based layer in the presence of either additive, we believe these results will generalize to light absorbers beyond CuGa₃Se₅. Given that CdS is an effective contact material for CIGS chalcopyrite and the multitude of other absorber chemistries,^{39,40} these additives, especially **Add. 2**, may more generally improve the stability of the Cd-based coating while substantially suppressing HER in favor of CO₂R. Differences in photovoltage provided by different absorber layers will likely alter the applied bias required to obtain the equivalent (unquantified) surface potential of the electrodes in the present work. The observation of CO₂R with high selectivity at a bias of 0.2 V vs RHE demonstrates that the turn-on potential for CO₂R photoelectrocatalysis is even higher, making these photocathodes competitive with state-of-the-art photocathodes, such as the Pt-TiO₂/GaN/n⁺-p-Si photocathodes with turn-on potentials near 0.47 V vs RHE⁴¹ and nanoporous Au thin films

on Si photoelectrodes with turn-on potentials >0.2 V vs RHE.⁴² To close, molecular additives such as those described herein are attractive for the continued improvement of the turn-on potential, durability, and CO₂R selectivity, which are all critical to realize photoelectrochemical generation of solar fuels.

3.4 References

- (1) Reinhard, P.; Chirilă, A.; Blösch, P.; Pianezzi, F.; Nishiwaki, S.; Buechelers, S.; Tiwari, A. N. Review of Progress toward 20% Efficiency Flexible CIGS Solar Cells and Manufacturing Issues of Solar Modules. In *2012 IEEE 38th Photovoltaic Specialists Conference (PVSC) PART 2*; 2012; pp 1–9. <https://doi.org/10.1109/PVSC-Vol2.2012.6656789>.
- (2) Green, M.; Dunlop, E.; Hohl-Ebinger, J.; Yoshita, M.; Kopidakis, N.; Hao, X. Solar Cell Efficiency Tables (Version 57). *Prog. Photovolt. Res. Appl.* **2021**, *29* (1), 3–15. <https://doi.org/10.1002/pip.3371>.
- (3) Yokoyama, D.; Minegishi, T.; Maeda, K.; Katayama, M.; Kubota, J.; Yamada, A.; Konagai, M.; Domen, K. Photoelectrochemical Water Splitting Using a Cu(In,Ga)Se₂ Thin Film. *Electrochem. Commun.* **2010**, *12* (6), 851–853. <https://doi.org/10.1016/j.elecom.2010.04.004>.
- (4) Mali, M. G.; Yoon, H.; Joshi, B. N.; Park, H.; Al-Deyab, S. S.; Lim, D. C.; Ahn, S.; Nervi, C.; Yoon, S. S. Enhanced Photoelectrochemical Solar Water Splitting Using a Platinum-Decorated CIGS/CdS/ZnO Photocathode. *ACS Appl. Mater. Interfaces* **2015**, *7* (38), 21619–21625. <https://doi.org/10.1021/acsami.5b07267>.

- (5) Hadke, S.; Huang, M.; Chen, C.; Tay, Y. F.; Chen, S.; Tang, J.; Wong, L. Emerging Chalcogenide Thin Films for Solar Energy Harvesting Devices. *Chem. Rev.* **2022**, *122* (11), 10170–10265. <https://doi.org/10.1021/acs.chemrev.1c00301>.
- (6) Frank, A. J.; Honda, K. Oxygen and Hydrogen Generation from Water on Polymer-Protected CdS Photoanodes. *J. Electroanal. Chem. Interfacial Electrochem.* **1983**, *150* (1), 673–678. [https://doi.org/10.1016/S0022-0728\(83\)80246-0](https://doi.org/10.1016/S0022-0728(83)80246-0).
- (7) Honda, K.; Frank, A. J. Polymer-Catalyst-Modified Cadmium Sulfide Photochemical Diodes in the Photolysis of Water. *J. Phys. Chem.* **1984**, *88* (23), 5577–5582. <https://doi.org/10.1021/j150667a024>.
- (8) Moriya, M.; Minegishi, T.; Kumagai, H.; Katayama, M.; Kubota, J.; Domen, K. Stable Hydrogen Evolution from CdS-Modified CuGaSe₂ Photoelectrode under Visible-Light Irradiation. *J. Am. Chem. Soc.* **2013**, *135* (10), 3733–3735. <https://doi.org/10.1021/ja312653y>.
- (9) Gaillard, N.; Prasher, D.; Kaneshiro, J.; Mallory, S.; Chong, M. Development of Chalcogenide Thin Film Materials for Photoelectrochemical Hydrogen Production. *MRS Online Proc. Libr.* **2013**, *1558* (1), 207. <https://doi.org/10.1557/opl.2013.1084>.
- (10) Ikeda, S.; Fujita, W.; Okamoto, R.; Nose, Y.; Katsube, R.; Yoshino, K.; Harada, T. Preparation of a CuGaSe₂ Single Crystal and Its Photocathodic Properties. *RSC Adv.* **2020**, *10* (66), 40310–40315. <https://doi.org/10.1039/D0RA07904A>.
- (11) Ikeda, S.; Okamoto, R.; Ishizuka, S. Enhancement of the Photoelectrochemical Properties of a CuGaSe₂-Based Photocathode for Water Reduction Induced by Loading of a Cu-Deficient Layer at the p–n Heterointerface. *Appl. Phys. Lett.* **2021**, *119* (8), 083902. <https://doi.org/10.1063/5.0060494>.

- (12) Gaillard, N.; Prasher, D.; Chong, M.; Deangelis, A.; Horsley, K.; Ishii, H. A.; Bradley, J. P.; Varley, J.; Ogitsu, T. Wide-Bandgap Cu(In,Ga)S₂ Photocathodes Integrated on Transparent Conductive F:SnO₂ Substrates for Chalcopyrite-Based Water Splitting Tandem Devices. *ACS Appl. Energy Mater.* **2019**, *2* (8), 5515–5524. <https://doi.org/10.1021/acsaem.9b00690>.
- (13) DeAngelis, A. D.; Horsley, K.; Gaillard, N. Wide Band Gap CuGa(S,Se)₂ Thin Films on Transparent Conductive Fluorinated Tin Oxide Substrates as Photocathode Candidates for Tandem Water Splitting Devices. *J. Phys. Chem. C* **2018**, *122* (26), 14304–14312. <https://doi.org/10.1021/acs.jpcc.8b02915>.
- (14) Zhang, L.; Minegishi, T.; Nakabayashi, M.; Suzuki, Y.; Seki, K.; Shibata, N.; Kubota, J.; Domen, K. Durable Hydrogen Evolution from Water Driven by Sunlight Using (Ag,Cu)GaSe₂ Photocathodes Modified with CdS and CuGa₃Se₅. *Chem. Sci.* **2015**, *6* (2), 894–901. <https://doi.org/10.1039/C4SC02346C>.
- (15) Zhang, L.; Minegishi, T.; Kubota, J.; Domen, K. Hydrogen Evolution from Water Using Ag_xCu_{1-x}GaSe₂ Photocathodes under Visible Light. *Phys. Chem. Chem. Phys.* **2014**, *16* (13), 6167–6174. <https://doi.org/10.1039/C3CP54590C>.
- (16) Pati, P. B.; Wang, R.; Boutin, E.; Diring, S.; Jobic, S.; Barreau, N.; Odobel, F.; Robert, M. Photocathode Functionalized with a Molecular Cobalt Catalyst for Selective Carbon Dioxide Reduction in Water. *Nat. Commun.* **2020**, *11* (1), 3499. <https://doi.org/10.1038/s41467-020-17125-4>.
- (17) Foster, B. M.; Paris, A. R.; Frick, J. J.; Blasini-Pérez, D. A.; Cava, R. J.; Bocarsly, A. B. Catalytic Mismatching of CuInSe₂ and Ni₃Al Demonstrates Selective

- Photoelectrochemical CO₂ Reduction to Methanol. *ACS Appl. Energy Mater.* **2020**, 3 (1), 109–113. <https://doi.org/10.1021/acsaem.9b01441>.
- (18) Hu, Z.; Gong, J.; Ye, Z.; Liu, Y.; Xiao, X.; Yu, J. C. Cu(In,Ga)Se₂ for Selective and Efficient Photoelectrochemical Conversion of CO₂ into CO. *J. Catal.* **2020**, 384, 88–95. <https://doi.org/10.1016/j.jcat.2020.02.015>.
- (19) Tran, P. D.; Wong, L. H.; Barber, J.; Loo, J. S. C. Recent Advances in Hybrid Photocatalysts for Solar Fuel Production. *Energy Environ. Sci.* **2012**, 5 (3), 5902–5918. <https://doi.org/10.1039/C2EE02849B>.
- (20) Zhang, S. B.; Wei, S.-H.; Zunger, A. Stabilization of Ternary Compounds via Ordered Arrays of Defect Pairs. *Phys. Rev. Lett.* **1997**, 78 (21), 4059–4062. <https://doi.org/10.1103/PhysRevLett.78.4059>.
- (21) Kim, J.; Minegishi, T.; Kobota, J.; Domen, K. Investigation of Cu-Deficient Copper Gallium Selenide Thin Film as a Photocathode for Photoelectrochemical Water Splitting. *Jpn. J. Appl. Phys.* **2011**, 51 (1R), 015802. <https://doi.org/10.1143/JJAP.51.015802>.
- (22) Kim, J.; Minegishi, T.; Kobota, J.; Domen, K. Enhanced Photoelectrochemical Properties of CuGa₃Se₅ Thin Films for Water Splitting by the Hydrogen Mediated Co-Evaporation Method. *Energy Environ. Sci.* **2012**, 5 (4), 6368–6374. <https://doi.org/10.1039/C1EE02280F>.
- (23) Kumagai, H.; Minegishi, T.; Moriya, Y.; Kubota, J.; Domen, K. Photoelectrochemical Hydrogen Evolution from Water Using Copper Gallium Selenide Electrodes Prepared by a Particle Transfer Method. *J. Phys. Chem. C* **2014**, 118 (30), 16386–16392. <https://doi.org/10.1021/jp409921f>.

- (24) Khan, I. S.; Muzzillo, C. P.; Perkins, C. L.; Norman, A. G.; Young, J. L.; Gaillard, N.; Zakutayev, A. Mg_xZn_{1-x}O Contact to CuGa₃Se₅ Absorber for Photovoltaic and Photoelectrochemical Devices. *J. Phys. Energy* **2021**, *3* (2), 024001. <https://doi.org/10.1088/2515-7655/abd3b3>.
- (25) Muzzillo, C. P.; Klein, W. E.; Li, Z.; DeAngelis, A. D.; Horsley, K.; Zhu, K.; Gaillard, N. Low-Cost, Efficient, and Durable H₂ Production by Photoelectrochemical Water Splitting with CuGa₃Se₅ Photocathodes. *ACS Appl. Mater. Interfaces* **2018**, *10* (23), 19573–19579. <https://doi.org/10.1021/acsami.8b01447>.
- (26) Palm, D. W.; Muzzillo, C. P.; Ben-Naim, M.; Khan, I.; Gaillard, N.; Jaramillo, T. F. Tungsten Oxide-Coated Copper Gallium Selenide Sustains Long-Term Solar Hydrogen Evolution. *Sustain. Energy Fuels* **2021**, *5* (2), 384–390. <https://doi.org/10.1039/D0SE00487A>.
- (27) Hilal, H. S.; Turner, J. A. Controlling Charge-Transfer Processes at Semiconductor/Liquid Junctions. *Electrochimica Acta* **2006**, *51* (28), 6487–6497. <https://doi.org/10.1016/j.electacta.2006.04.035>.
- (28) Guijarro, N.; Prévot, M. S.; Sivula, K. Surface Modification of Semiconductor Photoelectrodes. *Phys. Chem. Chem. Phys.* **2015**, *17* (24), 15655–15674. <https://doi.org/10.1039/C5CP01992C>.
- (29) Rovelli, L.; Tilley, S. D.; Sivula, K. Optimization and Stabilization of Electrodeposited Cu₂ZnSnS₄ Photocathodes for Solar Water Reduction. *ACS Appl. Mater. Interfaces* **2013**, *5* (16), 8018–8024. <https://doi.org/10.1021/am402096r>.

- (30) Han, Z.; Kortlever, R.; Chen, H.-Y.; Peters, J. C.; Agapie, T. CO₂ Reduction Selective for C₂ Products on Polycrystalline Copper with N-Substituted Pyridinium Additives. *ACS Cent. Sci.* **2017**, *3* (8), 853–859. <https://doi.org/10.1021/acscentsci.7b00180>.
- (31) Thevenon, A.; Rosas-Hernández, A.; Peters, J. C.; Agapie, T. In-Situ Nanostructuring and Stabilization of Polycrystalline Copper by an Organic Salt Additive Promotes Electrocatalytic CO₂ Reduction to Ethylene. *Angew. Chem. Int. Ed.* **2019**, *58* (47), 16952–16958. <https://doi.org/10.1002/anie.201907935>.
- (32) Li, F.; Thevenon, A.; Rosas-Hernández, A.; Wang, Z.; Li, Y.; Gabardo, C. M.; Ozden, A.; Dinh, C. T.; Li, J.; Wang, Y.; Edwards, J. P.; Xu, Y.; McCallum, C.; Tao, L.; Liang, Z.-Q.; Luo, M.; Wang, X.; Li, H.; O'Brien, C. P.; Tan, C.-S.; Nam, D.-H.; Quintero-Bermudez, R.; Zhuang, T.-T.; Li, Y. C.; Han, Z.; Britt, R. D.; Sinton, D.; Agapie, T.; Peters, J. C.; Sargent, E. H. Molecular Tuning of CO₂-to-Ethylene Conversion. *Nature* **2020**, *577* (7791), 509–513. <https://doi.org/10.1038/s41586-019-1782-2>.
- (33) Ozden, A.; Li, F.; García de Arquer, F. P.; Rosas-Hernández, A.; Thevenon, A.; Wang, Y.; Hung, S.-F.; Wang, X.; Chen, B.; Li, J.; Wicks, J.; Luo, M.; Wang, Z.; Agapie, T.; Peters, J. C.; Sargent, E. H.; Sinton, D. High-Rate and Efficient Ethylene Electrosynthesis Using a Catalyst/Promoter/Transport Layer. *ACS Energy Lett.* **2020**, *5* (9), 2811–2818. <https://doi.org/10.1021/acsenergylett.0c01266>.
- (34) Thevenon, A.; Rosas-Hernández, A.; Fontani Herreros, A. M.; Agapie, T.; Peters, J. C. Dramatic HER Suppression on Ag Electrodes via Molecular Films for Highly

- Selective CO₂ to CO Reduction. *ACS Catal.* **2021**, *11* (8), 4530–4537.
<https://doi.org/10.1021/acscatal.1c00338>.
- (35) Buckley, A. K.; Cheng, T.; Oh, M. H.; Su, G. M.; Garrison, J.; Utan, S. W.; Zhu, C.; Toste, F. D.; Goddard, W. A.; Toma, F. M. Approaching 100% Selectivity at Low Potential on Ag for Electrochemical CO₂ Reduction to CO Using a Surface Additive. *ACS Catal.* **2021**, *11* (15), 9034–9042. <https://doi.org/10.1021/acscatal.1c00830>.
- (36) Kim, C.; Bui, J. C.; Luo, X.; Cooper, J. K.; Kusoglu, A.; Weber, A. Z.; Bell, A. T. Tailored Catalyst Microenvironments for CO₂ Electroreduction to Multicarbon Products on Copper Using Bilayer Ionomer Coatings. *Nat. Energy* **2021**, *6* (11), 1026–1034. <https://doi.org/10.1038/s41560-021-00920-8>.
- (37) Jones, R. J. R.; Wang, Y.; Lai, Y.; Shinde, A.; Gregoire, J. M. Reactor Design and Integration with Product Detection to Accelerate Screening of Electrocatalysts for Carbon Dioxide Reduction. *Rev. Sci. Instrum.* **2018**, *89* (12), 124102. <https://doi.org/10.1063/1.5049704>.
- (38) Lai, Y.; Jones, R. J. R.; Wang, Y.; Zhou, L.; Gregoire, J. M. Scanning Electrochemical Flow Cell with Online Mass Spectroscopy for Accelerated Screening of Carbon Dioxide Reduction Electrocatalysts. *ACS Comb. Sci.* **2019**, *21* (10), 692–704. <https://doi.org/10.1021/acscombsci.9b00130>.
- (39) de Souza Lucas, F. W.; Zakutayev, A. Research Update: Emerging Chalcostibite Absorbers for Thin-Film Solar Cells. *APL Mater.* **2018**, *6* (8), 084501. <https://doi.org/10.1063/1.5027862>.

- (40) Haddout, A.; Raidou, A.; Fahoume, M. A Review on the Numerical Modeling of CdS/CZTS-Based Solar Cells. *Appl. Phys. A* **2019**, *125* (2), 124. <https://doi.org/10.1007/s00339-019-2413-3>.
- (41) Chu, S.; Ou, P.; Ghamari, P.; Vanka, S.; Zhou, B.; Shih, I.; Song, J.; Mi, Z. Photoelectrochemical CO₂ Reduction into Syngas with the Metal/Oxide Interface. *J. Am. Chem. Soc.* **2018**, *140* (25), 7869–7877. <https://doi.org/10.1021/jacs.8b03067>.
- (42) Song, J. T.; Ryoo, H.; Cho, M.; Kim, J.; Kim, J.-G.; Chung, S.-Y.; Oh, J. Nanoporous Au Thin Films on Si Photoelectrodes for Selective and Efficient Photoelectrochemical CO₂ Reduction. *Adv. Energy Mater.* **2017**, *7* (3), 1601103. <https://doi.org/10.1002/aenm.201601103>.

Chapter 4

IN SITU DEPOSITED POLYAROMATIC LAYER GENERATES
ROBUST COPPER CATALYST FOR SELECTIVE
ELECTROCHEMICAL CO₂ REDUCTION AT VARIABLE PH

Adapted from:

Watkins, N. B.; Wu, Y.; Nie, W.; Peters, J. C.; Agapie, T.

ACS Energy Lett. **2022**, 8 (1), 189–195.

10.1021/acsenergylett.2c02002.

4.1 Introduction

Electrochemical conversion of CO₂ into useful products by renewable electricity and water holds promise in contributing to a carbon-neutral economy.¹⁻³ To make this process viable, the development of electrocatalysts is essential to produce desirable products with high reaction rates and energy efficiency.^{4,5} C₂₊ products (e.g. ethylene and ethanol) are of particular interest due to their higher market values and versatility.⁶ With Cu-based electrocatalysts being capable of catalyzing CO₂ reduction (CO₂R) to multi-carbon products,^{7,8} a host of strategies have been employed to increase both activity and selectivity. These include alloying, morphological engineering, surface modification of Cu, as well as alteration of reaction parameters such as electrolyte composition, pH, and electrolysis conditions.⁸⁻¹¹

Previously, our laboratories discovered that N-aryl pyridinium-based additives in aqueous electrolyte undergo reduction and dimerization to generate a water-insoluble film on the electrode surface (Figure 4.1a).¹² We have proposed this molecular layer significantly enhances C₂₊ product selectivity on Cu and completely suppresses the competing hydrogen evolution reaction (HER) on Ag in a traditional H-type flow cell by limiting proton sources near the electrode surface (Figure 4.1b).¹³ In the case of Cu, the activity for C₂₊ products remains the same with or without an additive film, whereas the total current density is greatly diminished without nanostructuring of the metal surface.¹⁴ The efficacy of these existing additives, however, motivates the exploration of other chemical precursors to prepare similarly catalytically advantageous molecular films.¹⁵

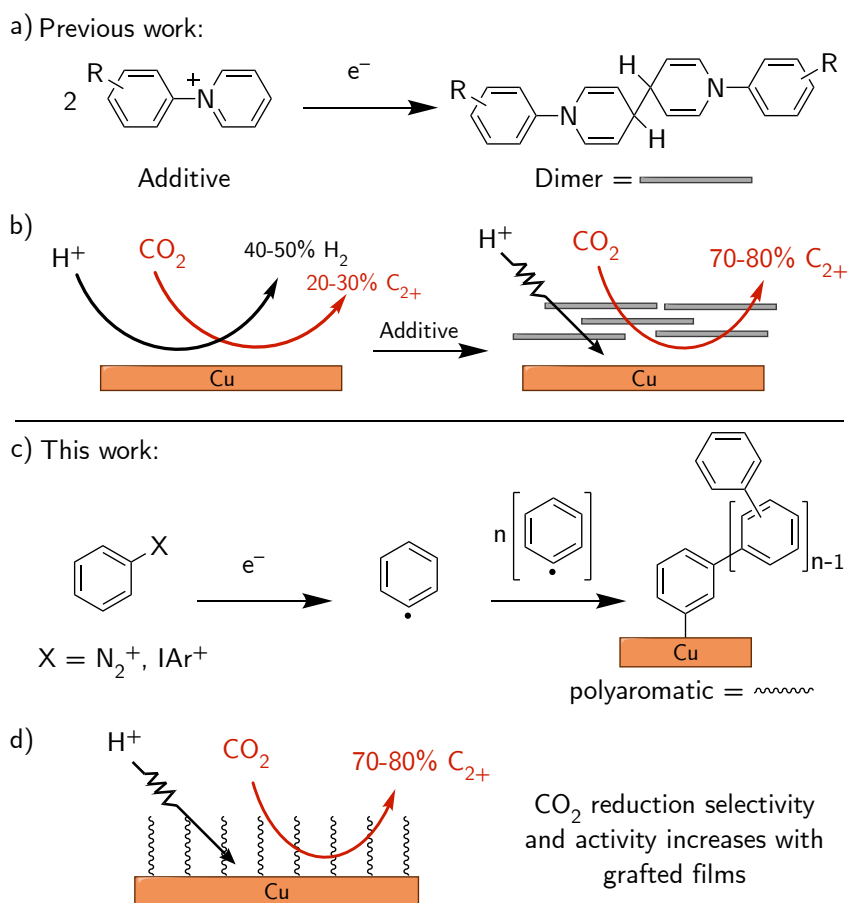


Figure 4.1: Preparation of hybrid electrodes. a) Reductive dimerization of N-aryl pyridinium additives provides a water insoluble dimer; b) Electrodeposition of the additive dimer onto copper surfaces boosts CO_2 reduction selectivity to carbon-coupled products; c) Grafting aryl groups onto the electrode surface using diazonium or iodonium salts d) provides a perpendicular film orientation, which affords high selectivity and similar C_{2+} selectivity compared to previous films in part a).

A notable limitation is the delamination of thin organic films during catalysis due to turbulence at the surface of the electrode.¹⁶ Electrografting molecules permits growth of an organic moiety onto an electrode surface through the formation of radical species with concomitant electron transfer to or from the molecules containing suitable activating groups, such as diazoniums or iodoniums (Figure 4.1c).¹⁷ This process affords an organic coating with strong adhesion to many conductive substrates, such as Cu, Ag, glassy carbon, and

stainless steel, that can withstand sonication even in organic solvents and could therefore be a promising alternative strategy to prolong catalytic performance.^{17–25} Unfortunately, reports using ethynyl and azide aryl radical precursors on copper surfaces have shown little promise for achieving significant enhancement to CO₂R selectivity, likely due to the conflation of effects from the highly functionalized film and the anodic grafting mechanism employed. Alternative methods that allow a decoupling of the effects of deposition techniques and film functionalization are therefore desirable to better understand the mechanism by which grafted films affect selectivity. Chemically simpler aryldiazonium and diaryliodonium salts are deposited using only a negative bias and are yet to be investigated on copper CO₂R, making them excellent grafting precursors to investigate for their effect on catalysis (Figure 4.1d).^{26,27}

4.2 Results and Discussion

Our initial efforts were dedicated towards surveying the electrochemical CO₂R performance of Cu foils after the electrodeposition of organic films from phenyldiazonium. Due to the instability of diazonium salts in aqueous solutions, phenyldiazonium modified Cu (PD-Cu) was prepared by electrodeposition of 10 mM phenyldiazonium tetrafluoroborate in acetonitrile at -1 V vs Ag/AgCl for 15 minutes (for the detailed procedure see the SI). CO₂ reduction electrolysis experiments were performed in a CO₂-saturated 0.1 M KHCO₃ solution in an H-type flow cell as reported previously (see SI, Figures S4.1-3).²⁸ At all electrode potentials examined, PD-Cu showed a significant increase in selectivity towards C₂₊ products compared to unmodified, bare Cu (Figure 4.2a, S4.4-5). Most notably, at -1.05 V vs RHE, PD-Cu showed 70.1±1.4 % selectivity for ethylene, ethanol, and 1-propanol

(Table S4.1). As a comparison, freshly polished Cu without surface modification only afforded 26.0 ± 2.0 % FE for C_{2+} products at the same electrode potential (Table S4.2), which is consistent with other reports on Cu.^{8,12} In other words, the surface modification boosts the selectivity and activity of C_{2+} products on Cu to up to 2.7-fold (Figure 4.2b, S4.4-5), while substantially suppressing H_2 and CH_4 formation. Given that the modified Cu is a composite material with an organic coating on top, controls were performed to ensure CO_2 was the only source of carbon in the CO_2R products (Figure S4.6, Table S4.4).

Despite the precedented stability of diazonium-grafted films, the catalytic effect of the polyaromatic layer decreased over the course of a 10 h electrolysis.¹⁷ The FE for C_2H_4 dropped from ca. 40% at the beginning of catalysis to ca. 20%, while the selectivity towards CH_4 and H_2 slowly increased to over 10% and 40%, respectively (Figure 4.3a). Atomic force microscopy (AFM) images of PD-Cu after 30 min of electrolysis show the agglomeration of particles in the organic layer, causing inhomogeneity in the film, despite observing no change in selectivity on this time scale. We suspect that the agglomerated film is less durable, and AFM images confirm the delamination of the polyaromatic layer after 10 h, exposing the underlying Cu (Figure S4.7). The instability of the deposited layer in this case likely contributes to the diminishing C_{2+} product selectivity and activity over time, although surface reconstruction and/or poisoning of Cu sites has been posited in a number of independent studies to be the cause of catalytic instability and cannot be ruled out here.⁸

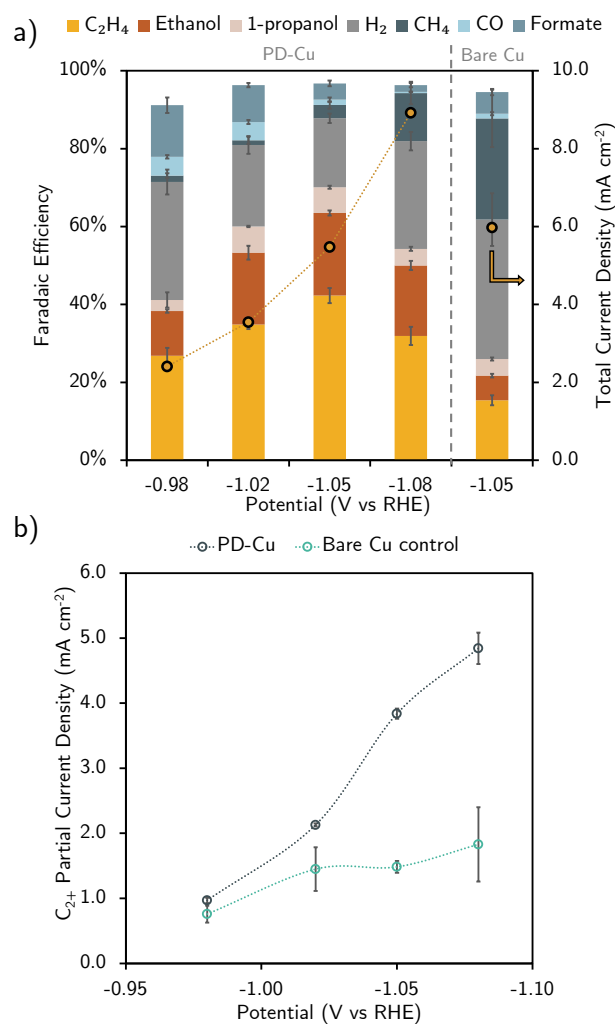


Figure 4.2. Enhanced C₂⁺ product selectivity by phenyldiazonium (PD) modification. a) Potential-dependent selectivity and activity of PD-Cu shows an increase in activity and selectivity for C₂⁺ products compared to bare Cu at its peak performing potential (see Table S4.2, Figure S4.4 for other bare Cu FEs), with bars indicating FE (left axis) and circles indicating total current densities (right axis); b) Comparing the C₂⁺ partial current densities to bare Cu controls highlights the increase in activity for PD-Cu.

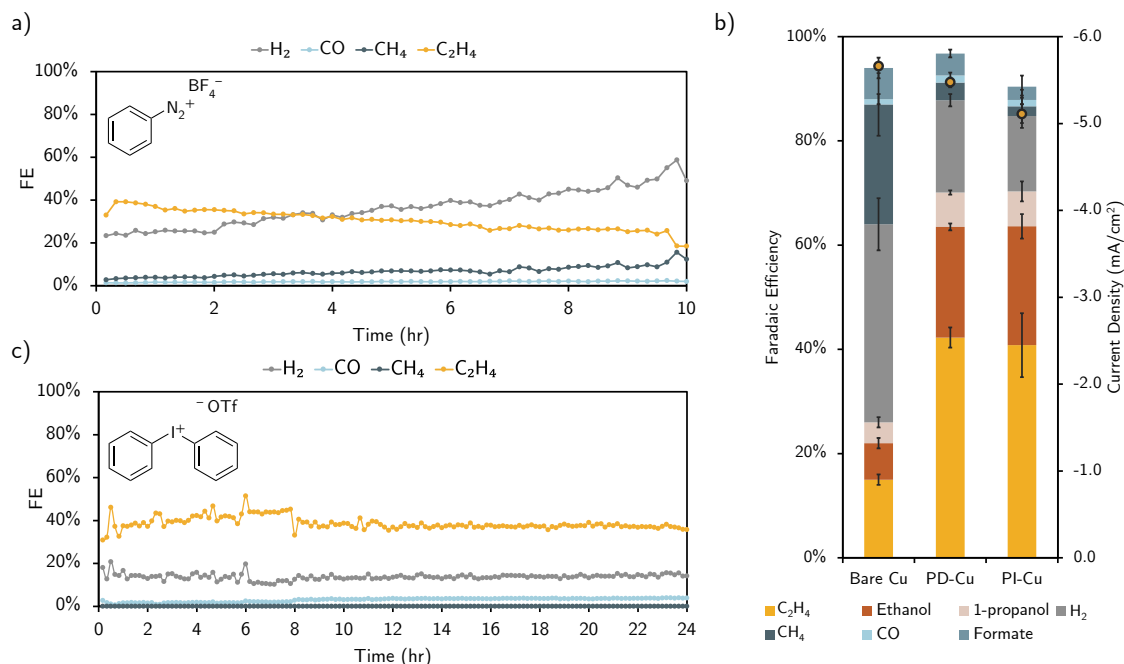


Figure 4.3. Comparison of catalytic performance over time during CO₂R. a) Gas product selectivity during 10 h CO₂ reduction with PD-Cu; b) Comparison of Cu, PD-Cu, and diphenyliodonium-Cu (PI-Cu) CO₂ reduction selectivities at near -1.05 V vs RHE, with markers indicating their respective total current densities after 35 minutes of electrolysis; c) Gas product selectivity during 24 h CO₂ reduction with PI-Cu.

We expect that the limited stability of the grafted film is due to the highly reactive diazonium precursor undergoing competing polymerization in solution, in addition to reactions at the electrode surface, followed by larger polyaryl fragments grafting to the electrode surface and resulting in uneven films. Commercially available diaryliodonium salts are markedly more stable than diazonium salts and their deposition is reported to be more controlled due to the formation of aryl radicals only at the electrode surface.²⁴ Iodonium salts have reduction potentials more negative than diazonium analogues and can therefore be dissolved in neutral aqueous solutions without decomposition (Figure S4.8,9).²⁹ Their stability enables the in-situ deposition of diphenyliodonium onto Cu (PI-Cu). PI-Cu affords nearly identical selectivity and activity to PD-Cu at -1.05 V vs RHE, with 70.3% selectivity

for C_{2+} products (Figure 4.3b, S4.4-5 Table S4.3). Notably, PI-Cu offers a more robust system than PD-Cu as it maintains selectivity for 24 hours and is especially outstanding as compared to bare Cu's deteriorating selectivity over time (Figure 4.3c, Figure S4.10). One possible explanation for the change in film integrity is the deposition mechanism of the iodonium salt enabling the formation of a denser film. AFM images of the grafted films show smaller surface height variation in the case of PD-Cu than PI-Cu, suggesting that diazonium film growth may be suppressed by solution polymerization (Figure 4.4a,b). Adding KI to the electrolyte with PD-Cu does not change product selectivity, suggesting that increased stability was indeed due to the more controlled in-situ deposition method and not iodide near the surface sourced from the iodonium precursor (Table S4.3, entry 4).

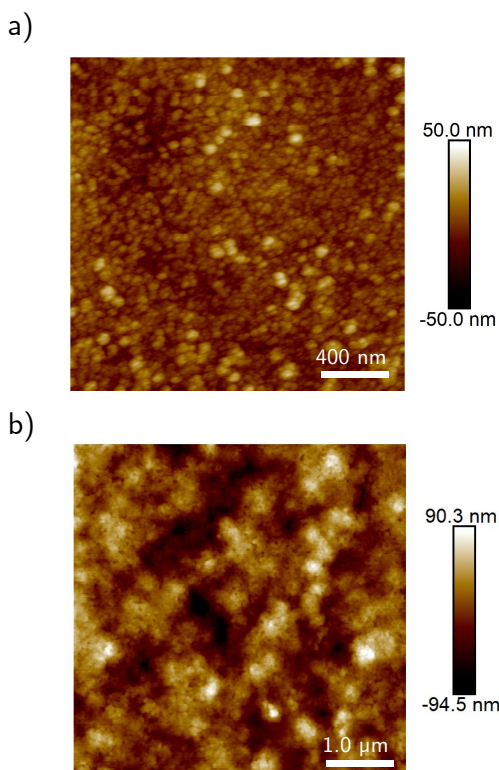


Figure 4.4. Comparison of diazonium- and iodonium-based polyaromatic electrode modification. a) AFM of PD-Cu surface; b) AFM of PI-Cu surface.

Reflectance Fourier-transform infrared spectroscopy confirms that the films are similar in nature, with PI-Cu having more intense peaks attributable to the increased thickness, and are consistent with those reported previously (Figure S4.11).²¹ Each show bands characteristic to phenyl rings in the range of 2900-3100 cm⁻¹, 1400-1600 cm⁻¹, and 700-900 cm⁻¹, whereas the features corresponding to diazonium group stretching (2295 cm⁻¹) are not present after electrodeposition (Figure S4.12, Tables S4.5-6). X-ray photoelectron spectroscopy (XPS) indicates the presence of C, N, O, and Cu on the surface of PD-Cu (Figure S4.13) and C, I, O, and Cu on the surface of PI-Cu (Figure S4.14). The atomic ratio of C to N in the deposited layer as probed by XPS is around 19 to 1 for PD-Cu and C to I is around 330 to 1 for PI-Cu. The minor presence of N 1s feature (Figure S4.13c) can be attributed to incomplete generation of N₂ from diazonium groups and the formation of aryl substituted -N=N- moieties during electrodeposition, as has been documented in other studies.^{30,31} The intensity ratios of carbon to copper and carbon to iodine in PI-Cu is consistent with a thicker film and fewer side reactions than PD-Cu, respectively. These data indicate that the iodonium-derived film provides a film that is significantly less contaminated with heteroatoms, important for catalytic comparisons where other organic films are rich in functionality.¹⁵

Previously, the strong adhesion of the coated layer to Cu was ascribed to the formation of covalent Cu-C and CuO-C bonds, which was established based on indirect XPS evidence in a study on the electroless grafting of phenyldiazonium on Cu under short exposure time.¹⁹ Notwithstanding the literature precedents (including studies on other metals^{30,32}), we are not sure whether the nature of interaction between the organic layer and

underlying Cu in PD-Cu and PI-Cu is covalent (Figure S4.14-15). However, the nature of the interaction between the film, cations, and intermediates is of considerable interest and warrants further investigation.

The surface coverage of the grafted layer was found to be critical for the catalytic performance of modified Cu. Exposure of Cu foil to electrodeposition conditions with either phenyl radical source for just 1 min yields a non-uniform and possibly thinner coating (Figure S4.16). The resulting catalytic performance of Cu with 1 min, and even 5 min, deposition times show lower selectivity for C_{2+} products than 10-minute pretreatment. Exposure to electrodeposition times beyond 10 min did not yield further catalytic benefits (Table S4.7-8, Figure S4.17). This can be rationalized by the self-limiting nature of the electrodeposition process. Accordingly, chronoamperometry with PD-Cu resulted in little additional film formation after 10 min under these conditions (Figure S4.18).

Given that PD-Cu and PI-Cu maintain total current density and increased C_{2+} partial current density relative to bare Cu (Figure 4.2b), a behavior that contrasts with that of N-aryl pyridinium additives and other organic-modified systems,¹⁴ where increased selectivity towards C_{2+} products comes at the expense of lower total current density, further studies were performed to understand the impact of the film (Figure 4.5).

Measurement of the double layer capacitance via cyclic voltammetry at various scan rates (Figure S4.19, Table S4.9) reveals that the post-catalysis modified catalyst has a similar electrochemical active surface area (ECSA) to that of unmodified Cu (Figure 4.5a). The previous tradeoff of activity for selectivity with N-aryl pyridinium additives can be rationalized based on lower ECSA caused by an insoluble and non-conductive film laying on top of active sites, thus limiting substrate access.¹³ Grafted films, however, have been

proposed to grow perpendicular to the surface and create a low density film with channels that may enable facile substrate transport through the film, maintaining catalytic activity.³³ However, since we cannot conclude that a covalent bond exists between the polyaryl layer and the metal surface in the present system, the unchanged ECSA may also be attributed to other phenomena, such as a tradeoff between a roughened and more active surface and film covering active sites.²⁴ Other considerations include a possible change in the specific capacitance of the system or changes in the ECSA being within error between measurements due to the thin nature of the film.

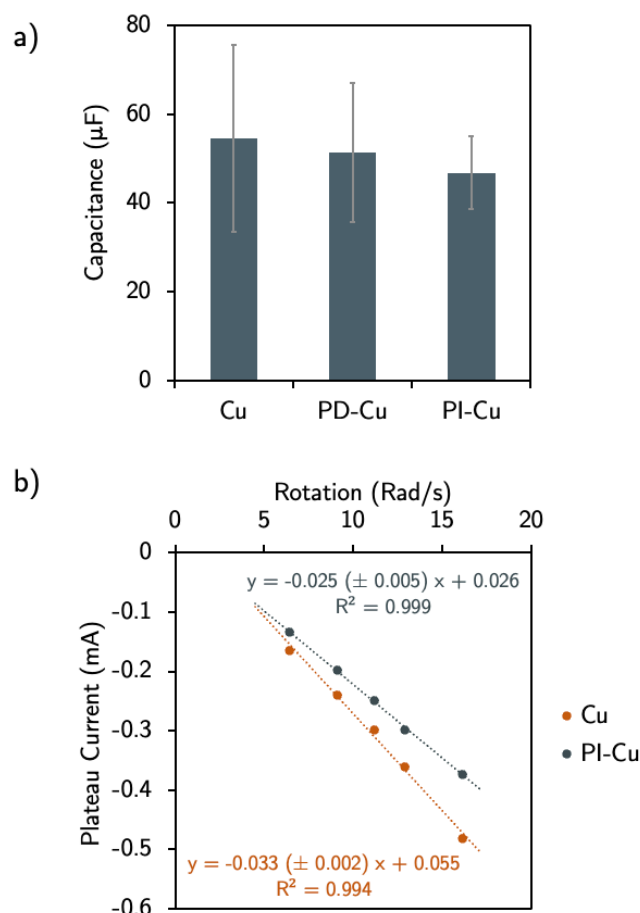


Figure 4.5. Electrochemical studies of the impact of the organic films. a) Relative ECSA of Cu does not change appreciably upon modification of surface with polyaryl layer; b) RDE studies show a change in the slope associated with HER, consistent with a decrease in the proton diffusion coefficient in the presence of the PI-Cu organic film.

Rotating disk electrode (RDE) experiments were performed in an unbuffered acidic solution to probe whether the polymeric organic coating studied herein affects the transport of protons. Previously, N-aryl pyridinium additives or surfactants have been shown to impede proton transport to the electrode surface and thereby enhance CO₂R selectivity.^{13,34,35} PD-Cu prepared through a 10 min deposition shows no decrease in plateau current and only a slight decrease in the irreversible water reduction wave compared to the bare surface (Figure S4.20, Table S4.10). Similar results were obtained with 10-minute deposition time PI-Cu, with no appreciable change in proton diffusion coefficient (Table S4.10). The small changes observed could be due to (i) these films having high proton diffusion, or (ii) the films being sufficiently thin that the decrease in proton diffusion is very small (<5%, Figure S4.21). PI-Cu with a 30-minute deposition time (analogous to a film formed in-situ during catalytic run) was evaluated by RDE experiments and showed a decrease in proton diffusion coefficient by 25±9%, in support of the second hypothesis (Figure 4.5b, Table S4.10). This result suggests that the source of the effects of the films reported herein is likely similar to those of pyridinium additives; nevertheless, it also reveals that the requisite decrease in proton availability needed to cause a substantial increase in C₂₊ selectivity is small.^{13,14}

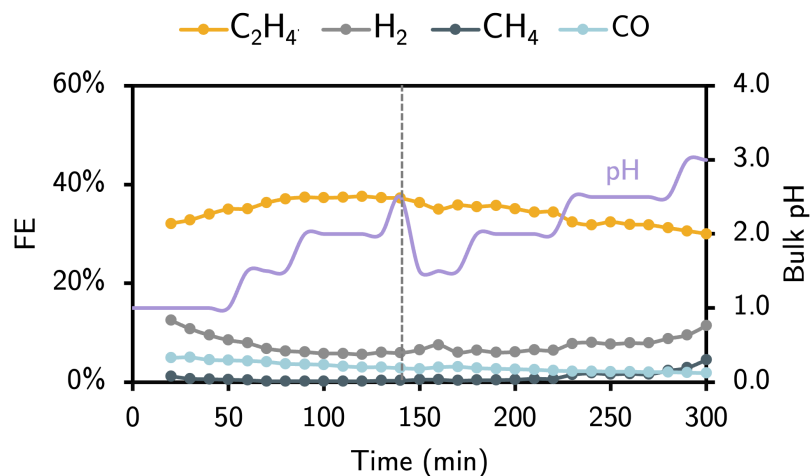


Figure 4.6. Product distribution and electrolyte pH over the course of 5 hours with PI-Cu in a gas diffusion electrode setting at -100 mA cm^{-2} with an initial $1 \text{ M H}_3\text{PO}_4$ electrolyte. The dashed line corresponds to the injection of additional fresh electrolyte to the system.

Given the promising stability observed for PI-Cu and the decrease in proton diffusion, the performance of the modified electrode was tested under the more demanding conditions of CO_2R under acidic conditions of $\text{pH} = 1$.^{36,37} Efforts to perform a blank experiment using 300 nm of Cu on PTFE in $1 \text{ M H}_3\text{PO}_4 / 1 \text{ M KCl}$ were stifled by the complete corrosion of the copper catalyst layer (Figure S4.22). Upon grafting the electrode with diphenyliodonium, over 65% FE C_{2+} was obtained at -100 mA/cm^2 (Figure S4.23). Reinjecting the system with fresh electrolyte did not change the selectivity, highlighting the durability of the film (Figure 4.6). Minor deterioration of the selectivity is attributable to mechanical failure of the electrode, rather than delamination of the film. In other tests, high selectivity could be maintained over 5 hours as the bulk pH of the electrolyte swung from ca. 1 to 10 (Figure S4.24). Since the selectivity is the same across the pH range, we suggest that the conditions of the catalyst microenvironment must be consistent throughout and shielded from the bulk solution. The grafted layer appears to sufficiently protect the electrode surface from corrosion at all operating conditions tested.

4.3 Conclusion

In summary, we have described the enhancement in selectivity and activity towards C_2^+ products for Cu-catalyzed electrochemical CO_2 reduction by thin polyaromatic layers. These coatings were readily accessed electrochemically from phenyldiazonium and phenyliodonium precursors. The thickness and uniformity of the deposited layer are shown to be critical to the catalytic enhancement by the film. PD-Cu and PI-Cu provide similar surfaces, but differences in chemical stability and deposition mechanism result in a significant difference in film stability. RDE studies indicate that the thicker films act as a barrier towards the diffusion of proton sources to the electrode surface, supporting previous hypotheses that decreased proton availability near the electrode surface increases C_2^+ selectivity. Taking advantage of the improved durability of these polyaromatic films, selective CO_2R can be achieved even under highly acidic ($pH = 1$) conditions for prolonged periods of time. The durability of the grafted film under nonaqueous and corrosive conditions electrode affirm the potential to use electrografted materials as electrocatalysts for electrocatalytic transformations where selectivity remains a challenge due to electrode decomposition, competing HER, and/or low gas solubility.

4.4 References

- (1) Schiffer, Z. J.; Manthiram, K. Electrification and Decarbonization of the Chemical Industry. *Joule* **2017**, 1 (1), 10–14. <https://doi.org/10.1016/j.joule.2017.07.008>.
- (2) Chen, C.; Khosrowabadi Kotyk, J. F.; Sheehan, S. W. Progress toward Commercial Application of Electrochemical Carbon Dioxide Reduction. *Chem* **2018**, 4 (11), 2571–2586. <https://doi.org/10.1016/j.chempr.2018.08.019>.
- (3) De Luna Phil; Hahn Christopher; Higgins Drew; Jaffer Shaffiq A.; Jaramillo Thomas F.; Sargent Edward H. What Would It Take for Renewably Powered Electrosynthesis to Displace Petrochemical Processes? *Science* **2019**, 364 (6438), eaav3506. <https://doi.org/10.1126/science.aav3506>.
- (4) Lu, Q.; Jiao, F. Electrochemical CO₂ Reduction: Electrocatalyst, Reaction Mechanism, and Process Engineering. *Electrocatalysis* **2016**, 29, 439–456. <https://doi.org/10.1016/j.nanoen.2016.04.009>.
- (5) Qiao, J.; Liu, Y.; Hong, F.; Zhang, J. A Review of Catalysts for the Electroreduction of Carbon Dioxide to Produce Low-Carbon Fuels. *Chem. Soc. Rev.* **2014**, 43 (2), 631–675. <https://doi.org/10.1039/C3CS60323G>.
- (6) Bushuyev, O. S.; De Luna, P.; Dinh, C. T.; Tao, L.; Saur, G.; van de Lagemaat, J.; Kelley, S. O.; Sargent, E. H. What Should We Make with CO₂ and How Can We Make It? *Joule* **2018**, 2 (5), 825–832. <https://doi.org/10.1016/j.joule.2017.09.003>.
- (7) Gattrell, M.; Gupta, N.; Co, A. A Review of the Aqueous Electrochemical Reduction of CO₂ to Hydrocarbons at Copper. *J. Electroanal. Chem.* **2006**, 594 (1), 1–19. <https://doi.org/10.1016/j.jelechem.2006.05.013>.

- (8) Nitopi, S.; Bertheussen, E.; Scott, S. B.; Liu, X.; Engstfeld, A. K.; Horch, S.; Seger, B.; Stephens, I. E. L.; Chan, K.; Hahn, C.; Nørskov, J. K.; Jaramillo, T. F.; Chorkendorff, I. Progress and Perspectives of Electrochemical CO₂ Reduction on Copper in Aqueous Electrolyte. *Chem. Rev.* **2019**, 119 (12), 7610–7672. <https://doi.org/10.1021/acs.chemrev.8b00705>.
- (9) Raciti, D.; Wang, C. Recent Advances in CO₂ Reduction Electrocatalysis on Copper. *ACS Energy Lett.* **2018**, 3 (7), 1545–1556. <https://doi.org/10.1021/acsenergylett.8b00553>.
- (10) Arquer, F. P. G. de; Dinh, C.-T.; Ozden, A.; Wicks, J.; McCallum, C.; Kirmani, A. R.; Nam, D.-H.; Gabardo, C.; Seifitokaldani, A.; Wang, X.; Li, Y. C.; Li, F.; Edwards, J.; Richter, L. J.; Thorpe, S. J.; Sinton, D.; Sargent, E. H. CO₂ Electrolysis to Multicarbon Products at Activities Greater than 1 A cm⁻². *Science* **2020**, 367 (6478), 661–666. <https://doi.org/10.1126/science.aay4217>.
- (11) Zhong, M.; Tran, K.; Min, Y.; Wang, C.; Wang, Z.; Dinh, C.-T.; De Luna, P.; Yu, Z.; Rasouli, A. S.; Brodersen, P.; Sun, S.; Voznyy, O.; Tan, C.-S.; Askerka, M.; Che, F.; Liu, M.; Seifitokaldani, A.; Pang, Y.; Lo, S.-C.; Ip, A.; Ulissi, Z.; Sargent, E. H. Accelerated Discovery of CO₂ Electrocatalysts Using Active Machine Learning. *Nature* **2020**, 581 (7807), 178–183. <https://doi.org/10.1038/s41586-020-2242-8>.
- (12) Han, Z.; Kortlever, R.; Chen, H.-Y.; Peters, J. C.; Agapie, T. CO₂ Reduction Selective for C_{≥2} Products on Polycrystalline Copper with N-Substituted Pyridinium Additives. *ACS Cent. Sci.* **2017**, 3 (8), 853–859. <https://doi.org/10.1021/acscentsci.7b00180>.

- (13) Thevenon, A.; Rosas-Hernández, A.; Fontani Herreros, A. M.; Agapie, T.; Peters, J. C. Dramatic HER Suppression on Ag Electrodes via Molecular Films for Highly Selective CO₂ to CO Reduction. *ACS Catal.* **2021**, 11 (8), 4530–4537. <https://doi.org/10.1021/acscatal.1c00338>.
- (14) Thevenon, A.; Rosas-Hernández, A.; Peters, J. C.; Agapie, T. In-Situ Nanostructuring and Stabilization of Polycrystalline Copper by an Organic Salt Additive Promotes Electrocatalytic CO₂ Reduction to Ethylene. *Angew. Chem. Int. Ed.* **2019**, 58 (47), 16952–16958. <https://doi.org/10.1002/anie.201907935>.
- (15) Nam, D.-H.; De Luna, P.; Rosas-Hernández, A.; Thevenon, A.; Li, F.; Agapie, T.; Peters, J. C.; Shekhah, O.; Eddaoudi, M.; Sargent, E. H. Molecular Enhancement of Heterogeneous CO₂ Reduction. *Nat. Mater.* **2020**, 19 (3), 266–276. <https://doi.org/10.1038/s41563-020-0610-2>.
- (16) Wang, J.; Cheng, T.; Fenwick, A. Q.; Baroud, T. N.; Rosas-Hernández, A.; Ko, J. H.; Gan, Q.; Goddard III, W. A.; Grubbs, R. H. Selective CO₂ Electrochemical Reduction Enabled by a Tricomponent Copolymer Modifier on a Copper Surface. *J. Am. Chem. Soc.* **2021**. <https://doi.org/10.1021/jacs.0c12478>.
- (17) Bélanger, D.; Pinson, J. Electrografting: A Powerful Method for Surface Modification. *Chem. Soc. Rev.* **2011**, 40 (7), 3995–4048. <https://doi.org/10.1039/C0CS00149J>.
- (18) Pinson, J.; Podvorica, F. Attachment of Organic Layers to Conductive or Semiconductive Surfaces by Reduction of Diazonium Salts. *Chem. Soc. Rev.* **2005**, 34 (5), 429. <https://doi.org/10.1039/b406228k>.

- (19) Hurley, B. L.; McCreery, R. L. Covalent Bonding of Organic Molecules to Cu and Al Alloy 2024 T3 Surfaces via Diazonium Ion Reduction. *J. Electrochem. Soc.* **2004**, 151 (5), B252. <https://doi.org/10.1149/1.1687428>.
- (20) Randriamahazaka, H.; Ghilane, J. Electrografting and Controlled Surface Functionalization of Carbon Based Surfaces for Electroanalysis. *Electroanalysis* **2016**, 28 (1), 13–26. <https://doi.org/10.1002/elan.201500527>.
- (21) Adenier, A.; Combellas, C.; Kanoufi, F.; Pinson, J.; Podvorica, F. I. Formation of Polyphenylene Films on Metal Electrodes by Electrochemical Reduction of Benzenediazonium Salts. *Chem. Mater.* **2006**, 18 (8), 2021–2029. <https://doi.org/10.1021/cm052065c>.
- (22) Baranton, S.; Bélanger, D. In Situ Generation of Diazonium Cations in Organic Electrolyte for Electrochemical Modification of Electrode Surface. *Electrochimica Acta* **2008**, 53 (23), 6961–6967. <https://doi.org/10.1016/j.electacta.2008.02.105>.
- (23) Bernard, M.-C.; Chaussé, A.; Cabet-Deliry, E.; Chehimi, M. M.; Pinson, J.; Podvorica, F.; Vautrin-UI, C. Organic Layers Bonded to Industrial, Coinage, and Noble Metals through Electrochemical Reduction of Aryldiazonium Salts. *Chem. Mater.* **2003**, 15 (18), 3450–3462. <https://doi.org/10.1021/cm034167d>.
- (24) Steeno, R.; Rodríguez González, M. C.; Eyley, S.; Thielemans, W.; Mali, K. S.; De Feyter, S. Covalent Functionalization of Carbon Surfaces: Diaryliodonium versus Aryldiazonium Chemistry. *Chem. Mater.* **2020**, 32 (12), 5246–5255. <https://doi.org/10.1021/acs.chemmater.0c01393>.
- (25) Abdinejad, M.; Irtem, E.; Farzi, A.; Sassenburg, M.; Subramanian, S.; Iglesias van Montfort, H.-P.; Ripepi, D.; Li, M.; Middelkoop, J.; Seifitokaldani, A.; Burdyny, T.

- CO₂ Electrolysis via Surface-Engineering Electrografted Pyridines on Silver Catalysts. *ACS Catal.* **2022**, 12 (13), 7862–7876. <https://doi.org/10.1021/acscatal.2c01654>.
- (26) Zouaoui, N.; Osseonon, B. D.; Fan, M.; Mayilukila, D.; Garbarino, S.; de Silveira, G.; Botton, G. A.; Guay, D.; Tavares, A. C. Electroreduction of CO₂ to Formate on Amine Modified Pb Electrodes. *J. Mater. Chem. A* **2019**, 7 (18), 11272–11281. <https://doi.org/10.1039/C8TA09637F>.
- (27) Abdinejad, M.; Santos da Silva, I.; Kraatz, H. B. Electrografting Amines onto Silver Nanoparticle-Modified Electrodes for Electroreduction of CO₂ at Low Overpotential. *J. Mater. Chem. A* **2021**, 9 (15), 9791–9797. <https://doi.org/10.1039/D1TA00260K>.
- (28) Lobaccaro, P.; Singh, M. R.; Clark, E. L.; Kwon, Y.; Bell, A. T.; Ager, J. W. Effects of Temperature and Gas–Liquid Mass Transfer on the Operation of Small Electrochemical Cells for the Quantitative Evaluation of CO₂ Reduction Electrocatalysts. *Phys. Chem. Chem. Phys.* **2016**, 18 (38), 26777–26785. <https://doi.org/10.1039/C6CP05287H>.
- (29) Koefoed, L.; Pedersen, S. U.; Daasbjerg, K. Grafting of Aryl Diazonium, Iodonium, and Sulfonium Salts in Unusual Patterns by Exploiting the Potential Gradient in Bipolar Electrochemistry. *ChemElectroChem* **2016**, 3 (3), 495–501. <https://doi.org/10.1002/celec.201500512>.
- (30) Jiang, D.; Sumpter, B. G.; Dai, S. Structure and Bonding between an Aryl Group and Metal Surfaces. *J. Am. Chem. Soc.* **2006**, 128 (18), 6030–6031. <https://doi.org/10.1021/ja061439f>.

- (31) Doppelt, P.; Hallais, G.; Pinson, J.; Podvorica, F.; Verneyre, S. Surface Modification of Conducting Substrates. Existence of Azo Bonds in the Structure of Organic Layers Obtained from Diazonium Salts. *Chem. Mater.* **2007**, 19 (18), 4570–4575. <https://doi.org/10.1021/cm0700551>.
- (32) Betelu, S.; Tijunelyte, I.; Boubekeur-Lecaque, L.; Ignatiadis, I.; Ibrahim, J.; Gaboreau, S.; Berho, C.; Toury, T.; Guenin, E.; Lidgi-Guigui, N.; Félidj, N.; Rinnert, E.; Chapelle, M. L. de la. Evidence of the Grafting Mechanisms of Diazonium Salts on Gold Nanostructures. *J. Phys. Chem. C* **2016**, 120 (32), 18158–18166. <https://doi.org/10.1021/acs.jpcc.6b06486>.
- (33) Chevalier, C. L.; Landis, E. C. Electrochemical Attachment of Diazonium-Generated Films on Nanoporous Gold. *Langmuir* **2015**, 31 (31), 8633–8641. <https://doi.org/10.1021/acs.langmuir.5b02302>.
- (34) Banerjee, S.; Han, X.; Thoi, V. S. Modulating the Electrode–Electrolyte Interface with Cationic Surfactants in Carbon Dioxide Reduction. *ACS Catal.* **2019**, 9 (6), 5631–5637. <https://doi.org/10.1021/acscatal.9b00449>.
- (35) Ovalle, V. J.; Waegele, M. M. Understanding the Impact of N -Arylpyridinium Ions on the Selectivity of CO₂ Reduction at the Cu/Electrolyte Interface. *J. Phys. Chem. C* **2019**, 123 (40), 24453–24460. <https://doi.org/10.1021/acs.jpcc.9b08666>.
- (36) Gu, J.; Liu, S.; Ni, W.; Ren, W.; Haussener, S.; Hu, X. Modulating Electric Field Distribution by Alkali Cations for CO₂ Electroreduction in Strongly Acidic Medium. *Nat. Catal.* **2022**, 5 (4), 268–276. <https://doi.org/10.1038/s41929-022-00761-y>.
- (37) Nie, W.; Gavin P. Heim; Nicholas B. Watkins; Agapie, T.; Peters, J. C. Organic Additive-Derived Films on Cu Electrodes Promote Electrochemical CO₂ Reduction

to C₂₊ Products Under Strongly Acidic Conditions. *Angewandte Chemie International Edition* **2023**, 62 (12), e202216102.
<https://doi.org/10.1002/anie.202216102>.

*Chapter 5*HYDRODYNAMICS CHANGE TAFEL SLOPES IN
ELECTROCHEMICAL CO₂ REDUCTION ON COPPER

Adapted from:

Watkins, N. B.; Schiffer, Z. J.; Lai, Y.; Musgrave, C. B. I.; Atwater, H. A.;

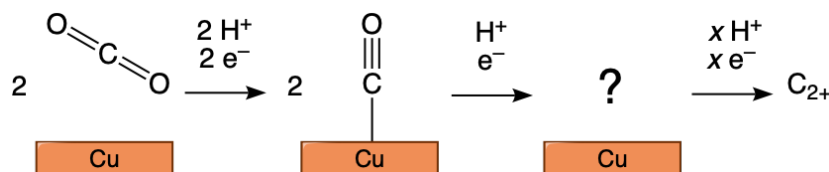
Goddard, W. A. I.; Agapie, T.; Peters, J. C.; Gregoire, J. M.

ACS Energy Lett. **2023**, 8 (5), 2185–2192.

10.1021/acsenergylett.3c00442.

5.1 Introduction

Heightened anthropogenic atmospheric CO₂ levels motivates the development of processes to mitigate CO₂ emissions associated with climate change.^{1,2} Electrochemical CO₂ reduction (CO₂R) is being pursued as one solution towards a carbon-neutral economy.^{3,4} However, many challenges remain, including those associated with selectivity for multi-carbon fuel candidates. Current trends focus on copper's crucial ability to form appreciable quantities of carbon-coupled products. As yet it is not possible to reliably tune the downstream C₂₊ products produced, such as ethylene and ethanol, and the mechanisms defining such selectivities are not firmly established (Scheme 5.1).⁵ Even on a planar catalyst, perhaps the simplest practical system for mechanistic studies, there are many effects to consider, including, but not limited to: concentration polarization effects from dissolved CO₂, intermediates, electrolytes, fluctuations in local pH, and the faceting and restructuring of the electrode surface.⁶



Scheme 5.1: Electrochemical reduction of CO₂ to CO requires two proton and electron transfers. Reduction of CO is proposed to be the rate-determining step for producing carbon-coupled products, but the exact species it is reduced to upon dimerization are still under investigation.⁵

Tafel analysis, derived from Butler-Volmer kinetics, is one powerful tool that has long been used to aid in the understanding of electrochemical mechanisms. By analyzing the logarithm of current versus applied potential, information can be obtained regarding the

number of proton and electron transfers occurring before the rate-determining step (RDS) (Equation 5.1).⁷ Through better mechanistic understanding, catalysts and systems can be optimized to reduce energy barriers and alter selectivity.

Recently, it has come to light that this approach provides only limited reliable insight, in part due to over-reliance on Tafel slopes and biases toward reporting cardinal values.⁸ Influences from mass transport can obscure observation of the desired Tafel behavior. CO, an intermediate on-path to carbon-coupled CO₂R products, has been used as the reactant to try to simplify mechanistic studies.⁹⁻¹¹ However, such strategies cannot replicate the catalyst micro- environment resulting from CO₂/HCO₃ equilibrium, pH gradients, and equilibration of the electrode with CO as a product, highlighting the importance of directly interrogating CO₂ reduction systems.

$$\text{Tafel slope} = \frac{60 \text{ mV dec}^{-1}}{n+q/2} \quad (1)$$

Equation 5.1: A simplified equation for the Tafel slope, α^{-1} , is derived from the Butler-Volmer equation, where n and q are the number of electron transfers before and during the RDS, respectively.⁸

Gas diffusion electrodes and gas sparging have been investigated to address the issues of low CO₂ solubility (34 mM) and low mass transport in aqueous CO₂ reduction.¹² Gas diffusion assemblies enhance CO₂ transport to the catalyst by decreasing the diffusion path length of CO₂ to the electrode surface, but inherently create a distribution of mass transport conditions and local electrochemical environments that impede their utilization for studying catalyst mechanisms.^{13,14}

H-cells, in which CO₂ is typically bubbled across the electrode surface, are widely adopted for mechanistic studies. Their limitations in elucidating intrinsic catalyst behavior

include the documented sensitivity of product distribution to the bubble rate and size.^{15,16}

Follow-up work on copper demonstrated that at -1.1 V vs RHE a difference in flow rate between 5 and 10 sccm would afford a 20% swing in Faradaic efficiency (FE) in favor of ethylene over hydrogen.¹⁷ The magnitude of the effect of bubble rate was further emphasized on silver electrodes using the same cell geometry.¹⁸ Increasing the sparging rate from 2.5 to 40 sccm resulted in a 60% increase in CO FE at -1.4 V vs RHE and a $>3\times$ increase in the partial current density (j_{CO}). Additionally, the authors determined that the average boundary layer thickness decreased up to four-fold as the flow rate of CO_2 was increased. However, the geometry of the diffusion layer as well as its variability are unclear due to the inconsistent hydrodynamics that sparging produces.

Even with vigorous bubbling, the electrolyte flow closest to the electrode is essentially stagnant, leading to well-defined Nernstian diffusion boundary layers.¹⁹ As the flow rate increases, the boundary layer becomes thinner and reduces the diffusion path length for reactants to travel from the bulk to the surface (Figure 5.1a). In CO_2R , the increased exchange between species in the boundary layer and the bulk solution mitigates large deviations in pH from the bulk electrolyte value.²⁰ While bubble formation from gaseous products can disrupt the flow field, model laminar systems have been successfully deployed to modulate CO_2 availability via flow rate and to facilitate cascade catalysis using multiple CO_2R catalysts (Ag and Cu).^{21,22} Rotating disk electrodes (RDEs) also serve as laminar systems of interest for inspecting electrochemical CO_2 reduction.^{23,24} Typical RDE setups are also challenged by bubble formation on the electrode surface, which has motivated the development of rotating cylinder electrode (RCE) systems.^{25,26}

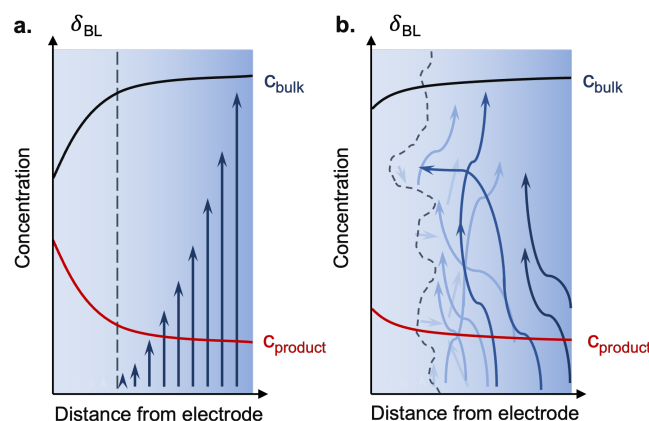


Figure 5.1: Graphical representation of the change in concentration of surface species due to electrolyte flow near the electrode surface with a) laminar flow and b) turbulent flow. Relative velocities and depth are indicated by arrow size and color, respectively (not to scale).

Unlike the electrolyte flow in an RDE, the RCE operates in a turbulent regime at nearly all rotation rates. This difference enables an increased dynamic range of mass transport to the electrode surface while mitigating the effect of bubble formation. While the uniformity of the boundary layer is disrupted in this system (Figure 5.1b), the mass transfer to the electrode surface can still be described well by mass transfer coefficient values.²⁷ As a result, increased rotation rates will see increased mass transfer and enable the study of mass transport limited electrokinetics. Such studies have been performed on copper and have revealed that increased turbulence results in a proportional increase in partial current densities for CO (j_{CO}) and decrease in rates for carbon-coupled products.^{25,26} This result supports the hypothesis that CO engages in a dynamic desorption-readsorption to the electrode surface. However, these experiments were performed at single potentials and do not provide greater insight into how these changes in the catalyst microenvironment affect the mechanism of CO₂R towards multi-carbon products as a whole. Additionally, while these

experiments facilitated well-defined turbulent hydrodynamics, they required the use of a hermetically sealed RCE, which limits data collection throughput.

In this study, we demonstrate that recirculation flow systems remove the complications of gas bubbling and can be deployed on a range of cell geometries, creating a combination of control and flexibility that complements traditional H-cell and RCE reactors. Studying the influence of a range of reactor designs and mass transport conditions elucidates the sensitivity of Tafel analysis to external factors in CO₂R catalysis. Importantly, CO₂ reduction kinetics towards multi-carbon products can be accelerated via increased convection. Additionally, our observation of systematic variation in product selectivity with hydrodynamics conditions provides an opportunity to better understand our team's recent high-throughput study of copper alloys. This study revealed a scaling relationship between $j_{\text{C}_2\text{H}_4}$ and j_{CH_4} that spanned more than three orders of magnitude of partial current densities and that organic additive-derived film coatings can break this scaling relationship.²⁸ The use of hydrodynamics to observe or alter scaling relationships highlights the importance of evaluating the sensitivity to mass transport in both mechanistic studies and reactor design.

5.2 Results and Discussion

To probe catalytic behavior with respect to hydrodynamics, we focus on two main cell designs: H-cells similar to those reported by the Jaramillo and Ager laboratories and a recirculation-based flow cell designed by the Gregoire group as part of the high throughput analytical electrochemistry (ANEC) system (See Appendix Fig. S5.1a and 5.1b for cell geometries).^{15,16,29}

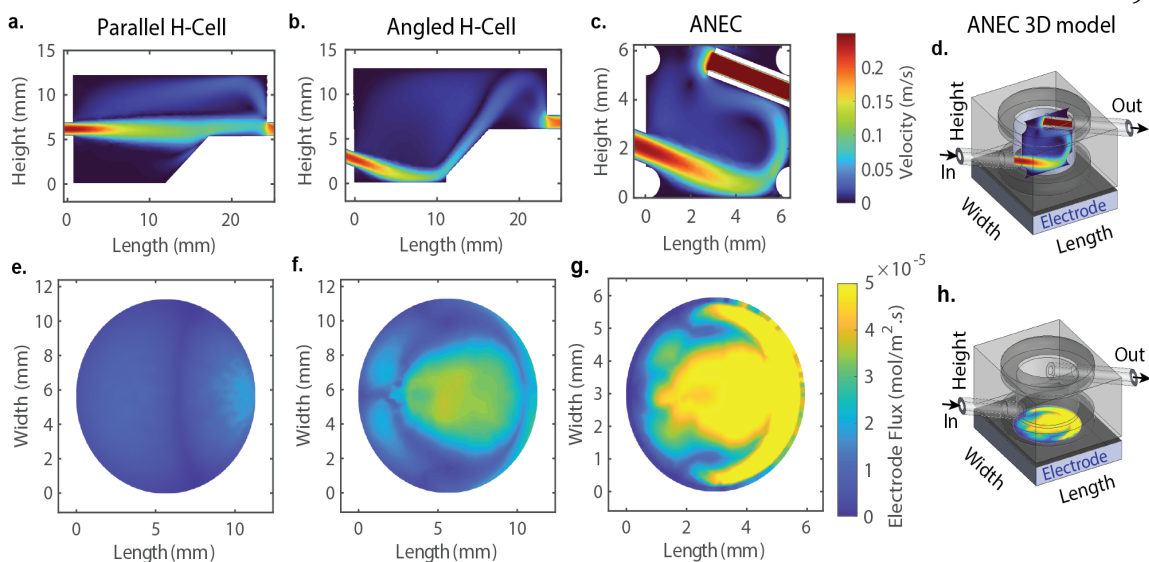


Figure 5.2: COMSOL simulations of electrolyte velocity in the a) parallel-flow H-cell, b) angled-flow H-cell, and c) ANEC cell are shown as cross-sections through the middle of each cell, as shown for ANEC in d), where the electrolyte flow is from left to right, the electrode is on the bottom, and the vertical axis is the height above the electrode surface. The distribution in flow velocity within 1 mm of the electrode surface is markedly different among the 3 flow geometries. By setting the concentration of a test species at the electrode to 1 mM, the simulated CO flux from the electrode surface can be estimated for each flow geometry in e), f), and g), respectively. This is shown schematically for ANEC in h). The increasing transport from a) to b) to c) therefore has a marked impact on CO extraction from the electrode surface.

ANEC was designed to deliver CO₂-saturated electrolyte to the electrode via an inlet oriented 20° from horizontal towards the surface, which enhances electrolyte convection and mitigates bubble formation on the electrode surface.²⁹ Recirculating flow conditions were also incorporated in a more traditional H-cell with 2 different flow paths: a horizontal inlet hereafter referred to as the parallel-flow H-cell (Figure S5.1c), and a 20° inlet oriented towards the working electrode, hereafter referred to as the angled-flow H-cell (Figure S5.1d).

COMSOL calculations were performed on the three variations of recirculation cells to quantify the hydrodynamics (Figure 5.2a-c) and evaluate its influence on extraction of desorbed reaction intermediates (Figure 5.2e-g). The modeling of the cell with CO₂-sparged

electrolyte is challenged by the ill-defined hydrodynamic conditions, although we expect that the parallel flow of gas will produce hydrodynamics that are most similar to the parallel-flow H-cell. Since the cells in question are not symmetric and have otherwise complex cell geometries, the turbulence in each cell cannot be quantified using typical chemical engineering parameters such as Reynolds or Sherwood numbers. For instance, the Reynolds number for the parallel flow and angled-flow H-cells will be the same since the fluid, velocities, and characteristic length scales are all the same. In the parallel-flow H-cell, the majority of the electrolyte flow passes directly through the cell because the flow inlet and outlet are aligned (Figure 5.2a). The only convection provided comes from mild eddy currents in the near-surface region, which is likely similar to what would be observed with vigorous bubbling. In the angled-flow H-cell, a large portion of the electrode area experiences relatively high flow rates, creating high convection and preventing bubble accumulation on the electrode surface (Figure 5.2b). The ANEC cell shows a similar electrolyte path to the angled-flow H-cell, but with a larger affected region due to the relative diameters of the electrode and tubing of the two systems (Figure 5.2c,d).

While the fluid dynamics calculations describe the convection of CO_2 to the electrode surface, they do not directly provide information about the residence time or flux of reaction products from the electrode surface. To resolve this, COMSOL calculations were performed on each cell design with Dirichlet boundary conditions at the electrode corresponding to a chemistry-agnostic test species (Figure 5.2d-h).

We find, qualitatively, that the flux of a chemistry-agnostic test species away from the electrode surface is, as expected, commensurate with the simulated hydrodynamics; namely, the flux away from the electrode surface is largest in the ANEC cell, followed by

the angled-flow H-cell, and then smallest in the parallel-flow H-cell. This is consistent with experimental findings using potassium ferricyanide reduction, with a 3-fold smaller average diffusion layer in the ANEC cell and angled-flow H-cell than in the parallel H-cell (see Figure S5.2, Table S5.1).

Consistent with previous findings with RCEs, we observe that the differences in convection are correlated with each system's CO partial current densities (Figure 5.3). Since the total CO₂R current density is comparable among the systems in question, we attribute the changes in selectivity to the changes in intermediate transport and not to differences in CO₂ availability (Figure S5.3a). The differences in partial current density are more apparent at higher overpotentials, likely due to increased activity, which is consistent with prior studies.³⁰ We therefore posit that j_{CO} can be used as a probe for the level of convection near the electrode in any electrochemical cell (with a Cu catalyst). This relationship is commensurate with the observations from Figure 5.2 and arises from the equilibration of adsorbed and desorbed CO, where increased convection facilitates removal of dissolved CO before it can be further electrochemically reduced.

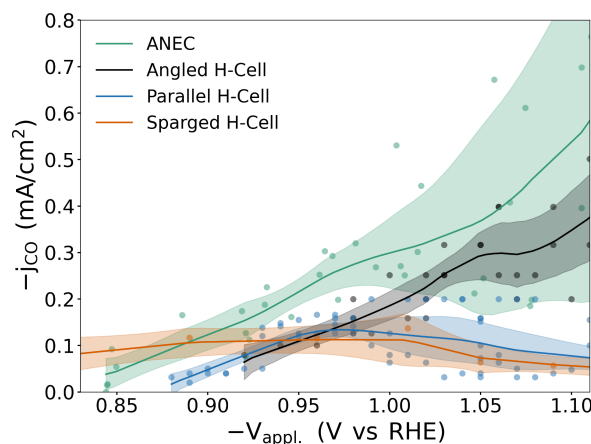


Figure 5.3: Measured partial current densities for CO in each cell geometry with respect to potential. Each data point corresponds to an individual experiment, with the exception of the Sparged H-cell data, reproduced from [15], which is an average of three experiments.^{15,16,29} The shaded regions correspond to a 95% confidence interval around a trend line fitting function calculated via locally weighted scatterplot smoothing (LOWESS, see Appendix 5 for calculation details).

Based on the trends on Figure 5.2, we anticipate that the ANEC cell provides the hydrodynamics that most substantially differ from a sparged H-cell, motivating comparison of their potential-dependent performance towards products more reduced than CO, commencing with $j_{C_2H_4}$ in Figure 5.4a and continuing with additional products in Figure 5.5a-c. To quantify the differences in product distribution in the context of Tafel analysis, the recently-reported Bayesian framework was adopted to generate the distribution of Tafel slopes for each of the 3 H-cell flow conditions as well as for ANEC.³¹ The maximum likelihood Tafel slope values for the ANEC cell are 39 and 41 mV dec⁻¹, respectively.⁸ These values are markedly different than those observed using data established by Kuhl, *et al.* for the sparged H-cell, 99 and 80 mV dec⁻¹, respectively (Figure 5.4a, S5.4a).¹⁵

Applying the same analysis to the parallel flow and angled-flow H-cells, with each increase in convection and corresponding increase in j_{CO} , a decrease in the Tafel slope for ethylene and methane was observed (Figure 5.4b, S5.4b, full probability distributions in

Figures S5.5-12). A larger change associated with the methane Tafel slope is consistent with previous reports of j_{CH_4} being more sensitive to p_{CO} than ethylene.³⁰ Based on Tafel analysis alone, these results suggest that the RDS of copper catalyzed CO_2 reduction changes with convection. Specifically, the Tafel slope suggests a shift in the RDS from an initial electron transfer with the sparged H-cell (expected 120 mV dec^{-1} for $n = 0$ and $q = 1$, see Scheme 5.1 and Equation 5.1), toward a later step in the CO_2R mechanism with ANEC ($n \geq 1$), such as a subsequent chemical step ($q = 0$, Tafel slope $\leq 60 \text{ mV dec}^{-1}$) or electron transfer step ($q = 1$, Tafel slope $\leq 40 \text{ mV dec}^{-1}$). The lowered Tafel slopes provide an opportunity for substantially increasing partial current densities with a modest increase in overpotential. Figure 5.4a indicates that the present cell designs cannot fully realize that opportunity due to a mass transport limit when the partial current density reaches ca. 10 mA cm^{-2} ; we expect future work on scalable reactor design can leverage the impact of convection on the Tafel slope to increase partial currents toward highly reduced products.

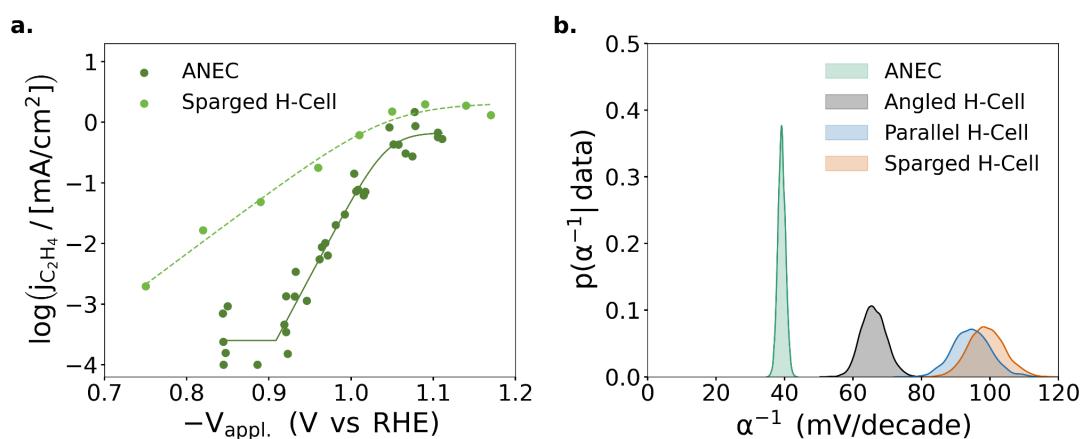
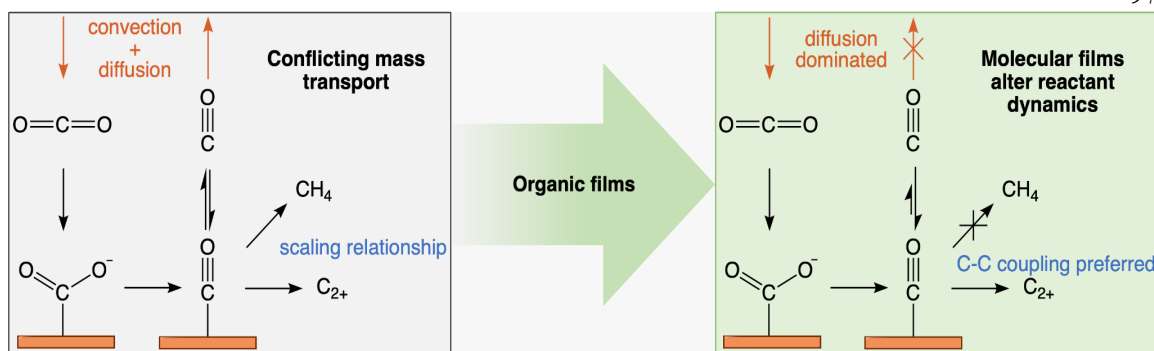


Figure 5.4: a) Tafel plots for ethylene comparing data from ANEC and the sparged H-cell. A small plateau exists on the bottom of each ANEC plot due to the noise floor of the instrument. Each data point corresponds to an individual experiment, with the exception of the Sparged H-cell data, reproduced from [15], which is an average of three experiments.¹⁵ b) Probability density curves for ethylene Tafel slope values using Bayesian statistics for each cell geometry investigated. An identical figure for methane exists in Figure S5.4.

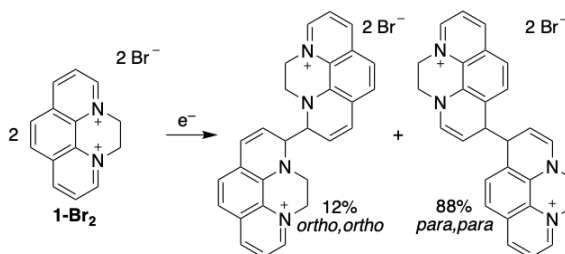
Given the systematic variation in observed Tafel slope with level of convection, we identify two predominant explanations for the underlying cause: increased CO₂ availability or decreased surface coverage of CO with increased hydrodynamics. The former explanation implies that insufficient convection causes depleted local CO₂ at the electrode surface, resulting in low molecular collision probabilities and making CO₂ activation the RDS.³² For the latter explanation, the combination of high near-surface [CO] under low-convection conditions and the dynamic desorption-readsorption process of CO may interfere with the activation of CO₂, which results in an apparent Tafel slope that conflates CO₂ activation with CO reduction. In either case these findings emphasize that the apparent Tafel slope reported for a Cu-based CO₂ reduction system, or any such system wherein intermediates such as CO may be further reduced, arises from both the catalyst's intrinsic kinetics *and* mass transfer conditions. As a result, these studies must carefully consider the convective conditions of the electrolyte, similar to how mechanistic studies in aqueous CO₂ reduction often include discussions of surface facets, electric double layers, etc.¹⁵⁻¹⁸



Scheme 5.2: CO₂ delivery to the electrode surface is promoted by increased transport in the cell, but so is the removal of CO produced at the electrode surface. In circumstances of high transport with relatively low CO surface coverage, a scaling relationship between CH₄ and C₂₊ products can be observed.²⁸ Molecular films disrupt the trade-off between CO₂ delivery and CO removal, breaking the scaling relationship in favor of increased selectivity for carbon-coupled products. The additive can act as a physical barrier for CO leaving the catalyst interface and attenuate the rate of CO removal.

Investigating changes to product selectivity and activity upon the addition of organic films, derived from a molecular additive via electrodeposition, provides an opportunity to differentiate whether CO₂ or CO availability is the primary driver of the hydrodynamics-dependent Tafel slope. When a hydrophobic film is used, it has been posited to maintain the local CO₂ concentration while inhibiting H₂O transport.³³ Accordingly, the local CO₂ concentration is maintained while the additive acts as a physical barrier to trap and boost the concentration of CO near the electrode surface (Scheme 5.2). Upon reductive deposition of N,N'-ethylene-phenanthroline dibromide (**1-Br₂**, Scheme 5.3) on Cu, the selectivities for CO and CH₄ in both the sparged H-cell and the ANEC cell are suppressed while the electrochemical active surface area is largely unchanged (Figure 5.5b,d, all other products in Table S5.2).^{15,34} Following our previous use of j_{CO} as an indicator of electrolyte convection, the attenuation of j_{CO} in the ANEC cell with an additive film (Figure 5.5d) suggests that the catalyst interface experiences small amounts of convection relative to the unmodified system.

Note that the reduction in j_{CH_4} is consistent with the previous observation of an inverse relationship between local CO concentration and j_{CH_4} .³⁰



Scheme 5.3: Reductive dimerization of **1-Br₂** creates an insoluble film on the surface of the electrode.

Analysis of the apparent Tafel slopes for systems with and without molecular additives reveals the RDS in the organic-modified systems is likely the first electron transfer (Figure 5.6). Maintaining similar Tafel slopes between the sparged H-cell and ANEC systems indicates that the **1-Br₂** coating creates similar surface microenvironments regardless of the cell's hydrodynamics. These results indicate that any change in the RDS induced by increased hydrodynamics is reverted upon addition of the **1-Br₂** coating. Furthermore, total CO₂R current density is comparable with and without organic films. Accordingly, we expect changes in product selectivity and activity to be due to changes in intermediate transport and not to differences in CO₂ availability (Figure S5.3b).

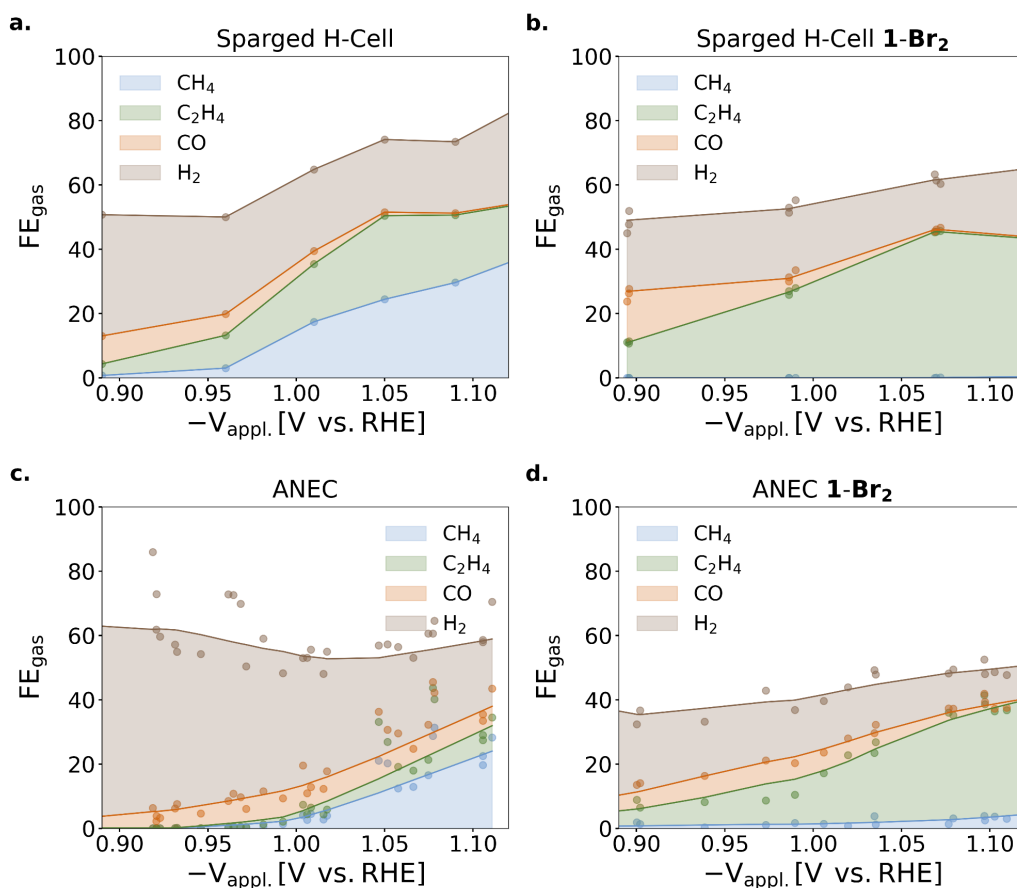


Figure 5.5: The distribution of gaseous products are shown as stack plots for a) bare¹⁵ and b) **1-Br₂**-modified³⁴ polycrystalline Cu electrodes with respect to potential in a CO₂-sparged H-cell. The product distribution from c) bare and d) **1-Br₂**-modified polycrystalline Cu electrodes in ANEC are shown with smooth trend lines calculated using LOWESS (see Appendix 5 for calculation details). Each data point corresponds to an individual experiment, with the exception of the Sparged H-cell data, reproduced from [15], which is an average of three experiments.¹⁵ The presence of **1-Br₂** mitigates the influence of the difference flow conditions in the H-Cell and ANEC cell.

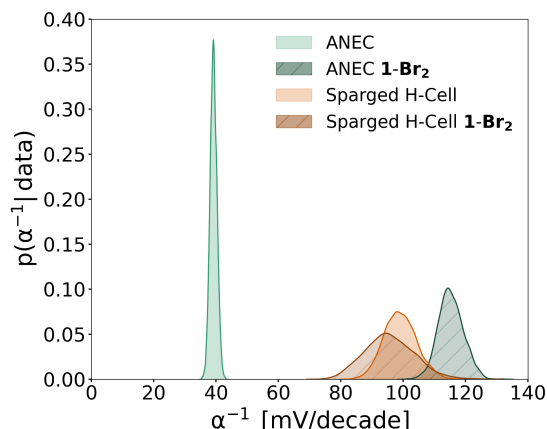


Figure 5.6: The distribution of ethylene Tafel slopes inferred from sparged H-cell¹⁵ and ANEC systems, both without a molecular additive (data reproduced from Figure 5.4b) and with **1-Br₂**.³⁴ The organic film induces a much larger change in Tafel slope for the ANEC system compared to the sparged H-cell system.

In addition to shielding the electrode from bulk electrolyte hydrodynamics, we additionally consider whether organic films further concentrate CO near the catalyst surface. Since the thin electrodeposited films are not amenable to experimental measurement of D_{CO} , we turn to computational investigation of CO transport near the electrode, with and without additive films. Molecular dynamics calculations were performed using a single CO molecule in a bath of either water or a mix of additive/water using LAMMPS (see S5.13-14 for additional computational details).³⁵ The diffusion coefficient of CO in the simulated film was determined to be less than 50% of that in pure H₂O at 298 K. Given that residence time scales inversely with diffusion coefficient (Equation 5.2), a decrease in the diffusion coefficient results in a corresponding increase in the residence time. Here, L is the length of the diffusion layer and τ_{res} is the residence time.³⁶

$$\tau_{res} \sim \frac{L^2}{D_{CO}} \quad (2)$$

Equation 5.2: The mathematical relationship between residence time and diffusion coefficient of intermediates is inversely proportional.

The increased residence time facilitates further reduction of electrochemically generated CO for any cell and flow configuration. This effect of increased residence time is more pronounced for systems with high electrolyte convection because the lowered diffusion constant provided by the organic coating is compounded by the increase in the minimum diffusion layer thickness (set by the film) atop the working electrode, above which any intermediates such as CO are rapidly removed. Without a molecular additive, the difference in product distribution between the sparged H-cell and ANEC systems (Figure 5.5a,c) is much more pronounced than the respective difference with the **1-Br₂** additive (Figure 5.5b,d). This finding highlights the opportunity to combine electrolyte convection and organic coatings for both fundamental studies and reactor design, where the former mitigates bubble formation at the working electrode and provides controlled and relatively uniform hydrodynamics, and the latter provides an increased local concentration of CO to promote C-C coupling and thus the formation of highly reduced products.

5.3 Conclusions

Systematic variation in hydrodynamics of Cu-based CO₂ reduction reactors was achieved via adoption of electrolyte flow systems, as opposed to traditional CO₂-sparged H-cells. We show that increased electrolyte convection causes a substantial decrease of the Tafel slope for ethylene and methane production. Since increased convection led to increased j_{CO} , an inferred change in the RDS for ethylene and methane production is induced by rapid extraction of desorbed CO under high-convection conditions. Furthermore, the lowered Tafel slopes provided by high-convection conditions provide opportunities for electrolyzers with high partial current density toward highly reduced products.

While our collective results do not negate the effects that local pH and cation identity may have on the Tafel slope value, they highlight that Tafel analyses to-date have been limited to a particular mass transport regime and that study of different regimes can help elucidate reaction mechanisms. This type of strategy was utilized herein for the study of organic additive-derived molecular coatings, which introduce a new mass transport regime where product distributions and Tafel slope values are not as influenced by electrolyte convection, due to diffusive transport within the coating. Furthermore, the relatively slow diffusion of CO within the coating promotes its further reduction, especially toward C-C coupled products. Together, these results provide context for the scaling relationship previously disclosed between ethylene and methane partial current densities, and the role of CO management within molecular coatings on electrodes towards the disruption of such a scaling relationship, in favor of C₂₊ products.

5.4 References

- (1) Liu, Z.; Deng, Z.; Davis, S. J.; Giron, C.; Ciais, P. Monitoring Global Carbon Emissions in 2021. *Nat. Rev. Earth Environ.* **2022**, *3* (4), 217–219. <https://doi.org/10.1038/s43017-022-00285-w>.
- (2) Foote, E. Circumstances Affecting the Heat of the Sun's Rays. *Am. J. Art Sci.* **1856**, 22.
- (3) Hori, Y.; Kikuchi, K.; Murata, A.; Suzuki, S. Production of Methane and Ethylene in Electrochemical Reduction of Carbon Dioxide at Copper Electrode in Aqueous Hydrogencarbonate Solution. *Chem. Lett.* **1986**, *15* (6), 897–898. <https://doi.org/10.1246/cl.1986.897>.
- (4) Lewis, N. S.; Nocera, D. G. Powering the Planet: Chemical Challenges in Solar Energy

- Utilization. *Proc. Natl. Acad. Sci.* **2006**, *103* (43), 15729–15735.
<https://doi.org/10.1073/pnas.0603395103>.
- (5) Nitopi, S.; Bertheussen, E.; Scott, S. B.; Liu, X.; Engstfeld, A. K.; Horch, S.; Seger, B.; Stephens, I. E. L.; Chan, K.; Hahn, C.; Nørskov, J. K.; Jaramillo, T. F.; Chorkendorff, I. Progress and Perspectives of Electrochemical CO₂ Reduction on Copper in Aqueous Electrolyte. *Chem. Rev.* **2019**, *119* (12), 7610–7672.
<https://doi.org/10.1021/acs.chemrev.8b00705>.
- (6) Bui, J. C.; Lees, E. W.; Pant, L. M.; Zenyuk, I. V.; Bell, A. T.; Weber, A. Z. Continuum Modeling of Porous Electrodes for Electrochemical Synthesis. *Chem. Rev.* **2022**, *acs.chemrev.1c00901*. <https://doi.org/10.1021/acs.chemrev.1c00901>.
- (7) Bard, A. J.; Faulkner, L. R.; Leddy, J.; Zoski, C. G. *Electrochemical Methods: Fundamentals and Applications*; Wiley, New York, 1980; Vol. 2.
- (8) Limaye, A. M.; Zeng, J. S.; Willard, A. P.; Manthiram, K. Bayesian Data Analysis Reveals No Preference for Cardinal Tafel Slopes in CO₂ Reduction Electrocatalysis. *Nat. Commun.* **2021**, *12* (1), 703. <https://doi.org/10.1038/s41467-021-20924-y>.
- (9) Lum, Y.; Cheng, T.; Goddard, W. A.; Ager, J. W. Electrochemical CO Reduction Builds Solvent Water into Oxygenate Products. *J. Am. Chem. Soc.* **2018**, *140* (30), 9337–9340. <https://doi.org/10.1021/jacs.8b03986>.
- (10) Peng, H.; Tang, M. T.; Liu, X.; Schlexer Lamoureux, P.; Bajdich, M.; Abild-Pedersen, F. The Role of Atomic Carbon in Directing Electrochemical CO₂ Reduction to Multicarbon Products. *Energy Environ. Sci.* **2021**, *14* (1), 473–482.
<https://doi.org/10.1039/D0EE02826F>.
- (11) Kastlunger, G.; Wang, L.; Govindarajan, N.; Heenen, H. H.; Ringe, S.; Jaramillo, T.;

- Hahn, C.; Chan, K. Using PH Dependence to Understand Mechanisms in Electrochemical CO Reduction. *ACS Catal.* **2022**, 4344–4357. <https://doi.org/10.1021/acscatal.1c05520>.
- (12) Han, X.; Yu, Z.; Qu, J.; Qi, T.; Guo, W.; Zhang, G. Measurement and Correlation of Solubility Data for CO₂ in NaHCO₃ Aqueous Solution. *J. Chem. Eng. Data* **2011**, 56 (4), 1213–1219. <https://doi.org/10.1021/je1011168>.
- (13) Sassenburg, M.; de Rooij, R.; Nesbitt, N. T.; Kas, R.; Chandrashekar, S.; Firet, N. J.; Yang, K.; Liu, K.; Blommaert, M. A.; Kolen, M.; Ripepi, D.; Smith, W. A.; Burdyny, T. Characterizing CO₂ Reduction Catalysts on Gas Diffusion Electrodes: Comparing Activity, Selectivity, and Stability of Transition Metal Catalysts. *ACS Appl. Energy Mater.* **2022**, 5 (5), 5983–5994. <https://doi.org/10.1021/acsaem.2c00160>.
- (14) Baumgartner, L. M.; Koopman, C. I.; Forner-Cuenca, A.; Vermaas, D. A. Narrow Pressure Stability Window of Gas Diffusion Electrodes Limits the Scale-Up of CO₂ Electrolyzers. *ACS Sustain. Chem. Eng.* **2022**, [acssuschemeng.2c00195](https://doi.org/10.1021/acssuschemeng.2c00195). <https://doi.org/10.1021/acssuschemeng.2c00195>.
- (15) Kuhl, K. P.; Cave, E. R.; Abram, D. N.; Jaramillo, T. F. New Insights into the Electrochemical Reduction of Carbon Dioxide on Metallic Copper Surfaces. *Energy Environ. Sci.* **2012**, 5 (5), 7050–7059. <https://doi.org/10.1039/C2EE21234J>.
- (16) Lobaccaro, P.; Singh, M. R.; Clark, E. L.; Kwon, Y.; Bell, A. T.; Ager, J. W. Effects of Temperature and Gas–Liquid Mass Transfer on the Operation of Small Electrochemical Cells for the Quantitative Evaluation of CO₂ Reduction Electrocatalysts. *Phys. Chem. Chem. Phys.* **2016**, 18 (38), 26777–26785. <https://doi.org/10.1039/C6CP05287H>.
- (17) Resasco, J.; Chen, L. D.; Clark, E.; Tsai, C.; Hahn, C.; Jaramillo, T. F.; Chan, K.; Bell,

- A. T. Promoter Effects of Alkali Metal Cations on the Electrochemical Reduction of Carbon Dioxide. *J. Am. Chem. Soc.* **2017**, *139* (32), 11277–11287. <https://doi.org/10.1021/jacs.7b06765>.
- (18) Clark, E. L.; Resasco, J.; Landers, A.; Lin, J.; Chung, L.-T.; Walton, A.; Hahn, C.; Jaramillo, T. F.; Bell, A. T. Standards and Protocols for Data Acquisition and Reporting for Studies of the Electrochemical Reduction of Carbon Dioxide. *ACS Catal.* **2018**, *8* (7), 6560–6570. <https://doi.org/10.1021/acscatal.8b01340>.
- (19) Lin, T. Y.; Baker, S. E.; Duoss, E. B.; Beck, V. A. Analysis of the Reactive CO₂ Surface Flux in Electrocatalytic Aqueous Flow Reactors. *Ind. Eng. Chem. Res.* **2021**, *60* (31), 11824–11833. <https://doi.org/10.1021/acs.iecr.1c01851>.
- (20) Gupta, N.; Gattrell, M.; MacDougall, B. Calculation for the Cathode Surface Concentrations in the Electrochemical Reduction of CO₂ in KHCO₃ Solutions. *J. Appl. Electrochem.* **2006**, *36* (2), 161–172. <https://doi.org/10.1007/s10800-005-9058-y>.
- (21) Gurudayal; Perone, D.; Malani, S.; Lum, Y.; Haussener, S.; Ager, J. W. Sequential Cascade Electrocatalytic Conversion of Carbon Dioxide to C–C Coupled Products. *ACS Appl. Energy Mater.* **2019**, *2* (6), 4551–4559. <https://doi.org/10.1021/acsaem.9b00791>.
- (22) Monroe, M. M.; Lobaccaro, P.; Lum, Y.; Ager, J. W. Membraneless Laminar Flow Cell for Electrocatalytic CO₂ Reduction with Liquid Product Separation. *J. Phys. Appl. Phys.* **2017**, *50* (15), 154006. <https://doi.org/10.1088/1361-6463/aa6359>.
- (23) Moreno-García, P.; Kovács, N.; Grozovski, V.; Gálvez-Vázquez, M. de J.; Vesztegom, S.; Broekmann, P. Toward CO₂ Electroreduction under Controlled Mass Flow Conditions: A Combined Inverted RDE and Gas Chromatography Approach. *Anal.*

- Chem.* **2020**, *92* (6), 4301–4308. <https://doi.org/10.1021/acs.analchem.9b04999>.
- (24) Goyal, A.; Marcandalli, G.; Mints, V. A.; Koper, M. T. M. Competition between CO₂ Reduction and Hydrogen Evolution on a Gold Electrode under Well-Defined Mass Transport Conditions. *J. Am. Chem. Soc.* **2020**, *142* (9), 4154–4161. <https://doi.org/10.1021/jacs.9b10061>.
- (25) Lim, C. F. C.; Harrington, D. A.; Marshall, A. T. Effects of Mass Transfer on the Electrocatalytic CO₂ Reduction on Cu. *Electrochimica Acta* **2017**, *238*, 56–63. <https://doi.org/10.1016/j.electacta.2017.04.017>.
- (26) Jang, J.; Rüscher, M.; Winzely, M.; Morales-Guio, C. G. Gastight Rotating Cylinder Electrode: Toward Decoupling Mass Transport and Intrinsic Kinetics in Electrocatalysis. *AIChE J.* **2022**. <https://doi.org/10.1002/aic.17605>.
- (27) Gabe, D. R.; Walsh, F. C. The Rotating Cylinder Electrode: A Review of Development. *J. Appl. Electrochem.* **1983**, *13* (1), 3–21. <https://doi.org/10.1007/BF00615883>.
- (28) Lai, Y.; Watkins, N. B.; Rosas-Hernández, A.; Thevenon, A.; Heim, G. P.; Zhou, L.; Wu, Y.; Peters, J. C.; Gregoire, J. M.; Agapie, T. Breaking Scaling Relationships in CO₂ Reduction on Copper Alloys with Organic Additives. *ACS Cent. Sci.* **2021**, *7* (10), 1756–1762. <https://doi.org/10.1021/acscentsci.1c00860>.
- (29) Jones, R. J. R.; Wang, Y.; Lai, Y.; Shinde, A.; Gregoire, J. M. Reactor Design and Integration with Product Detection to Accelerate Screening of Electrocatalysts for Carbon Dioxide Reduction. *Rev. Sci. Instrum.* **2018**, *89* (12), 124102. <https://doi.org/10.1063/1.5049704>.
- (30) Schreier, M.; Yoon, Y.; Jackson, M. N.; Surendranath, Y. Competition between H and CO for Active Sites Governs Copper-Mediated Electrosynthesis of Hydrocarbon Fuels.

Angew. Chem. Int. Ed. **2018**, *57* (32), 10221–10225.

<https://doi.org/10.1002/anie.201806051>.

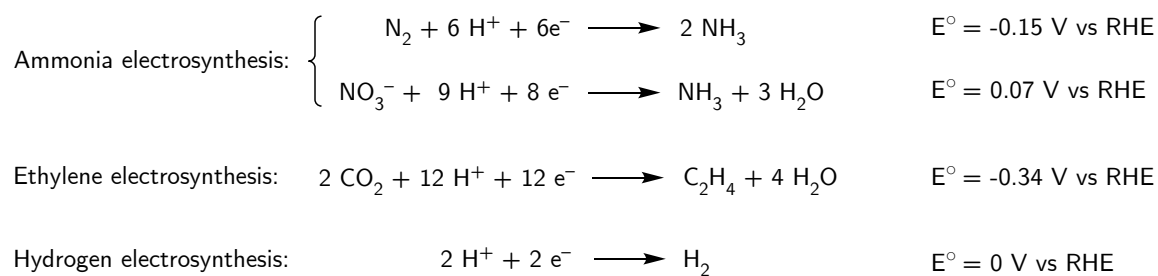
- (31) Agbo, P.; Danilovic, N. An Algorithm for the Extraction of Tafel Slopes. *J. Phys. Chem. C* **2019**, *123* (50), 30252–30264. <https://doi.org/10.1021/acs.jpcc.9b06820>.
- (32) Yang, K.; Kas, R.; Smith, W. A. In Situ Infrared Spectroscopy Reveals Persistent Alkalinity near Electrode Surfaces during CO₂ Electroreduction. *J. Am. Chem. Soc.* **2019**, *141* (40), 15891–15900. <https://doi.org/10.1021/jacs.9b07000>.
- (33) Thevenon, A.; Rosas-Hernández, A.; Fontani Herreros, A. M.; Agapie, T.; Peters, J. C. Dramatic HER Suppression on Ag Electrodes via Molecular Films for Highly Selective CO₂ to CO Reduction. *ACS Catal.* **2021**, *11* (8), 4530–4537. <https://doi.org/10.1021/acscatal.1c00338>.
- (34) Thevenon, A.; Rosas-Hernández, A.; Peters, J. C.; Agapie, T. In-Situ Nanostructuring and Stabilization of Polycrystalline Copper by an Organic Salt Additive Promotes Electrocatalytic CO₂ Reduction to Ethylene. *Angew. Chem. Int. Ed.* **2019**, *58* (47), 16952–16958. <https://doi.org/10.1002/anie.201907935>.
- (35) Poudyal, I.; Adhikari, N. P. Temperature Dependence of Diffusion Coefficient of Carbon Monoxide in Water: A Molecular Dynamics Study. *J. Mol. Liq.* **2014**, *194*, 77–84. <https://doi.org/10.1016/j.molliq.2014.01.004>.
- (36) Deen, W. M. *Analysis of Transport Phenomena*; 2012.

*Chapter 6***ELECTRODE SURFACE HEATING WITH ORGANIC FILMS
IMPROVES CO₂ REDUCTION KINETICS ON COPPER**

In collaboration with Yungchieh Lai, Zachary J. Schiffer, and Virginia Canestraight.

6.1 Introduction

Decarbonization of the chemical industry is an important step towards halting the progress of anthropogenic climate change. Electrochemical reactions driven with solar power and other renewable energy sources to manufacture commodity chemicals, such as ammonia, ethylene, and hydrogen have been recent targets to achieve this goal.¹ While these commodity chemicals are currently being produced by well-established thermochemical processes, such as the Haber-Bosch process, each product has a clear alternative electrochemical synthetic pathway.² Ammonia can be produced either via nitrogen reduction or nitrate reduction, ethylene via CO₂ reduction (CO₂R), and hydrogen via water reduction (Scheme 6.1).^{3,4} In addition, while the simplest operation is to drive these processes using grid-based renewable electricity alone, eventual electrolyzers can be integrated with solar-driven cells to afford photoelectrochemical (PEC) devices that directly harness the sun's energy and enable distributed chemical manufacturing. While these processes are currently not economically viable, the development of improved catalysts, membranes, photovoltaics, and government incentives drive forward their feasibility.⁵



Scheme 6.1: Electrochemical pathways for the production of ammonia, ethylene, and hydrogen. Next to each equation is the standard cell potential required for the reductive transformation taken from Ref. 3 & 4.

Thermocatalysis involves thermally-activated traversal of reaction barrier, which is well described by the Arrhenius expression for the rate constant k (Equation 1).^{6,7} Here, A is a pre-exponential factor, E_a is the activation energy for the reaction, R is the universal gas constant, and T is the temperature of the reaction. Since lowering the activation energy is not always possible, methodologies for increasing reaction temperature are therefore desirable.

$$k = Ae^{\frac{-E_a}{RT}} \quad (1)$$

The electrochemical analogue to Equation 1 is the Butler-Volmer expression for the kinetic current, i_k (Equation 2). In the Butler-Volmer expression, in addition to the same temperature dependent exponential with an activation energy, there is also a linear, potential dependent term in the exponential. More complex theories expand on Butler-Volmer by, e.g., adding a quadratic potential term to the exponential, as is done with Marcus theory. Here, α is the transfer coefficient, which is a function of the pre-equilibrium electron transfers and the rate-determining step, and ϕ is the applied potential with respect to a reference potential.⁸ In all cases, Butler-Volmer retains the qualitative form of the traditional Arrhenius expression, and elevated temperatures will increase the kinetic current.⁹

$$i_k = Ae^{\frac{-E_a + \alpha\phi}{RT}} \quad (2)$$

Since temperature will improve reaction kinetics, the question remains how to efficiently heat the system. Industrial water splitting and CO₂ reduction processes heat the entire electrolyzer to 40-60 °C and operate at current densities of or above 500 mA/cm².^{10,11} It is of note that the limitation for these operating temperatures is typically the stability of the membrane and not of the catalyst.¹² While uniform heating is beneficial for homogeneous reactions associated with many traditional thermochemical processes, electrochemistry is

localized to the electrode surface; heating the bulk may therefore result in wasted energy.

Additionally, resistive heating at industrially-relevant current densities causes electrode surface temperature variation from the bulk by more than 10 °C.^{13,14} In photoelectrochemically driven systems, irradiative heating can cause local heating of the electrode surface by a similar margin.¹⁵ Given the sensitivity of electrochemistry to changes in temperature, these differences between set point and actual electrode temperature may have significant impacts on catalysis.

Bulk heating experiments in electrochemical CO₂ reduction on copper have shown variable results. While all reports show increasing hydrogen and decreasing methane at elevated temperatures, ethylene promotion has varied between studies.^{16–19} We expect that this discrepancy may be due to variable convective mass transport between systems, which has been shown to have a significant effect on selectivity at 25 °C and would become especially important at elevated temperatures due to decreased CO₂ solubility.^{20–22} There is evidence from the electrochemical sensor literature that enhanced reactivity can be achieved by using local heating.^{23–25} In the case of CO₂ reduction, this would overcome the tradeoff associated with decreasing bulk CO₂ solubility.²⁰ Recently, this concept has been applied to CO₂R catalysis with both surface heating and cooling, achieving altered performance without significantly affecting the bulk temperature.^{26,27} In these works, Bi rotating disk electrodes (RDEs) increased their activity for formate by a factor of 1.7 upon raising surface temperatures to 65 °C and planar Cu electrodes boosted their methane selectivity to 80% by cooling the electrode to -4.4 °C (and applying pulsed electrolysis). In contrast to previous works, surface heating on copper showed no clear trend in ethylene or methane Faradaic efficiencies with respect to temperature, especially in the absence of supporting EDTA in the

electrolyte, supporting the fact that hydrodynamics can significantly impact performance.²⁷ In this work, we evaluate how mass transport and electrodeposited organic films affect the performance of heated electrodes for ferricyanide and CO₂ reduction to C₂₊ products.

6.2 Results and Discussion

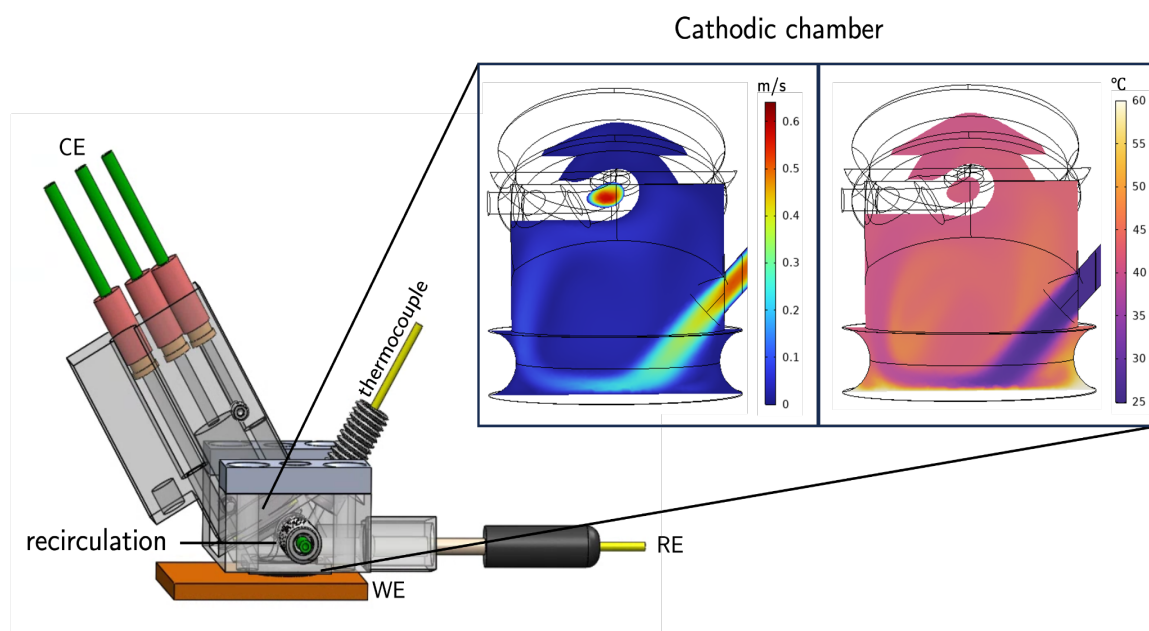


Figure 6.1: A) Schematic of the high throughput analytical electrochemistry (HT-ANEC) screening system utilized in this report. The working electrode is placed on top of a Peltier heating element to accurately modulate surface temperature and the internal temperature can be monitored using a thermocouple inserted in the top of the cell. In the inset are cross sectional images of the simulated velocity and temperature profiles within the cell given a flow rate of 150 $\mu\text{L/s}$ and a surface temperature of 60 $^{\circ}\text{C}$.

To establish a system with variable electrode temperature and hydrodynamics, we expanded the high throughput analytical electrochemistry (HT-ANEC) screening system to include a Peltier heating element that is electrically isolated and thermally coupled to the planar working electrode. To characterize the behavior of the cell with a heated working

electrode and electrolyte flow, we invoked multiphysics modeling to establish the distribution of electrolyte flow rate and temperature throughout the working electrode chamber (Figure 6.1).²⁸ The design of the cell varies slightly from our previous report on the effects of hydrodynamics on Tafel slopes to allow for a thermocouple to be placed inside the working compartment to monitor internal temperature.²² We measured internal and outlet temperatures at five temperature points with surface heating (SH) to evaluate the degree of global heating of the system. At a surface temperature of 60 °C, we experimentally measure an internal temperature of $36 \text{ °C} \pm 1.1 \text{ °C}$ and an outlet temperature of 26.8 ± 0.1 , which supports our goal of mitigating bulk electrolyte heating. Our simulations further support this claim, with the average temperature in the cell showing Gaussian temperature distributions at temperatures far below the surface temperature (Figure S6.1, Table S6.1).

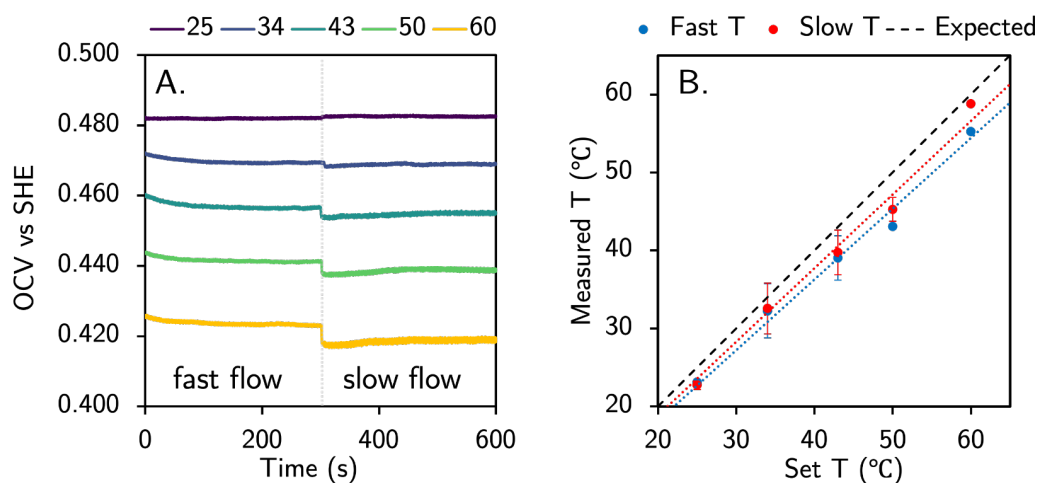


Figure 6.2: A) OCV measurements at variable electrode temperatures over time changing from a fast electrolyte recirculation rate to a slower one at 300 s. B) Comparison of measured temperature values for the two recirculation rates compared to the set temperatures. Error bars indicate the standard deviation between two measurements for each temperature. Electrochemistry was performed using a sputtered platinum film working electrode, a platinum wire counter electrode, and a leakless Ag/AgCl reference electrode, in 0.5 M KCl with 5 mM $\text{K}_3\text{Fe}(\text{CN})_6$ and 5 mM $\text{K}_4\text{Fe}(\text{CN})_6$.

To characterize the effective temperature of electrochemical reactions under the condition with a heated working electrode and ambient recirculating electrolyte, we measured the open circuit potential with an electrolyte containing equal concentrations of potassium ferri/ferrocyanide, whose temperature-dependent equilibrium potential is well established.²⁹ We performed open circuit voltage (OCV) measurements at our standard flow rate of 150 $\mu\text{L/s}$ as well as a reduced flow rate (Figure 6.2A). While the observed temperatures reflect the expectation that rapidly flowing ambient electrolyte lowers the effective reaction temperature with respect to the electrode temperature, these deviations are within ca. 5 $^{\circ}\text{C}$ (Figure 6.2B, Table S6.2, Figure S6.2) and demonstrate our ability to systematically vary with reaction temperature via electrode heating. To further understand the differences between surface and bulk heating, we identified the mass transport limited current for each heating system by performing constant potential electrolyses at variable temperatures and using Fick's second law to determine the average concentration boundary layer (δ_c) thickness (Figure S6.3-5).³⁰ Upon changing the temperature, we find that the δ_c decreases in thickness for both systems, but marginally less with SH, which we expect is due to incomplete/inhomogeneous heating of the concentration boundary layer with SH (Figure S6.6). Partial heating is consistent also with the changes in cell resistance since we observe slightly lower resistances with BH than SH. (Figure S6.7).

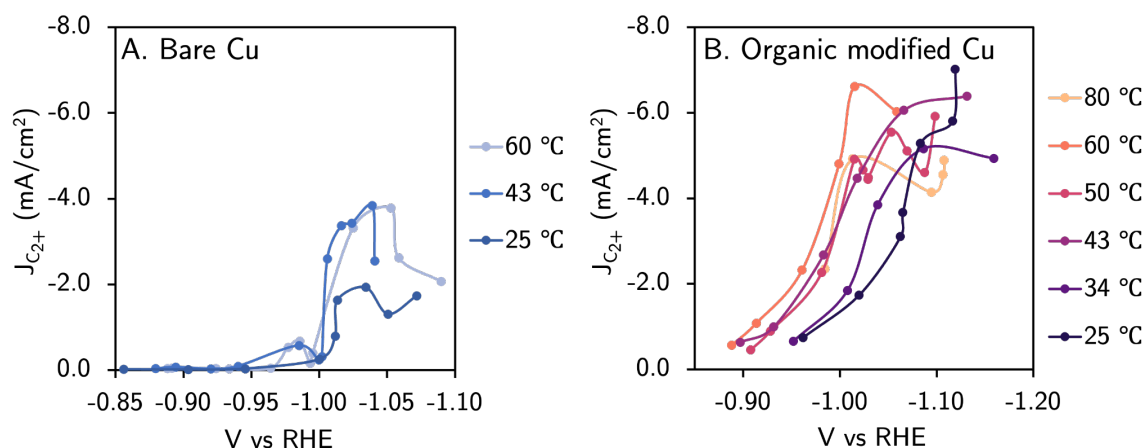
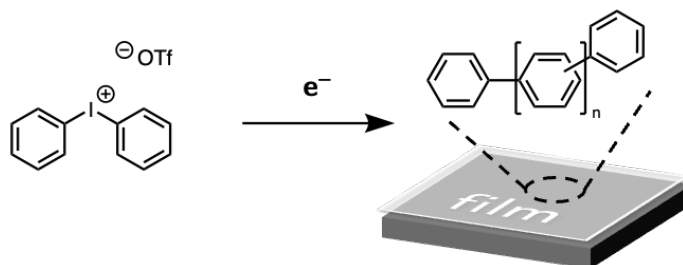


Figure 6.3: Electrochemical CO₂ reduction performance without (left) and with (right) organic films in 0.1 M KHCO₃. Each data point corresponds to an individual experiment. The organic film was deposited via a 10-minute pre-deposition of 10 mM diphenyliodonium triflate at -1.2 V vs RHE in CO₂-sparged 0.1 M KHCO₃. 10 mM diphenyliodonium was present during electrolysis in the case of the additive film, as well to heal minor delamination, as reported previously.³¹

Applying surface heating to CO₂ reduction, we observe an increase in activity for both CO₂R and HER, which is consistent with previous reports (Figure S6.8).^{16–19} However, importantly, we see a 2x increase in partial current density and up to 10% increase in Faradaic efficiency at -1.03 V vs RHE for carbon-coupled products, suggesting that previous reports with this trend had higher levels of mass transfer (Figure 6.3A).¹⁶ We observe no appreciable improvement in C₂₊ partial current density heating the surface from from 43 to 60 °C, supporting the hypothesis from Koper et. al that other factors, such as structural changes, may be significant factors at these elevated temperatures.¹⁹ Unexpectedly, we do not observe a noticeable shift in onset potential for C₂₊ products. We suspect this may be the case due to the increase in partial current density towards hydrogen evolution dominating at more positive potentials or the high convection in the system convoluting the transport of intermediates at the surface.



Scheme 6.2: Under reductive bias, diphenyliodonium triflate polymerizes on the electrode surface to form a robust polyaromatic coating that is electronically insulating, but permeable to reactants and solvent.³¹

In our previous work, we determined organic films create hydrodynamically isolated electrode microenvironments.²² We hypothesized that the addition of an additive film would protect intermediates for long enough close to the electrode surface to allow for them to equilibrate with SH electrode temperatures. While we previously investigated films based on N,N'-ethylenephenanthroline dibromide, herein we investigate those derived from diphenyliodonium triflate due to their increased robustness (Scheme 6.2).³¹ Upon the incorporation of an organic film, we observe a boost in C₂₊ FE and a systematic increase in activity for carbon-coupled products with temperature. In addition to the change in catalytic performance, we observe a positive shift in onset potential for carbon-coupled product formation (Figure 6.3B; Figure S6.9, Table S6.2). The highest activity for C₂₊ products was observed at -1.02 V vs RHE and SH=60 °C, where we obtained a FE_{C₂₊} of 44% and a partial current density of 6.61 mA/cm². With the organic coating, at ambient temperature an additional 0.1 V of overpotential is needed to obtain comparable C₂₊ activity, highlighting how the temperature-based improvements to electrokinetics enable operation at lower overpotentials. This activity and selectivity are beyond those observed without an organic coating, regardless of temperature. The systematic increase in electrokinetics with increasing

surface temperature is more apparent in the presence of the organic coating than in its absence. This systematic improvement to C_{2+} activity is observed up to 60 °C, above which we suspect that the loss in improvement may be from delamination of the organic coating

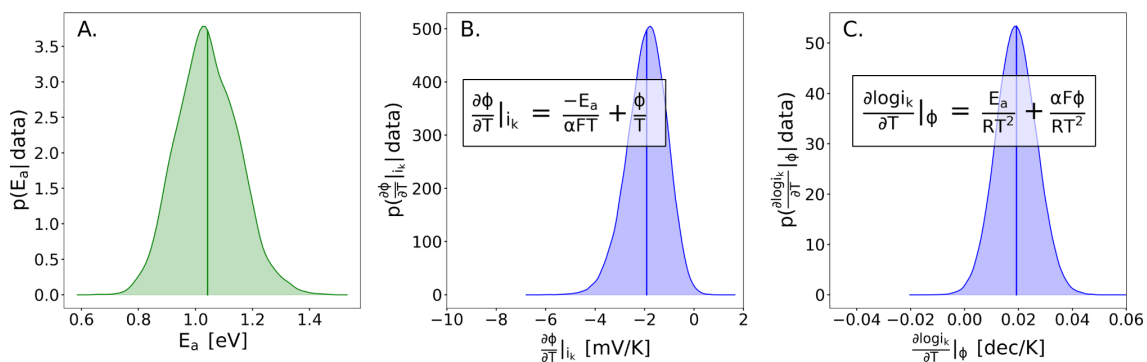


Figure 6.4: Probability distributions of the A) activation energy, E_a , for CO_2 reduction with molecular films using surface heating, B) observed change in applied potential with respect to temperature given a fixed kinetic current, C) observed change in kinetic current with respect to temperature given a fixed applied potential.

While the Butler-Volmer expression is analogous to a traditional Arrhenius rate constant expression, calculating the activation energy for an electrochemical reaction is non-trivial because any temperature dependent analysis (such as plotting $\log_{10}(i_k)$ vs $1/T$) will result in the calculation of a convolution of activation energy, transfer coefficient, and applied potential. Specifically, the slope on a $\log_{10}(i_k)$ vs $1/T$ plot is not the activation energy as it is with a thermochemical reaction, but instead is the quantity $(-E_a + \alpha\phi)$. Thus, to calculate the activation energy of an electrochemical reaction, a comprehensive analysis of a range of potentials and temperatures is necessary, which is seldom done due to limitations in sufficient data collection for rigorous parameter estimation procedures. As a result, we took additional data points at intermediate temperatures to better describe the transition in onset potential across temperatures and fit the resulting data to a temperature dependent Butler-Volmer

model coupled with a mass-transfer limiting current (Figure S6.10).^{8,22} Using the data collected from HT-ANEC at a range of temperatures and potentials with a surface film, we simultaneously calculated posterior distributions for the activation energy (Figure 6.4A, See Appendix for discussion and derivation). The result is an activation energy for CO₂ reduction of ca. 1.0 eV, differs from previously reported values (ca. 0.5 eV), because here we calculate *just* the activation energy, while previous analyses calculate the value of the expression ($-E_a + \alpha\phi$).¹⁸ Note that we include all carbon-coupled products in this analysis due to their presumed common rate determining step, and therefore activation barrier. In addition to the activation energy, we can calculate practical system parameters such as the rate of change of the onset potential with changing temperature (Figure 6.4B) and the rate of change of the current with changing temperature (Figure 6.4C). These derivatives reveal that we expect ca. 2 mV/K shift in onset potential with changing temperature or 0.02 dec/K shift in $\log_{10}(i_k)$ with changing temperatures. Overall, the estimation of these values and derivatives for CO₂ reduction is only possible with the breadth of data achievable with the HT-ANEC as well as comprehensive analysis of the complete data set with an accurate model for the current as a function of temperature and voltage. Furthermore, we find that organic modification was essential to enable the calculation of these fundamental parameters.

6.3 Conclusions

In this work, we identify surface heating with molecular films as an alternative to bulk heating in electrocatalysis. We used the change in open circuit voltage of ferri/ferrocyanide to show that we are able to maintain relatively cooled bulk temperatures, even with heated electrode surfaces. Furthermore, we show that the high convection in the HT-ANEC cell

affects the electrokinetics observed, supporting the fact that macroscopic forces are able to directly affect the catalyst microenvironment. With CO₂ reduction, we show that without additive films, SH enhances activity, but only marginally alters selectivity. Upon the incorporation of an organic film, we demonstrate improved catalytic performance and shifting onset potentials that are consistent with values suggested by fundamental equations. Bayesian analysis of 40 electrolysis experiments at different potentials and temperatures enables identification of a reaction barrier with a probability distribution centered around 1.0 eV for the rate determining step for C₂₊ product formation with elevated temperature also providing a decrease in overpotential of ca. 2 mV/K. The benefits of electrode heating are observed up to 60 °C, above which other effects such as surface reconstruction and delamination of the organic film disrupt the activity vs. temperature trend. Collectively, the results illustrate the importance of decoupling mass transport and temperature effects for establishing fundamental reaction parameters.

6.4 References

- (1) Schiffer, Z. J.; Manthiram, K. Electrification and Decarbonization of the Chemical Industry. *Joule* **2017**, *1* (1), 10–14. <https://doi.org/10.1016/j.joule.2017.07.008>.
- (2) Orella, M. J.; Román-Leshkov, Y.; Brushett, F. R. Emerging Opportunities for Electrochemical Processing to Enable Sustainable Chemical Manufacturing. *Curr. Opin. Chem. Eng.* **2018**, *20*, 159–167. <https://doi.org/10.1016/j.coche.2018.05.002>.
- (3) Wang, Y.; Xu, A.; Wang, Z.; Huang, L.; Li, J.; Li, F.; Wicks, J.; Luo, M.; Nam, D.-H.; Tan, C.-S.; Ding, Y.; Wu, J.; Lum, Y.; Dinh, C.-T.; Sinton, D.; Zheng, G.; Sargent, E. H. Enhanced Nitrate-to-Ammonia Activity on Copper–Nickel Alloys via Tuning of

- Intermediate Adsorption. *J. Am. Chem. Soc.* **2020**, *142* (12), 5702–5708.
<https://doi.org/10.1021/jacs.9b13347>.
- (4) Sun, Z.; Ma, T.; Tao, H.; Fan, Q.; Han, B. Fundamentals and Challenges of Electrochemical CO₂ Reduction Using Two-Dimensional Materials. *Chem* **2017**, *3* (4), 560–587. <https://doi.org/10.1016/j.chempr.2017.09.009>.
- (5) Shaner, M. R.; Atwater, H. A.; Lewis, N. S.; McFarland, E. W. A Comparative Technoeconomic Analysis of Renewable Hydrogen Production Using Solar Energy. *Energy Environ. Sci.* **2016**, *9* (7), 2354–2371. <https://doi.org/10.1039/C5EE02573G>.
- (6) Arrhenius, S. Über die Dissociationswärme und den Einfluss der Temperatur auf den Dissociationsgrad der Elektrolyte. *Z. Für Phys. Chem.* **1889**, *4U* (1), 96–116. <https://doi.org/10.1515/zpch-1889-0408>.
- (7) Bard, A. J.; Faulkner, L. R.; Leddy, J.; Zoski, C. G. *Electrochemical Methods: Fundamentals and Applications*; Wiley, New York, 1980; Vol. 2.
- (8) Limaye, A. M.; Zeng, J. S.; Willard, A. P.; Manthiram, K. Bayesian Data Analysis Reveals No Preference for Cardinal Tafel Slopes in CO₂ Reduction Electrocatalysis. *Nat. Commun.* **2021**, *12* (1), 703. <https://doi.org/10.1038/s41467-021-20924-y>.
- (9) Schiffer, Z. J.; Biswas, S.; Manthiram, K. Ammonium Formate as a Safe, Energy-Dense Electrochemical Fuel Ionic Liquid. *ACS Energy Lett.* **2022**, *7* (10), 3260–3267. <https://doi.org/10.1021/acsenergylett.2c01826>.
- (10) Bernt, M.; Gasteiger, H. A. Influence of Ionomer Content in IrO₂/TiO₂ Electrodes on PEM Water Electrolyzer Performance. *J. Electrochem. Soc.* **2016**, *163* (11), F3179. <https://doi.org/10.1149/2.0231611jes>.
- (11) Arquer, F. P. G. de; Dinh, C.-T.; Ozden, A.; Wicks, J.; McCallum, C.; Kirmani, A. R.;

- Nam, D.-H.; Gabardo, C.; Seifitokaldani, A.; Wang, X.; Li, Y. C.; Li, F.; Edwards, J.; Richter, L. J.; Thorpe, S. J.; Sinton, D.; Sargent, E. H. CO₂ Electrolysis to Multicarbon Products at Activities Greater than 1 A Cm⁻². *Science* **2020**, *367* (6478), 661–666. <https://doi.org/10.1126/science.aay4217>.
- (12) Lindquist, G. A.; Oener, S. Z.; Krivina, R.; Motz, A. R.; Keane, A.; Capuano, C.; Ayers, K. E.; Boettcher, S. W. Performance and Durability of Pure-Water-Fed Anion Exchange Membrane Electrolyzers Using Baseline Materials and Operation. *ACS Appl. Mater. Interfaces* **2021**, *13* (44), 51917–51924. <https://doi.org/10.1021/acsami.1c06053>.
- (13) Phillips, A.; Ulsh, M.; Neyerlin, K. C.; Porter, J.; Bender, G. Impacts of Electrode Coating Irregularities on Polymer Electrolyte Membrane Fuel Cell Lifetime Using Quasi In-Situ Infrared Thermography and Accelerated Stress Testing. *Int. J. Hydrog. Energy* **2018**, *43* (12), 6390–6399. <https://doi.org/10.1016/j.ijhydene.2018.02.050>.
- (14) Iglesias van Montfort, H.-P.; Burdyny, T. Mapping Spatial and Temporal Electrochemical Activity of Water and CO₂ Electrolysis on Gas-Diffusion Electrodes Using Infrared Thermography. *ACS Energy Lett.* **2022**, *7* (8), 2410–2419. <https://doi.org/10.1021/acsenergylett.2c00984>.
- (15) Kistler, T. A.; Um, M. Y.; Cooper, J. K.; Sharp, I. D.; Agbo, P. Exploiting Heat Transfer to Achieve Efficient Photoelectrochemical CO₂ Reduction under Light Concentration. *Energy Environ. Sci.* **2022**, *15* (5), 2061–2070. <https://doi.org/10.1039/D1EE03957A>.
- (16) Hori, Y.; Kikuchi, K.; Murata, A.; Suzuki, S. Production of Methane and Ethylene in Electrochemical Reduction of Carbon Dioxide at Copper Electrode in Aqueous Hydrogencarbonate Solution. *Chem. Lett.* **1986**, *15* (6), 897–898.

<https://doi.org/10.1246/cl.1986.897>.

- (17) Ahn, S. T.; Abu-Baker, I.; Palmore, G. T. R. Electroreduction of CO₂ on Polycrystalline Copper: Effect of Temperature on Product Selectivity. *Catal. Today* **2017**, *288*, 24–29. <https://doi.org/10.1016/j.cattod.2016.09.028>.
- (18) Zong, Y.; Chakthranont, P.; Suntivich, J. Temperature Effect of CO₂ Reduction Electrocatalysis on Copper: Potential Dependency of Activation Energy. *J. Electrochem. Energy Convers. Storage* **2020**, *17* (4). <https://doi.org/10.1115/1.4046552>.
- (19) Vos, R. E.; Kolmeijer, K. E.; Jacobs, T. S.; van der Stam, W.; Weckhuysen, B. M.; Koper, M. T. M. How Temperature Affects the Selectivity of the Electrochemical CO₂ Reduction on Copper. *ACS Catal.* **2023**, 8080–8091. <https://doi.org/10.1021/acscatal.3c00706>.
- (20) Lobaccaro, P.; Singh, M. R.; Clark, E. L.; Kwon, Y.; Bell, A. T.; Ager, J. W. Effects of Temperature and Gas–Liquid Mass Transfer on the Operation of Small Electrochemical Cells for the Quantitative Evaluation of CO₂ Reduction Electrocatalysts. *Phys. Chem. Chem. Phys.* **2016**, *18* (38), 26777–26785. <https://doi.org/10.1039/C6CP05287H>.
- (21) Clark, E. L.; Resasco, J.; Landers, A.; Lin, J.; Chung, L.-T.; Walton, A.; Hahn, C.; Jaramillo, T. F.; Bell, A. T. Standards and Protocols for Data Acquisition and Reporting for Studies of the Electrochemical Reduction of Carbon Dioxide. *ACS Catal.* **2018**, *8* (7), 6560–6570. <https://doi.org/10.1021/acscatal.8b01340>.
- (22) Watkins, N. B.; Schiffer, Z. J.; Lai, Y.; Musgrave, C. B. I.; Atwater, H. A.; Goddard, W. A. I.; Agapie, T.; Peters, J. C.; Gregoire, J. M. Hydrodynamics Change Tafel Slopes in Electrochemical CO₂ Reduction on Copper. *ACS Energy Lett.* **2023**, *8* (5), 2185–

2192. <https://doi.org/10.1021/acseenergylett.3c00442>.
- (23) Gründler, P.; Kirbs, A.; Zerihun, T. Hot-Wire Electrodes: Voltammetry above the Boiling Point. *The Analyst* **1996**, *121* (12), 1805–1810. <https://doi.org/10.1039/AN9962101805>.
- (24) Zerihun, T.; Gründler, P. Electrically Heated Cylindrical Microelectrodes. The Reduction of Dissolved Oxygen on Pt. *J. Electroanal. Chem.* **1996**, *404* (2), 243–248. [https://doi.org/10.1016/0022-0728\(95\)04390-X](https://doi.org/10.1016/0022-0728(95)04390-X).
- (25) Flechsig, G.-U. New Electrode Materials and Devices for Thermoelectrochemical Studies and Applications. *Curr. Opin. Electrochem.* **2018**, *10*, 54–60. <https://doi.org/10.1016/j.coelec.2018.04.002>.
- (26) Qin, S.-F.; Yang, S.; Zhao, L.-C.; Xie, Y.-J.; Wang, Y.; You, L.-X.; Li, J.; Sun, J.-J. Temperature Dependent Electrochemical Reduction of CO₂ at Temperature Controllable-Rotating Disk Electrode Modified with Bismuth Film. *Electrochimica Acta* **2023**, *461*, 142627. <https://doi.org/10.1016/j.electacta.2023.142627>.
- (27) Jo, S. W.; Kim, J. Y.; Lee, M. W.; Kim, Y.; Ahn, H. S. Highly Selective Reduction of CO₂ to Methane Induced by Subzero Depression of the Electrode Surface Temperature. *ACS Catal.* **2023**, 5122–5126. <https://doi.org/10.1021/acscatal.3c00311>.
- (28) Jones, R. J. R.; Wang, Y.; Lai, Y.; Shinde, A.; Gregoire, J. M. Reactor Design and Integration with Product Detection to Accelerate Screening of Electrocatalysts for Carbon Dioxide Reduction. *Rev. Sci. Instrum.* **2018**, *89* (12), 124102. <https://doi.org/10.1063/1.5049704>.
- (29) Huang, B.; Muy, S.; Feng, S.; Katayama, Y.; Lu, Y.-C.; Chen, G.; Shao-Horn, Y. Non-Covalent Interactions in Electrochemical Reactions and Implications in Clean Energy

Applications. *Phys. Chem. Chem. Phys.* **2018**, *20* (23), 15680–15686.

<https://doi.org/10.1039/C8CP02512F>.

- (30) Williams, K.; Corbin, N.; Zeng, J.; Lazouski, N.; Yang, D.-T.; Manthiram, K.

Protecting Effect of Mass Transport during Electrochemical Reduction of Oxygenated Carbon Dioxide Feedstocks. *Sustain. Energy Fuels* **2019**, *3* (5), 1225–1232.

<https://doi.org/10.1039/C9SE00024K>.

- (31) Watkins, N. B.; Wu, Y.; Nie, W.; Peters, J. C.; Agapie, T. In Situ Deposited

Polyaromatic Layer Generates Robust Copper Catalyst for Selective Electrochemical CO₂ Reduction at Variable PH. *ACS Energy Lett.* **2022**, *8* (1), 189–195.

<https://doi.org/10.1021/acseenergylett.2c02002>.

*Appendix 1***UNFINISHED WORK FOR FUTURE INVESTIGATION: CELL DESIGN
FOR WELL-DEFINED HYDRODYNAMICS**

Work performed in collaboration with Virginia Canestraight

A1.1 Introduction:

Electrocatalytic processes driven by renewable energy have the potential to decarbonize the chemical industry and drive forward a more sustainable future.¹ The optimization of electrocatalytic systems can be separated into catalyst and reactor design; the former is focused on increasing the intrinsic activity for the desired product, whereas the latter is focused on controlling the transport of starting materials and reaction intermediates near the electrode surface. H-cells commonly used for catalyst benchmarking and high-performance cells, such as gas diffusion electrode (GDE) assemblies, rely on stir bars or the flowing of gas or electrolyte across the electrode surface to refresh reactants near the surface. However, the large regions of stagnant electrolyte in H-cells and the low transport within the pores of the GDE, as exemplified by the large pH gradients and salt precipitation observed, lead to ill-defined mass transport catalyst interface.²⁻⁵ These uncertainties make it difficult to model the reaction surface accurately or decouple the effects of mass transport from the intrinsic electrokinetics of the catalyst employed within these cell architectures.

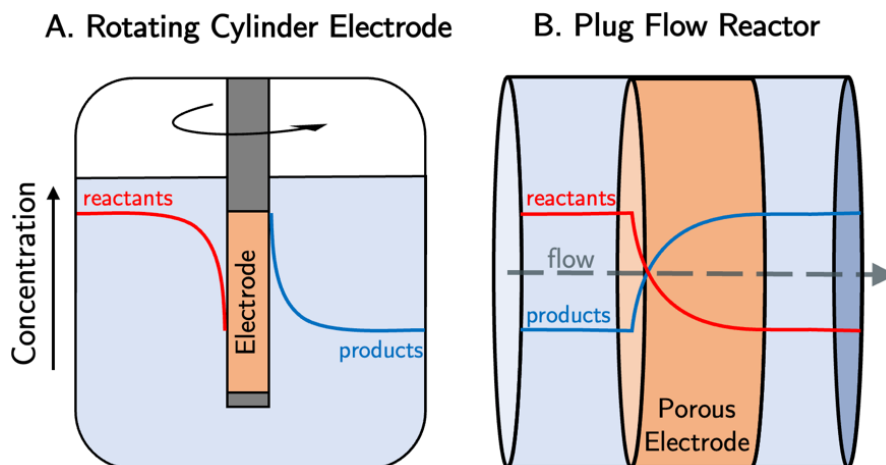


Figure S1.1: Representations of A. rotating cylinder electrode and B. plug flow reactor assemblies with their respective reactant and product concentration profiles.

The classical examples for studying reactions under idealized transport conditions are via the use of continuously stirred tank reactors (CSTR) and plug flow reactors (PFR) because they can be nondimensionalized and simplified into 0-1D kinetic models. CSTRs benefit lower- or negative-order reactions due to their dilute reactant and product streams, whereas the input stream in PFRs can be modified to suit either high- or low-order reactions.⁶ In electrochemistry, these two systems can be most closely represented by rotating electrode and porous electrode flow-through assemblies (Figure 1).^{7,8} However, it is advantageous for experiment throughput to rapidly concentrate products and minimize the effect of support materials on catalysis, making both of these systems undesirable for broad use.⁹ One solution would be to use a thin, parallel plate flow reactor, which enables small electrolyte volume and easily modeled mass transport in two dimensions. These reactors have been used to experimentally validate theoretical models of how gas and electrolyte transport alter the local pH and reactant availability at the electrode surface.¹⁰ It is of note that this design mimics the microfluidic cells that have been used broadly in electrochemistry but benefits from increased electrode surface area.¹¹⁻¹³

A1.2 Cell Design

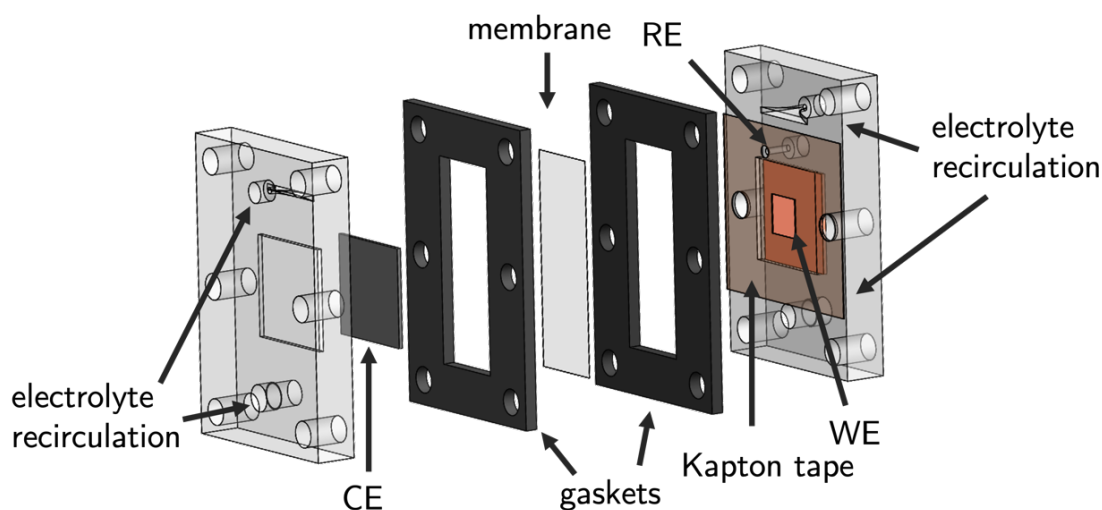


Figure S1.2: Schematic of the parallel plate reactor used in initial experiments.

A thin parallel plate reactor was fabricated using resin-based additive manufacturing (FormLabs Clear V4 resin) to enable accelerated optimization and fewer design constraints. The objectives were to minimize electrolyte volume, while also minimizing the effects of boundary conditions on the flow over the electrode surface (Figure S1.2).¹⁴ To achieve such goals, the electrolyte path was defined by the gaskets that seal the compression cell. Additionally, the electrode is partially masked by nonconductive Kapton tape, to center the working area in the cell. The minimum electrolyte required to operate the cell is ca. 6 mL in each compartment but can be decreased depending on the flow regime of interest (due to minimum tubing sizes for peristaltic pump operation).

To ensure that the electrode only sees uniform flow velocities, the conformity of the fluidics of the cell must be evaluated along two planes (Figure S1.3). Since the reactor can be simplified to a parallel plate model the liquid flow can be described by Equations S1.1,

where v_z is the electrolyte velocity in the z direction, μ is the viscosity of water, and P is pressure.¹⁵

$$\frac{dP}{dz} = \mu \left(\frac{\delta^2 v_z}{\delta x^2} + \frac{\delta^2 v_z}{\delta y^2} \right) \quad (\text{S1.1})$$

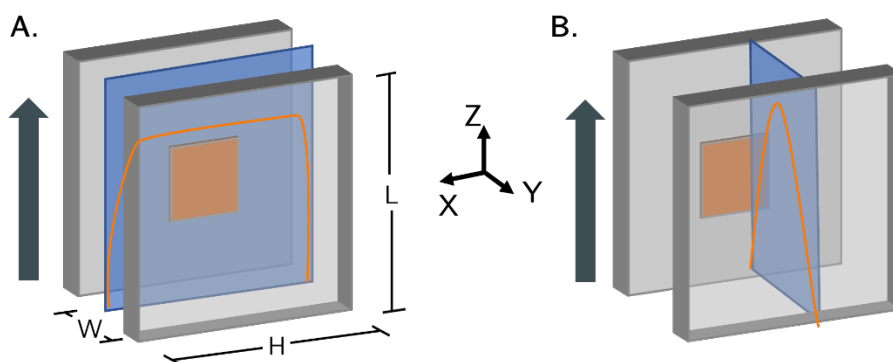


Figure S1.3: Qualitative descriptions of how boundary conditions will affect the electrolyte flow velocity in the plane A. parallel and B. perpendicular to the flow in a parallel plate reactor given liquid flow along the direction of the arrow.

A1.3 Evaluation of Cell Design

Along the width, H , of the cell, dye visualization can map the liquid velocity profile and along the section of the cell, W , ferricyanide reduction can inform concentration boundary layer thicknesses.¹⁶ Furthermore, continuum simulations can support these approximations to inform accuracy of our real-world system.

Dye visualization

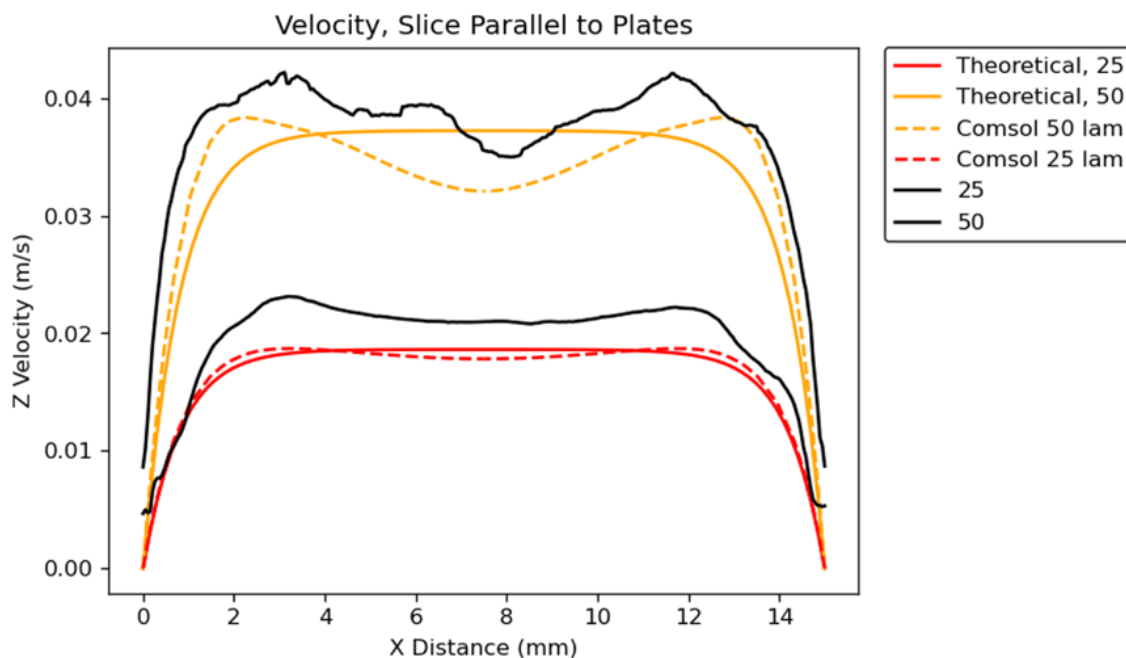


Figure S1.4: Comparison of velocity profiles over the width of the cell using fundamental, continuum, and experimental models at varying flow rates. In the legend, the numbers correspond to the flow rate in mL/min, and “lam” corresponds to the laminar flow model employed in COMSOL.

Using a syringe inserted into the recirculation tubing, pulses of 10 mM red 40 were introduced under varying flow rates. A video was taken of dye front at 60 fps as it passed across the electrode surface and analyzed using a python script to determine the change in dye front position with respect to time. We find that at slow flow speeds, we achieve excellent agreement between experimental, COMSOL, and theoretical models (Figure 1.4). However, at faster flow rates, such as 50 mL/minute we begin to observe an inhomogeneity in the front. Furthermore, performing dye visualization at faster flow rates proved challenging due to the rapid dilution of the dye. Fortunately, we find that our COMSOL calculations still show good agreement with experimental results and can therefore be relied upon to revise the cell design.

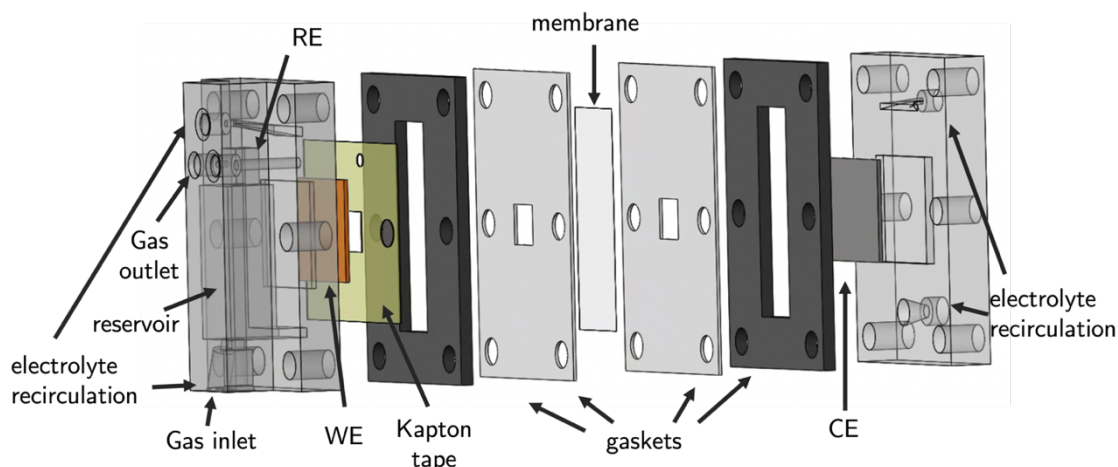


Figure S1.5: Schematic of the finalized parallel plate reactor used in electrolysis experiments.

To improve the delivery of electrolyte across the electrode surface, a reservoir was incorporated into the back of the working electrode manifold with a rectangular inlet the width of the channel defined by the gaskets (Figure S1.5). This increased the total volume of the system by only 2 mL and, according to COMSOL simulations, significantly improved the uniformity of the flow (Figure S1.6) We predict a smooth dye front even at recirculation rates of 150 mL/min, which is a marked improvement from the previous design. In addition to the reservoir, several other changes were made. Due to an issue with the membrane buckling upon compression, two thin gaskets were incorporated on either side of the membrane. The cell was always tightened using a torque wrench to 15 in-lbs of torque. The resistance of the new cell, according to impedance measurements, in 0.1 M KHCO_3 was ca. 4 Ω . To allow for gas sparging throughout catalysis, a gas inlet and outlet were added to the working electrode manifold.

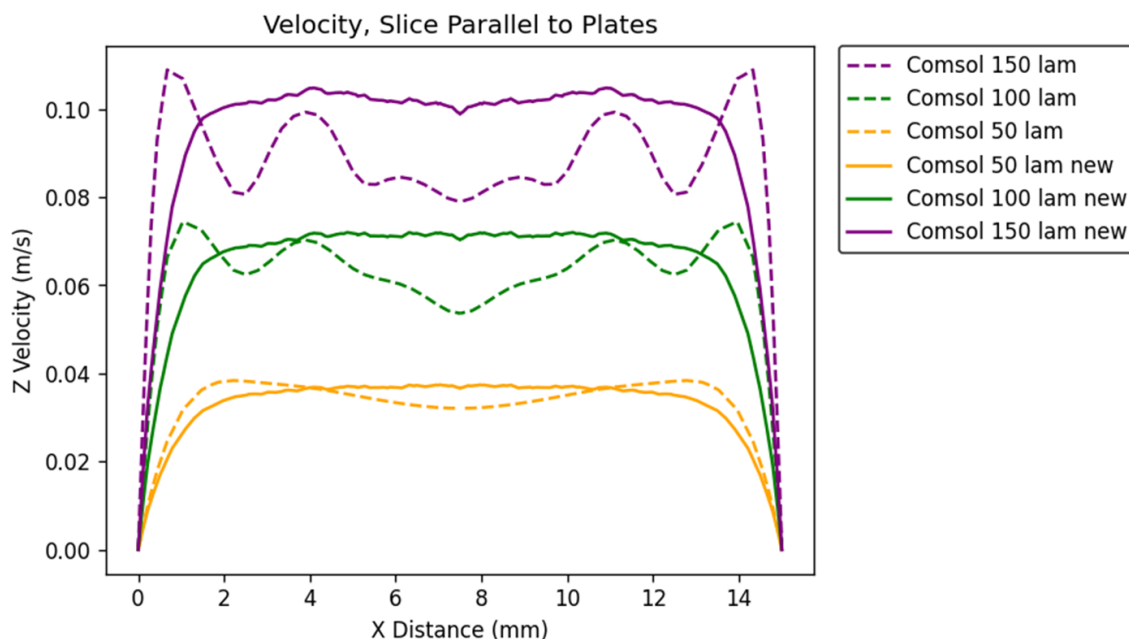


Figure S1.6: Comparison of velocity profiles over the width of the original parallel plate reactor with the “new” version. In the legend, the numbers correspond to the flow rate in mL/min, and “lam” corresponds to the laminar flow model employed in COMSOL.

Ferricyanide Reduction

Since dye visualization is not readily accessible along the perpendicular plane to the electrode, the electrochemical reduction of ferricyanide can be used to provide insight into the diffusion boundary layer of the cell at variable flow rates. Using Fick’s second law, Equation S1.2, we can calculate the concentration boundary layer using the mass transport limited current density, j_{ss} , the diffusion coefficient of potassium ferricyanide, D_{Fe} , the concentration, C_{Fe} , and Faraday’s constant.^{17,18}

$$\delta_{BL} = \frac{nFD_{Fe}C_{Fe}}{j_{ss}} \quad (S1.2)$$

Similar to the horizontal section of the cell, due to the cell’s simplicity, we can model the surface flux both using continuum simulations and fundamental equations. The

theoretical model is based on the continuity equation for a dilute species in flow, Equation S1.3, and describes the flux, $j_{ss,theoretical}$, at the electrode surface.¹⁵

$$j_{ss,theoretical} = \frac{-F}{1\text{ cm}} \int_0^{1\text{ cm}} D_{Fe} \frac{\delta[Fe]}{\delta y} \Big|_{y=0} dz \quad (\text{S1.3})$$

Upon performing cyclic voltammograms to determine where the mass transport limited plateau exists in our system, we identified -0.8 V vs Ag/AgCl as a viable potential to evaluate j_{ss} at. We then performed chronoamperometry at varying flow rates and converted the current density into boundary layer thicknesses. Comparing this result to theoretical and simulated models, we can identify how well-behaved our mass transport is in the perpendicular plane (Figure S1.7).

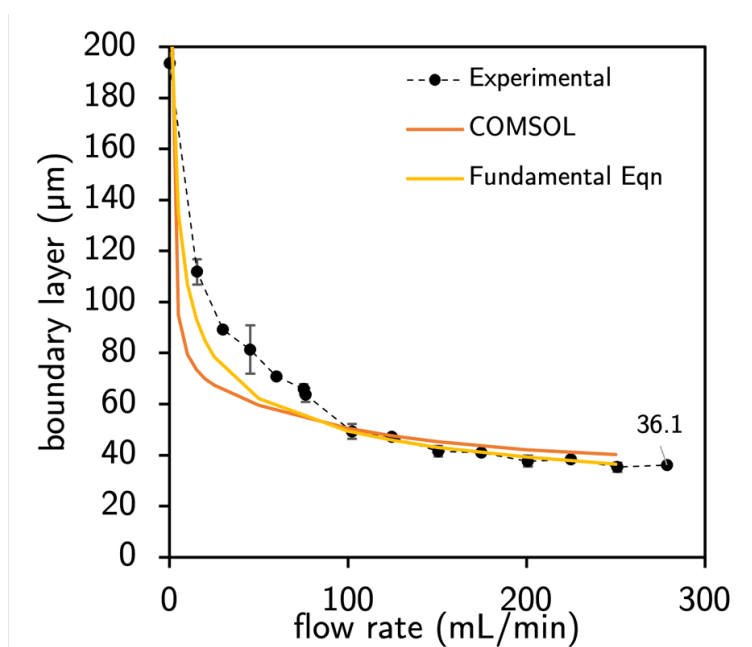


Figure S1.7: Graph showing the change in concentration boundary layer with respect to flow rate using 10 mM $K_3Fe(CN)_6$ in 0.1 M $KHCO_3$ sparged with CO_2 using a gold working electrode, leakless Ag/AgCl reference electrode, and an IrO_x counter electrode. Error bars show the standard deviation from two measurements.

We see good agreement at between the three models at high flow rates but observe some divergence at lower flow rates. We expect that this may be due to three main factors:

1) the periodicity of the peristaltic pump lowering the surface flux, 2) background HER varying between different flow rates, and 3) nonidealities in flow due to the membrane or gaskets buckling. To alleviate these issues in the future, a pump with more rollers should be employed for electrolyses at a more positive overpotential that is still in the mass transport limited plateau with more rigid gaskets. Notwithstanding the small deviation, the designed cell exhibits well-defined hydrodynamics and is viable for the study of electrocatalytic reactions. It is of note, however, that CO₂ reduction was attempted with this cell only to obtain statistically insignificant results. We believe this derived from the peristaltic pump degassing the electrolyte at the accelerated recirculation rates, leading to multiple variables changing simultaneously.¹⁹ Therefore, we recommend that this cell only be used to examine the effect of transport for reactions that do not involve dissolved gasses in the future.

A 1.4 Conclusions

In this work, we developed an electrochemical cell that exhibits well-defined hydrodynamics. Furthermore, we highlight how its simplicity enables the fluid dynamics and surface flux to be described not only using continuum modeling, but also using fundamental equations. This capability differs vastly from the majority of reports in literature where the description of mass transport within the cell is exceedingly difficult. Given the significance of mass transport in reaction performance and in mechanistic study, the wide range of convective laminar transport afforded by this cell make it a valuable electrochemical research tool.^{5,8} While we find that the scope of electrochemical reactions that can be investigated with this cell at this time is limited to those not involving dissolved gasses due to the peristaltic pump, we believe that the merits of the cell designed herein warrants its wider application.

A1.5 References

- (1) Schiffer, Z. J.; Manthiram, K. Electrification and Decarbonization of the Chemical Industry. *Joule* 2017, 1 (1), 10–14. <https://doi.org/10.1016/j.joule.2017.07.008>.
- (2) Lobaccaro, P.; Singh, M. R.; Clark, E. L.; Kwon, Y.; Bell, A. T.; Ager, J. W. Effects of Temperature and Gas–Liquid Mass Transfer on the Operation of Small Electrochemical Cells for the Quantitative Evaluation of CO₂ Reduction Electrocatalysts. *Phys. Chem. Chem. Phys.* 2016, 18 (38), 26777–26785. <https://doi.org/10.1039/C6CP05287H>.
- (3) Zhang, B. A.; Ozel, T.; Elias, J. S.; Costentin, C.; Nocera, D. G. Interplay of Homogeneous Reactions, Mass Transport, and Kinetics in Determining Selectivity of the Reduction of CO₂ on Gold Electrodes. *ACS Cent. Sci.* 2019, 5 (6), 1097–1105. <https://doi.org/10.1021/acscentsci.9b00302>.
- (4) Nesbitt, N. T.; Burdyny, T.; Simonson, H.; Salvatore, D.; Bohra, D.; Kas, R.; Smith, W. A. Liquid–Solid Boundaries Dominate Activity of CO₂ Reduction on Gas-Diffusion Electrodes. *ACS Catal.* 2020, 10 (23), 14093–14106. <https://doi.org/10.1021/acscatal.0c03319>.
- (5) Watkins, N. B.; Schiffer, Z. J.; Lai, Y.; III, C. B. M.; Atwater, H. A.; Goddard III, W. A.; Agapie, T.; Peters, J. C.; Gregoire, J. M. Tunable Hydrodynamics in Electrochemical CO₂ Reduction Facilitate Changes in Tafel Slope. Submitted 2023.
- (6) Foutch, G. L.; Johannes, A. H. Reactors in Process Engineering. In *Encyclopedia of Physical Science and Technology*; Elsevier, 2003; pp 23–43. <https://doi.org/10.1016/B0-12-227410-5/00654-2>.

- (7) Bard, A. J.; Faulkner, L. R.; Leddy, J.; Zoski, C. G. *Electrochemical Methods: Fundamentals and Applications*; Wiley, New York, 1980; Vol. 2.
- (8) Jang, J.; Rüscher, M.; Winzely, M.; Morales-Guio, C. G. Gastight Rotating Cylinder Electrode: Toward Decoupling Mass Transport and Intrinsic Kinetics in Electrocatalysis. *AIChE J.* 2022. <https://doi.org/10.1002/aic.17605>.
- (9) Jones, R. J. R.; Wang, Y.; Lai, Y.; Shinde, A.; Gregoire, J. M. Reactor Design and Integration with Product Detection to Accelerate Screening of Electrocatalysts for Carbon Dioxide Reduction. *Rev. Sci. Instrum.* 2018, 89 (12), 124102. <https://doi.org/10.1063/1.5049704>.
- (10) Ibrahim, O. A.; Navarro-Segarra, M.; Sadeghi, P.; Sabaté, N.; Esquivel, J. P.; Kjeang, E. Microfluidics for Electrochemical Energy Conversion. *Chem. Rev.* 2022, 122 (7), 7236–7266. <https://doi.org/10.1021/acs.chemrev.1c00499>.
- (11) Whipple, D. T.; Finke, E. C.; Kenis, P. J. A. Microfluidic Reactor for the Electrochemical Reduction of Carbon Dioxide: The Effect of PH. *Electrochem. Solid-State Lett.* 2010, 13 (9), B109. <https://doi.org/10.1149/1.3456590>.
- (12) Wu, K.; Birgersson, E.; Kim, B.; Kenis, P. J. A.; Karimi, I. A. Modeling and Experimental Validation of Electrochemical Reduction of CO₂ to CO in a Microfluidic Cell. *J. Electrochem. Soc.* 2015, 162 (1), F23–F32. <https://doi.org/10.1149/2.1021414jes>.
- (13) Abolhasani, M.; Günther, A.; Kumacheva, E. Microfluidic Studies of Carbon Dioxide. *Angew. Chem. Int. Ed.* 2014, 53 (31), 7992–8002. <https://doi.org/10.1002/anie.201403719>.

- (14) Pickett, D. J.; Stanmore, B. R. Ionic Mass Transfer in Parallel Plate Electrochemical Cells. *J. Appl. Electrochem.* 1972, 2 (2), 151–156. <https://doi.org/10.1007/BF00609131>.
- (15) Bird, R. B.; Stewart, W. E.; Lightfoot, E. N. *Transport Phenomena*, Revised 2nd Edition, 2nd edition.; John Wiley & Sons, Inc.: New York, 2006.
- (16) López-García, U. M.; Hidalgo, P. E.; Olvera, J. C.; Castañeda, F.; Ruiz, H.; Orozco, G. The Hydrodynamic Behavior of a Parallel-Plate Electrochemical Reactor. *Fuel* 2013, 110, 162–170. <https://doi.org/10.1016/j.fuel.2012.11.016>.
- (17) Clark, E. L.; Resasco, J.; Landers, A.; Lin, J.; Chung, L.-T.; Walton, A.; Hahn, C.; Jaramillo, T. F.; Bell, A. T. Standards and Protocols for Data Acquisition and Reporting for Studies of the Electrochemical Reduction of Carbon Dioxide. *ACS Catal.* 2018, 8 (7), 6560–6570. <https://doi.org/10.1021/acscatal.8b01340>.
- (18) Williams, K.; Corbin, N.; Zeng, J.; Lazouski, N.; Yang, D.-T.; Manthiram, K. Protecting Effect of Mass Transport during Electrochemical Reduction of Oxygenated Carbon Dioxide Feedstocks. *Sustain. Energy Fuels* 2019, 3 (5), 1225–1232. <https://doi.org/10.1039/C9SE00024K>.
- (19) Blicher-Mathiesen, G.; McCarty, G. W.; Nielsen, L. P. Denitrification and Degassing in Groundwater Estimated from Dissolved Dinitrogen and Argon. *J. Hydrol.* 1998, 208 (1), 16–24. [https://doi.org/10.1016/S0022-1694\(98\)00142-5](https://doi.org/10.1016/S0022-1694(98)00142-5).

Appendix 2

SUPPLEMENTARY INFORMATION FOR CHAPTER 2:
BREAKING SCALING RELATIONSHIPS IN CO₂ REDUCTION ON
COPPER ALLOYS WITH ORGANIC ADDITIVES

Adapted from:

Lai, Y.; Watkins, N. B.; Rosas-Hernández, A.; Thevenon, A.; Heim, G. P.;
Zhou, L.; Wu, Y.; Peters, J. C.; Gregoire, J. M.; Agapie, T.

ACS Cent. Sci. **2021**, 7 (10), 1756–1762.

DOI: 10.1021/acscentsci.1c00860

Material Synthesis

Cu thin film electrocatalysts were fabricated using DC magnetron sputtering of a 2” Cu metal target at 50 W in 6 mTorr Ar onto a 100 mm-diameter Si wafer with an approximately 170 nm SiO₂ diffusion barrier and 10 nm Ti adhesion layer, using a previously described sputter system with 10⁻⁵ Pa base pressure.¹ After deposition, the films were stored in a nitrogen purge box until the day of electrochemical testing, although no other catalyst treatment was performed prior to electrocatalyst screening. The Cu-X (X: Co, Zn, Mn, In) thin film electrodes were deposited under similar conditions from elemental metal targets with DC power adjusted to obtain designed composition in the wafer center. All the metal targets were pre-cleaned in the presence of 6 mTorr Ar for 10 min to remove any contaminants from the target surface. The non-confocal sputtering geometry provided a continuous composition gradient across the Si wafer with the composition variation within each 5 mm diameter electrode being less than 1% for the most Cu-rich catalysts and about 2% for the most Cu-poor catalysts.

Electrochemistry

ANEC Analytical and Electro-chemistry (ANEC) is an analytical electrochemistry system previously published by our group that can efficiently detects a wide range of CO₂R product.² This system is applied in this study to further explore those Cu-X catalysts that are representative of the primary conclusions. Prior to the electrolysis, the electrolyte 0.1 or 0.25 M Potassium bicarbonate (>= 99.95% trace metals basis) with or without 0.1 mM **1-Br₂** was purged with CO₂ (99.999%, Airgas) for at least 30 min. A bipolar membrane (Fumasep® FBM single film, Fumatech) was used to separate the working and counter electrodes.

Platinum wire (99.9%, Sigma Aldrich) was used as the counter electrode. The surface area of the counter electrode was about 0.25 cm^2 , while the working electrode surface area was 0.32 cm^2 . The working electrode chamber has headspace volume $\sim 3.3 \text{ ml}$ and electrolyte volume $\sim 1.1 \text{ ml}$ which is the optimized ratio to maximize product concentration for detection.² Electrolysis was carried out with a Gamry Reference 600™ potentiostat. The uncompensated solution resistance was measured by performing electrochemical impedance spectroscopy (EIS) in the frequency range of 100 Hz to 500 kHz with an amplitude of 10 mV at the open circuit potential of a Pt-Pt Working Electrode-Counter Electrode system. The uncompensated resistance, R_u , was measured by using a Nyquist plot of the EIS spectra and was found to be 70 and 32 Ohms for 0.1 and 0.25 M KHCO_3 , respectively. All electrochemical data was collected vs. a Ag/AgCl reference electrode (LF2, Innovative Instruments) and converted to a reversible hydrogen electrode (RHE) scale. Prior to electrolysis, a constant potential at -1 V vs RHE (without IR compensation) was conducted as pretreatment for each composition of the library. Since the co-sputtered plate was used as is (unlike Cu foil which would be polished prior to tests), such pre-electrolysis was performed to 1) reduce any impurity oxide on the surface and 2) to pre-deposit additives on the surface. To be consistent, 15 min CA was applied to all libraries tested. Electrolyses were then performed at constant potentials (chronoamperometry) mostly between -0.9 to -1.3 V vs RHE (without IR compensation). While electrolysis, the electrolyte was recirculated to quickly accumulate reaction product for detection at a flow rate $\sim 150 \text{ uL/s}$. This high flow rate, compared to other flow cells reported for CO_2R (typically with 1-2 uL/s), creates an environment for less mass transport limitations.³ It is noted that any electrolysis tests associated with additive electrolytes used is in the presence of 0.1 mM **1-Br₂**. The duration

for electrolysis typically ranging from 5 to 15 mins depends on the total current of each test to maximize the concentration of reaction product while maintaining high throughput experimentation and avoiding pH hikes in the case >5% of CO₂ in the headspace is consumed.² To assure this varying reaction durations will not change the product ratios, we do multiple tests on one Cu sample with different CA durations and range it from 3 to 15min. The results show CO₂R products grow linearly with time, for example, Figure S2.11 shows [CH₄]/[C₂₊] remains constant at this time range. At the end of each electrolysis, gaseous and liquid products were sampled by the robotic sample handling system (RSHS) and analyzed by GC (Thermo Scientific™ TRACE™ 1300) and HPLC (Thermo Scientific UltiMate 3000). Detailed product detection (method) can be found at the previous publication.² The cell and all solution handling lines are purged with fresh electrolyte and CO₂ between electrolysis to avoid cross-contamination. The actual (compensated) potential shown in this manuscript was corrected with the uncompensated resistance R_u measured above prior to further data analysis.

Experimental Uncertainty

Variation in the current during an electrolysis experiment leads to a variation in the compensated resistance, and the standard deviation thereof is illustrated as horizontal error bars in Figure 2.2A. For correlation analysis of partial current densities, since each pair of partial current densities result from the same electrolysis, this variation in potential is negligible under the assumption that it does not span multiple kinetic regimes. The uncertainty in partial current density has one contribution from the aliquot and analytic chemistry processes, which we characterize during chromatography calibration for each

product. The uncertainty is well modelled as a relative error in each measured concentration, which corresponds to the same relative error in partial current densities. For example, the relative error in CH₄ quantification is 2.7%. The relative error in C₂₊ quantification varies depending on the specific combination of products and is between 2% and 7% for all electrolyses reported herein. For every partial current density data point in Figures 2.2a-c, and 2.2f, the corresponding error bars are smaller than the marker size. While this sampling error is negligible, more substantial sources of variability in measured partial current densities may result from the impacts of turbulent flow, bubble occlusion of part of the working electrode, etc., which are unquantified in the present work. Rather than perform many repetitions of a single experiment to quantify this variability, we perform a breadth of experiments to better characterize the universality of the relationships, where a large unquantified uncertainty would obscure the observation of correlations or other relationships; fortunately, this is not the case.

Influence of Local pH

Local pH is important for CO₂R product distribution, however, our current cell is not capable of measuring the pH at the electrode surface. It is particularly difficult to accurately measure the pH of the microenvironment at the catalyst surface and would be a significant challenge to take these measurements. However, given the rapid flow condition, a substantial pH change will be limited to the diffusion layer and will be driven by the total current density. Therefore, an indirect study of any influence of pH shift can be made by evaluating whether the current density is related to the observed product ratio. The Figure S2.18 shows that the current density is not a primary determinant of the product ratio.

Impact of [CO] on CH₄ and C₂₊ formation

Since *CO is understood to be the precursor for both CH₄ and C₂₊ products, as opposed to formic acid per various mechanisms reported in the literature, we specifically investigate whether there is evidence of molecular CO being a reactant for CH₄ and C₂₊ formation.^{4,5} Figure S2.19 shows the corresponding partial current densities as a function of the [CO], showing no systematic relationship and especially not a strong positive correlation that would result from CO reduction being a significant source of these products. In the presence of the additive, the negative correlation between CO and both CH₄ and C₂₊ shows that the competition for the common *CO intermediate is more prominent than CO reduction. In the time-dependent measurements (Figure S2.11), the proportionality of both CH₄ and C₂₊ with electrolysis time for Cu further corroborates that CO reduction is insignificant. This finding is also intuitive in the context of the concentration data shown in Figure S2.19, where a ~2% maximum CO concentration corresponds to a partial pressure of 0.02 atm of CO that equilibrates to $0.02 \text{ atm} * 9.5\text{E-}4 \text{ mol/L/atm} = 19 \text{ }\mu\text{M}$, more than 1000× less than the concentration of dissolved CO₂ (~32 mM).

With a given population of *CO that may or may not be equilibrated with a local aqueous [CO], Figure 2.3A illustrates that the reactions pathways fall into 3 important categories labelled by the resulting (measured) products: CO, CH₄ and C₂₊. For a given catalyst and potential there is some branching ratio for each of these paths. Prior literature does not address whether the relative free energy barriers for these products could be changed independently. Since CO production can vary drastically without a systematic change in the other 2 types of products, this indicates that no free energy scaling relationship exists between CO and either CH₄ or C₂₊ products. Those null results are equally important observations as

the scaling relationship that we did identify, although each null result demonstrates that we don't need a mechanism to break that (nonexistent) scaling relationships. Hence the focus on the CH₄-C₂₊ relationship and its disruption via addition of 1-Br₂. Although we find no evidence of a CO-CH₄ or CO-C₂₊ power law relationship, these products are linked through their common intermediates, which is most evident in the presence of the additive where a negative correlation coefficient indicates the kinetic competition for the intermediate.

Material Characterization

The bulk compositions of the Cu-X alloys were characterized via x-ray fluorescence (XRF, EDAX Orbis MicroXRF). The composition of all the alloys screened is shown in table S1. Additional XRD characterization shown in Figures S2.12-16.

Table S2.1: Alloy compositions tested in ANEC cell for performance in CO₂ reduction.

Cu	CuMn	CuIn	CuZn	CuCo
–	26.5 : 73.5	–	29.5 : 70.5	–
–	48.5 : 51.5	–	48.7 : 51.3	–
–	–	–	79 : 21	–
–	84 : 16	83.5 : 16.5	87 : 13	83.5 : 16.5
–	97 : 3	–	95.8 : 4.2	96.7 : 3.3
–	–	–	97.0 : 3.0	–
100: 0	98 : 2	97.8 : 2.2	97.4 : 2.6	97.8 : 2.2

Synthetic Procedures

Synthesis of N,N'-ethylene-phenanthroline dibromide (**1-Br₂**) In a round bottom flask charged with a magnetic stir bar, phenanthroline (500 mg, 2.8 mmol, 1 equiv.) was dissolved in dibromoethane (5 mL, 67.4 mmol, > 24 equiv.) and the final mixture was heated to 110 °C for 18 h. The precipitate formed was collected by filtration and washed with hexane (3 x 10 mL) and acetone (3 x 10 mL) to afford the final product. Yield: 970 mg (94 %, 2.6 mmol). ¹H and ¹³C NMR spectra were in accordance with reported values.⁶

Raw Data

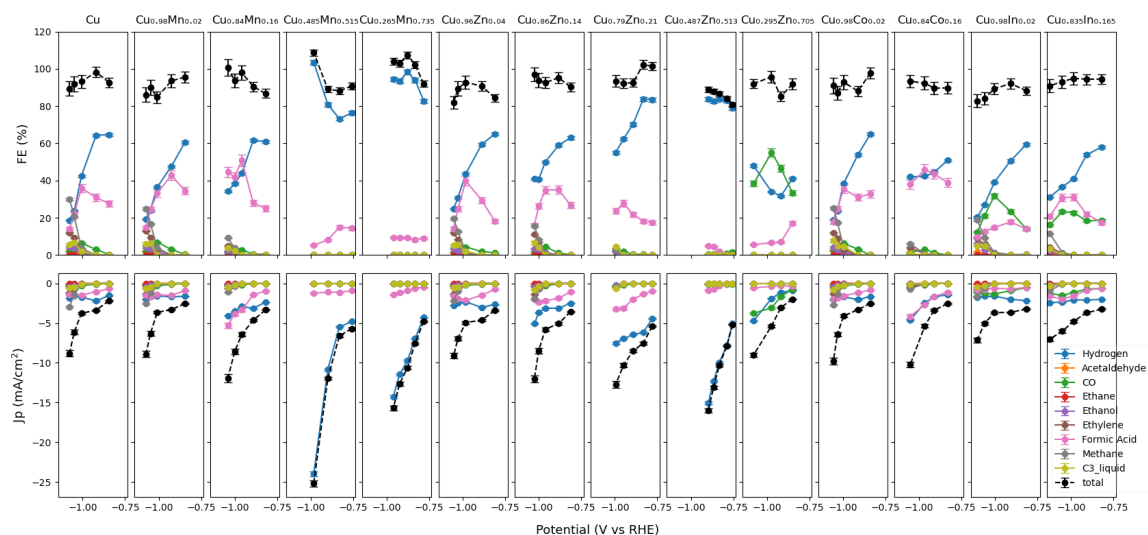


Figure S2.1: Cu alloy product distribution in the absence of additives in 0.1M KHCO₃. The error bars shown in the figure include sampling/leak as well as the analytical instrument calibration errors.

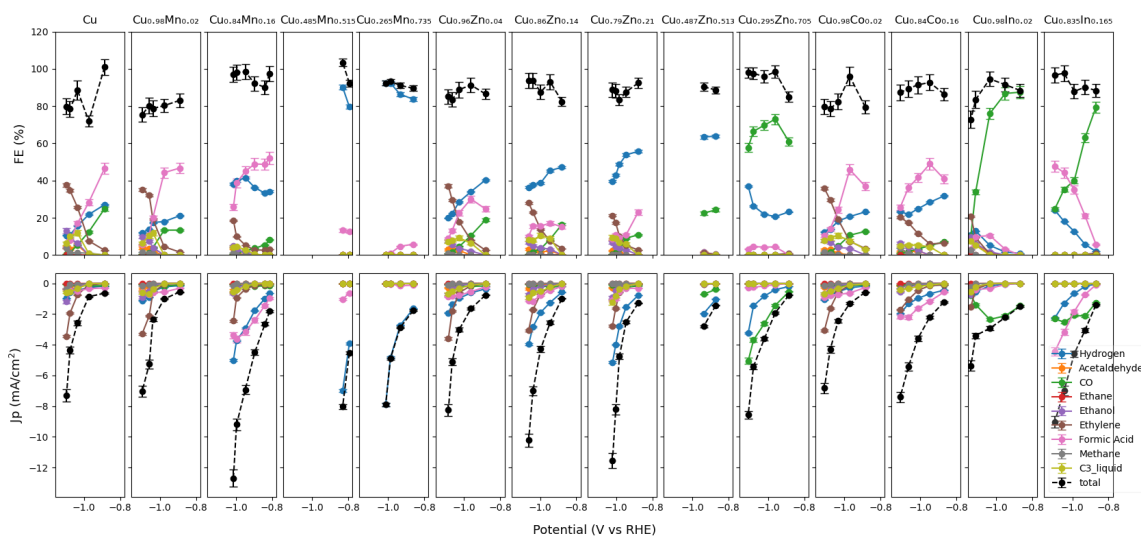


Figure S2.2: Cu alloy product distribution with 0.1 mM 1-Br₂ in 0.1 M KHCO₃. The error bars shown in the figure include sampling/leak as well as the analytical instrument calibration errors.

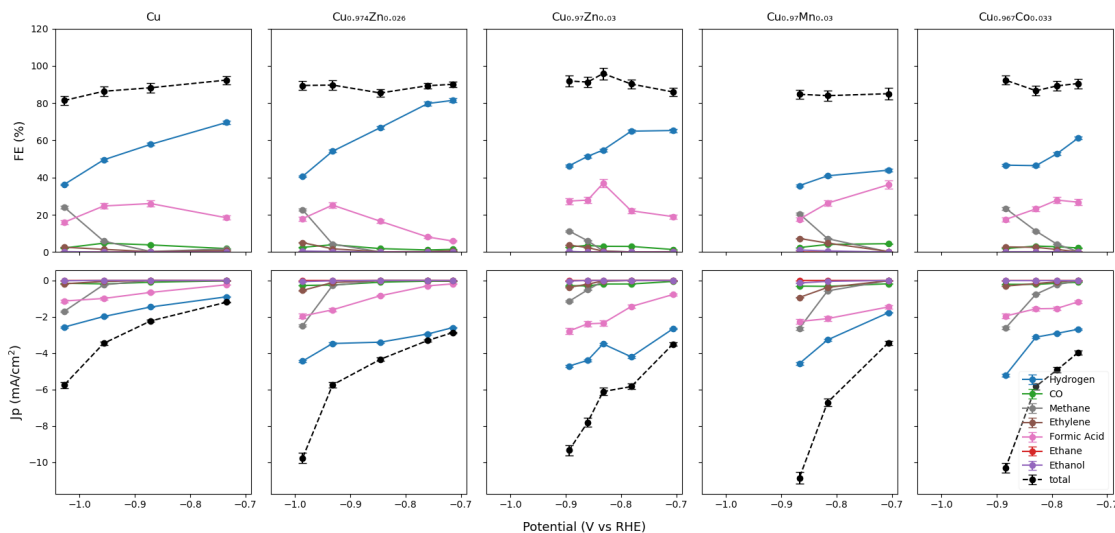


Figure S2.3: Cu alloy product distribution in the absence of additives in 0.25 M KHCO₃ (pH=7.15). The error bars shown in the figure include sampling/leak as well as the analytical instrument calibration errors.

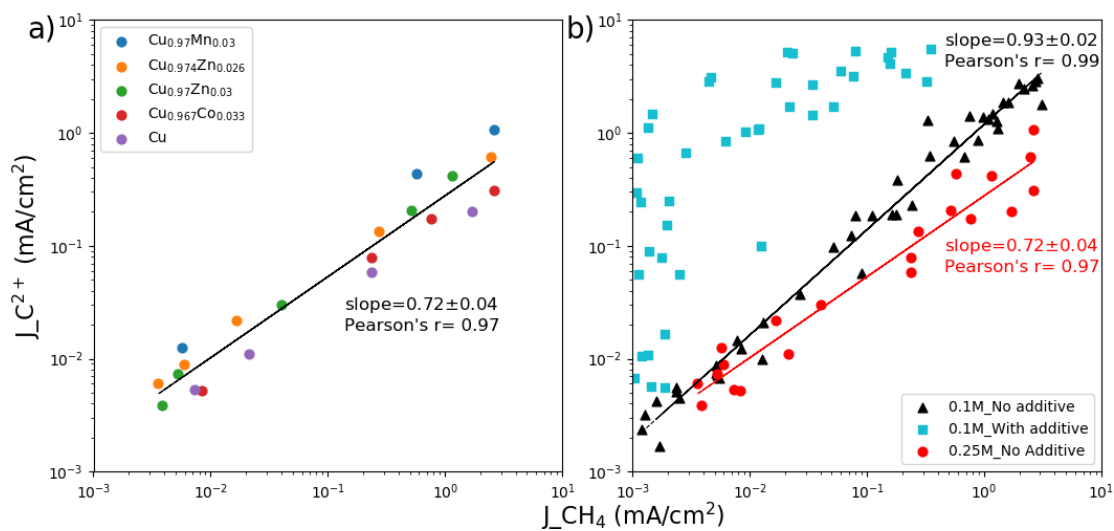


Figure S2.4: a) The data underlying the correlation analysis from 0.25 M KHCO₃. b) Comparison for the trends between 0.1 and 0.25 M KHCO₃. The latter shows a relatively gradual slope suggests an increased selectivity toward methane at higher bicarbonate concentrations.

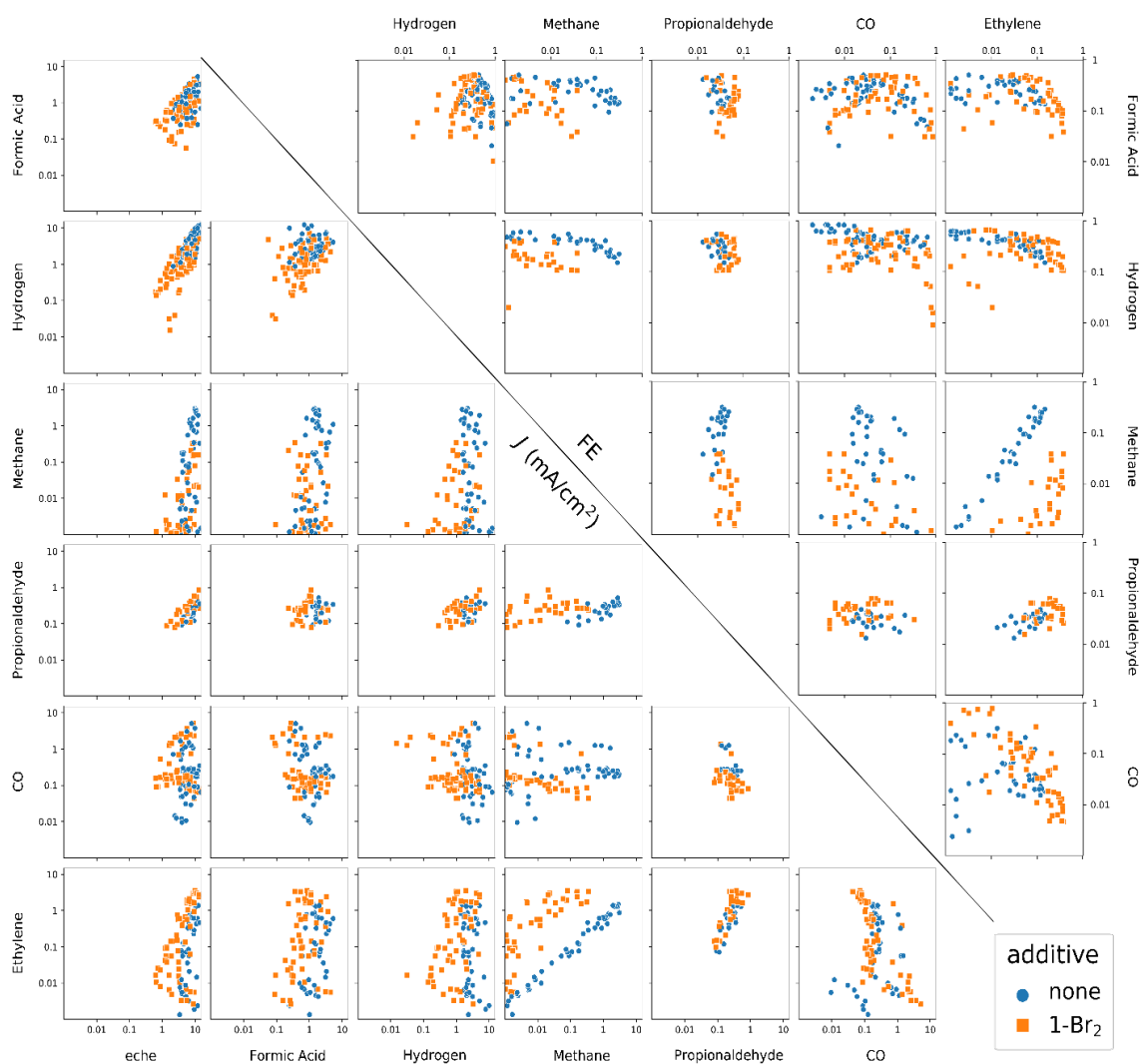


Figure S2.5: Visualization of the pairwise relationships in the current density (bottom-left) and FE (upper-right). Each data point corresponds to a single catalyst composition and potential. The pairwise relationships are shown for representative reaction products, and in the current density plots the total cathodic current density is also shown.

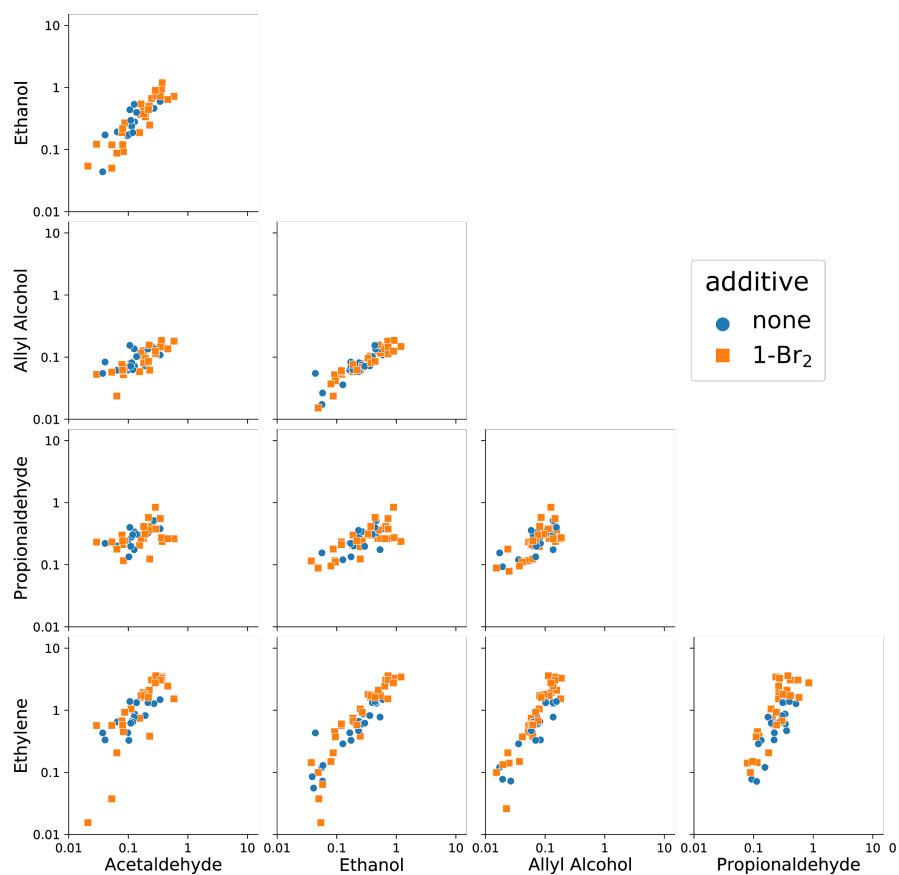


Figure S2.6: For the 5 prominent C₂ and C₃ products, the 10 pairwise relationships of the partial current densities (mA cm⁻²) are shown, illustrating a high degree of correlation among these products, both in the presence and absence of the additive, which is expected given common initial pathways for formation of each product.

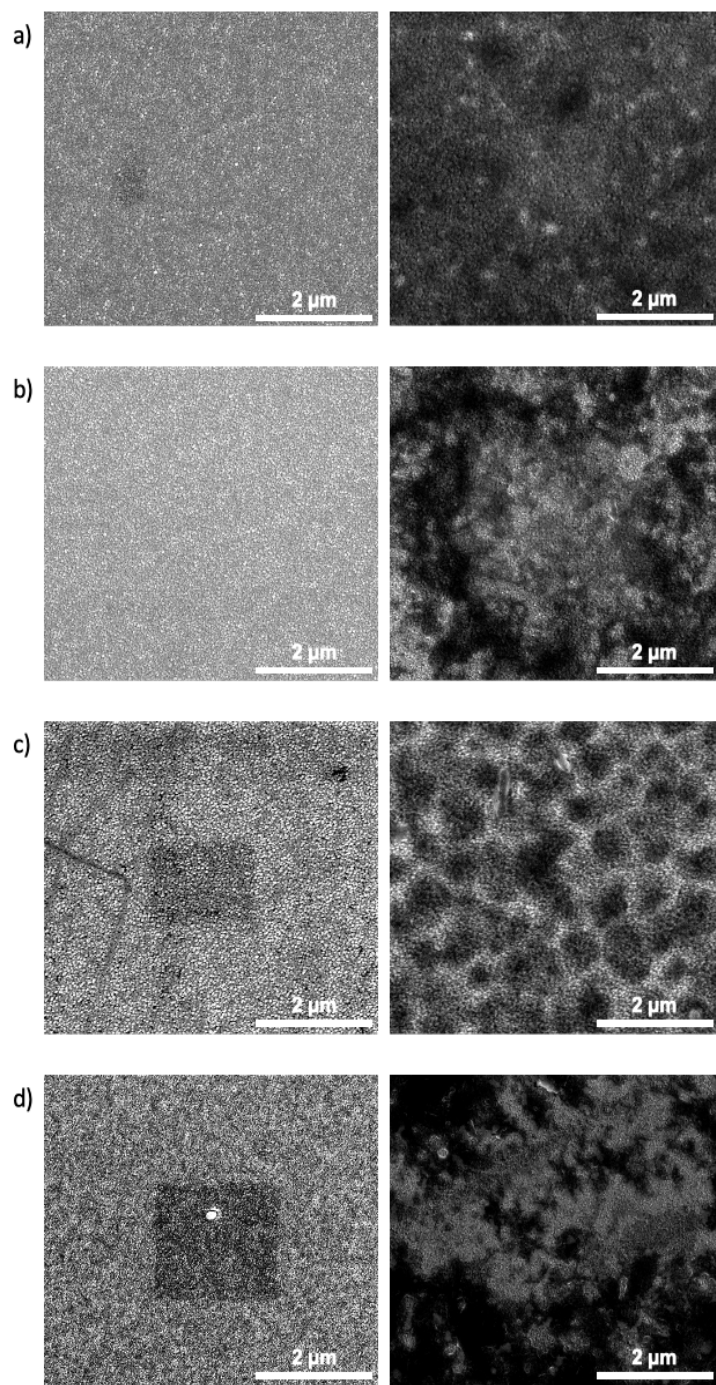


Figure S2.7: SEM of catalysts before (left column) and after (right column) catalysis with molecular additives. a) CuZn samples b) CuMn samples c) CuIn samples d) CuCo samples. Due to being deposited on SiO₂ disks, charging of the surface with SEM was notable. In the second column with molecular additives, the dark charging regions correspond to additive on the surface. No significant surface restructuring was observed for any catalyst tested. Any texture observed in the right column corresponds to thicker regions of the film on the surface of the catalyst.

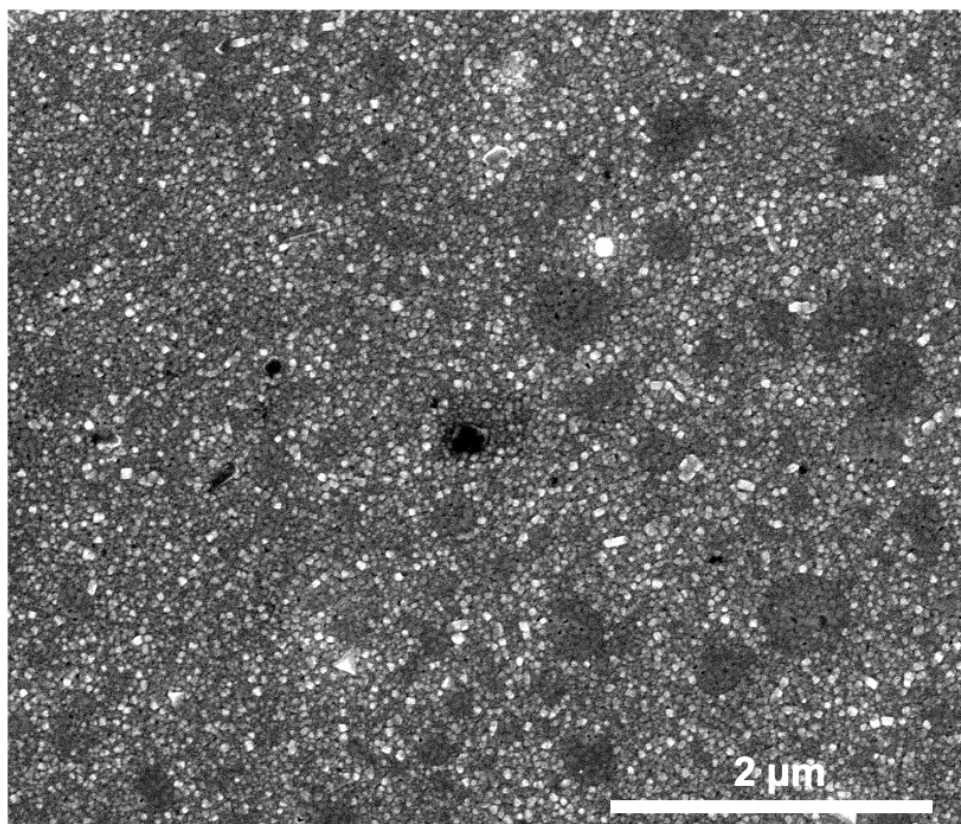


Figure S2.8: SEM of Cu catalyst after catalysis without molecular additives —no notable nanostructuring is observed.

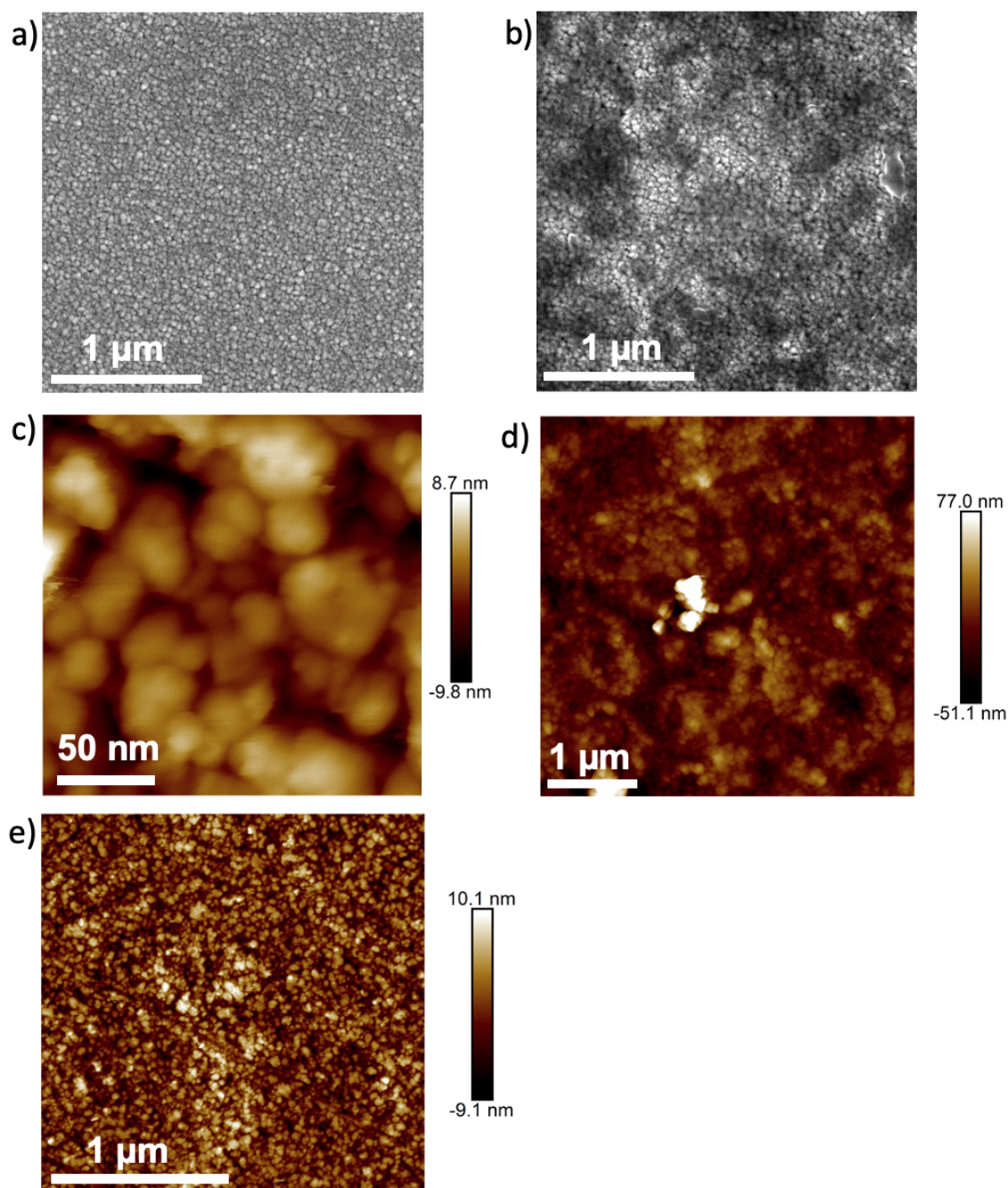


Figure S2.9: a) Precatalysis SEM of CuMn shows a grain size of 34.2 ± 18.5 nm. b) Zoomed in postcatalysis SEM of CuMn with additive shows there is a film on the surface and the surface structure underneath remains unchanged. c) AFM of precatalysis CuMn with grain size of approximately 40.5 nm. d) Postcatalysis AFM of CuMn with additive shows agglomerated film on surface, as shown by the increase in magnitude of the scale bar. e) AFM of CuMn postcatalysis surface with additive after washing off film shows consistent grain size with the precatalysis surface of approximately 38.7 ± 14.1 nm.

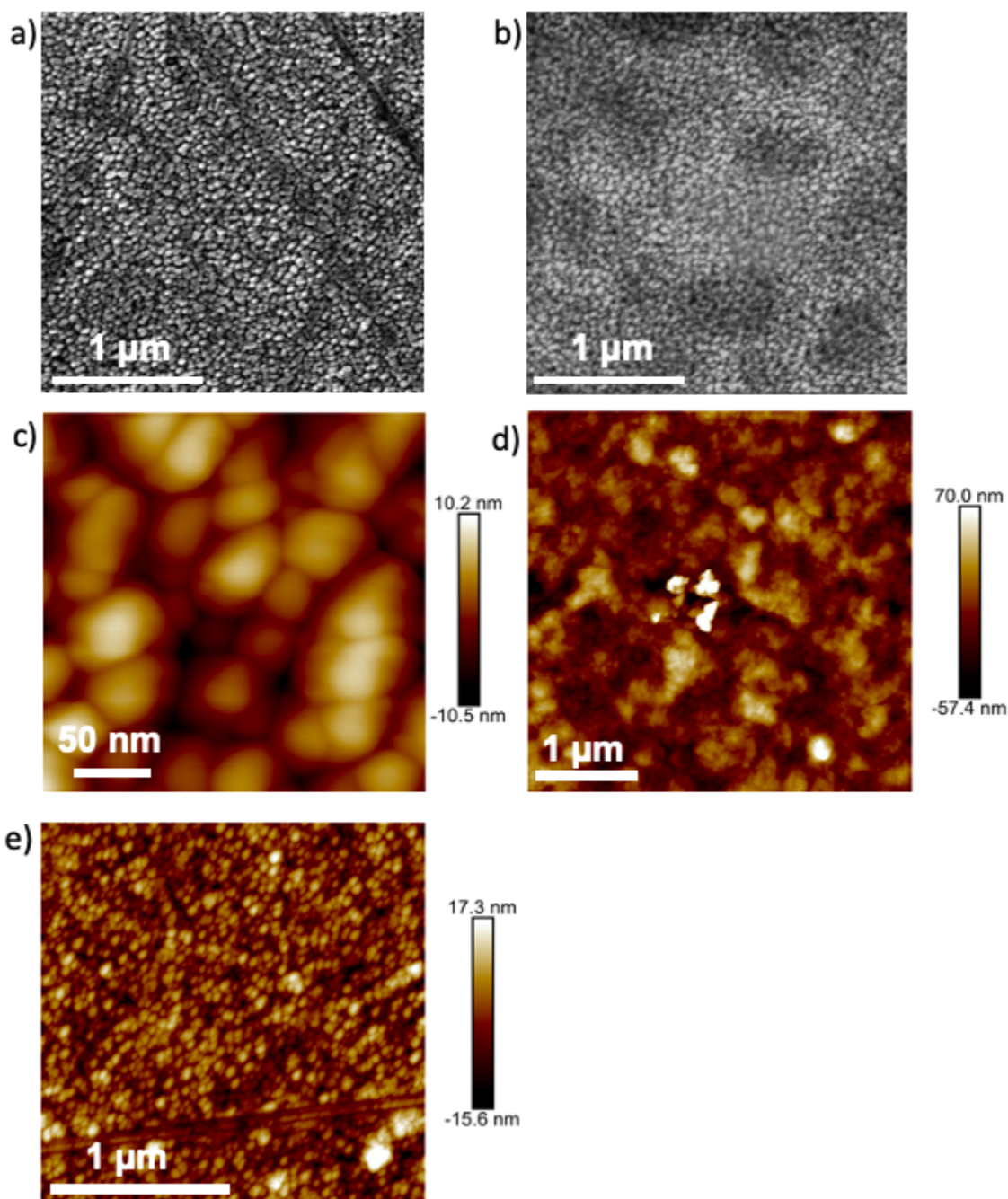


Figure S2.10: a) Precatalysis SEM of CuIn shows a grain size of 50.2 ± 17.3 nm. b) Zoomed in postcatalysis SEM of CuIn with additive shows there is a film on the surface and the surface structure underneath remains unchanged. c) AFM of precatalysis CuIn has a grain size of approximately 35 nm. d) Postcatalysis AFM of CuIn with additive shows agglomerated film on surface, as shown by the increase in magnitude of the scale bar. e) AFM of CuIn postcatalysis surface with additive after washing off film shows consistent grain size with the precatalysis surface of approximately 37.7 ± 16.0 nm.

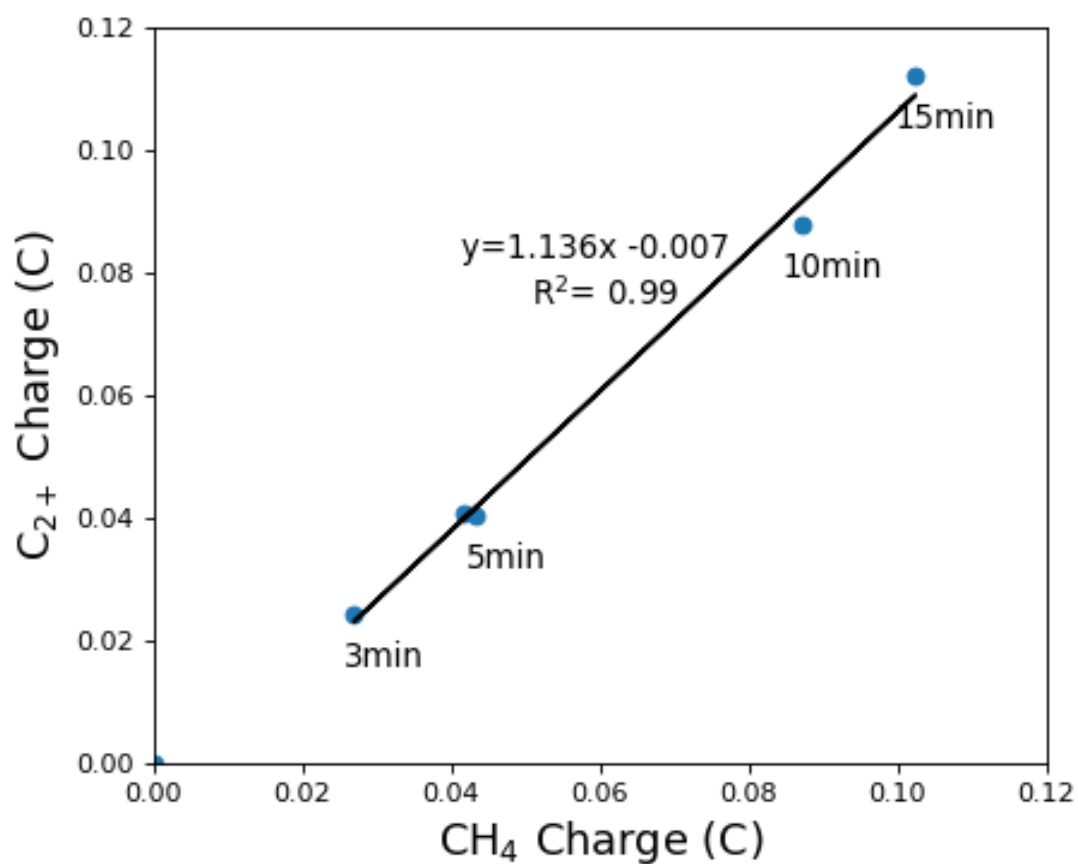


Figure S2.11: Resulting CH₄ vs C₂₊ from CA at -1.04 V vs RHE with different durations on Cu in 0.1 M KHCO₃. The testing sequence was 5, 3, 10, 15, and then 5 mins. The repeated 5 min CA experiment was conducted to check for variation after multiple experimental runs at different duration. The lack of variation at 5 min suggests that the electrode performs consistently and reproducibly over time

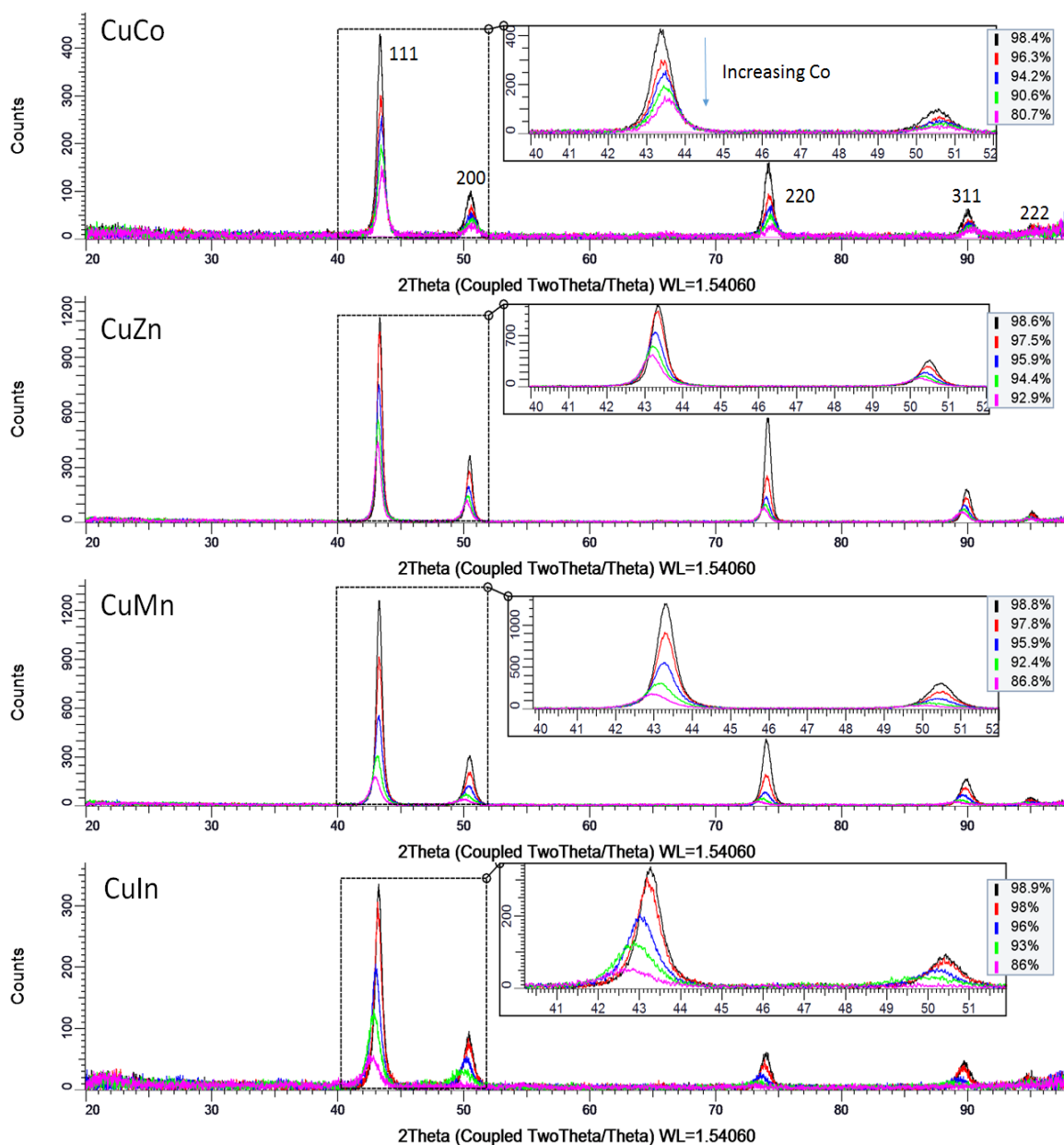


Figure S2.12: XRD for the as-synthesized alloys investigated. All compositions shown are alloyed cubic Cu structure and are with space group of Fm-3m. For In, Mn, Zn alloys, peaks shift to smaller 2-theta (larger d-spacing) with increasing alloy content. For Co, peaks shift to larger 2-theta (smaller d-spacing) with increasing Co.

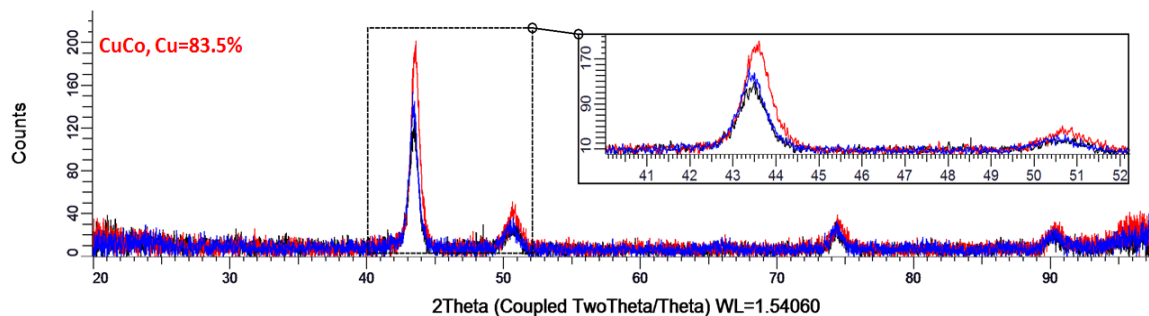
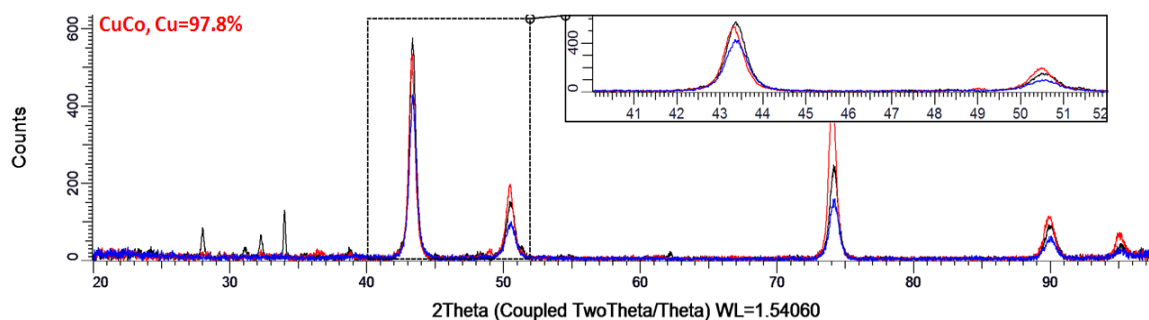


Figure S2.13: XRD for alloy CuCo before and after electrolysis. Blue: pristine, red: absence of additive, and black: presence of additive. The slight shift of peak position is due to slight sample composition variation from sample to sample and is estimated to be < 1% for the Cu-rich catalysts and < 2% for the Cu-poor catalysts.

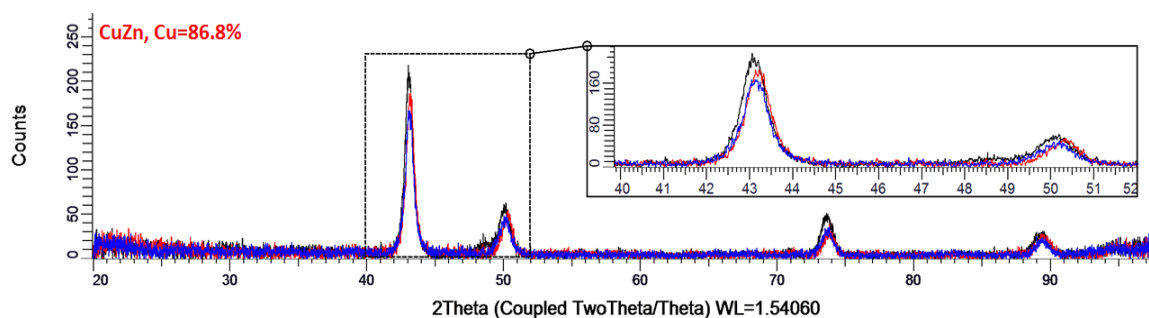
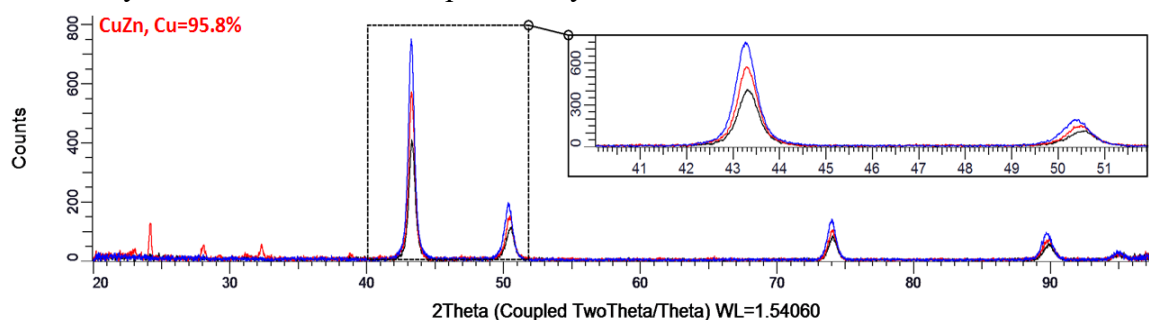


Figure S2.14: XRD for alloy CuZn before and after electrolysis. Blue: pristine, red: absence of additive, and black: presence of additive. The slight shift of peak position is due to slight sample composition variation from sample to sample and is estimated to be < 1% for the Cu-rich catalysts and < 2% for the Cu-poor catalysts.

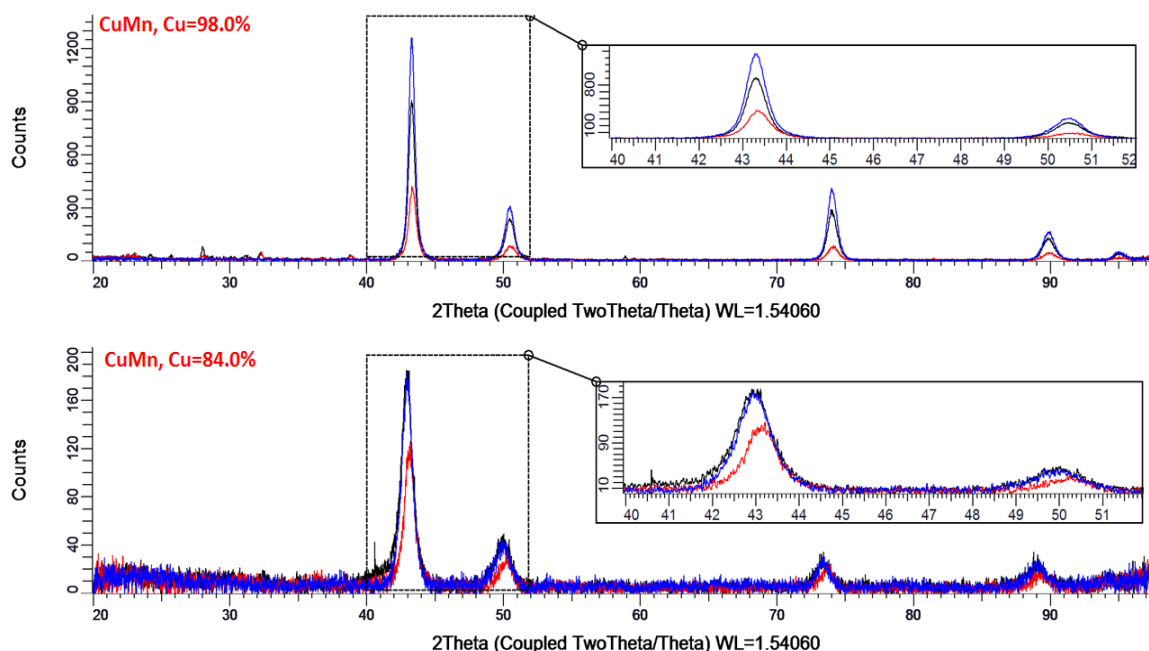


Figure S2.15: XRD for alloy CuMn before and after electrolysis. Blue: pristine, red: absence of additive, and black: presence of additive. The slight shift of peak position is due to slight sample composition variation from sample to sample and is estimated to be < 1% for the Cu-rich catalysts and < 2% for the Cu-poor catalysts.

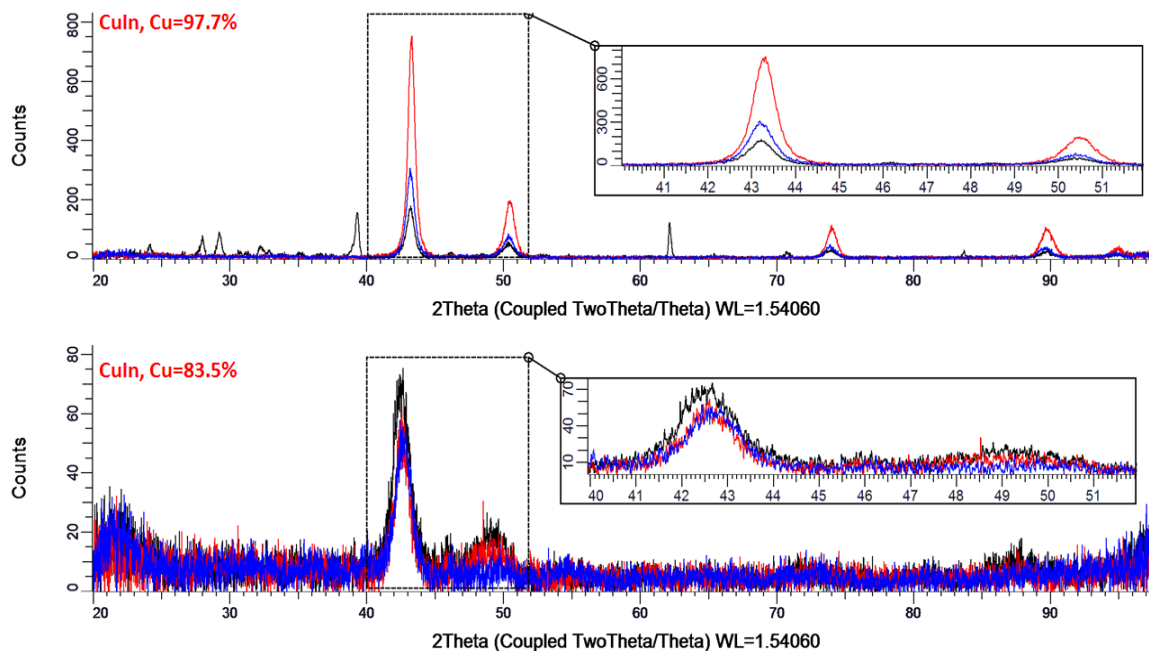


Figure S2.16: XRD for alloy CuIn before and after electrolysis. Blue: pristine, red: absence of additive, and black: presence of additive. The slight shift of peak position is due to slight sample composition variation from sample to sample and is estimated to be < 1% for the Cu-rich catalysts and < 2% for the Cu-poor catalysts.

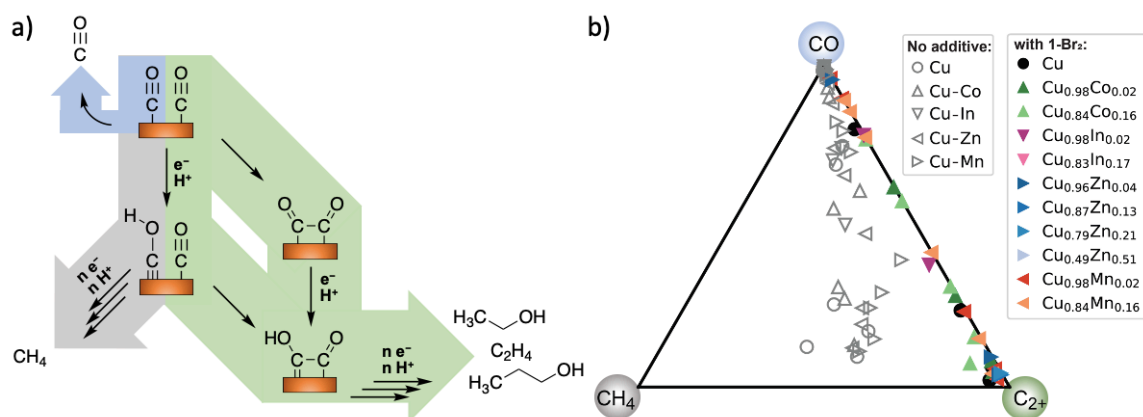


Figure S2.17: A complementary figure for Figure 2.3 in the main text.

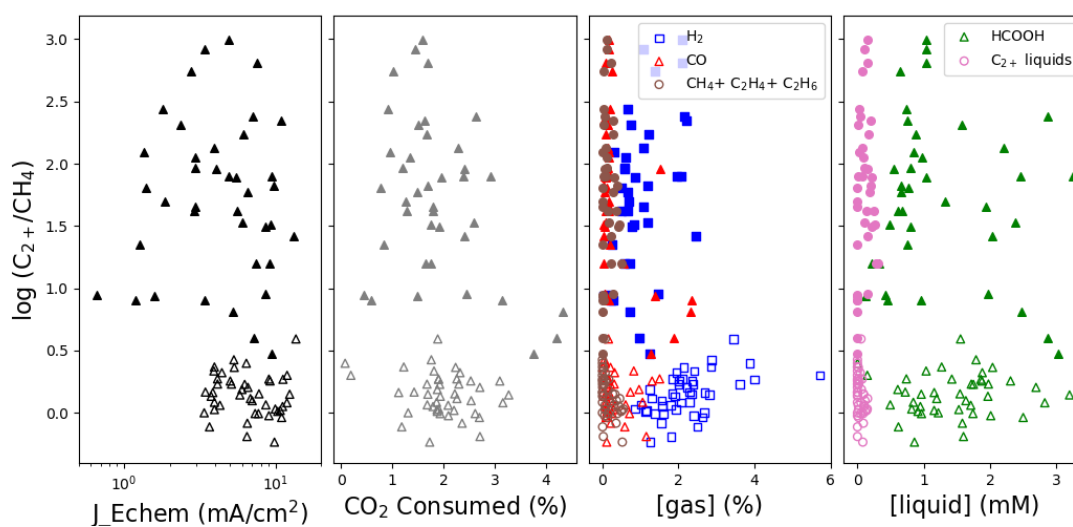


Figure S2.18: Electrochemical current density, CO₂ consumption (in the headspace) at the end of electrolysis, gas product concentration, and liquid product concentration vs log (C₂₊/CH₄). Solid symbol: electrolyses with additive; hollow symbol: electrolyses without additive in 0.1 M KHCO₃.

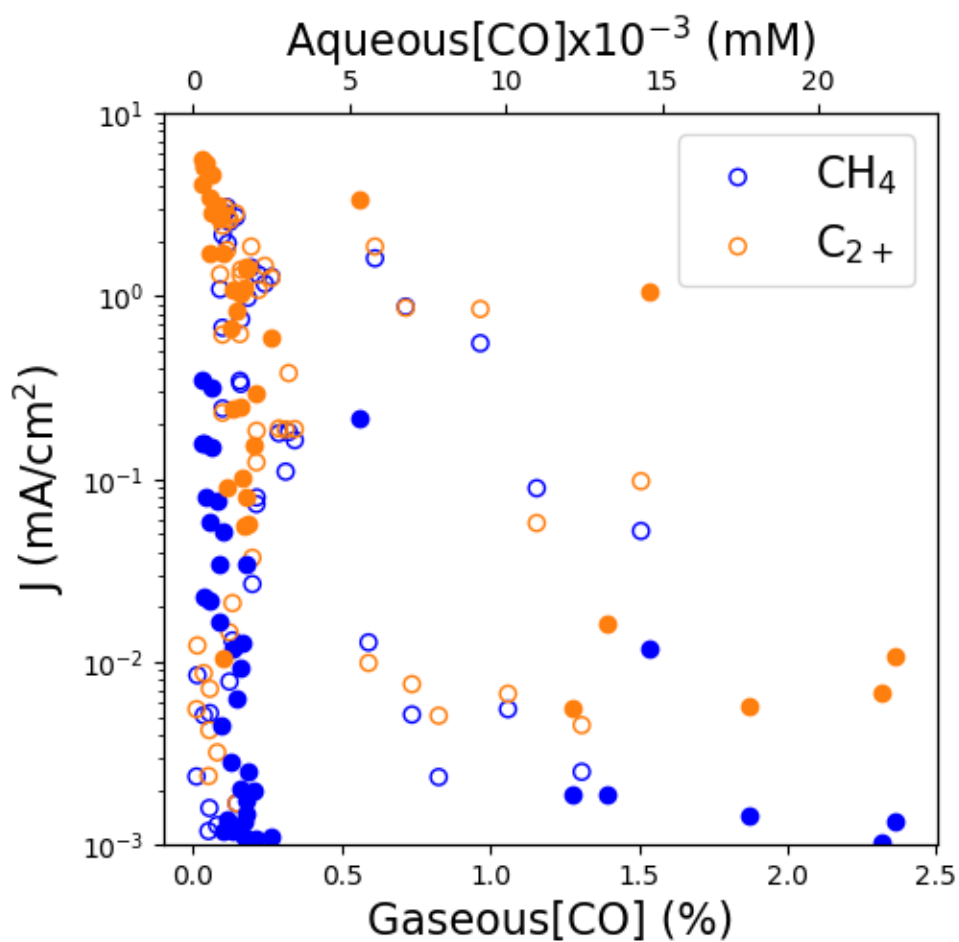


Figure S2.19: Product CO concentration vs partial current density of CH₄ and C₂H₄. The gaseous (headspace) CO concentration was measured by GC at the end of each electrolysis, while aqueous CO was estimated from the measured CO by Henry's law. Solid symbol: electrolyses with additive; hollow symbol: electrolyses without additive in 0.1M KHCO₃.

References

- (1) Lai, Y.; Jones, R. J. R.; Wang, Y.; Zhou, L.; Gregoire, J. M. Scanning Electrochemical Flow Cell with Online Mass Spectroscopy for Accelerated Screening of Carbon Dioxide Reduction Electrocatalysts. *ACS Comb. Sci.* **2019**, *21* (10), 692–704. <https://doi.org/10.1021/acscombsci.9b00130>.
- (2) Jones, R. J. R.; Wang, Y.; Lai, Y.; Shinde, A.; Gregoire, J. M. Reactor Design and Integration with Product Detection to Accelerate Screening of Electrocatalysts for Carbon Dioxide Reduction. *Rev. Sci. Instrum.* **2018**, *89* (12), 124102. <https://doi.org/10.1063/1.5049704>.
- (3) Clark, E. L.; Singh, M. R.; Kwon, Y.; Bell, A. T. Differential Electrochemical Mass Spectrometer Cell Design for Online Quantification of Products Produced during Electrochemical Reduction of CO₂. *Anal. Chem.* **2015**, *87* (15), 8013–8020. <https://doi.org/10.1021/acs.analchem.5b02080>.
- (4) Garza, A. J.; Bell, A. T.; Head-Gordon, M. Mechanism of CO₂ Reduction at Copper Surfaces: Pathways to C₂ Products. *ACS Catal.* **2018**, *8* (2), 1490–1499. <https://doi.org/10.1021/acscatal.7b03477>.
- (5) Nitopi, S.; Bertheussen, E.; Scott, S. B.; Liu, X.; Engstfeld, A. K.; Horch, S.; Seger, B.; Stephens, I. E. L.; Chan, K.; Hahn, C.; Nørskov, J. K.; Jaramillo, T. F.; Chorkendorff, I. Progress and Perspectives of Electrochemical CO₂ Reduction on Copper in Aqueous Electrolyte. *Chem. Rev.* **2019**, *119* (12), 7610–7672. <https://doi.org/10.1021/acs.chemrev.8b00705>.
- (6) Thevenon, A.; Rosas-Hernández, A.; Peters, J. C.; Agapie, T. In-Situ Nanostructuring and Stabilization of Polycrystalline Copper by an Organic Salt

Additive Promotes Electrocatalytic CO₂ Reduction to Ethylene. *Angew. Chem.*

Int. Ed. **2019**, 58 (47), 16952–16958. <https://doi.org/10.1002/anie.201907935>.

Appendix 3

SUPPLEMENTARY INFORMATION FOR CHAPTER 3:
MOLECULAR COATINGS IMPROVE THE SELECTIVITY AND
DURABILITY OF CO₂ REDUCTION CHALCOGENIDE
PHOTOCATHODES

Adapted from:

Lai, Y.; Watkins, N. B.; Muzzillo, C.; Richter, M.; Kan, K.; Zhou, L.;
Haber, J. A.; Zakutayev, A.; Peters, J. C.; Agapie, T.; Gregoire, J. M.
ACS Energy Lett. 2022, 7 (3), 1195–1201.
10.1021/acseenergylett.1c02762.

Experimental Methods

Photocathode synthesis

CuGa₃Se₅ absorbers were deposited on soda-lime glass substrates with Mo back contact deposited by sputtering. The deposition was performed at 600 °C using a three-stage co-evaporation process, with Ga-Se sourced in the 1st stage, Cu-Se sourced in the 2nd stage, and Ga-Se sourced in the 3rd stage. The solution for CdS deposition contained 1.2 mM of cadmium sulfate (CdSO₄) and 59 mM of thiourea (CH₄N₂S) in NH₄OH and DI water, and was heated to 65°C during the coating process. More details about these experiments can be found in prior publications.^{22,23}

Additive synthesis and characterization

Additives were synthesized according to previously published procedures using chemicals as received from commercial suppliers without further purification.^{30,31}

High throughput electrochemical testing

Prior to the electrolysis, the electrolyte (0.1 M KHCO₃, ≥99.95% trace metals basis, Sigma Aldrich) with or without additives (**add. 1** or **add.2**, also referred to as 1,4PhPy₂) was purged with CO₂ (99.999%, Airgas) for at least 30 min. A bipolar membrane (BPM, Fumasep® FBM single film, Fumatech) was used to separate the working and counter electrodes. Platinum wire (99.9%, Sigma Aldrich) was used as the counter electrode. Electrolysis was carried out with a Gamry Reference 600TM potentiostat. All electrochemical data were collected using an Ag/AgCl reference electrode (LF2, Innovative Instruments) and converted to a reversible hydrogen electrode (RHE) scale using the measured solution pH of 6.8. All

cells and all solution handling lines were purged with fresh electrolyte and CO₂ between electrolysis to avoid cross-contamination. These systems were coupled with front-side electrode illumination using fiber-coupled LEDs. The surface area of the counter electrodes were about 0.25 cm², while the working electrode surface areas were 0.32 cm². The flow rate of electrolyte was 160 μL/s throughout the tests.

Two cell designs were used for the bulk testing of photocathodes.

(1) An electrochemical mass spectrometry (ECMS) system was previously published for rapid CO₂R electrocatalyst screening.⁴⁰ Mass spectra were acquired on a Hiden HPR20 mass spectrometer connected to the outlet of the desiccant chamber. An electron energy of 70 eV was used for ionization of all species, with an emission current of 500 μA to maximize detection sensitivity. Hydrogen ($m/z = 2$), methane ($m/z = 15$), and ethylene ($m/z = 26$) ions were accelerated with a voltage of 3 V. All mass-selected product cations were detected by a secondary electron multiplier with a detector voltage of 1050 V.

(2) Analytical and Electro-chemistry (HT-ANEC) is an analytical electrochemistry system previously published by our group to efficiently detect a wide range of CO₂R products.³⁵ At the end of each (photo)electrolysis, gaseous and liquid products were sampled by the robotic sample handling system (RSHS) and analyzed by GC (Thermo Scientific™ TRACE™ 1300) and HPLC (Thermo Scientific UltiMate 3000). Detailed product detection (method) can be found at the previous publication.³⁵

Durability test by H-cell

For photoelectrochemical CO₂ reduction durability experiments in an H-Cell a custom peek cell was utilized.⁴¹ The anode and membrane had an area of 1 cm² whereas the area of the cathode was further reduced by a Viton mask to 0.5 cm². CO₂ saturated 0.10 M potassium bicarbonate with and without additive was used as the electrolyte. A Pt foil anode was used behind a bipolar membrane (Fumasep® FBM single film, Fumatech) membrane. A leakless Ag/AgCl electrode was used as a reference electrode. A monochromatic LED illumination with a wavelength of 450 nm and an intensity of 65 mW/cm² was used.

Carbon dioxide was provided to the electrochemical cell at a flow rate of 5 sccm as controlled by an Alicat flow controller. The gas stream was humidified by a gas bubbler connected in series between the electrochemical cell and flow controller. The gas exhaust stream of the electrochemical cell was passed through a liquid trap before flowing through the gas sampling loop of an Agilent 7820a GCMS/TCD with an Alicat flow meter connected to its exhaust. Quantitative analysis of gaseous products was based on calibrations with several gas standards over many orders of magnitude in concentration. With the help of the calibration, the Faradaic efficiency towards CO₂R and hydrogen evolution products could be calculated from the measured current density. For isotope labeling experiments the same experimental configurations as described above were employed except ¹³CO₂ was used as the CO₂ source.

Pre- and post- (photo)electrochemistry sample characterization

TEM/EDS

Cd(S) layer in CdS/CuGa₃Se₅ at different conditions was characterized by cross-sectional Transmission electron microscopy (TEM) and energy-dispersive X-ray spectroscopy (EDS). To prepare a cross-sectional TEM specimen, a FEI DualBeam Focused Ion Beam/scanning electron microscope (FIB/SEM) was used and the sample was capped carbon/I-C prior to milling. TEM experiments were carried out in a FEI Tecnai Osiris FEG/TEM operated at 200 kV in bright-field (BF) and high-resolution (HR) TEM mode. The EDX elemental mapping was acquired using Bruker Quantax. This characterization was performed by Eurofins EAG Precision TEM in Santa Clara, California.

XRF and ICP-MS

The Cd in CdS/CuGa₃Se₅ sample was characterized by X-ray fluorescence (XRF) using an EDAX Orbis Micro-XRF system to identify if any was leached out during the photo(electrochemistry) measurements. Inductively coupled plasma mass spectrometry (ICP-MS) by Thermo Fisher Scientific iCAP™ RQ instrument was used to determine the concentration of dissolved metals in electrolytes used for electrochemistry.

SEM

Morphology of the Cd(S) layer and additives were characterized by Cross-sectional and top-down view Scanning-electron microscopy images and were obtained with a FEI Nova NanoSEM 450 microscope.

XPS

X-ray photoelectron spectroscopic (XPS) data were collected using a Kratos Axis Nova system with a base pressure of 1×10^{-9} Torr. The X-ray source was a monochromatic Al K α line at 1486.6 eV. Photoelectrons were collected at 0° from the surface normal with a retarding pass energy of 160 eV for survey XPS scans with a step size of 0.5 eV, and a pass energy of 20 eV for high-resolution core level scans with a step size of 0.05 eV. No charge neutralization was used. The XPS was calibrated using the Au 4f_{7/2} line (84 eV) of a sputtered gold foil. Data was analyzed using CasaXPS. To calculate the composition (atomic ratio) a Shirley background was subtracted. The core level intensities were corrected by the analyzer transmission function and relative sensitivity factors to obtain corrected peak intensities which were used to calculate the atomic ratios.

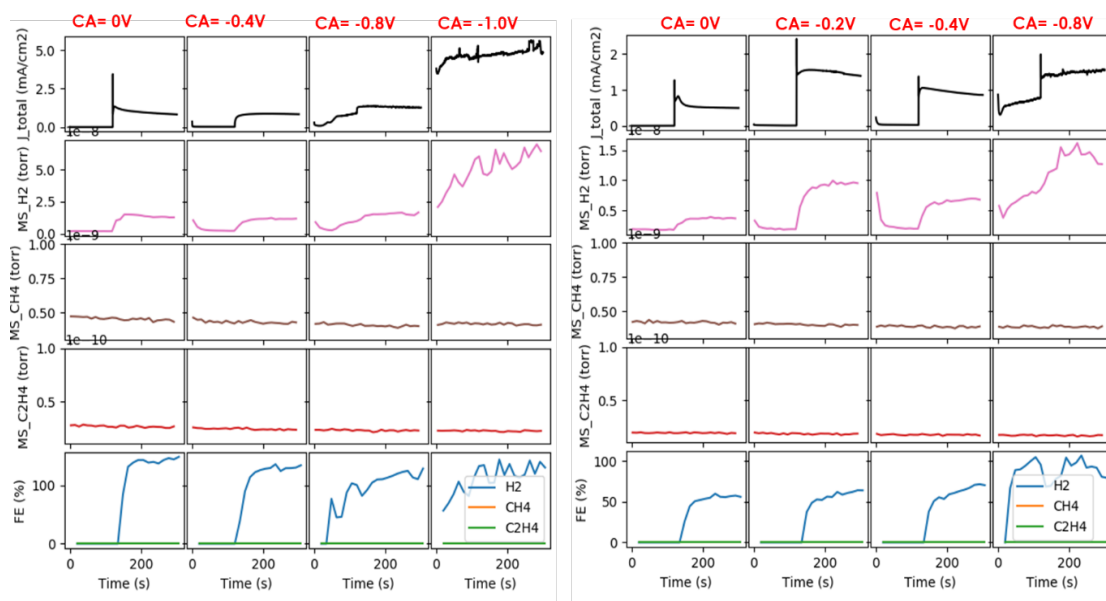


Figure S3.1: Initial experiments in an electrochemical flow cell where for each of 2 electrodes without (left) and with (right) CdS coating were operated as a sequence of applied bias, chronologically from left to right. At each potential, after 120 s operation in the dark illumination from a 455 nm LED was used to observe any photocurrent and change in H₂, CH₄, and C₂H₄ production rate, which were quantified using mass spectrometry via a pervaporation cell in the effluent of the electrolyte from the electrochemical reactor. Both samples show negligible dark current and appreciable photocurrent from 0 to -0.4 V vs RHE with undesirably large dark current at more negative bias. While no hydrocarbons are observed, the observed H₂ signal is used to estimate the Faradaic efficiency, which is near 100% without the CdS coating and is lower with CdS, indicating formation of a non-detected product such as CO or another electrochemical reaction occurring.

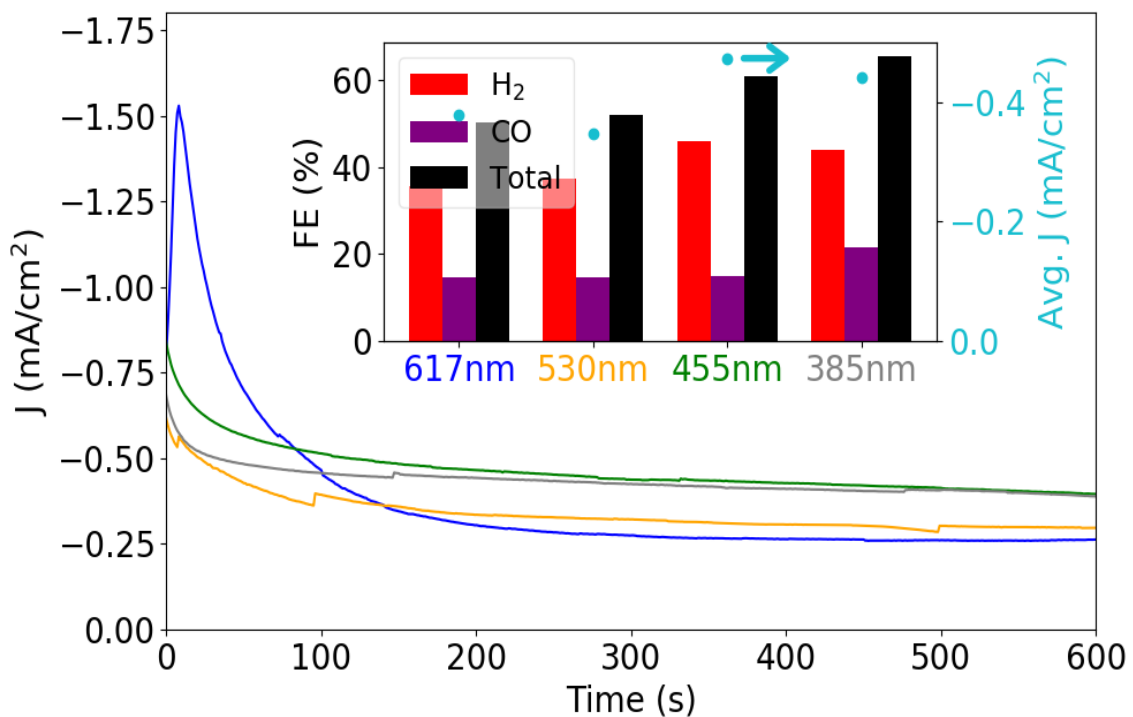


Figure S3.2: Evaluation of the product distribution with illumination ranging from 617 nm to 385 nm at 0V vs RHE. The testing sequence is 617, 530, 455, and then 385nm. The FE, especially for CO, is similar for the first 3 illumination sources and increases at 385 nm illumination. The 455 nm illumination was chosen for further experimentation to represent visible illumination. Note that xrf was used to monitor the Cd corrosion with 81 (counts) prior to test and 14.5 (counts) after photoelectrolysis with the four wavelengths.

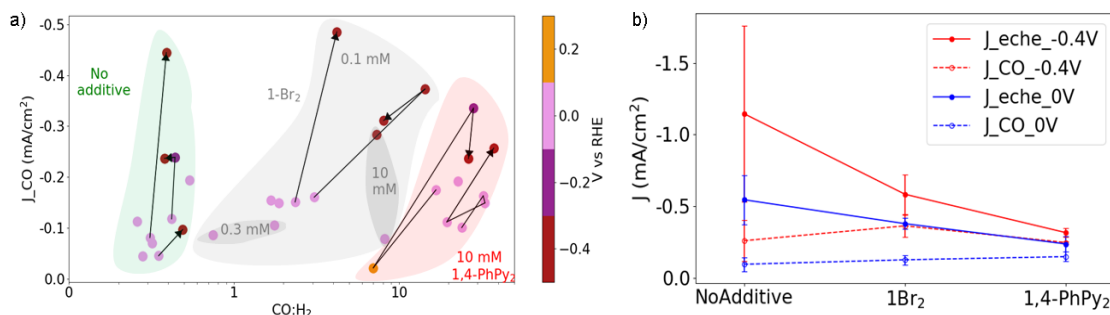


Figure S3.3: a) The data from Figure 3.2 is shown using the partial current density for CO as opposed to the total current density, and multiple experiments on a given electrode are shown with arrows indicating the sequence of measurements. b) Aggregation of the experiments in a) for the -0.4 and 0V, indicating that the primary mechanism of selectivity enhancement with the additives is suppression of HER. The error bars for both J_{eche} and J_{CO} at -0.4 V and 0 V vs RHE represent the standard deviation of the respective measurements over the several photoelectrocatalysis experiments shown in a).

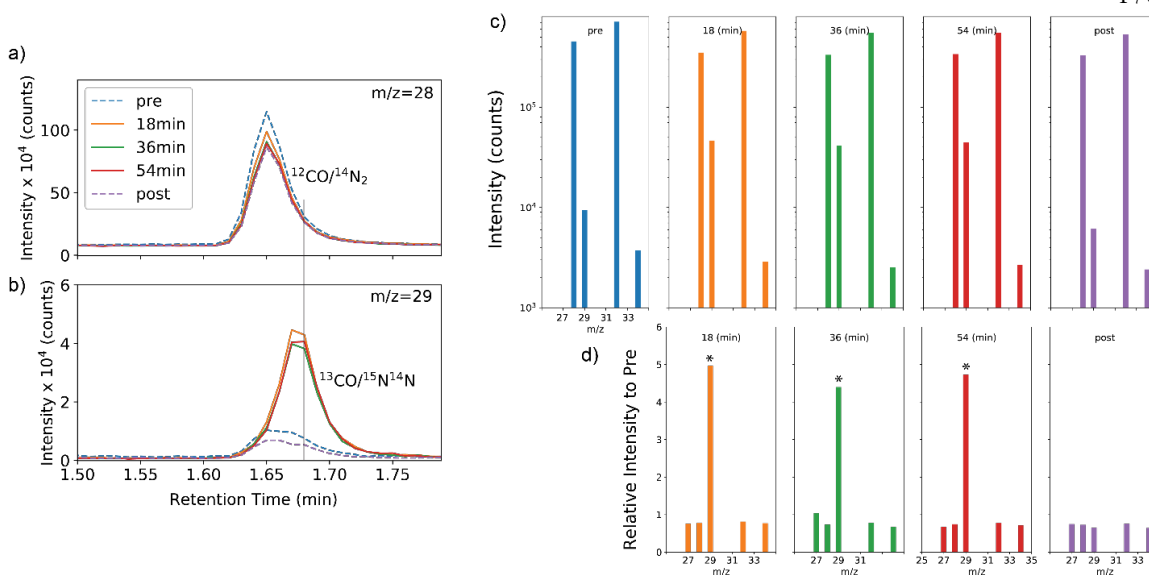


Figure S3.4: GC-MS analyses before (“pre”), at 3 time intervals during photoelectrolysis at 0 V vs RHE with 10 mM Add. 2, and after photoelectrolysis (“post”). For each of these 5 headspace samples, mass spectra were acquired at a series of GC retention times. The 2 m/z values of interest are 28 and 29, which correspond to ^{12}CO and ^{13}CO , respectively. The N_2 from air contamination has similar retention time as that of CO and contributes to both a) $m/z=28$ and b) $m/z=29$ signals as shown in the “pre” and “post” measurements. The mass spectrum acquired at 1.68 min retention time best characterizes CO with some contribution from N_2 . For each of the 5 conditions, the relevant portion of the mass spectrum is shown in c) where the colors match the legend in a). To compare the signals during photoelectrolysis to those of the “pre” baseline, d) contains the relative intensity for each m/z value with detected intensity. The approximately 5-fold enhancement in $m/z=29$ signal in each of the measurements during photoelectrolysis is marked with an asterisk. As shown in a), the $m/z=28$ “pre” signal, which is from $^{14}\text{N}_2$, is similar to the $m/z=28$ signals in subsequent measurements. The concomitant $m/z=29$ signal from $^{15}\text{N}^{14}\text{N}$ is thus also similar in each measurement, demonstrating that the ~5-fold increase in $m/z=29$ signal for the measurements during photoelectrolysis arises from photoelectrochemical generation of ^{13}CO from $^{13}\text{CO}_2$.

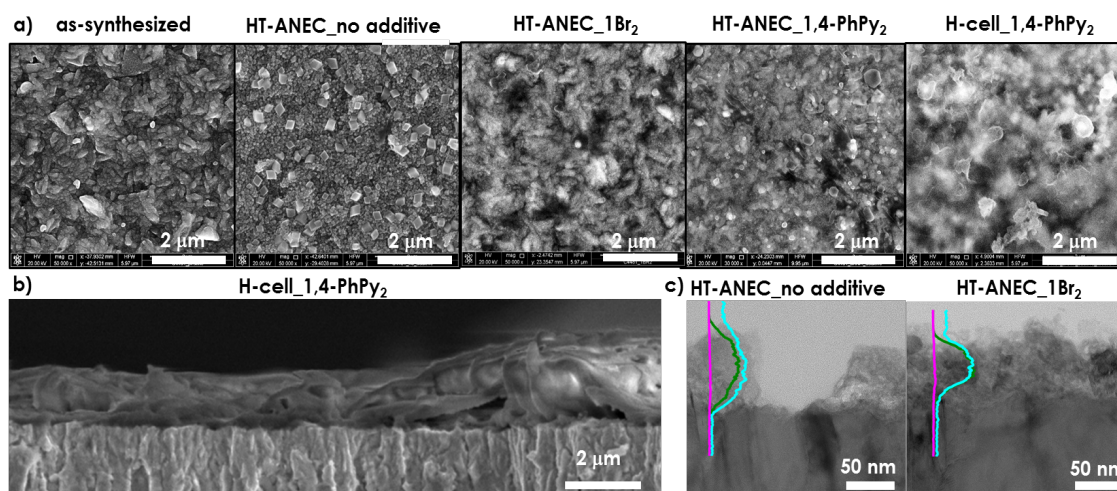


Figure S3.5: a) Plan-view SEM images of electrodes including as-synthesized, each condition from the HT-ANEC measurements of Figure 3.2, and the H-cell measurement of Figures 3.3b-c. Without additives, the surface restructures into nanocubes. The images from experiments with a molecular additive exhibit a morphology that is more similar to the as-synthesized electrode with some apparent restructuring and/or changes in morphology due to heterogeneities in organic coating. b) cross-sectional view for H-cell_1,4-PhPy₂ which shows variations in the film thickness.

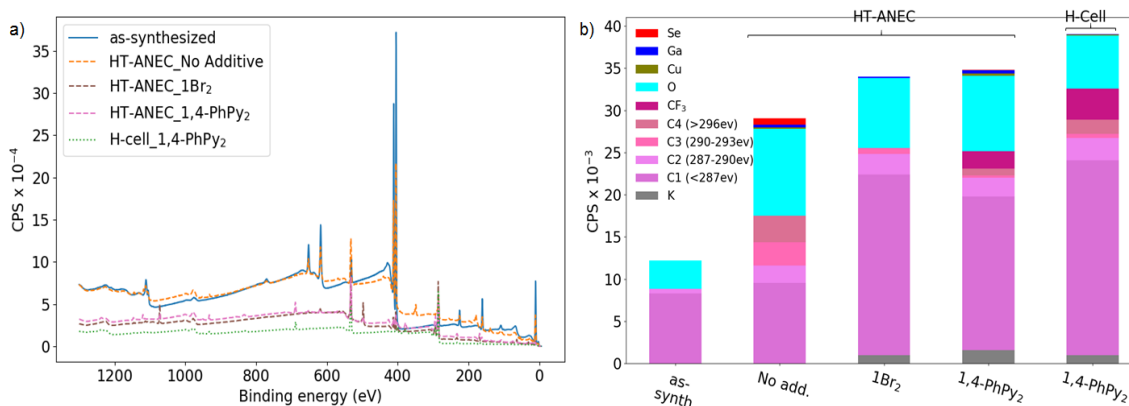


Figure S3.6: a) XPS survey scans for the 5 electrode conditions of Figures 3.4a-b. The analysis of the detected species from each electrode are shown in b) and figure 3.4c. All samples that underwent electrochemistry have a signal near a binding energy of 293 eV that is likely from precipitates of KCO_3 from the electrolyte. The samples with 1,4-PhPy₂ also show F and C signals corresponding to CF_3 , which is the counterion in the molecular additive (the CPS of the corresponding C 1s peak is shown in b), which may also result from precipitates of the electrolyte. Adventitious carbon and the molecular additive both

contribute to C1, C2 can be assigned to carbonate species (CO_3), C3 and C4 are satellite and shake-up peaks.

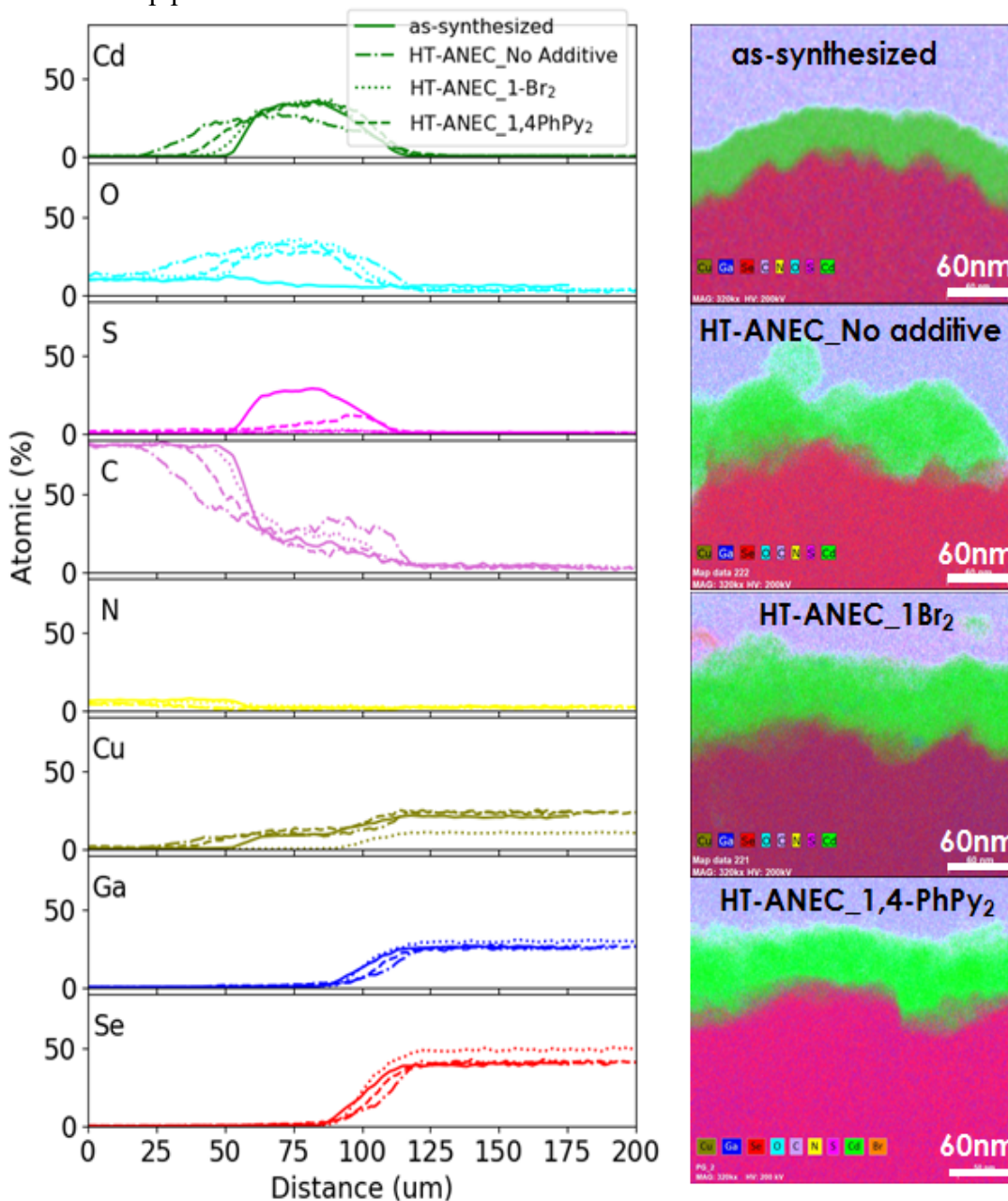


Figure S3.7: Additional TEM data supporting Figure 3.4b. The depth profile of elemental composition is obtained by horizontal averaging of the EDS mapping images for each sample.

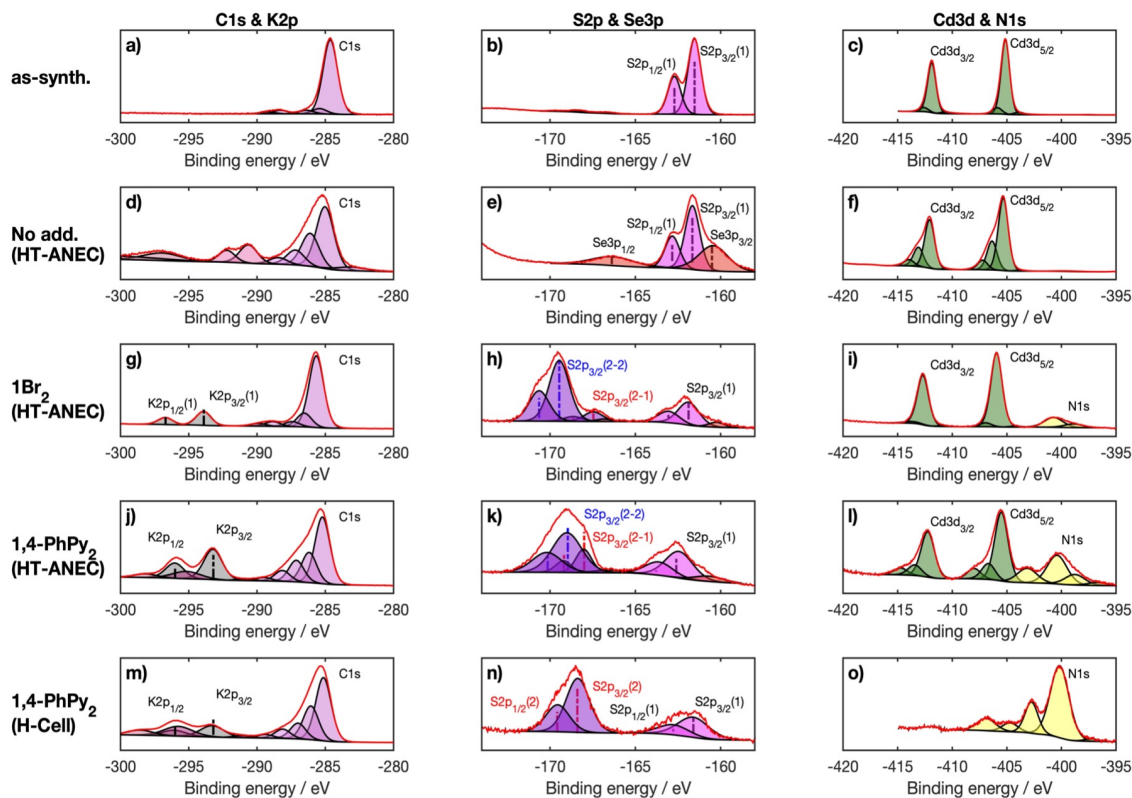


Figure S3.8: High resolution core level spectra for the energy regions containing C 1s and K 2p (a, d, g, j, m), S 2p and Se 3p (b,e, h, k, n) and Cd 3d and N 1s (c, f,i,l,o) core levels. The N originating from the additive molecules is also apparent in the respective samples. XPS signals from the as-synthesized and no-additive samples include an S $2p_{3/2}$ binding energy near 161.5 eV (S_{sulfide} in Figure 3.4c), as expected for a CdS.⁴² The electrodes with additive show an additional S signal with $2p_{3/2}$ binding energy of 168-169 eV (S_{sulfate} in Figure 3.4c), which is more characteristic of sulfate species.⁴³⁻⁴⁵ In the **1-Br₂** sample, this signal may arise from CdSO₄ from oxidation of the CdS layer, although the low Cd signal may suggest some sulfate complexation in the molecular coating, which initially contains no sulfur. In the **1,4-PhPy₂** samples, this signal may arise from the triflate counterion to the molecular additive. The C 1s signal involves multiple components whose intensities vary with condition (Figure S3.5), although the multiple sources of carbon from the electrolyte, additive, and adventitious sources preclude detailed interpretation at this time. The XPS signals collectively corroborate the findings from electron microscopy and provide guidance for future detailed exploration of the chemistry.

Table S3.1: The photocurrent and product distribution, as well as XRF and ICP-MS characterization of Cd corrosion, from each electrolysis experiment tested with 455 nm LED (450nm LED for H-cell tests). The measured Cd concentration prior to (photo)electrolysis by ICP-MS ranges between 0-4 ppb, which is considered to be noise. The Cd characterized by XRF prior to (photo)electrolysis is 80 ± 6 (counts) and for post-run characterization it is only conducted after all photo-electrolysis on a sample are completed.

Spot #	Additive protocol	V vs RHE	J _{eche} (mA/cm ²) ^d	FE H ₂ (%)	FE CO (%)	ICP-MS (ppb) ^a	ICP-MS (ppb) ^b	Xrf (counts) ^c
1	No Additive	0	-0.32	41.05	14.31	N/M	N/M	N/M
1	No Additive	-0.4	-0.47	41.72	20.42	N/M	N/M	30.83
2	No Additive	0	-0.82	43.83	23.58	N/M	N/M	9.2
3	No Additive	0	-0.47	45.94	14.88	N/M	N/M	14.5
4	No Additive	0	-0.5	51.28	16.04	N/M	N/M	N/M
4	No Additive	-0.4	-1.96	58.49	22.73	N/M	N/M	5
5	No Additive	0	-0.57	49.15	20.71	4.2	45.53	N/M
5	No Additive	-0.2	-0.98	55.37	24.41	4.2	38.06	N/M
5	No Additive	-0.4	-1.01	60.93	23.45	4.2	40.94	19
6	No Additive	0	-0.38	41.99	11.86	2.9	39.05	68
7	No Additive	0	-0.76	56.67	14.93	0	30.59	69
8	0.1mM add.1	0	-0.38	13.78	42.37	N/M	N/M	N/M
8	0.1mM add.1	-0.4	-0.54	4.83	69.53	N/M	N/M	N/M
8	0.1mM add.1	-0.4	-0.5	7.62	61.66	N/M	N/M	22
9	0.1mM add.1	0	-0.38	16.95	39.84	5.3	3.88	N/M
9	0.1mM add.1	-0.4	-0.82	14.05	59.18	5.3	23.13	N/M
10	0.1mM add.1	0	-0.44	20.82	34.91	6.8	28.20	67

11	0.1mM add.1	0	-0.41	19.29	36.22	2.9	4.27	74
12	0.3mM add.1	0	-0.35	17.27	30.41	4.4	32.50	60
13	0.3mM add.1	0	-0.38	30.4	22.67	1.5	48.70	52
14	10mM add.1	0	-0.32	3.02	24.79	3.6	37.13	64
15	10mM add.1	-0.4	-0.47	8.18	59.91	3.6	0.58	54
16	10mM add.2	0	-0.28	2.96	67.36	6.59	4.08	82
17	10mM add.2	0	-0.19	2.21	53.16	1.32	0.76	N/M
17	10mM add.2	0	-0.25	1.99	64.57	1.32	0.57	N/M
17	10mM add.2	0	-0.22	2.03	67.52	1.32	0.46	N/M
17	10mM add.2	0	-0.16	3.63	70.86	1.32	0.36	N/M
17	10mM add.2	-0.4	-0.35	1.97	74	1.32	0.31	83
18	10mM add.2	0	-0.32	3.3	55.36	0.73	0.46	N/M
18	10mM add.2	0.2	-0.06	4.86	34.01	0.73	0.59	N/M
18	10mM add.2	-0.2	-0.44	2.68	75.92	0.73	0.17	N/M
18	10mM add.2	-0.4	-0.28	3.15	83.28	0.73	0.32	82
19 ^e	10mM add.2	0	-0.13	8.7	53.89	N/M	N/M	N/M
19 ^f	No Additive	0	-0.13	14.0	50.96	N/M	0.23	79

N/M: not measured

- a. Pre-PEC electrolyte measured for Cd by ICP-MS and it is only measured once prior to 1st PEC of each sample spot
- b. Post-PEC electrolyte measured for Cd by ICP-MS
- c. Post-PEC sample measured for Cd by Xrf
- d. Averaged J_eche current during the CA period
- e. First 1.2 hour of stability test by H-cell from figure 3b
- f. Continued 3.3 hour of stability test by H-cell from figure 3c

Appendix 4

SUPPLEMENTARY INFORMATION FOR CHAPTER 4:
IN SITU DEPOSITED POLYAROMATIC LAYER GENERATES
ROBUST COPPER CATALYST FOR SELECTIVE
ELECTROCHEMICAL CO₂ REDUCTION AT VARIABLE PH

Adapted from:

Watkins, N. B.; Wu, Y.; Nie, W.; Peters, J. C.; Agapie, T.

ACS Energy Lett. **2022**, 8 (1), 189–195.

10.1021/acsenergylett.2c02002.

Materials and Methods

All solvents and reagents were obtained from commercial sources and used as received, unless stated otherwise. Cu foils (99.999% Cu, 25 mm × 25 mm × 0.5 mm), potassium carbonate (99.995%), acetonitrile (anhydrous, 99.8%), sodium nitrite (97+%), iodotoluene (98%), m-CPBA ($\leq 77\%$), triflic acid (98%), and aniline (99%) were purchased from Sigma Aldrich. Carbon rods (99.999% C) were purchased from Strem Chemicals. Glassy carbon plate, platinum foil (99.99% Pt, 25 mm × 25 mm × 0.05 mm), fluoroboric acid (48 wt% in water) were purchased from Alfa Aesar. Acetone, diethyl ether, benzene, dichloromethane, and methanol were purchased from Fisher Chemical. Natural abundance CO₂ (Research grade) was purchased from Airgas. Tetrabutylammonium tetrafluoroborate (TBABF₄) was purchased from Combi-blocks and recrystallized from hot mixture of ethanol and water (v:v = 3:2) before use. Water was purified by a Nanopure Analytical Ultrapure Water System (Thermo Scientific) or a Milli-Q Advantage A10 Water Purification System (Millipore) with specific resistance of 18.2 M Ω ·cm at 25 °C. Deuterium dioxide (D 99.96%) and d₃-acetonitrile (D 99.8%) were purchased from Cambridge Isotope Laboratories.

Prior to each use, copper foil was mechanically polished to a mirror-like finish using nanodiamond suspension (first 3 μm then 0.1 μm , Buehler) followed by rinsing in water and drying under a stream of nitrogen gas. The copper foil was then electropolished using a method similar to the one employed by Kuhl *et al.*: In a 85% phosphoric acid bath, +2.1 V versus a carbon rod counter electrode was applied to the Cu foil for 5 minutes and the foil was subsequently washed with copious amounts of ultra-pure water and dried under a stream of nitrogen gas. Prior to each use, glassy carbon plate was mechanically polished using nanodiamond suspension (0.1 μm , Buehler) and then subjected to 30 s sonication in water,

ethanol and water in sequence before drying under a stream of nitrogen gas. Prior to each use, platinum foil was washed with water and flame-annealed using a butane torch for 10 s. CO₂-saturated potassium bicarbonate electrolyte (KHCO₃, 0.1 M) was prepared by sparging an aqueous solution of potassium carbonate (K₂CO₃, 0.05 M) with CO₂ for at least 1 h prior to electrolysis.

For GDE experiments, 300 nm of copper was sputtered onto a 0.45 μm Sterlitech PTFE GDL using AJA radio frequency (rf) magnetron sputtering from a Cu target (Kurt J. Lesker, 99.95%, 2-in. diameter). The argon (Ar) flow was kept at 20 sccm and the working pressure was held at 5 μbar. The rf power was 100 W and the deposition rate was ~0.55 Å s⁻¹. Trace metals basis H₃PO₄ and KCl were used for the electrolyte. 1.5 x 1.5 cm² electrodes were cut out and used in a custom GDE cell with a working electrode area of 1 cm². Pt was used as the anode to do OER and Selemion was used to separate the cathodic and anodic chambers. CO₂ was flowed across the back of the GDE at 10 sccm.

Nuclear Magnetic Resonance (NMR)

¹H-NMR spectra were recorded on a Bruker 400 MHz instrument with a prodigy broadband cryoprobe. Chemical shifts were reported relative to the residual solvent peak.

Fourier-transform Infrared Spectroscopy (FT-IR)

FT-IR spectra were recorded on a Thermo Scientific Nicolet iS5 FTIR instrument (for powder samples) and a Thermo Scientific Nicolet 6700 FTIR instrument fitted with the

Harrick Seagull accessory (for PD-Cu and PI-Cu). Measurements were performed at both 45° and 80°.

X-ray Photoelectron Spectroscopy (XPS)

XPS data were collected using a Kratos Axis Nova system with a base pressure of 1×10^{-9} Torr. The X-ray source was a monochromatic Al K α line at 1486.6 eV. Data were analyzed using CasaXPS. Spectral energy for all spectra were calibrated using the Cu 2p^{3/2} peak (932.63 eV). To calculate the atomic ratio of elements, a Shirley background was subtracted. The core-level intensities were corrected by the analyzer transmission function and relative sensitivity factors to obtain corrected peak intensities, which were used to calculate the atomic ratios.

Atomic force microscopy (AFM)

AFM images were recorded on a Bruker Dimension Icon using the Scan-Assyst mode. A ScanAssyst-air cantilever was used with a spring constant of 0.4 N/m and a resonant frequency of 70 KHz.

Synthesis of Phenyl diazonium Tetrafluoroborate

The synthetic protocol of phenyl diazonium tetrafluoroborate was adapted from the established aqueous general synthesis of aryl diazonium tetrafluoroborate salt.¹ Specifically, 10 mmol aniline was added to a 20 mL glass vial containing 4 mL fluoroboric acid and 5 mL deionized water. The vial was kept at 0 °C in a mixture of ice and water. 1 mL of 10 M

aqueous sodium nitrite solution was then added dropwise to the reaction mixture under magnetic stirring. The product crashed out as white solids. After 30 min, the mixture was filtered under vacuum and washed with 1 mL of water. The precipitate was collected and then redissolved in minimal amount of acetone/methanol (v/v = 1:1) mixture to form a yellow solution. Diethyl ether (~ 5 times the volume of the mixture) was then slowly added to the solution to precipitate out phenyldiazonium tetrafluoroborate which was then filtered under vacuum, washed with diethyl ether and dried under vacuum for 3 h. After the synthesis and after each use, the vial containing phenyldiazonium tetrafluoroborate was filled with N₂ and stored in a freezer at -18°C. The as-synthesized phenyldiazonium tetrafluoroborate was characterized by ¹H NMR in d₃-acetonitrile (400 MHz) δ(ppm): 7.97 (t, *J* = 8.90 Hz, 2H), 8.30 (t, *J* = 7.70 Hz, 1H), 8.49 (d, *J* = 8.99 Hz, 2H), and FT-IR (635, 655, 755, 1024, 1310, 1570, 2295, 3103 cm⁻¹) (Figure S25, S12).

The redox property of the as-synthesized phenyldiazonium tetrafluoroborate was studied by cyclic voltammetry in acetonitrile containing 0.1 M tetrabutylammonium tetrafluoroborate on a glassy carbon plate electrode. A redox wave at around -0.4 V vs Ag/AgCl is present in the first scan but diminishes with further scans (Figure S5). This is consistent with observation in the previous studies that aryl groups form a multi-layer molecular structure covalently bound to the glassy carbon surface under reductive condition to in a self-limiting process while liberating N₂.^{2,3}

Synthesis of Diphenyliodonium Triflate

The synthesis of diphenyliodonium triflate was performed as reported.⁴ The as-synthesized compound was characterized by ¹H NMR in d₆-DMSO (400 MHz) δ(ppm): 8.26 (d, *J* = 7.0 Hz, 1H), 7.68 (t, *J* = 7.5 Hz, 1H), 7.54 (t, *J* = 7.8 Hz, 2H) (Figure S26).

Electrochemical Measurements

All electrochemical experiments were carried out using a Biologic VMP3 multichannel potentiostat. Chronoamperometry measurements were carried out in a custom-made PEEK flow cell setup similar to the one reported by Ager et al. using a copper foil as the working electrode and a platinum foil as the counter electrode. The cathode compartment was separated from the anode compartment by a Selemion AMV anion-exchange membrane (AGC Engineering Co.). All potentials were measured versus a leakless Ag/AgCl reference electrode (Innovative Instruments) with an outer diameter of 5 mm that was inserted into the cathode compartment. The reference electrode was calibrated against H⁺/H₂ on Pt in a 0.5 M sulfuric acid solution (0 V vs. standard hydrogen electrode).

Potentiostatic electrochemical impedance spectroscopy (PEIS) measurements were carried out prior to each electrolysis experiment to determine the Ohmic resistance of the flow cell. The impedance measurements were carried out at frequencies ranging from 100 Hz to 200 KHz to measure the solution resistance. A Nyquist plot was plotted and in the high-frequency part a linear fit was performed, and the axis intersection was identified, the value of which represents the Ohmic resistance of the cell. Typical values of the resistance range from 45 to 60 Ω.

All chronoamperometric experiments (unless stated otherwise) were performed for 30 min at 25 °C using CO₂-saturated 0.1 M KHCO₃ as electrolyte. The potentiostat was set to compensate for 85 % of the Ohmic drop, with the remaining 15 % being compensated for after the measurements. The effluent gas stream coming from the flow cell (10 mL/min) was flowed into the sample loops of a gas chromatograph (GC-FID/TCD, SRI 8610C, in Multi Gas 5 configuration) equipped with a HayeSep D column. Methane, ethylene and carbon monoxide were detected by a methanizer-flame ionization detector (FID) and the hydrogen was detected by a thermal conductivity detector (TCD). Every 10 minutes, 1 mL of gas was sampled to determine the concentration of gaseous products. After electrolysis, the main liquid products (formate, ethanol and 1-propanol) in catholytes were quantified by HPLC (Thermo Scientific Ultimate 3000). Other minor liquid products were identified by ¹H NMR where solutions containing 80% catholyte and 20% D₂O (v/v) using a water suppression technique.

Electroreductive Deposition of Phenyldiazonium Tetrafluoroborate

Deposition of the polyaryl layer was performed in a one-compartment three-electrode cell. 10 mL 0.1 M TBABF₄ acetonitrile solution was added to the cell vessel containing 9.4 mg phenyldiazonium tetrafluoroborate (5mM). To deaerate the reaction mixture, a steady flow of N₂ was bubbled into the solution for ~15 min after which the cell cap was installed which was fitted a freshly polished Cu foil (or a glassy carbon plate) as the working electrode (active area: ~1.8 cm × 2 cm, double sides), Ag/AgCl reference electrode (Pine Research) and a carbon rod as the counter electrode. Chronoamperometry was then immediately started at -1 V vs Ag/AgCl without Ohmic drop compensation for different duration during which

N₂ was continuously flown into the headspace of the cell. After electrodeposition, the modified Cu electrode was first washed by acetone and then sonicated in acetone for 30 s before drying under a stream of N₂.

Cyclic voltammetry and ECSA Measurements

Cyclic voltammetry (CV) measurement on the glassy carbon plate (active area: ~ 1.8 cm \times 2 cm, double sides) was recorded without Ohmic drop compensation using a one-compartment cell as previously described containing 5 mM phenyldiazonium tetrafluoroborate in 0.1 M TBABF₄ acetonitrile solution.

CV measurements for determining electrochemical active surface area (ECSA) were done in the same two-compartment flow cell as described for CO₂ reduction electrolysis in CO₂-saturated 0.1 M KHCO₃. The cathode potential was scanned between -0.25 V and -0.45 V vs Ag/AgCl with 85% Ohmic drop compensation at 5, 10, 25, 50, 100, 250, 500 mV/s. 10 cycles were done at 5 mV/s and 5 cycles were done at all other scan rates. Data from the last cycle at each scan rate was used in the calculation of ECSA where the anodic and cathodic current values at -0.35 V were extracted. The plot of $|j_{\text{anodic}}|$ and $|j_{\text{cathodic}}|$ against the scan rate were generated and linear fits were performed. The average value of the slopes of the two curves signifies the double layer capacitance (C_{dl}) and therefore was used to represent ECSA.

Rotating Disk Electrode (RDE) Experiments

Experiments were performed using a Pine Research MSR Rotator in a 0.1 M HClO₄ electrolyte, pH adjusted to ~ 2.2 using KOH, sparged with N₂ for 30 minutes before

experimentation. Copper disk electrodes were mechanically polished with 9 μm , 6 μm , 3 μm , and 0.1 μm diamond pastes, and then sonicated in nanopure H_2O for 5 minutes before use. A carbon rod was used as the counter electrode and an SCE was used as the reference electrode. Cyclic voltammograms were collected between OCV and -1.8 V vs SCE at 400, 800, 1200, 1600, and 2500 RPM. Limiting current values were selected at the same potential for all rotation rates and used for subsequent Levich analysis.

Supporting Tables and Figures

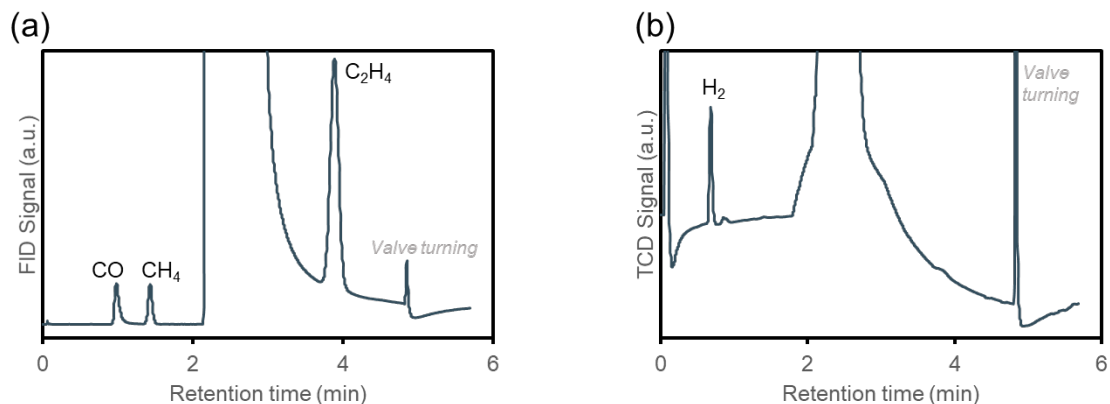


Figure S4.1. Representative gas chromatographs of product stream from CO_2 reduction. (a) GC trace from FID. (b) GC trace from TCD.

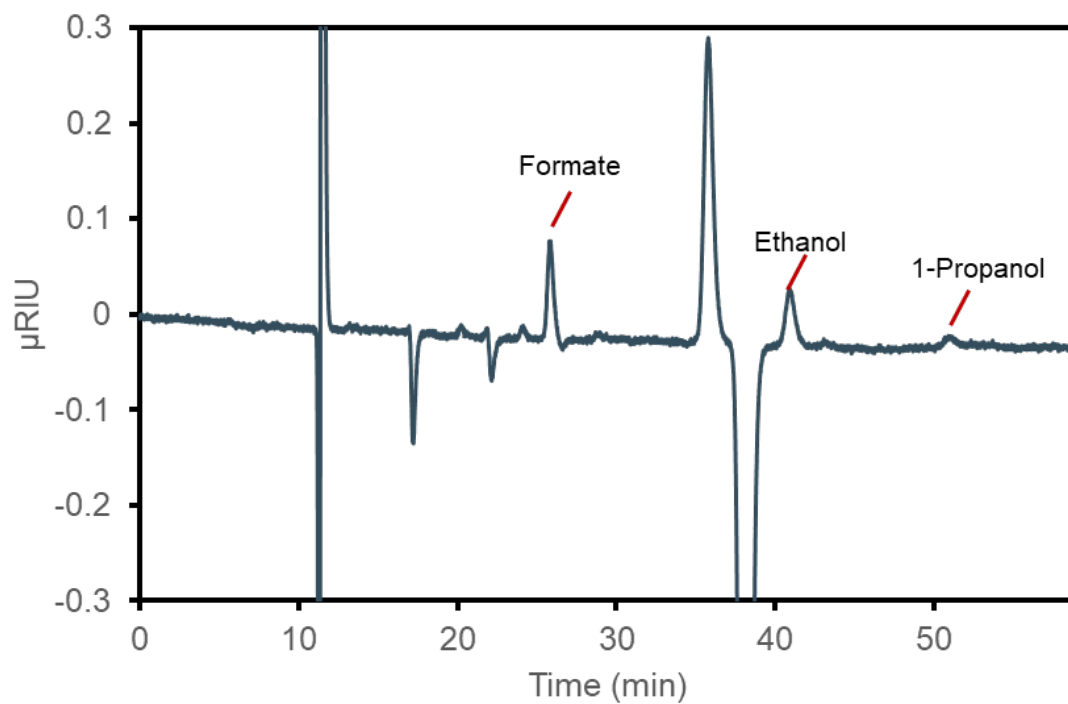


Figure S4.2. Representative HPLC trace of catholyte solution after reaction.

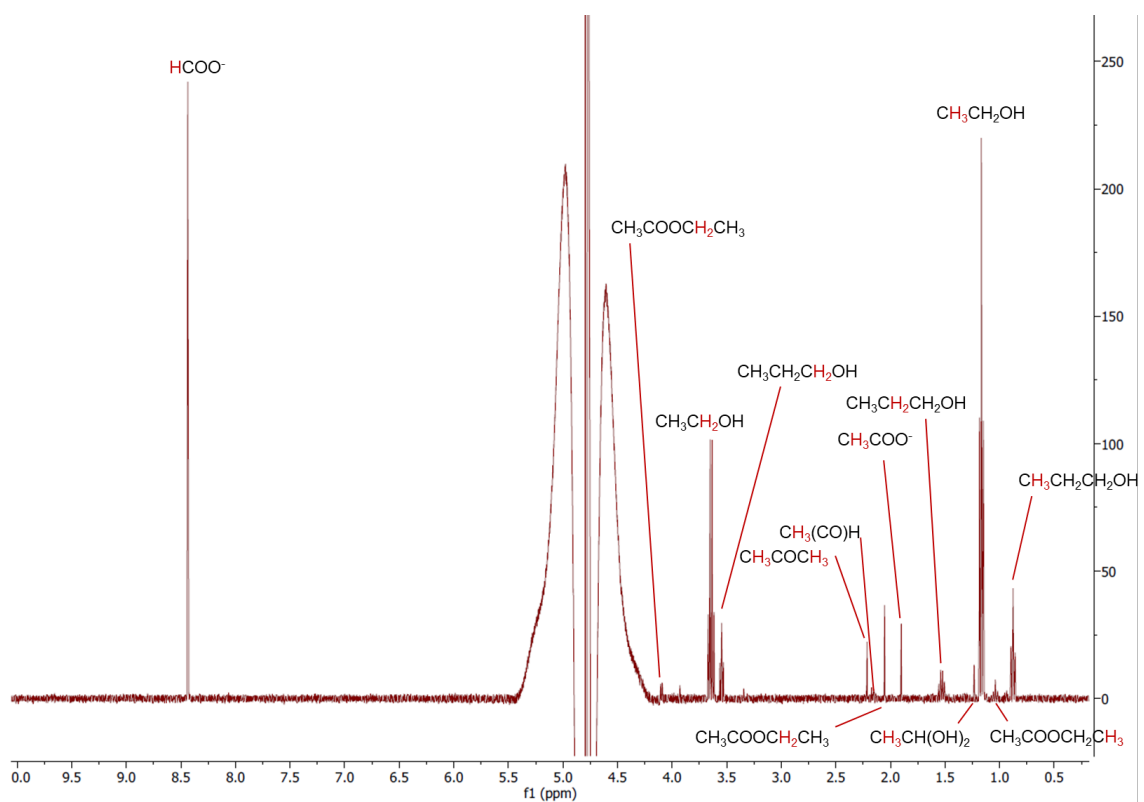


Figure S4.3. Representative $^1\text{H-NMR}$ spectrum of the sample prepared from catholyte solution after CO_2 reduction electrolysis by PD-Cu. Assignment of the spectrum is based on our previous publication.⁶

Table S4.1. Current density and faradaic efficiency towards different products by PD-Cu during CO₂ reduction at various cathode potentials

V vs RHE	Run #	j (mA cm ⁻²)	Faradaic Efficiency (%)							
			H ₂	CO	CH ₄	C ₂ H ₄	Formate	EtOH	1-PrOH	Total C _{≥2}
-0.98	1	-2.73	25.2	5.4	1.1	29.9	10.1	11.9	5.5	47.4
	2	-2.14	34.0	5.0	1.2	24.4	15.6	11.8	0.0	36.3
	3	-2.35	31.6	4.1	2.6	26.1	14.0	10.7	0.0	36.8
	Avg	-2.41 ±0.21	30.3 ±3.2	4.8 ±0.5	1.6 ±0.6	26.8 ±2.0	13.3 ±2.0	11.5 ±0.5	2.8 ±2.0	40.2 ±1.7
-1.02	1	-3.52	21.6	3.8	2.6	34.2	8.6	18.2	7.0	59.4
	2	-3.55	17.4	5.2	0.0	36.8	9.8	16.0	6.8	59.6
	3	-3.56	23.7	5.0	1.0	33.7	10.0	21.0	6.5	61.1
	Avg	-3.55 ±0.02	20.9 ±2.3	4.7 ±0.5	1.2 ±0.9	34.9 ±1.2	9.5 ±0.5	18.4 ±1.8	6.8 ±0.2	60.0 ±0.7
-1.05	1	-5.76	18.2	1.2	3.8	41.9	3.7	21.6	6.3	69.7
	2	-5.39	15.9	1.7	4.3	41.5	5.2	20.6	6.8	69.0
	3	-5.20	18.6	2.4	4.3	38.9	5.1	22.5	6.8	68.2
	Avg	-5.47 ±0.46	17.7 ±1.2	1.4 ±0.6	3.4 ±0.9	42.3 ±1.9	4.2 ±0.8	21.2 ±0.7	6.6 ±0.4	70.1 ±1.4
-1.08	1	-10.55	23.8	0.3	10.7	35.0	1.5	19.6	4.1	58.7
	2	-7.54	29.6	0.4	17.0	28.5	2.6	18.3	5.1	51.9
	3	-8.68	29.6	0.2	9.4	32.3	1.1	16.3	3.6	52.2
	Avg	-8.92 ±1.07	27.7 ±2.4	0.3 ±0.1	12.4 ±2.9	31.9 ±2.3	1.7 ±0.5	18.1 ±1.2	4.3 ±0.5	54.3 ±2.7

Table S4.2. Current density and faradaic efficiency towards different products by unmodified Cu control during CO₂ reduction at various cathode potentials.

V vs RHE	Run #	j (mA cm ⁻²)	Faradaic Efficiency (%)							
			H ₂	CO	CH ₄	C ₂ H ₄	Formate	EtOH	1-PrOH	Total C _{≥2}
-0.98	1	-2.37	34.3	2.4	5.0	26.4	6.4	8.0	0.0	34.4
	2	-3.98	57.7	1.7	4.3	10.7	9.2	9.0	3.8	23.5
	3	-1.85	44.1	4.8	5.0	18.1	18.8	7.3	0.0	25.4
	Avg	-2.73 ±0.91	45.4 ±9.6	3.0 ±1.3	4.8 ±0.3	18.4 ±6.4	11.4 ±5.3	8.1 ±0.7	1.3 ±1.8	27.8 ±4.8
-1.02	1	-4.92	35.1	2.1	20.0	15.6	9.2	9.6	3.1	28.3
	2	-3.32	29.0	1.7	22.9	20.6	9.9	6.5	0.0	27.1
	3	-4.18	31.1	1.0	20.1	24.0	7.9	9.8	5.9	39.7
	Avg	-4.14 ±0.65	31.7 ±2.5	1.6 ±0.4	21.0 ±1.3	20.1 ±3.4	9.0 ±0.8	8.6 ±1.5	3.0 ±2.4	31.7 ±5.7
-1.05	1	-5.73	43.6	1.0	17.1	16.8	6.0	6.7	4.8	28.3
	2	-6.13	27.1	1.7	35.2	13.7	4.5	5.7	4.0	23.3
	3	-6.06	36.6	0.8	25.7	15.7	6.3	6.7	4.0	26.3
	Avg	-5.97 ±0.17	35.8 ±6.8	1.2 ±0.4	26.0 ±7.4	15.4 ±1.3	5.6 ±0.8	6.4 ±0.5	4.3 ±0.4	26.0 ±2.0
-1.08	1	-7.74	34.2	0.3	29.0	20.5	1.8	9.8	2.3	32.6
	2	-7.44	30.3	0.3	27.8	22.8	2.8	9.0	3.0	34.8
	3	-6.99	32.3	0.5	39.3	11.2	3.8	5.9	0.0	17.1
	Avg	-7.39 ±0.31	32.3 ±1.6	0.4 ±0.1	32.0 ±5.2	18.2 ±5.0	2.8 ±0.8	8.3 ±1.7	1.8 ±1.3	28.2 ±7.9

Table S4.3. Current density and faradaic efficiency towards different products by PI-Cu during CO₂ reduction at various cathode potentials using a 5-minute pre-deposition of film.

V vs RHE	Run #	<i>j</i> (mA cm ⁻²)	Faradaic Efficiency (%)							
			H ₂	CO	CH ₄	C ₂ H ₄	Formate	EtOH	1-PrOH	Total C _{≥2}
-0.99	1	-2.4	27.3	9.2	0.2	33.2	14.9	7.5	7.0	47.7
	2	-2.3	35.4	11.2	0.7	34.5	9.5	5.9	5.6	46.0
	3	-2.8	27.7	7.8	0.6	36.3	11.3	11.7	6.0	54.0
	Avg	-2.47	30.4	9.6	0.5	34.5	12.0	7.7	6.2	48.5
		±0.2	±6.1	±1.7	±0.3	±1.8	±2.7	±2.4	±0.7	±1.8
-1.02	1	-3.2	23.5	3.6	0.2	44.6	9.8	16.2	8.7	69.5
	2	-3.2	23.9	7.6	1.3	42.1	8.6	11.9	6.1	60.1
	3	-4.1	22.2	4.5	0.5	45.8	9.6	13.5	8.1	67.4
	Avg	-3.48	23.2	5.2	0.7	44.2	9.3	13.9	7.6	65.7
		±0.51	±0.9	±2.1	±0.6	±1.9	±0.6	±2.2	±1.4	±4.9
-1.05	1	-6.0	16.9	1.2	0.4	56.9	2.8	22.7	5.0	77.0
	2	-5.7	17.8	1.4	0.7	54.3	2.8	20.9	5.7	73.2
	3	-5.3	20.2	1.2	1.0	49.8	3.2	19.7	5.7	68.9
	Avg	-5.66	18.3	1.2	0.7	53.7	2.9	21.1	5.3	73.0
		±0.34	±1.8	±0.1	±0.3	±3.4	±0.3	±1.3	±0.4	±3.7
-1.07	1	-6.0	22.4	1.2	1.2	49.5	2.9	22.0	5.4	69.6
	2	-6.2	24.5	1.1	1.9	48.7	2.3	21.9	4.9	67.6
	3	-5.7	27.2	0.9	2.5	47.0	2.4	21.3	5.4	66.1
	Avg	-5.96	24.7	1.1	1.9	48.4	2.5	21.7	5.2	67.7
		±0.23	±2.4	±0.1	±0.6	±1.4	±0.3	±0.3	±0.3	±2.8

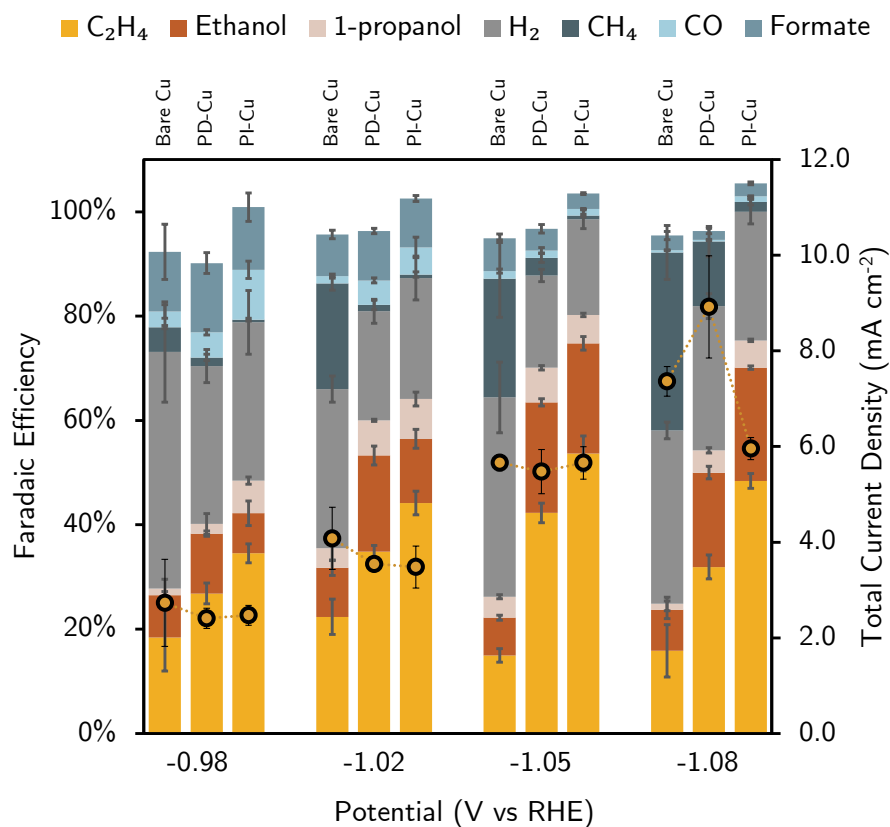


Figure S4.4: Potential dependent selectivity and activity of bare Cu, PD-Cu, and PI-Cu. The black/yellow circles correspond to the total current density of the catalyst shown on the second axis.

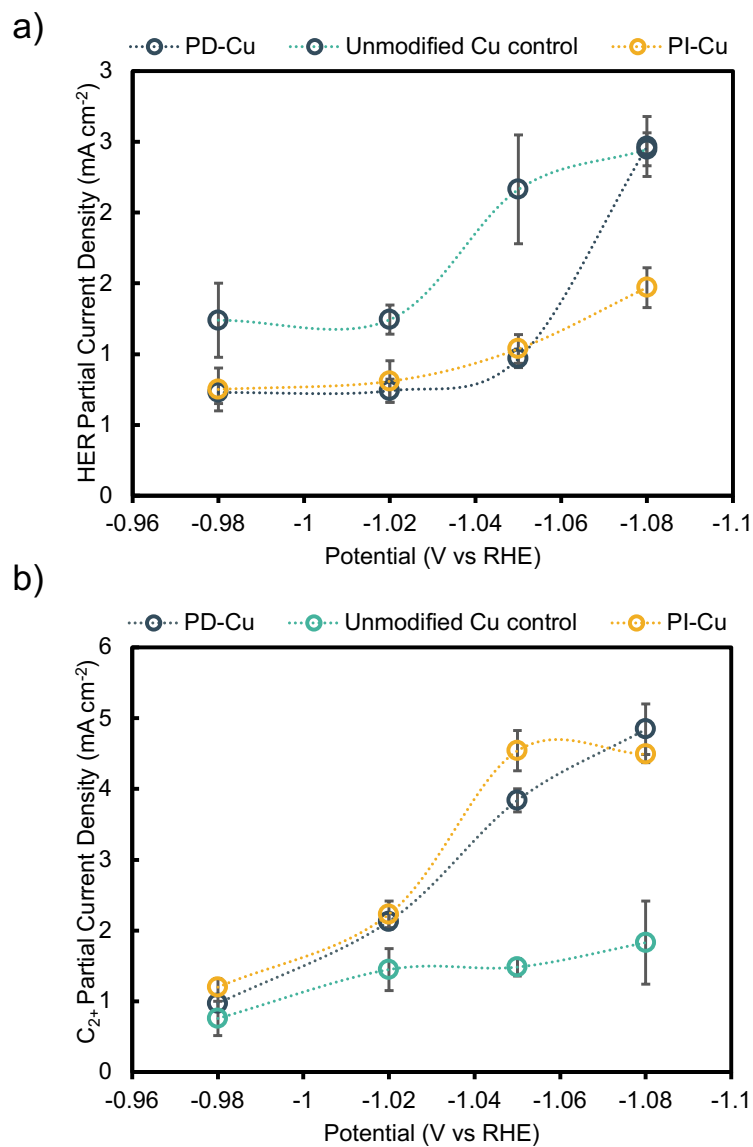


Figure S4.5. Comparisons of (a) HER and (b) C₂₊ partial current density for PD-Cu and PI-Cu with respect to bare Cu.

Table S4.4. Current density and faradaic efficiency towards different products in control electrolyses

Entry	V vs RHE	Run #	j (mA cm ⁻²)	Faradaic Efficiency (%)						
				H ₂	CO	CH ₄	C ₂ H ₄	Formate	EtOH	1-PrOH
1	-1.03	1	-8.81	107.7	0.0	0.0	0.0	0.0	0.0	0.0
2	-1.10	1	-0.15	43.3	0.0	0.0	0.0	27.1	0.0	0.0
3	-1.05	1	-6.06	46.8	1.2	14.1	13.9	6.3	7.7	4.0
	-1.05	2	-6.86	49.1	0.7	16.9	15.4	5.2	6.8	3.5
		Avg	-6.46	48.0	1.0	15.5	14.6	5.7	7.2	3.8
			±0.40	±1.2	±0.3	±1.4	±0.8	±0.6	±0.4	±0.2
4	-1.04	1	-8.00	18.0	2.0	4.9	36.4	7.4	19.9	6.4

Entry 1: electrolysis by PD-Cu in Ar-bubbled 0.1 M KHCO₃

Entry 2: electrolysis by glassy carbon plate after being subjected to the electroreductive deposition of phenyldiazonium tetrafluoroborate

Entry 3: electrolyses by Cu after being subjected to the electroreductive deposition condition in 0.1 M TBABF₄ in acetonitrile without phenyldiazonium

Entry 4: electrolysis with 10 min PD-Cu with 10 mM KI added into 0.1 M KHCO₃ electrolyte

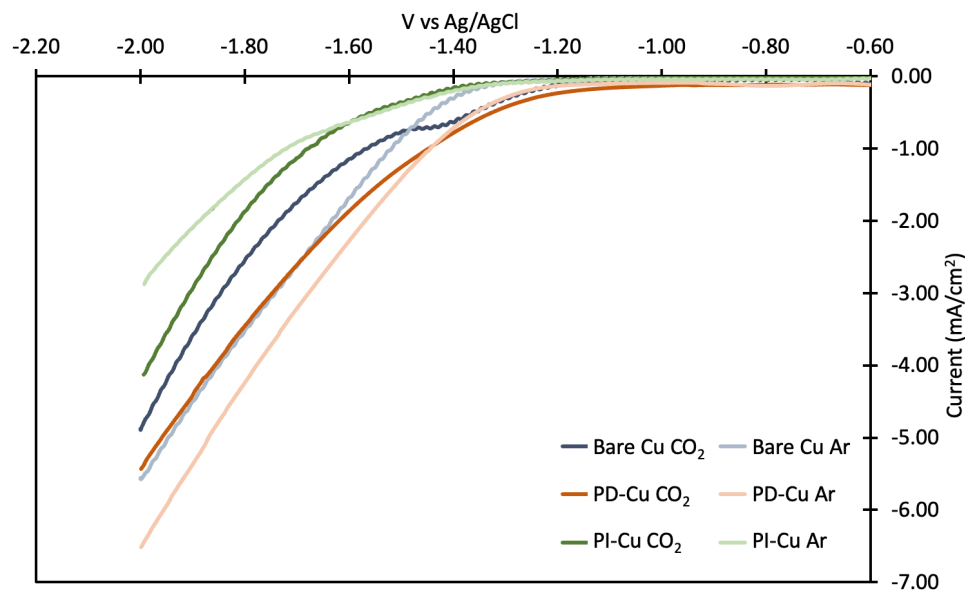


Figure S4.6. LSV measurements of bare Cu, PD-Cu, and PI-Cu under CO₂ and argon.

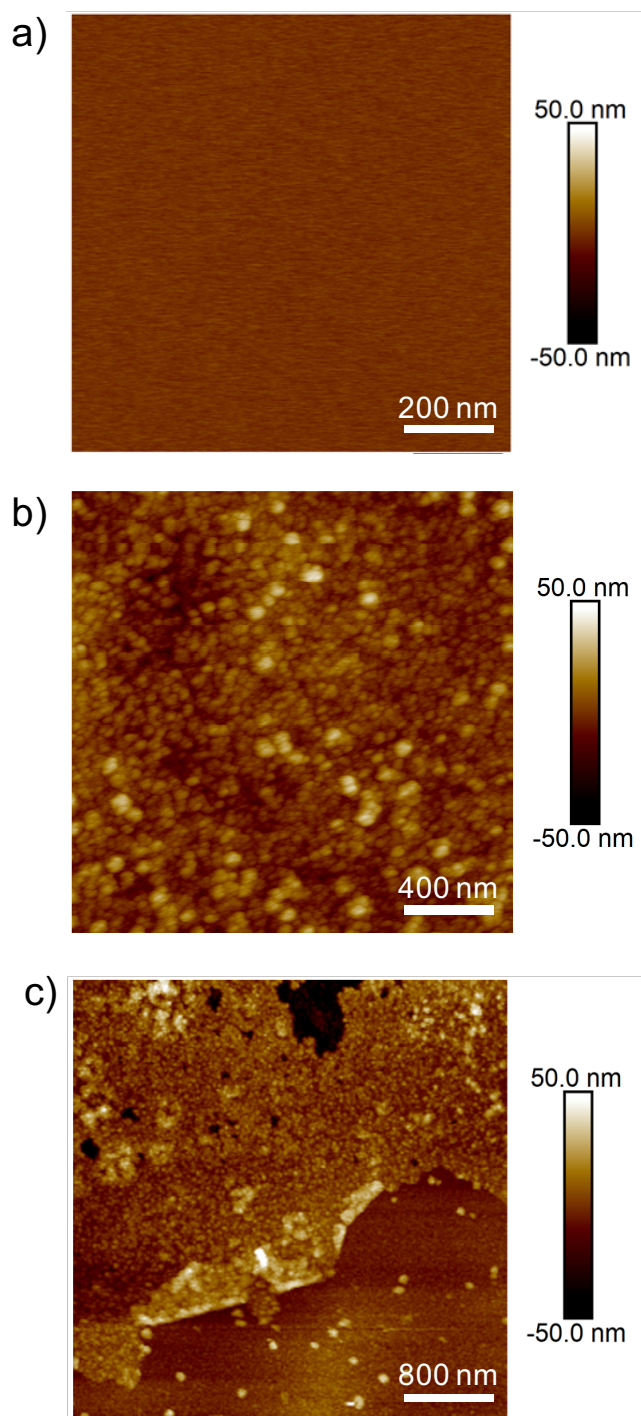


Figure S4.7. AFM images of (a) unmodified polished Cu, (b) PD-Cu, (c) Delaminated PD-Cu post 10 h electrolysis.

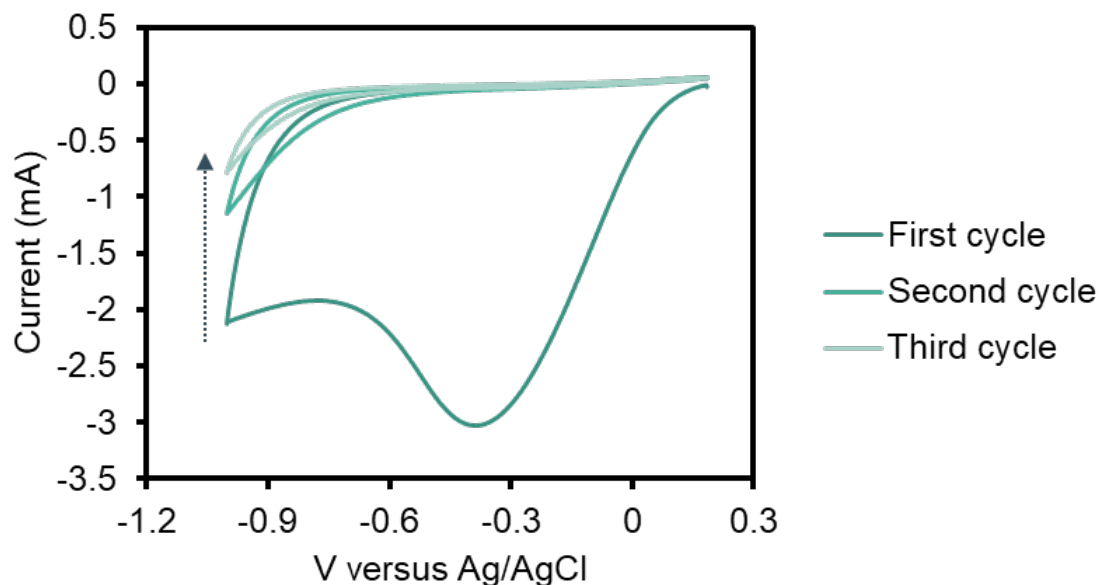


Figure S4.8. Cyclic voltammogram of 5 mM phenyldiazonium tetrafluoroborate in 0.1 M TBABF₄ in acetonitrile. Scan rate: 50 mV/s.

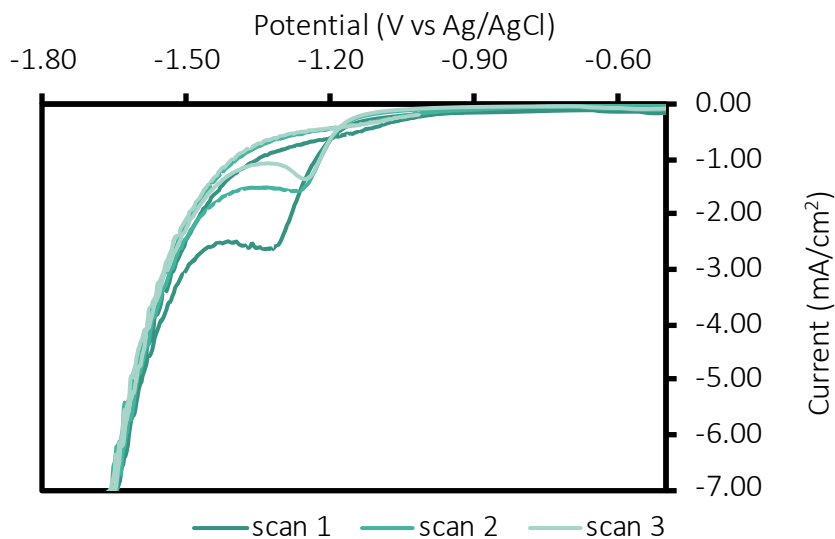


Figure S4.9. Cyclic voltammogram of 10 mM diphenyliodonium triflate in 0.1 M KHCO₃. Scan rate: 100 mV/s. Decreasing peak intensity attributed to the self-inhibiting nature of additive deposition is consistent with previous reports using N-aryl pyridinium additives.⁶

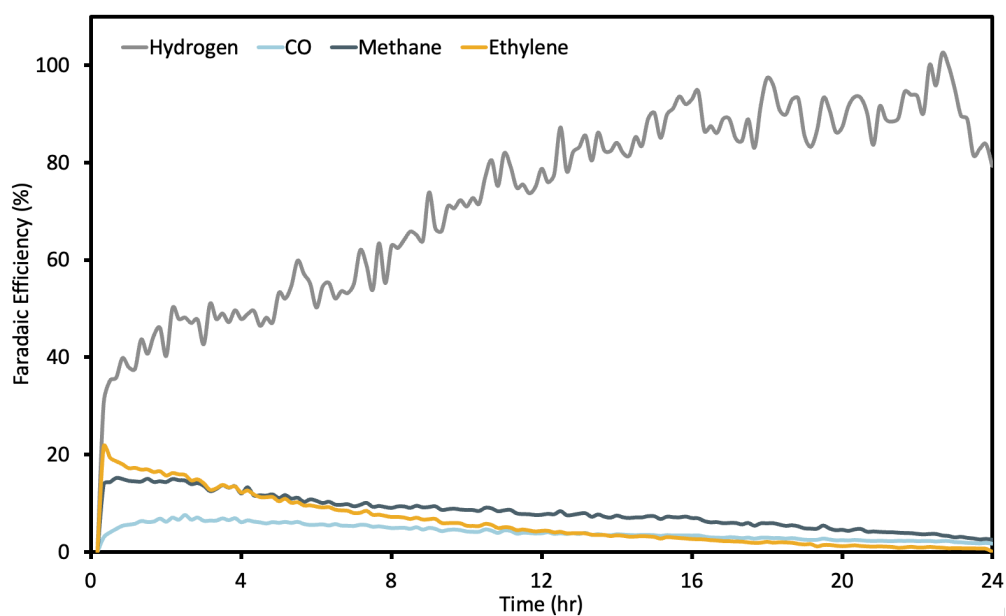


Figure S4.10. Long term electrolysis of bare Cu in 0.1 M KHCO₃ at an applied voltage of -1.1 V vs RHE. The loss of selectivity with time has been attributed in the literature to the deposition of trace metal impurities on the electrode surface.¹⁰

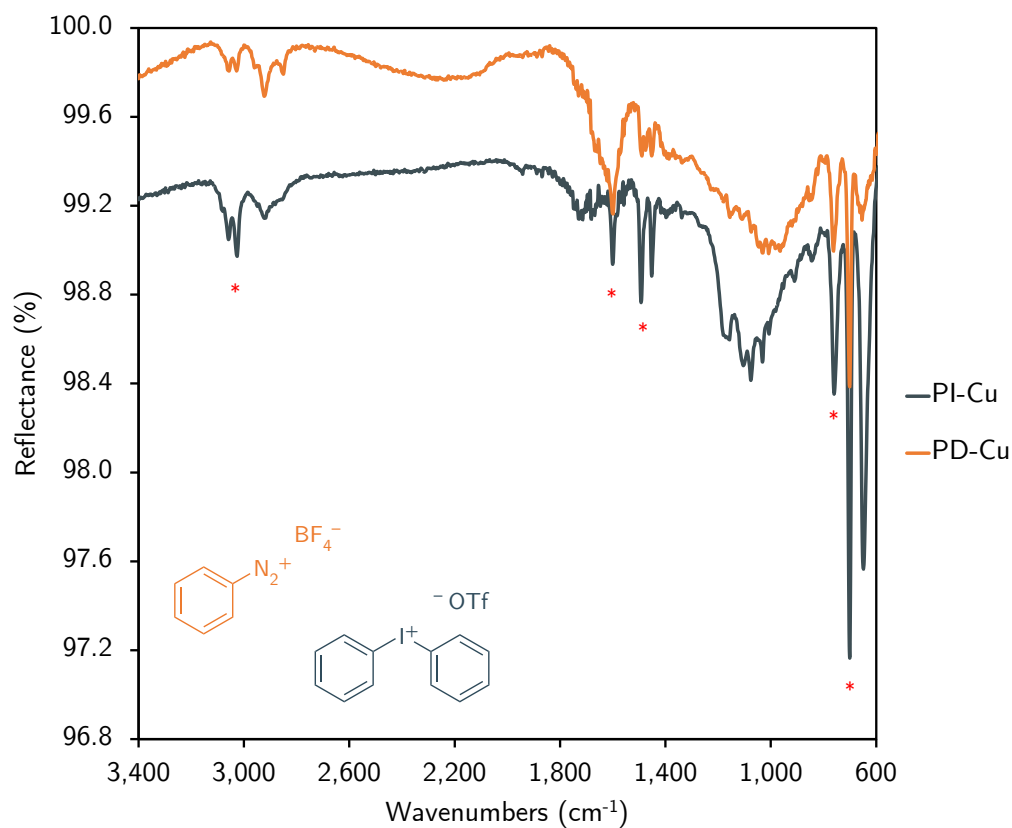


Figure S4.11. FT-IR spectrum of PD-Cu and PI-Cu.

Table S4.5. Assignment of IR bands in PD-Cu attributed to polyphenylene. Bands are assigned based on literature report on polyphenylene deposited on Fe.⁵

Wavenumber of the band (cm ⁻¹)	Assignment
700	Aromatic C-H out-of-plane vibrations
764	Aromatic C-H out-of-plane vibrations
839	Aromatic C-H out-of-plane vibrations
1448	Aromatic C=C stretching vibrations
1493	Aromatic C=C stretching vibrations
1603	Aromatic C=C stretching vibrations
3024	Aromatic C-H stretching
3053	Aromatic C-H stretching

Table S4.6. Assignment of IR bands in PI-Cu attributed to polyphenylene. Bands are assigned based on literature report on polyphenylene deposited on Fe.⁵

Wavenumber of the band (cm⁻¹)	Assignment
702	Aromatic C-H out-of-plane vibrations
762	Aromatic C-H out-of-plane vibrations
845	Aromatic C-H out-of-plane vibrations
1080	In-plane C-H bending
1450	Aromatic C=C stretching vibrations
1490	Aromatic C=C stretching vibrations
1600	C-H out-of-plane deformation
3020	Aromatic C-H stretching

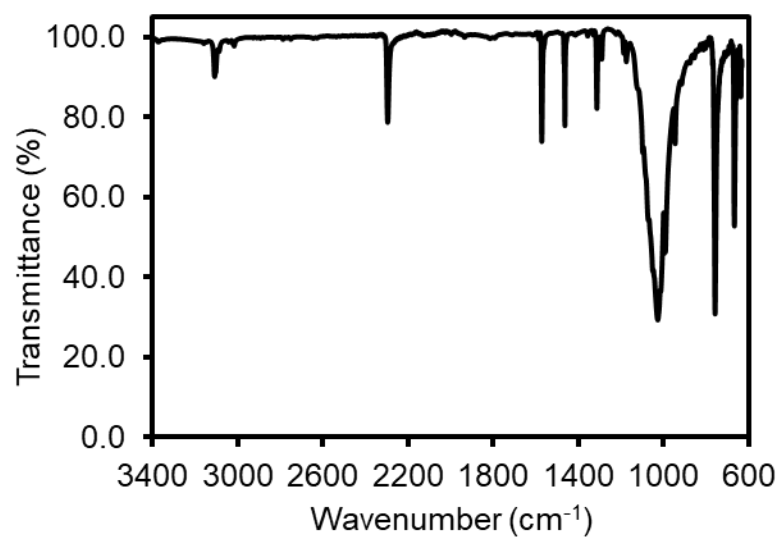


Figure S4.12. FT-IR spectrum of as-synthesized phenyldiazonium tetrafluoroborate.

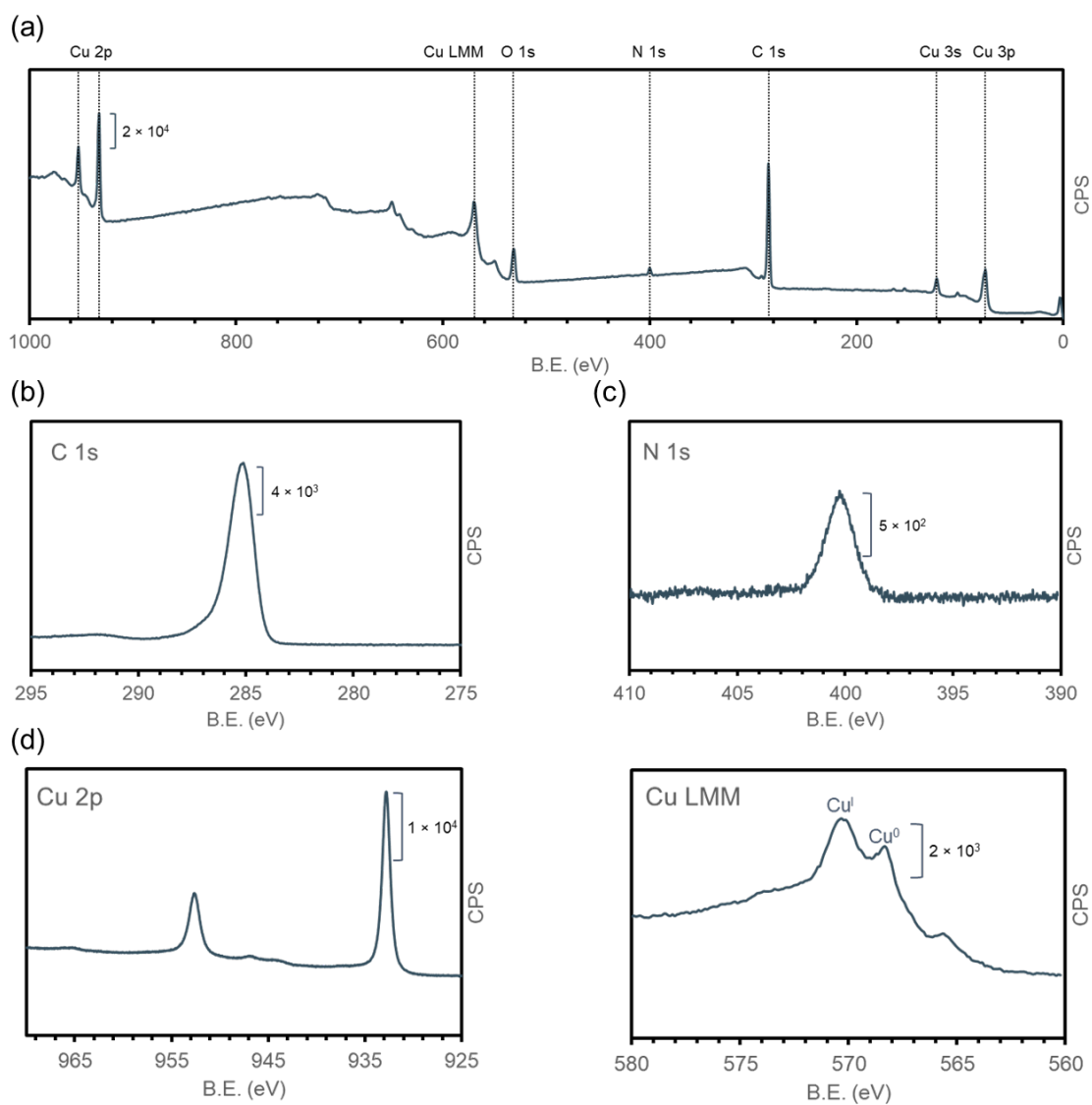


Figure S4.13. XPS characterization of PD-Cu. (a) Survey spectrum. (b) C 1s spectrum. (c) N 1s spectrum. (d) Cu 2p and Cu LMM spectra.

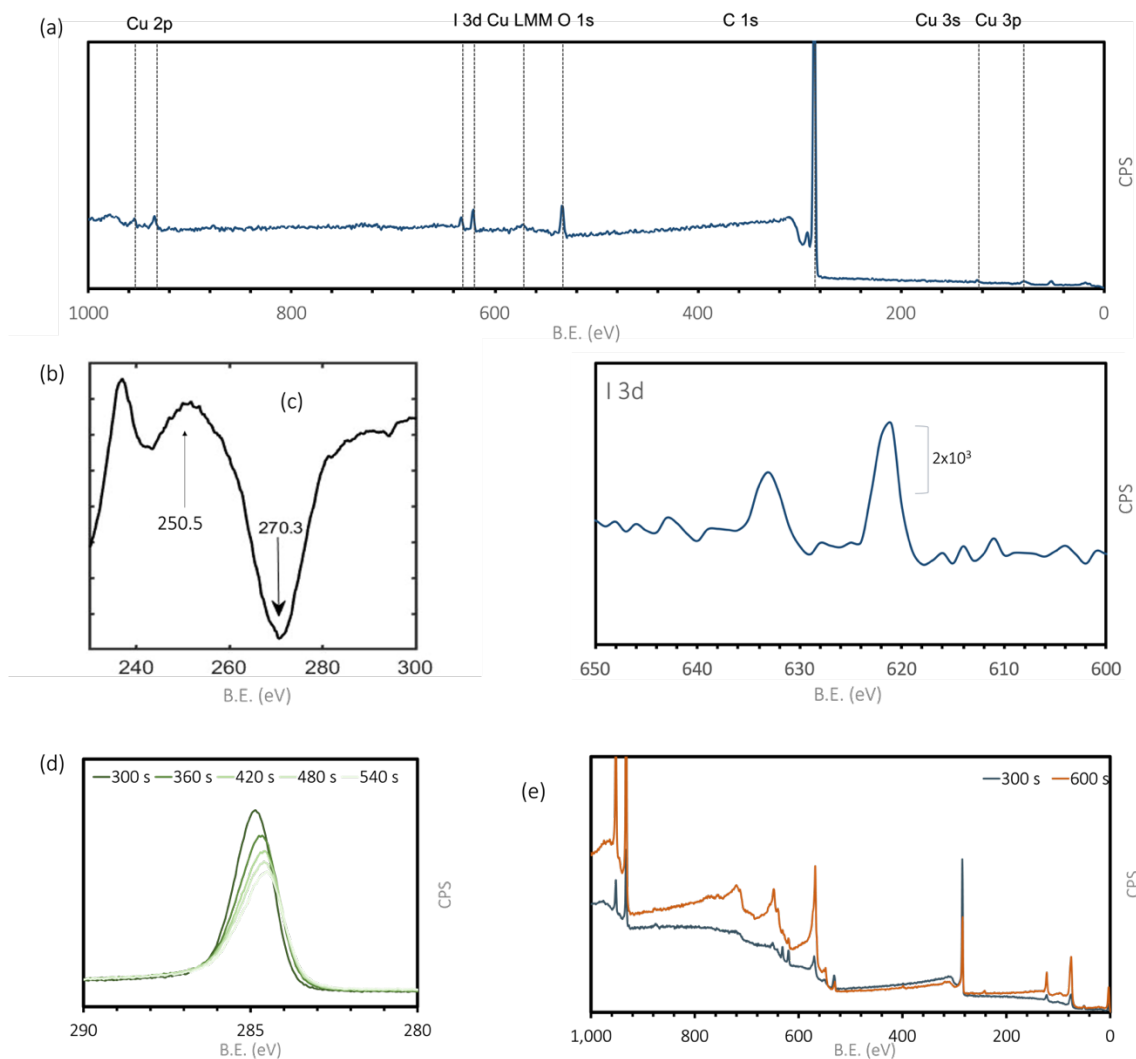


Figure S4.14. XPS characterization of PI-Cu. (a) Survey spectrum. (b) First derivative of C KLL. The spacing between the trough and the peak has been attributed to the ratio between $sp^2:sp^3$ carbons; a 20 eV gap corresponds to near 100% sp^2 content.⁷ (c) I 3d spectrum. Given the reported bond between grafted films and metal surfaces, depth profiling XPS studies were performed. (d) High-res spectra of the C 1s peak at five different etching times reveals no shoulders indicative of a Cu-C bond. The shift in peak B.E. is associated with changing sample conductivity, and not anything chemical in nature. (e) The survey spectrum of the etched sample after 300 s and 600 s reveals only increased Cu features.

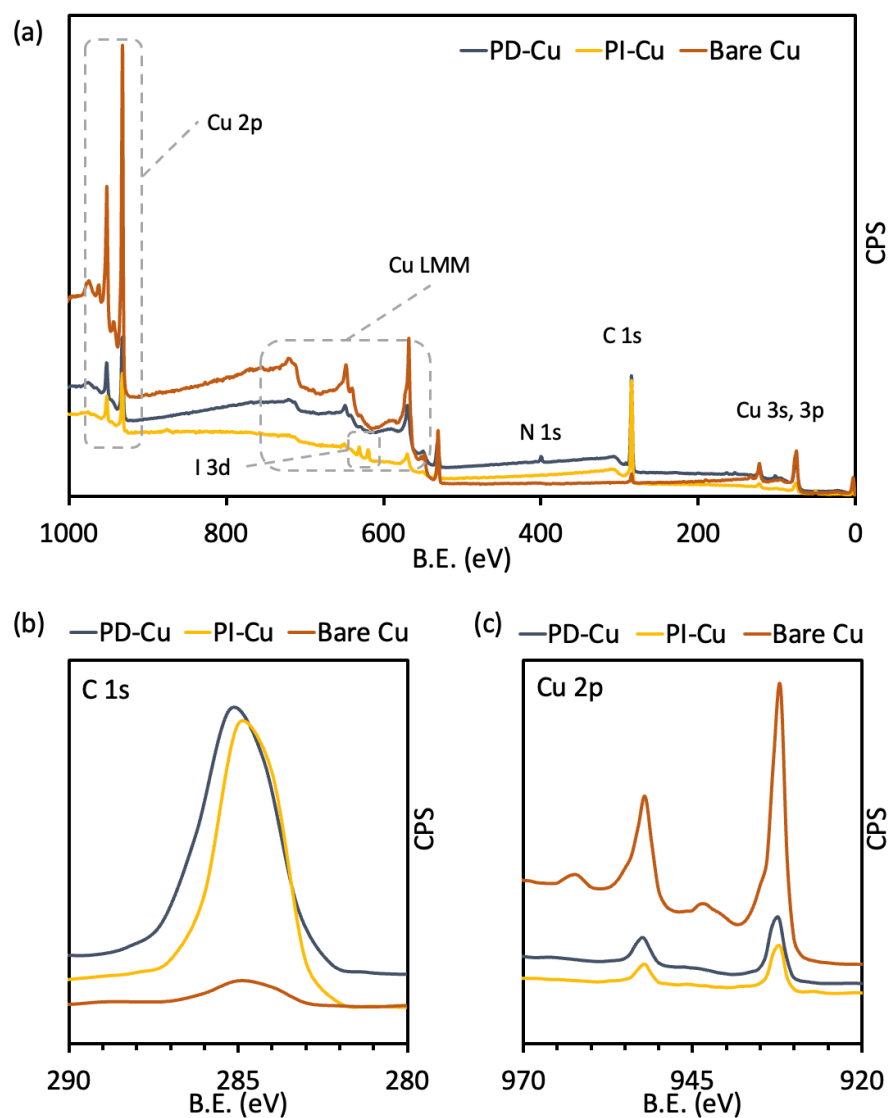


Figure S4.15. Comparison of XPS for bare Cu, PD-Cu, and PI-Cu. (a) Survey, (b) C 1s, and (c) Cu 2p spectra of the three Cu catalysts reported in this study. The PI-Cu is taken after 300 s of etching to aid in the visualization of the Cu bands. There are no remarkable differences between the Cu and C features that enable us to identify whether a Cu-C bond definitively exists.

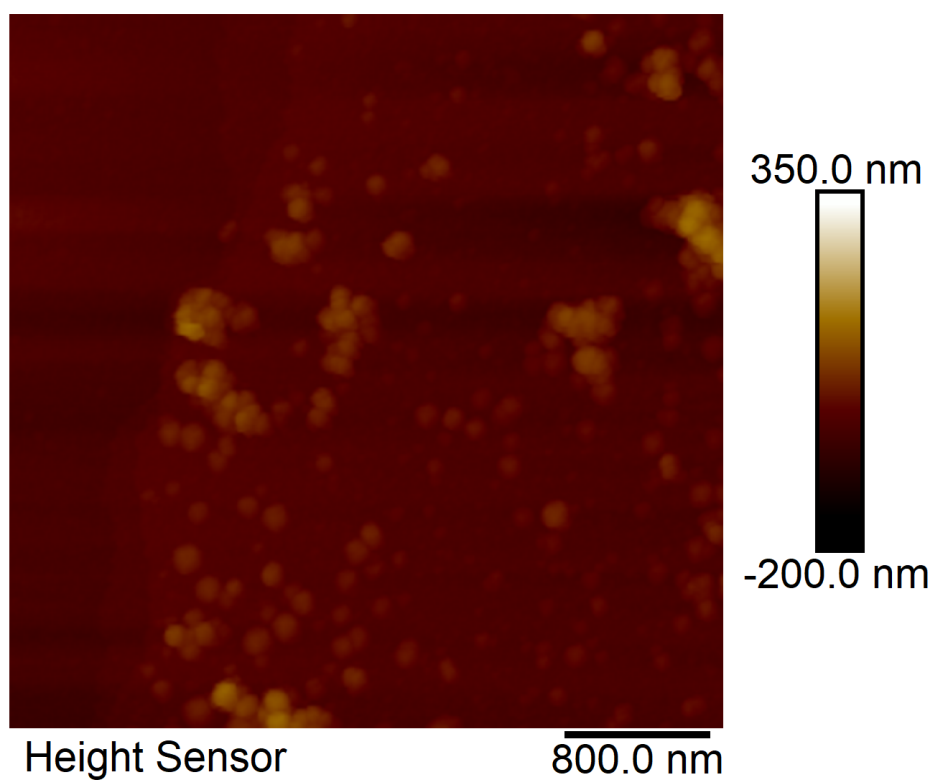


Figure S4.16. AFM image of a modified Cu after exposure to the electrodeposition condition for 1 min. The image was taken of a $4 \times 4 \mu\text{m}^2$ at the interface of unmodified polished Cu and electrodeposited Cu.

Table S4.7. Current density and faradaic efficiency towards different CO₂ reduction products by PD-Cu prepared using different deposition times

Dep. time	Run #	<i>j</i> (mA cm ⁻²)	Faradaic Efficiency (%)							
			H ₂	CO	CH ₄	C ₂ H ₄	Formate	EtOH	1-PrOH	Total C _{≥2}
1 min	1	-4.15	37.0	5.9	16.2	15.0	10.2	9.8	6.4	31.2
	2	-4.53	36.6	1.7	17.3	17.0	5.7	7.6	4.6	29.3
	3	-5.81	32.7	1.0	22.7	19.2	6.4	8.0	4.6	31.9
	Avg	-4.83	35.5	2.9	18.7	17.1	7.5	8.5	5.2	30.8
		±0.71	±1.9	±2.1	±2.8	±1.7	±2.0	±1.0	±0.8	±0.8
5 min	1	-6.94	34.0	0.7	5.8	33.1	1.8	15.5	3.4	52.0
	2	-3.94	27.9	4.1	8.2	25.0	9.3	10.2	4.7	40.0
	3	-4.63	27.9	1.1	6.2	34.1	3.5	13.6	4.9	52.6
	Avg	-5.17	29.9	2.0	6.7	30.7	4.9	13.1	4.3	48.2
		±1.28	±2.0	±1.5	±1.0	±4.1	±3.2	±2.2	±0.7	±5.8
10 min	Avg	-5.47	17.7	1.4	3.4	42.3	4.2	21.2	6.6	70.1
		±0.46	±1.2	±0.6	±0.9	±1.9	±0.8	±0.7	±0.4	±1.4
15 min	1	-6.88	18.3	0.7	2.8	42.1	3.3	20.4	5.1	67.6
	2	-5.34	29.2	0.7	2.7	36.6	2.8	18.6	5.8	61.0
	3	-5.70	17.3	1.1	1.5	40.8	7.2	18.5	5.9	65.2
	Avg	-5.97	21.6	0.9	2.3	39.8	4.5	19.2	5.6	64.6
		±0.66	±5.4	±0.2	±0.6	±2.3	±2.0	±0.9	±0.3	±2.7

Table S4.8. Current density and faradaic efficiency towards different CO₂ reduction products by PI-Cu prepared using different deposition times

Dep. me	Run #	j (mA cm ⁻²)	Faradaic Efficiency (%)							
			H ₂	CO	CH ₄	C ₂ H ₄	For mate	EtOH	1-PrOH	Total C _{≥2}
1 min	1	-7.03	39.3	0.8	23.9	14.3	1.3	10.7	3.0	28.0
	2	-5.92	34.2	0.4	12.0	10.1	1.0	15.7	4.9	30.7
	3	-4.82	21.2	2.4	9.4	33.1	2.7	18.2	4.9	56.2
	Avg	-5.92 ±1.11	31.6 ±9.4	1.17 ±1.1	15.1 ±7.7	19.2 ±12.3	1.7 ±0.9	14.9 ±3.8	4.3 ±1.1	38.3 ±15.6
5 min	1	-3.86	14.0	2.2	0.0	34.9	5.0	21.4	8.9	65.2
	2	-5.92	12.5	0.5	0.0	47.1	1.3	25.5	5.9	78.5
	3	-5.55	17.0	1.0	5.5	40.4	1.3	21.5	5.3	67.2
	Avg	-5.11 ±1.10	14.5 ±2.3	1.2 ±0.84	1.8 ±3.1 9	40. ±6.13	2.5 ±2.14	22.8 ±2.3	6.7 ±1.93	70.3 ±7.2
10 min	1	-3.84	11.1	2.2	0.7	45.0	4.1	23.2	7.8	76.0
	2	-4.14	17.4	2.4	5.6	44.9	2.5	23.0	8.3	76.2
	3	-3.66	17.6	1.8	0.0	43.2	6.2	22.6	9.4	75.2
	4	-3.19	18.2	2.2	0.2	47.5	3.9	19.4	8.3	75.2
Avg	-3.71 ±0.40	16.1 ±3.3	2.2 ±0.3	1.6 ±2.7	45.2 ±1.8	4.2 ±1.5	22.1 ±1.8	8.5 ±0.7	75.7 ±0.5	
15 min	1	-4.00	20.8	0.6	1.0	40.8	2.4	26.4	7.9	75.1
	2	-3.88	16.2	1.2	0.0	45.8	4.6	25.8	8.1	79.7
	3	-3.54	15.4	1.4	2.0	46.5	3.0	24.9	8.1	79.5
	Avg	-3.80 ±0.24	17.5 ±3.0	1.1 ±0.5	1.0 ±1.0	44.3 ±3.1	3.3 ±1.1	25.7 ±0.8	8.0 ±0.1	78.1 ±2.6

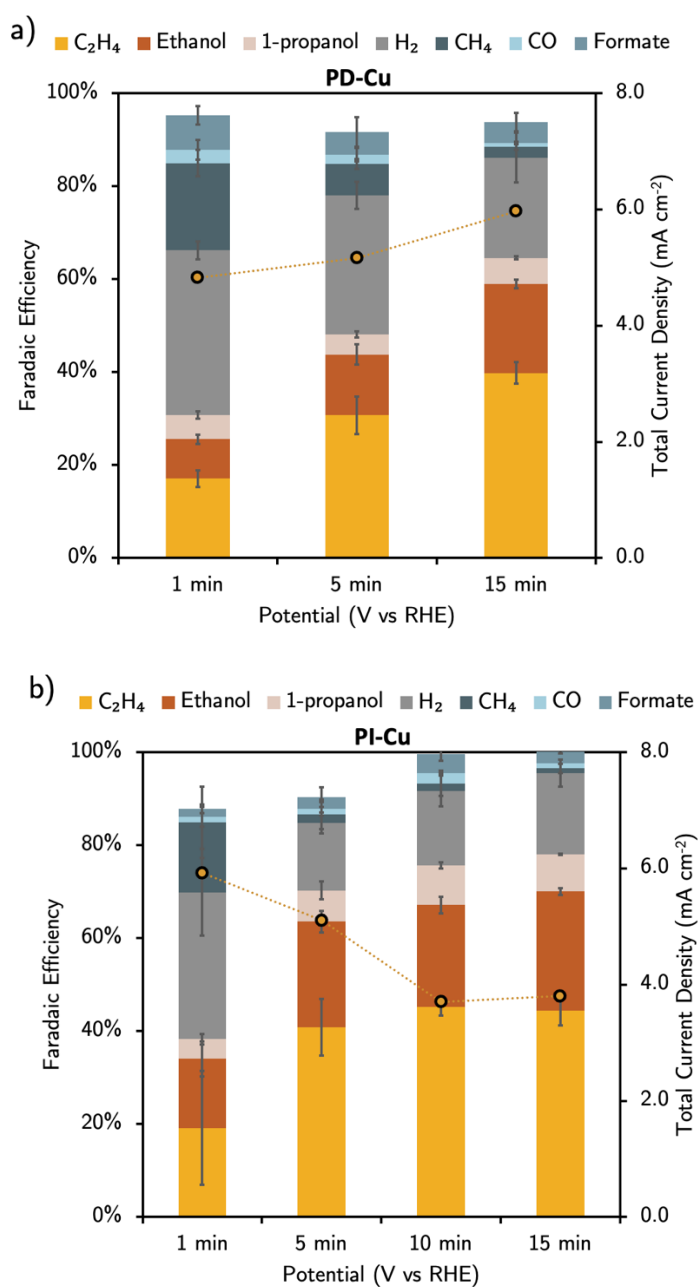


Figure S4.17: Deposition-time dependent selectivity and activity of a) PD-Cu and b) PI-Cu. The black/yellow circles correspond to the total current density of the catalyst shown on the second axis.

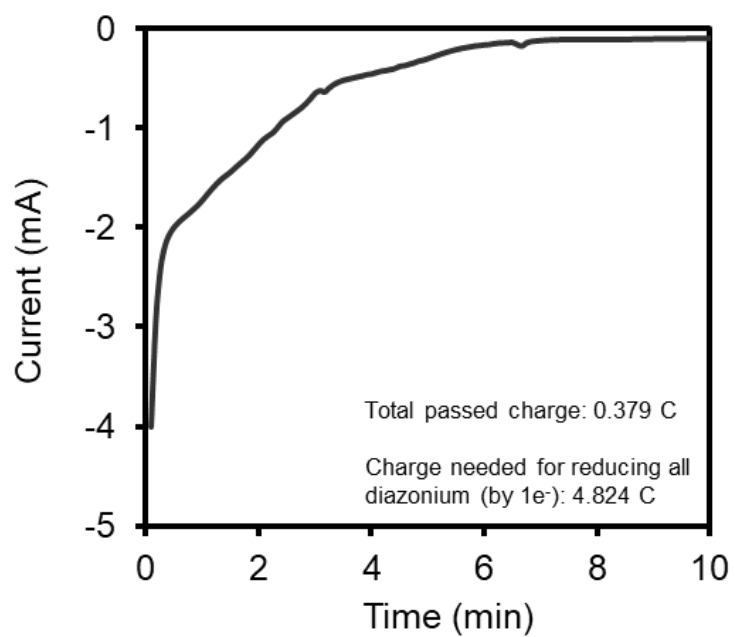


Figure S4.18. A representative current-time profile during electrodeposition of polyphenylene from phenyldiazonium.

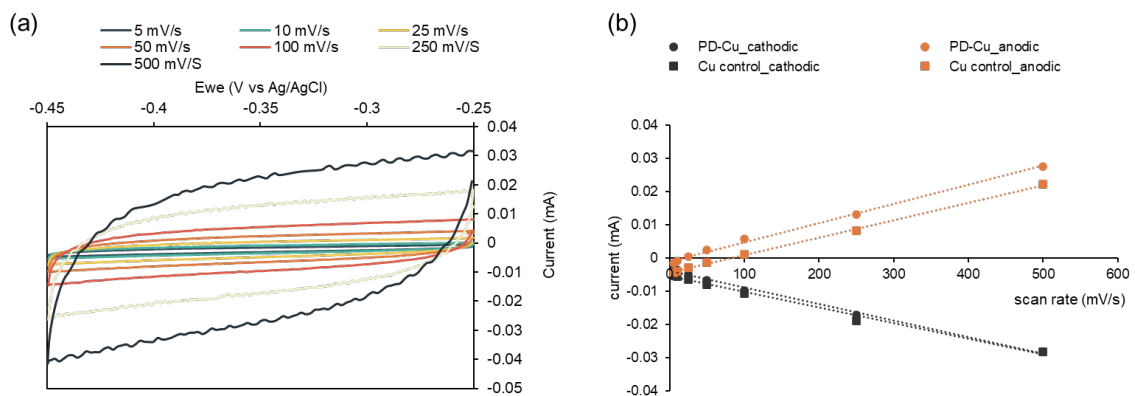


Figure S4.19. CV characterization of ECSA of PD-Cu and Cu control. (a) Representative CV traces of PD-Cu between -0.25 and -0.45 V vs Ag/AgCl at different scan rates. **(b)** Cathodic and anodic current value at -0.35 V vs Ag/AgCl of PD-Cu and Cu control versus scan rates. The slope of linear fitting represents double layer capacitance.

Table S4.9. Summary of ECSA values of PD-Cu and polished Cu as measured in CO₂-saturated 0.1 M KHCO₃

Sample	Run number	ECSA (F cm⁻²)
Polished Cu	1	8.38E-05
	2	4.69E-05
	3	5.57E-05
	4	6.24E-05
	5	4.58E-05
	6	2.64E-05
	7	5.54E-05
	8	5.89E-05
	Average	5.44±1.53E-05
PD-Cu	1	3.07E-05
	2	3.76E-05
	3	5.39E-05
	4	7.07E-05
	5	7.07E-05
	6	6.84E-05
	7	4.04E-05
	8	3.77E-05
	Average	5.13±1.57E-05
PI-Cu	1	5.48E-05
	2	4.74E-05
	3	3.83E-05
	Average	4.68±0.83E-05

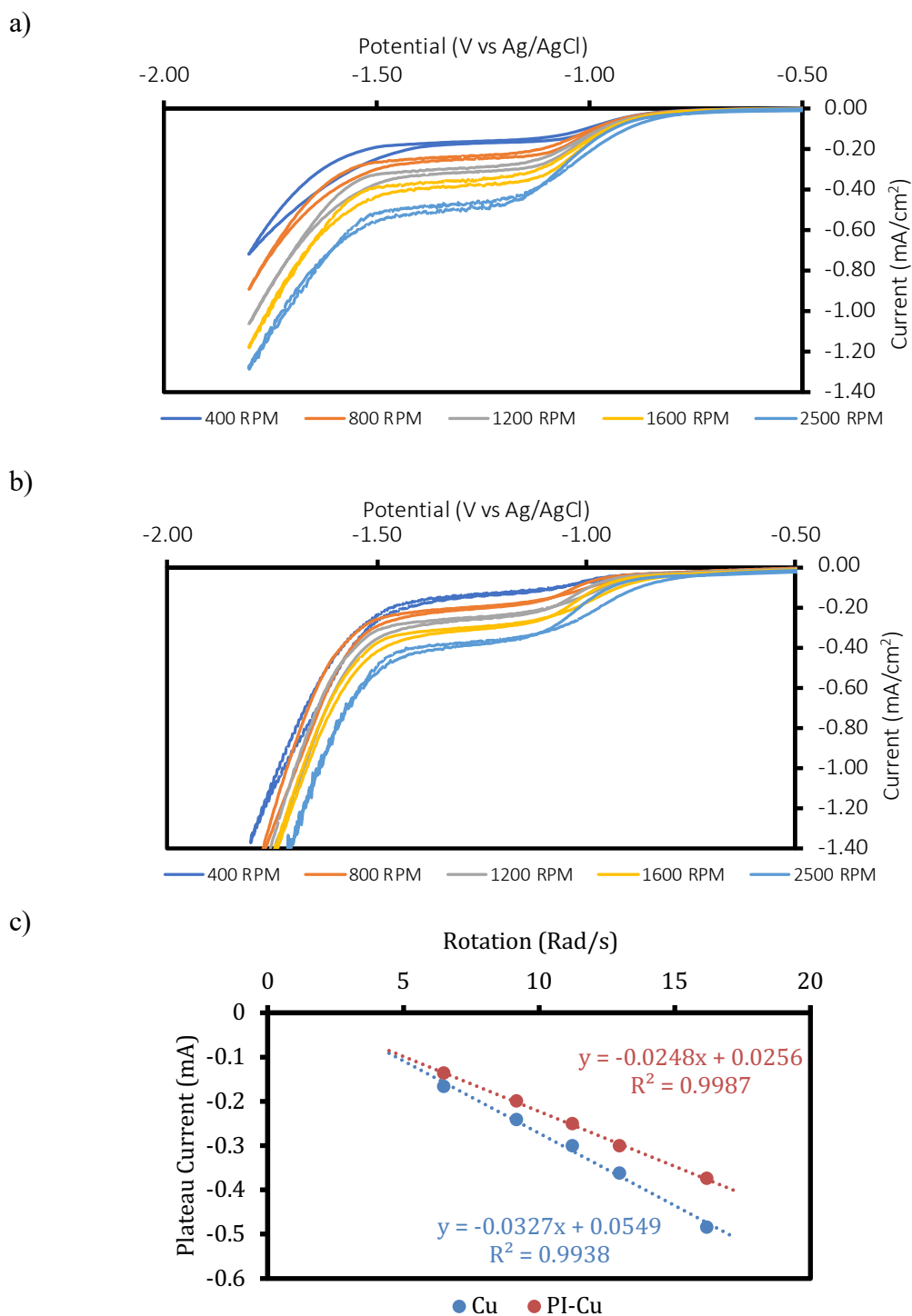


Figure S4.20: Example Rotating Disk Electrode Data. (a) Bare copper cyclic voltammetry data at five different rotation rates. **(b)** 30 min PI-Cu cyclic voltammetry data at five different rotation rates. **(c)** Plotting the plateau current versus rotation rate gives two linear functions, whose slopes are proportional to the proton diffusion coefficient.

Table S4.10. Summary of RDE values for PD-Cu and PI-Cu as measured in pH ~2.1 0.1 M KClO₄. Note: In Figure S18 we observe via SEM that there is significant delamination of the polyaryl layer in the 10-minute deposition cases. Due to the consistency of the 30-minute data, we expect that this data is further evidence regarding the increased robustness of the iodonium-based film.

Sample	Run number	Change in Proton Diffusion wrt bare Cu
PD-Cu (10-minute deposition)	1	118 %
	2	90 %
	Average	104 ± 14%
PI-Cu (10 min deposition)	1	90%
	2	117%
	3	110%
	Average	106 ± 13%
PI-Cu (30 min deposition)	1	66%
	2	75%
	3	84%
	Average	75 ± 9%

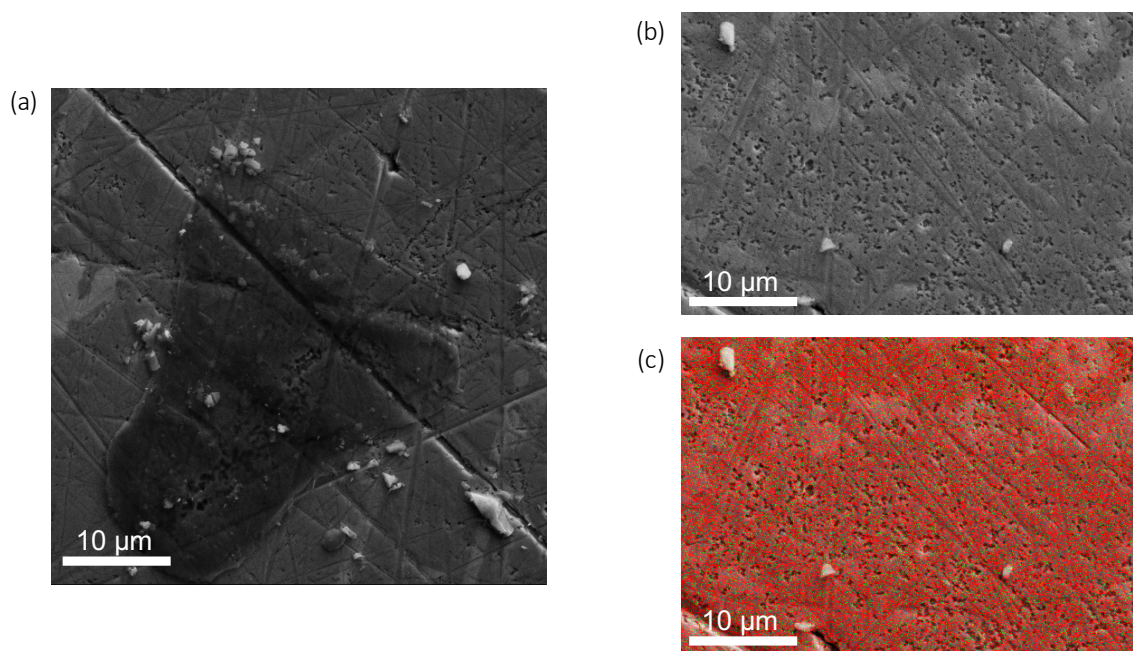


Figure S4.21: SEM of PD-Cu RDE post measurements. (a) The distinctive dark area in the center of the image corresponds to the charging of thick carbonaceous film on top of the electrode. **(b)** SEM image of a separate region of the electrode to probe whether a thinner film still exists on the surface. **(c)** EDX analysis indicates that there is 40.6 atomic % carbon, 57.2% copper, and 2.2% oxygen on the surface of the electrode (red-Cu, green-C). This suggests that the film may not have fully delaminated, but is thinned to an extent where proton diffusion is no longer inhibited.

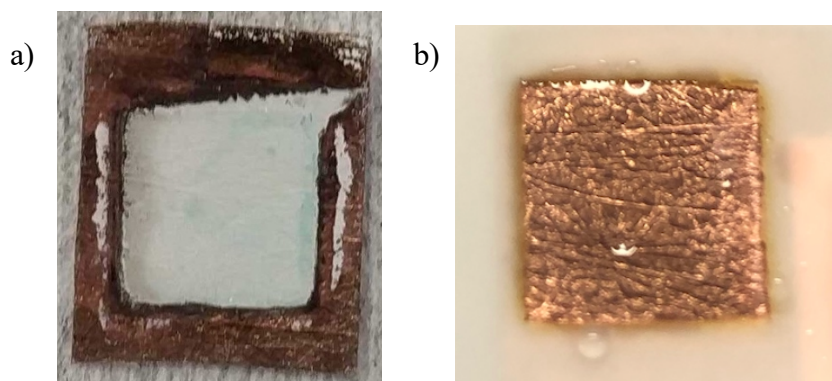


Figure S4.22: Visual comparison of a (a) post-electrolysis unmodified electrode versus a (b) PI-Cu GDE (white material around is a silicon gasket).

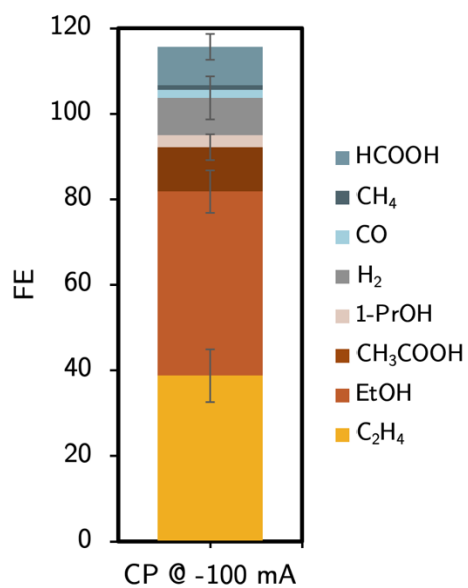


Figure S4.23: Average of three multiple 30 minute electrolyses at $-100\text{mA}/\text{cm}^2$, either using *in-situ* deposition or pre-deposition in 1 M KHCO_3 .

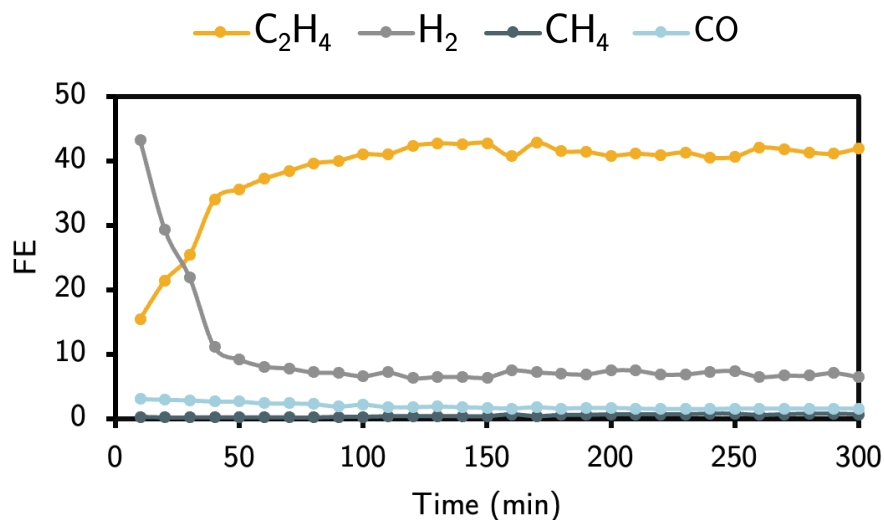


Figure S4.24: 6-hour electrolysis at -100 mA/cm^2 . The electrolyte pH was measured before and after electrolysis, with the beginning and ending pH being ca. 1 and 10, respectively.

Author's note:

The first three injections show poor selectivity due to rinsing the system with DI water between the pre-deposition of diphenyliodonium in 1.0 M KHCO_3 and beginning the electrolysis in $1 \text{ M H}_3\text{PO}_4$. This can be remedied, as in the case of Figure 6, by depositing in 1 M K^+ phosphate buffer and then immediately switching to the $1 \text{ M H}_3\text{PO}_4 / 1 \text{ M KCl}$ electrolyte.

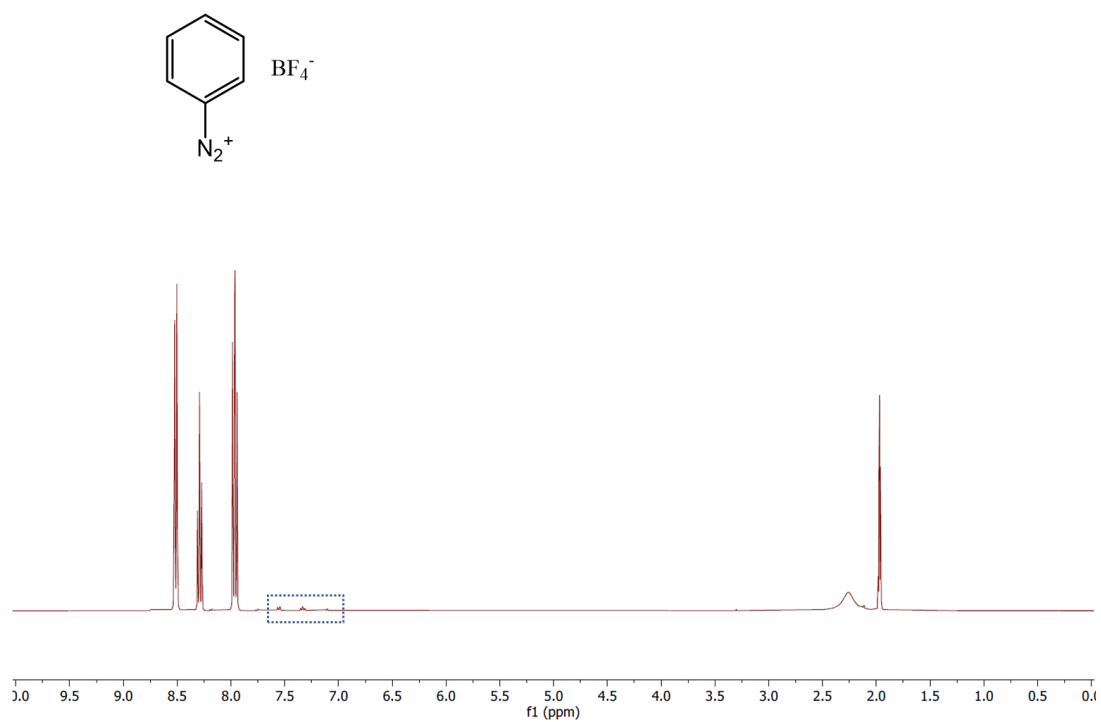


Figure S4.25. 1H -NMR of as-synthesized phenyldiazonium tetrafluoroborate in d_3 -acetonitrile. Extra peaks in the aromatic region are due to the slow decomposition of phenyldiazonium tetrafluoroborate (likely into fluorobenzene) in polar solvents.^{8,9}

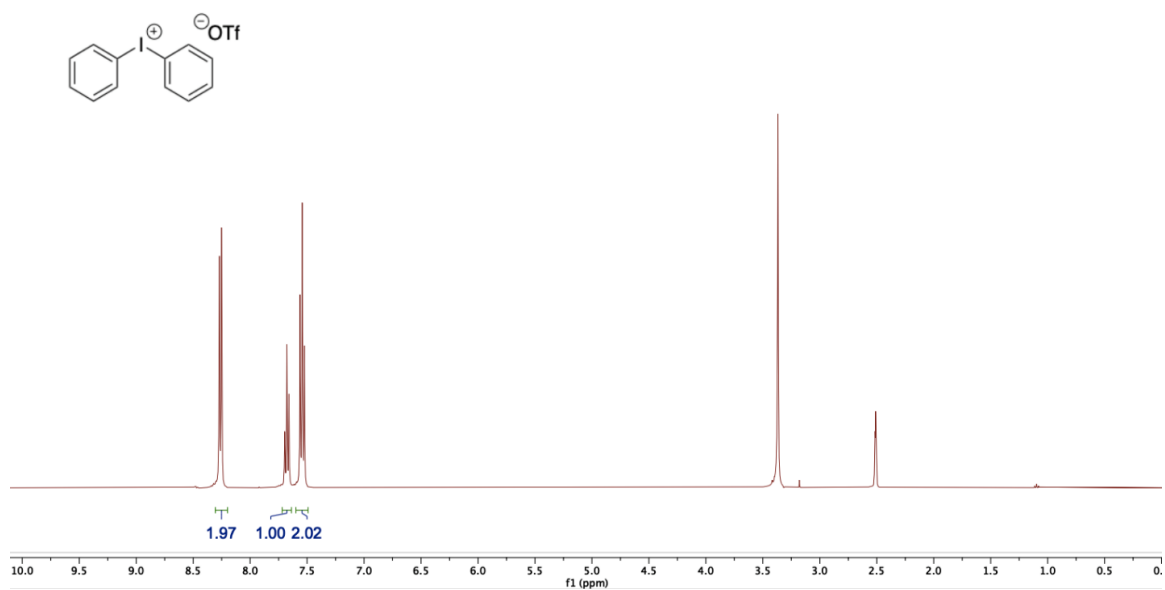


Figure S4.26. $^1\text{H-NMR}$ of as-synthesized diphenyliodonium triflate in $\text{d}_6\text{-DMSO}$. Extra peaks in the alkyl region correspond to water and solvent used in recrystallization.

References

- (1) Griбанov, P. S.; Topchiy, M. A.; Golenko, Y. D.; Lichtenstein, Y. I.; Eshtukov, A. V.; Terekhov, V. E.; Asachenko, A. F.; Nechaev, M. S. An Unprecedentedly Simple Method of Synthesis of Aryl Azides and 3-Hydroxytriazenes. *Green Chem.* **2016**, *18* (22), 5984–5988. <https://doi.org/10.1039/C6GC02379G>.
- (2) Pinson, J.; Podvorica, F. Attachment of Organic Layers to Conductive or Semiconductive Surfaces by Reduction of Diazonium Salts. *Chem. Soc. Rev.* **2005**, *34* (5), 429. <https://doi.org/10.1039/b406228k>.
- (3) Combellas, C.; Kanoufi, F.; Pinson, J.; Podvorica, F. I. Time-of-Flight Secondary Ion Mass Spectroscopy Characterization of the Covalent Bonding between a Carbon Surface and Aryl Groups. *Langmuir* **2005**, *21* (1), 280–286. <https://doi.org/10.1021/la048106l>.
- (4) Bielawski, M.; Olofsson, B. High-Yielding One-Pot Synthesis of Diaryliodonium Triflates from Arenes and Iodine or Aryl Iodides. *Chem. Commun.* **2007**, No. 24, 2521–2523. <https://doi.org/10.1039/B701864A>.
- (5) Adenier, A.; Combellas, C.; Kanoufi, F.; Pinson, J.; Podvorica, F. I. Formation of Polyphenylene Films on Metal Electrodes by Electrochemical Reduction of Benzenediazonium Salts. *Chem. Mater.* **2006**, *18* (8), 2021–2029. <https://doi.org/10.1021/cm052065c>.
- (6) Han, Z.; Kortlever, R.; Chen, H.-Y.; Peters, J. C.; Agapie, T. CO₂ Reduction Selective for C_{≥2} Products on Polycrystalline Copper with N-Substituted Pyridinium Additives. *ACS Cent. Sci.* **2017**, *3* (8), 853–859. <https://doi.org/10.1021/acscentsci.7b00180>.

- (7) Lee, S. Y.; Lyu, J.; Kang, S.; Lu, S. J.; Bielawski, C. W. Ascertaining the Carbon Hybridization States of Synthetic Polymers with X-Ray Induced Auger Electron Spectroscopy. *J. Phys. Chem. C* **2018**, *122* (22), 11855–11861. <https://doi.org/10.1021/acs.jpcc.8b02217>.
- (8) Abramovitch, R. A.; Saha, J. G. ARYLATION OF AROMATIC COMPOUNDS WITH BENZENEDIAZONIUM BOROFLUORIDE: NATURE OF THE ARYLATING SPECIES. *Can. J. Chem.* **1965**, *43* (12), 3269–3278. <https://doi.org/10.1139/v65-457>.
- (9) Ishida, K.; Kobori, N.; Kobayashi, M.; Minato, H. Decomposition of Benzenediazonium Tetrafluoroborate in Aprotic Polar Solvents. *Bull. Chem. Soc. Jpn.* **1970**, *43* (1), 285–286. <https://doi.org/10.1246/bcsj.43.285>.
- (10) Wuttig, A.; Surendranath, Y. Impurity Ion Complexation Enhances Carbon Dioxide Reduction Catalysis. *ACS Catal.* **2015**, *5* (7), 4479–4484. <https://doi.org/10.1021/acscatal.5b00808>.

Appendix 5

SUPPLEMENTARY INFORMATION FOR CHAPTER 5:
HYDRODYNAMICS CHANGE TAFEL SLOPES IN
ELECTROCHEMICAL CO₂ REDUCTION ON COPPER

Adapted from:

Watkins, N. B.; Schiffer, Z. J.; Lai, Y.; Musgrave, C. B. I.; Atwater, H. A.;
Goddard, W. A. I.; Agapie, T.; Peters, J. C.; Gregoire, J. M.
ACS Energy Lett. **2023**, *8* (5), 2185–2192.
10.1021/acseenergylett.3c00442.

Materials and Methods

All solvents and reagents were obtained from commercial sources and used as received, unless stated otherwise. Cu foils (99.999% Cu, 25 mm × 25 mm × 0.5 mm), potassium carbonate (99.995%), phenanthroline ($\geq 99\%$), and dibromoethane ($\geq 99\%$) were purchased from Sigma Aldrich. Carbon rods (99.999% C) were purchased from Strem Chemicals. Platinum foil (99.99% Pt, 25 mm × 25 mm × 0.05 mm), was purchased from Alfa Aesar. Natural abundance CO₂ (Research grade) was purchased from Airgas. Water was purified by a Nanopure Analytical Ultrapure Water System (Thermo Scientific) or a Milli-Q Advantage A10 Water Purification System (Millipore) with specific resistance of 18.2 MΩ·cm at 25 °C.

Prior to each use, copper foil was mechanically polished to a mirror-like finish using nanodiamond suspension (first 3 μm then 0.1 μm, Buehler) followed by rinsing in water and drying under a stream of nitrogen gas. The copper foil was then electropolished using a method similar to the one employed by Kuhl *et al.*: in an 85% phosphoric acid bath, +2.1 V versus a carbon rod counter electrode was applied to the Cu foil for 5 minutes and the foil was subsequently washed with copious amounts of ultra-pure water and dried under a stream of nitrogen gas. Prior to each use, platinum foil was washed with water and flame-annealed using a butane torch for 10 s. CO₂-saturated potassium bicarbonate electrolyte (KHCO₃, 0.1 M) was prepared by sparging an aqueous solution of potassium carbonate (K₂CO₃, 0.05 M) with CO₂ for at least 1 h prior to electrolysis.

Cu thin film electrocatalysts were fabricated using DC magnetron sputtering of a 2'' Cu metal target at 50 W in 6 mTorr Ar onto a 100 mm-diameter Si wafer with an approximately 170 nm SiO₂ diffusion barrier and 10 nm Ti adhesion layer, using a

previously described sputter system with 10^{-5} Pa base pressure.¹ After deposition, the films were stored in a nitrogen purge box until the day of electrochemical testing, although no other catalyst treatment was performed prior to electrocatalyst screening. The Cu-X (X: Co, Zn, Mn, In) thin film electrodes were deposited under similar conditions from elemental metal targets with DC power adjusted to obtain designed composition in the wafer center. All the metal targets were pre-cleaned in the presence of 6 mTorr Ar for 10 min to remove any contaminants from the target surface. The non-confocal sputtering geometry provided a continuous composition gradient across the Si wafer with the composition variation within each 5 mm diameter electrode being less than 1% for the most Cu-rich catalysts and about 2% for the most Cu-poor catalysts.

Synthetic Procedures

Synthesis of N,N'-ethylene-phenanthroline dibromide (**1-Br₂**) In a round bottom flask charged with a magnetic stir bar, phenanthroline (500 mg, 2.8 mmol, 1 equiv.) was dissolved in dibromoethane (5 mL, 67.4 mmol, > 24 equiv.) and the final mixture was heated to 110 °C for 18 h. The precipitate formed was collected by filtration and washed with hexane (3 x 10 mL) and acetone (3 x 10 mL) to afford the final product. Yield: 970 mg (94 %, 2.6 mmol). ¹H and ¹³C NMR spectra were in accordance with reported values.²

Electrochemical Measurements

All H-cell electrochemical experiments were carried out using a Biologic VMP3 multichannel potentiostat with copper foil as the working electrode and a platinum foil as the counter electrode. The cathode compartment was separated from the anode compartment by

a Selemion AMV anion-exchange membrane (AGC Engineering Co.). All potentials were measured versus a leakless Ag/AgCl reference electrode (Innovative Instruments) with an outer diameter of 5 mm that was inserted into the cathode compartment. The reference electrode was calibrated against H^+/H_2 on Pt in a 0.5 M sulfuric acid solution (0 V vs. standard hydrogen electrode).

Potentiostatic electrochemical impedance spectroscopy (PEIS) measurements were carried out prior to each electrolysis experiment to determine the Ohmic resistance of the flow cell. The impedance measurements were carried out at frequencies ranging from 100 Hz to 200 KHz to measure the solution resistance. A Nyquist plot was plotted and in the high-frequency part a linear fit was performed, and the axis intersection was identified, the value of which represents the Ohmic resistance of the cell. Typical values of the resistance range from 45 to 60 Ω .

All chronoamperometric experiments (unless stated otherwise) were performed for 30 min at 25 °C using CO_2 -saturated 0.1 M $KHCO_3$ as electrolyte. The potentiostat was set to compensate for 85 % of the Ohmic drop, with the remaining 15 % being compensated for after the measurements. The effluent gas stream coming from the flow cell (10 mL/min) was flowed into the sample loops of a gas chromatograph (GC-FID/TCD, SRI 8610C, in Multi Gas 5 configuration) equipped with a HayeSep D column. Methane, ethylene, and carbon monoxide were detected by a methanizer-flame ionization detector (FID) and the hydrogen was detected by a thermal conductivity detector (TCD). Every 10 minutes, 1 mL of gas was sampled to determine the concentration of gaseous products. Liquid products were quantified by HPLC. Liquid products were only quantified in ANEC because the concentrations in the recirculation H-cells were too low due to the requisite volume for recirculation.

COMSOL Modeling Information

The governing equations (material balances and fluid dynamics) were used within the Multiphysics Module and were solved with the general solver in COMSOL Multiphysics 5.6 with default tolerances. The modeling domain was discretized with a nonuniform physics-controlled mesh generated by COMSOL. To aid with convergence, all fluid dynamics systems were first solved using the turbulence - model, then the result of that solution was used with the Low Re - turbulent model, and finally the results of the Low Re model were used as initial conditions for a laminar fluid dynamics model. Inlet velocity boundary conditions were set to fully developed flow with the flow rate set to experimental values. Outlet boundary conditions were set to fully developed flow with an average pressure of 0 Pa. For the flux calculations, the concentration at the electrode was set to 1 mM and the inlet concentration was set to 0 mM. The diffusion constant was set to $2.7E^{-9} \text{ m}^2/\text{s}$.³

LOWESS Fitting Function

For Figures 5.3 and 5.5 in the main text, lines to guide the eye and provide a continuous function of the data are plotted. These lines are calculated via a Locally Weighted Scatterplot Smoothing (LOWESS) model in Python. Essentially, for each x-value in the dataset, a “smoothed” y-value is calculated by taking a weighted linear fit of the nearest n data points. This value of n is, by default in the Python implementation, $\frac{2}{3}$ of the total data points. The weights for the linear fit are from a tricube function. Subsequent iterations of the refitting can be done with altered weights according to the residuals of the previous fitting. See Python’s

statsmodels.nonparametric.smoothers_lowess.lowess function for details on implementation and usage. In the case of Figure 5.3, in addition to a fitting, a qualitative metric for error bars on the data is shown. This error was calculated by taking a random sample of data points and then fitting the LOWESS to that sample. The average of 500 such samples is taken to represent the “error” qualitatively of the fit. The following Python code was used to generate the error from this fitting. Note that although this fitting procedure is “model-free”, there are still parameters that we selected, including number of iterations, fraction of data points to fit, etc. Changing these parameters will quantitatively change the fit (primarily the error bars), but will not qualitatively change the results.

```
def smooth(x, y, xgrid):
    samples = np.random.choice(len(x), len(x), replace=True)
    y_s = y[samples]
    x_s = x[samples]
    y_sm = sm.nonparametric.lowess(y_s,x_s,
                                   return_sorted = False, frac=0.5)
    # regularly sample it onto the grid
    y_grid = scipy.interpolate.interp1d(x_s, y_sm,
                                         fill_value='extrapolate')(xgrid)
    return y_grid

def lowess_std(x,y,K = 500):
    xgrid = np.linspace(x.min(),x.max())
    smooths = np.stack([smooth(x, y, xgrid) for k in range(K)]).T
    mean = np.nanmean(smooths, axis=1)
    stderr = np.nanstd(smooths, axis=1, ddof=0)
    return (xgrid,mean,stderr)
```

For Figure 5.5, the Faradaic efficiencies for the various gaseous products were fit using the LOWESS model as implemented in Python. The raw data points are summed up and plotted, i.e., first the FE toward methane is plotted, then the sum of FEs toward methane and ethylene is plotted as “ethylene”, etc. A similar procedure is used to sum up the smoothed fits and label them on the plot.

Cell Design

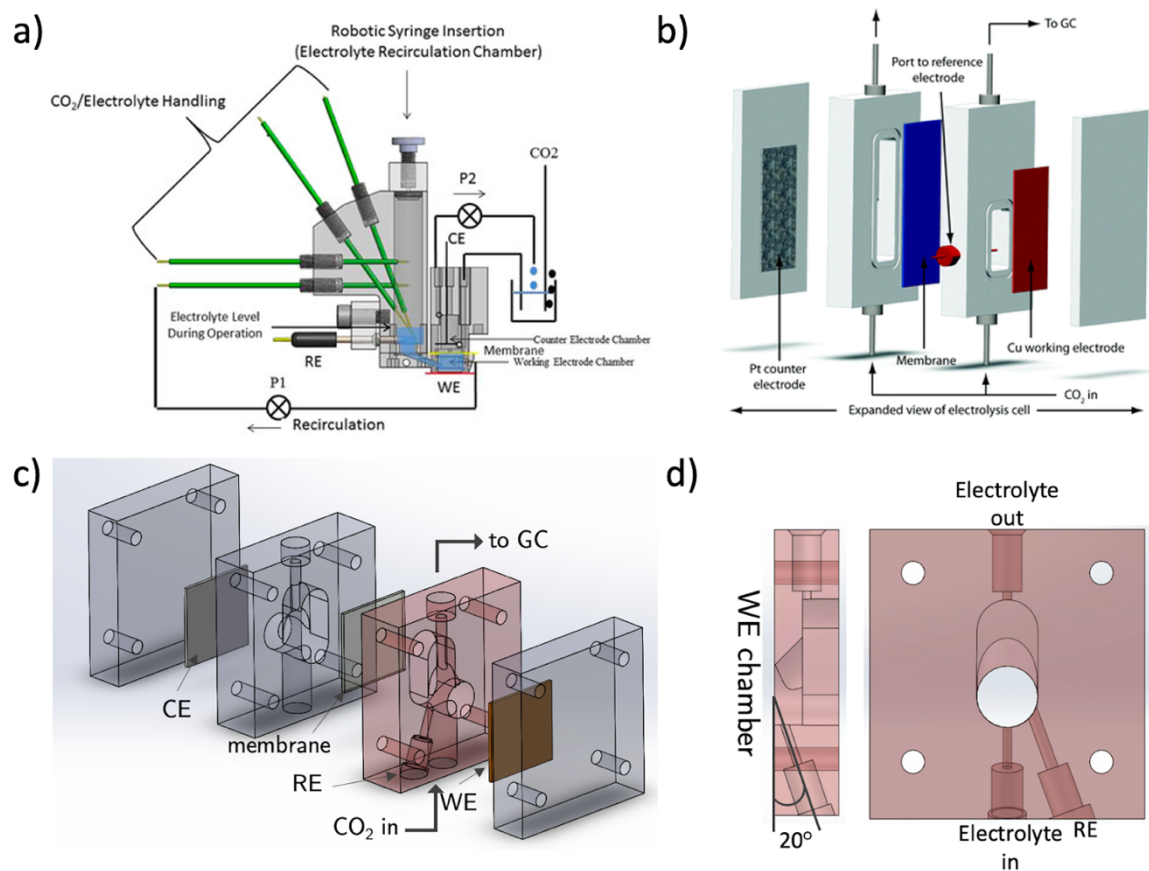
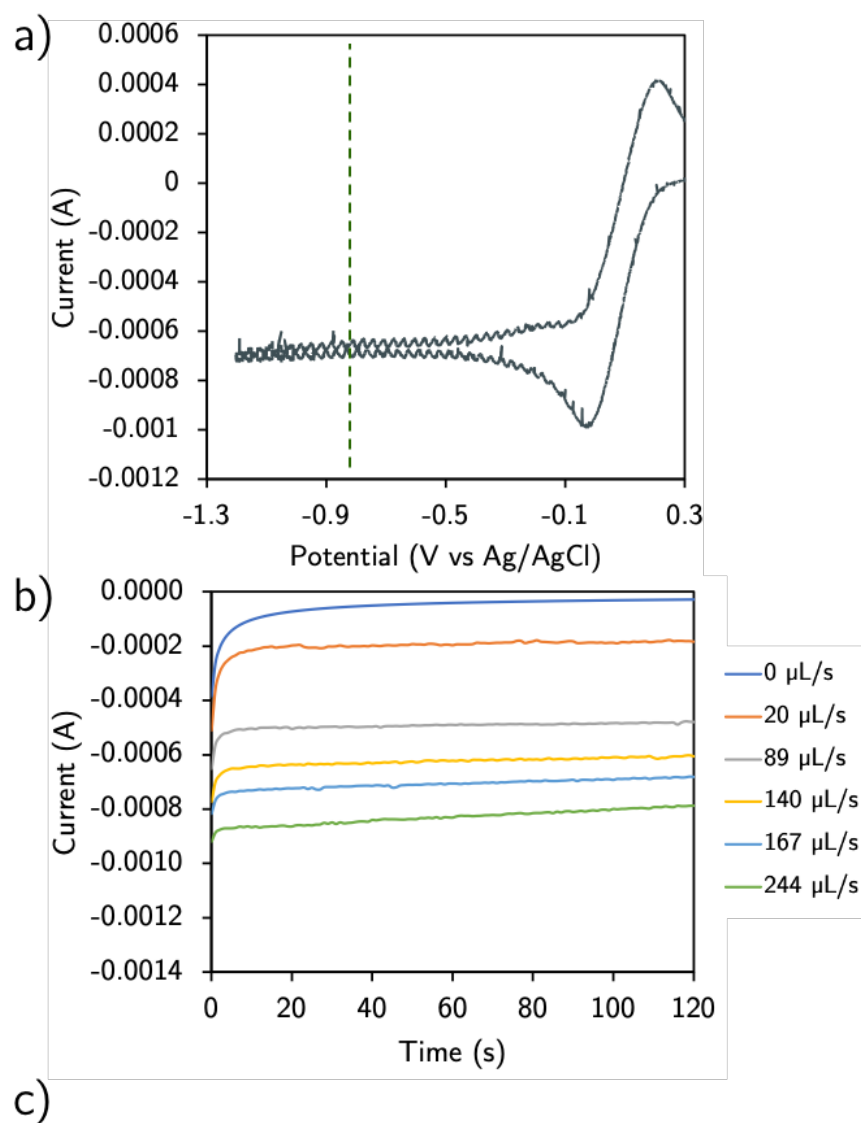


Figure S5.1: **a)** A schematic of ANalytical and ElectroChemistry (ANEC), which is an analytical electrochemistry system previously published by our group that can efficiently detect a wide range of CO₂R products.⁴ **b)** A schematic of the sparged H-cell used by Kuhl *et al.*, whose schematic is reproduced herein.⁵ **c)** The H-cell used for parallel flow experiments herein is a modification of that used by Ager *et al.*⁶ **d)** The angled H-cell is similar to that of the cell designed by Ager *et al.*, but with the bottom inlet adjusted to face the electrode surface at a 20° angle.

Boundary Layer Experiments



$$\delta_{BL} = \frac{F \cdot D_{\text{Fe}(\text{CN})_6^{3-}} \cdot C^*_{\text{Fe}(\text{CN})_6^{3-}}}{i_{SS}}$$

Figure S5.2: These experiments were performed according to section SI-4 from Clark et al.⁷ Sample data with ANEC, where a) a CV is initially performed to determine the mass transport limited regime, and then a potential is chosen (indicated by the dashed line) for subsequent constant potential experiments to determine the boundary layer at different recirculation rates. c) The boundary layer was calculated using the equation below, where F is Faraday's constant, $D[\text{Fe}(\text{CN})_6^{3-}]$ is the diffusivity of the ferricyanide ion ($0.720 \times 10^{-5} \text{ cm}^2 \text{ s}^{-1}$), $C^*[\text{Fe}(\text{CN})_6^{3-}]$ is the concentration of ferricyanide ion in the bulk of the electrolyte (10 mM), and i_{SS} is the steady-state current.

Table S5.1: Cells and their associated boundary layer thicknesses.

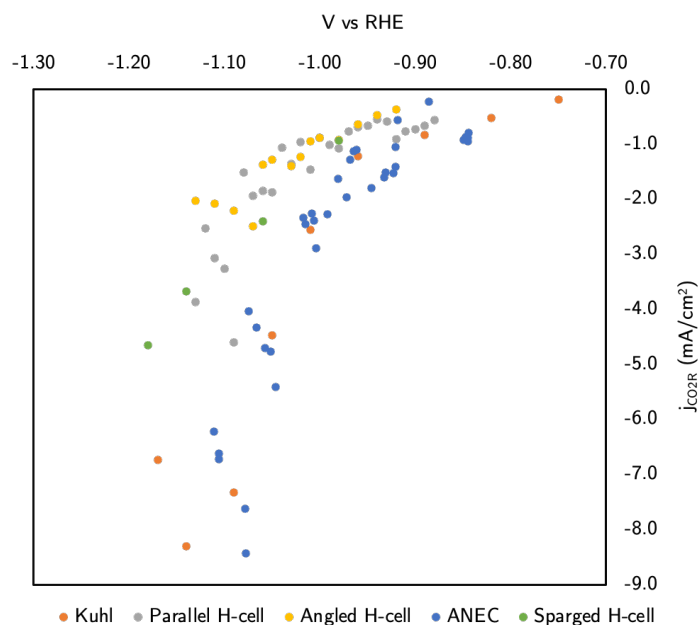
Cell Geometry (flow rate)	Experimental Boundary Layer Thickness (μm)	COMSOL Boundary Layer Thickness (μm)	Ethylene Tafel slope (mV/dec)
Ager et al. H-cell (20 sccm)	$177.9 \pm 21.6^*$	–	99.0
Parallel H-cell (280 $\mu\text{L/s}$)	106.9	242	94.9
Angled H-cell (280 $\mu\text{L/s}$)	33.4	128	66.1
ANEC (140 $\mu\text{L/s}$)**	36.2	57	39.2

* The average and associated error for 6 separate experiments

** 140 $\mu\text{L/s}$ is the typical flow rate for ANEC experiments

CO₂ reduction partial current densities at different mass transport

a.



b.

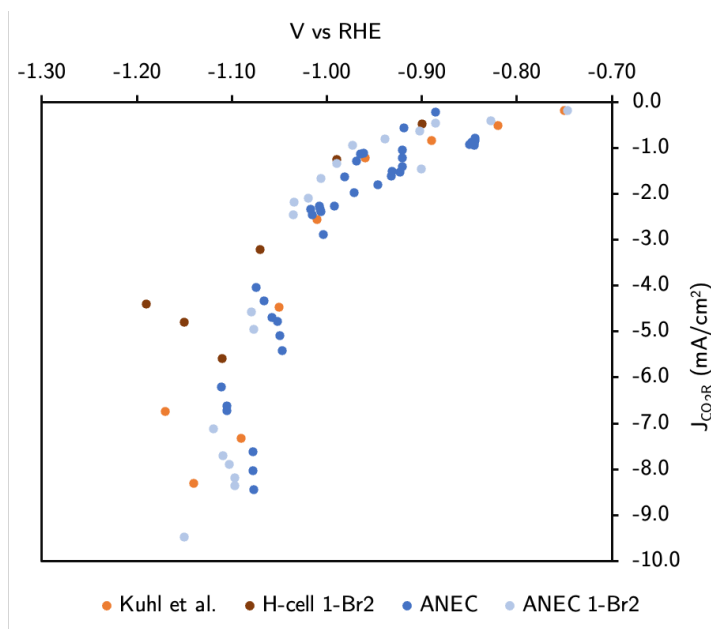


Figure S5.3: The partial current density towards CO₂ reduction products does not greatly change between a) cells at different convective ratios or b) with the addition of **1-Br₂**. The parallel and angled cells have slightly lower current densities as compared to ANEC or Kuhl, but are comparable to that of sparged H-cell Cu control data published previously in our own group.² This change may be attributable to the type of polycrystalline copper used in each experimentation.⁸

Potential-dependent selectivity data for all cells

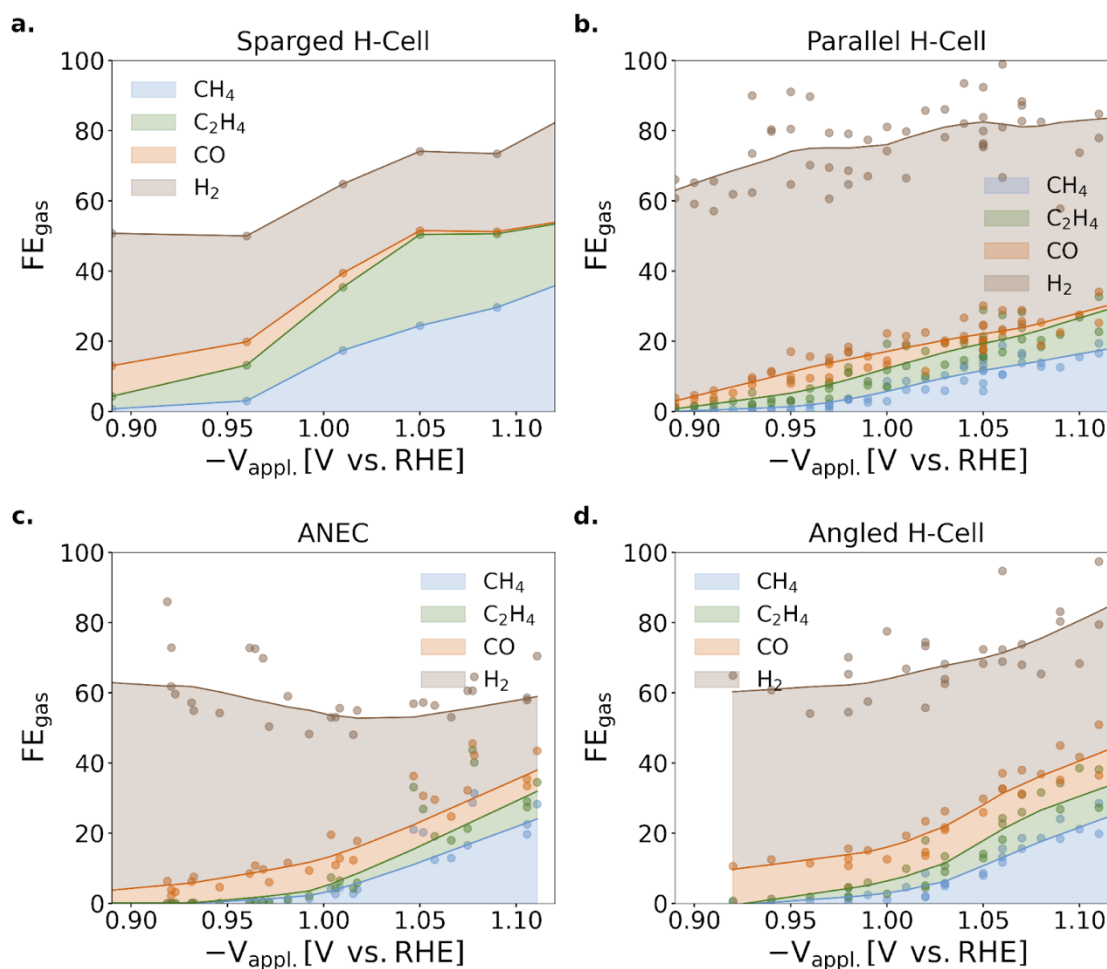


Figure S5.4: The distribution of gaseous products are shown as stack plots for the a) sparged H-cell, b) parallel H-cell, c) ANEC, and d) angled H-cell. The product distributions are shown with smooth trend lines calculated using LOWESS (see page 4). Each data point corresponds to an individual experiment, with the exception of the Sparged H-cell data, reproduced from [5], which is an average of three experiments.

Methane Bayesian Statistics Summary

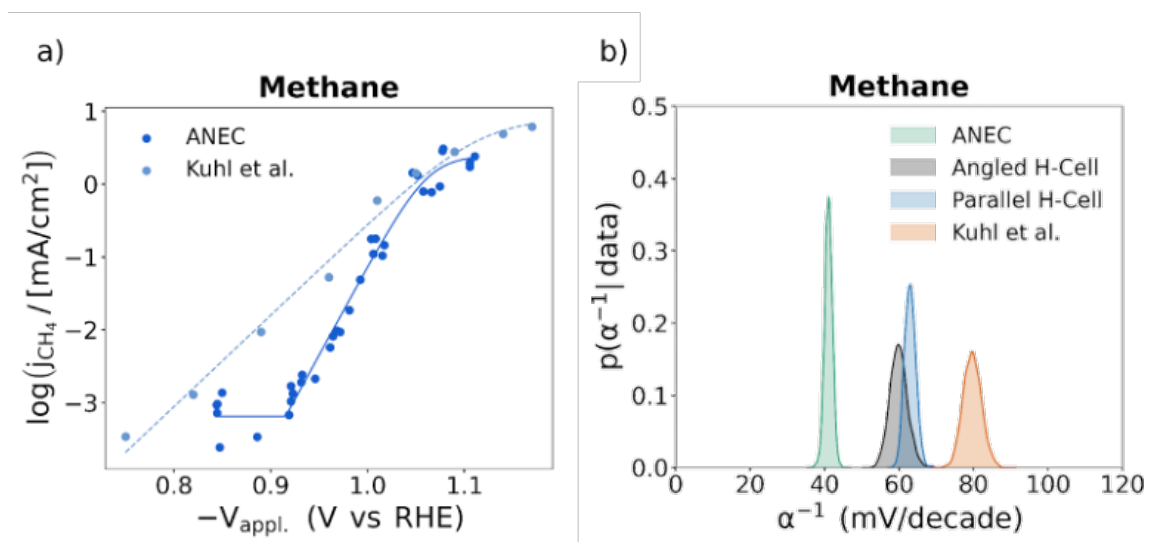


Figure S5.5: Tafel plots for a) methane from ANEC and Kuhl, et al.⁵ A small plateau exists on the bottom of each ANEC plot due to the noise floor of the instrument. All ANEC data points are single experiment values whereas Kuhl, et al. are the averages of three independent experiments. b) Probability density curves for methane Tafel slope values using Bayesian statistics for each cell geometry investigated.

Discussion Regarding Methane vs Ethylene Tafel

In Surendranath et al., their analysis indicates that ethylene will have a second order dependence at low CO coverage and zeroth order at high CO coverage, and that methane will have a limiting-to-zero dependence at high CO coverage and first order dependence at low CO coverage.⁹ Based on their experimental results, their electrochemical conditions of an ethanol-based electrolyte at -35°C provides a sufficiently high CO coverage at all pCO to realize the zeroth-order relationship for ethylene and limiting-to-zero dependence for methane. We believe that we are operating in a regime with low surface coverage of CO due to the mass transport removing CO from the surface; in this regime, we expect there to be a second order dependence on CO for ethylene and first order for methane. As a result, the sensitivity of the Tafel slope to local [CO] concentration should be higher for methane than ethylene, which is what we observe.

Ethylene full Bayesian probability distributions

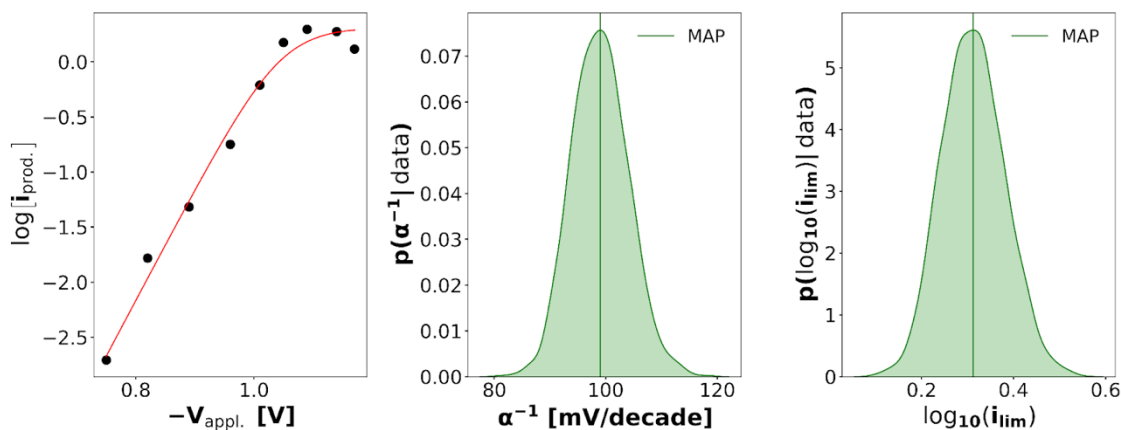


Figure S5.6. Bayesian analysis of the data from Kuhl et al. Data and mean *a posteriori* (MAP) fit are shown on left. Probability distributions for the slope and limiting current are shown with MAP drawn.

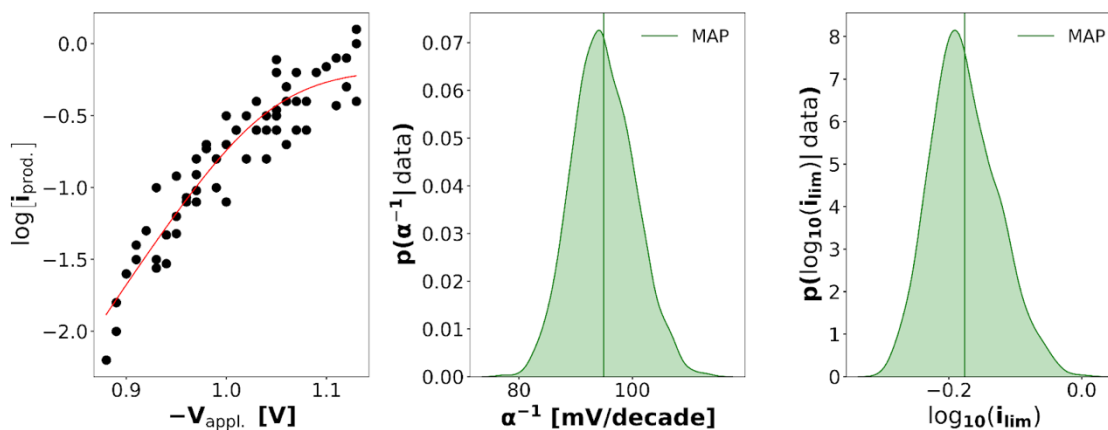


Figure S5.7. Bayesian analysis of the data from parallel flow H-Cell and mean *a posteriori* (MAP) fit are shown on left. Probability distributions for the slope and limiting current are shown with MAP drawn.

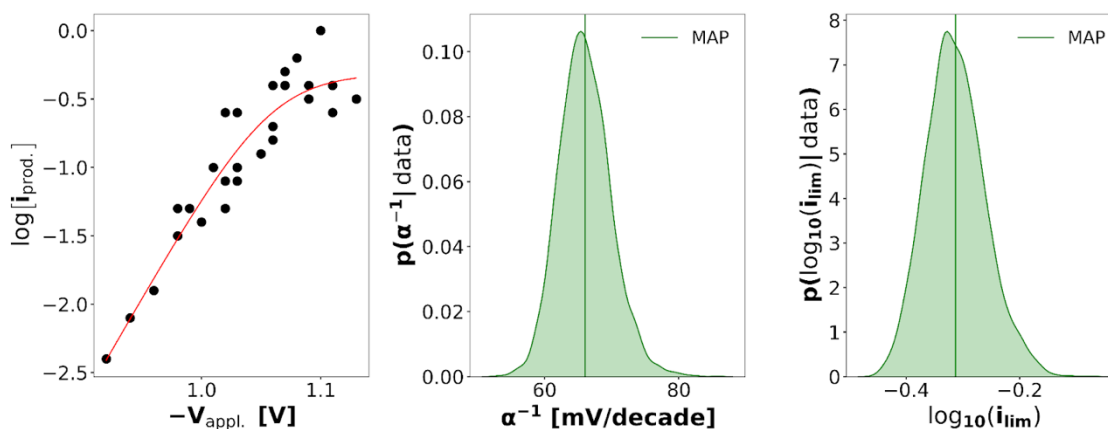


Figure S5.8. Bayesian analysis of the data from angled flow H-Cell and mean *a posteriori* (MAP) fit are shown on left. Probability distributions for the slope and limiting current are shown with MAP drawn.

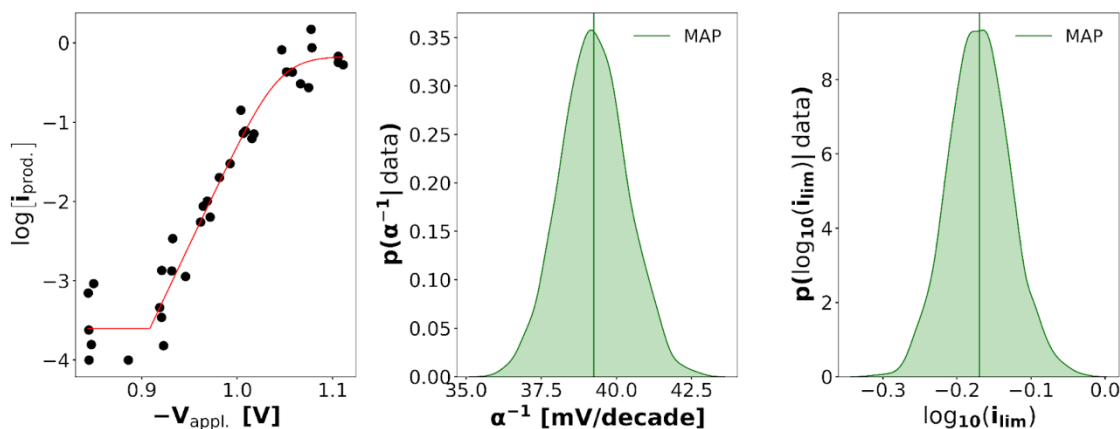


Figure S5.9. Bayesian analysis of the data from ANEC cell and mean *a posteriori* (MAP) fit are shown on left. Probability distributions for the slope and limiting current are shown with MAP drawn. Not shown is the probability distribution for the plateau at the bottom. This plateau is a simple “kink” in the system representing the lower detectability limit of the instruments.

Methane full Bayesian probability distributions

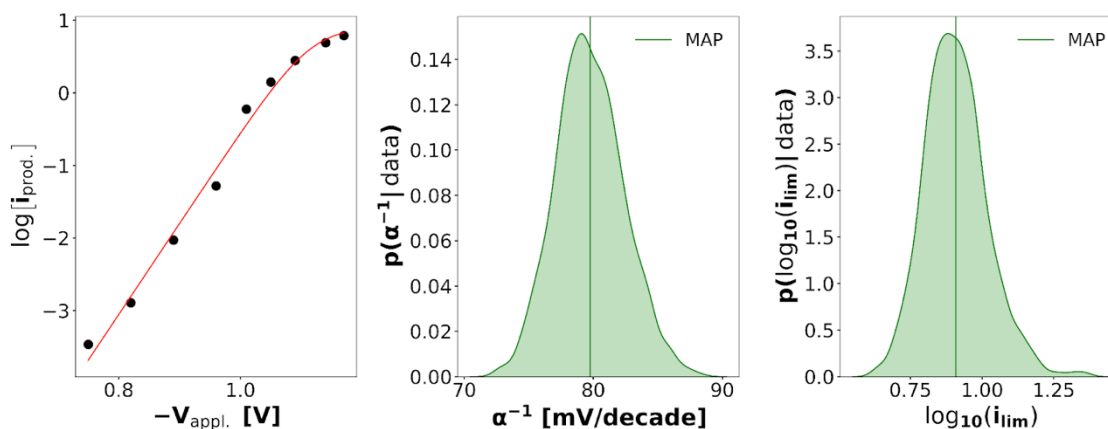


Figure S5.10. Bayesian analysis of the data from Kuhl et al. Data and mean *a posteriori* (MAP) fit are shown on left. Probability distributions for the slope and limiting current are shown with MAP drawn.

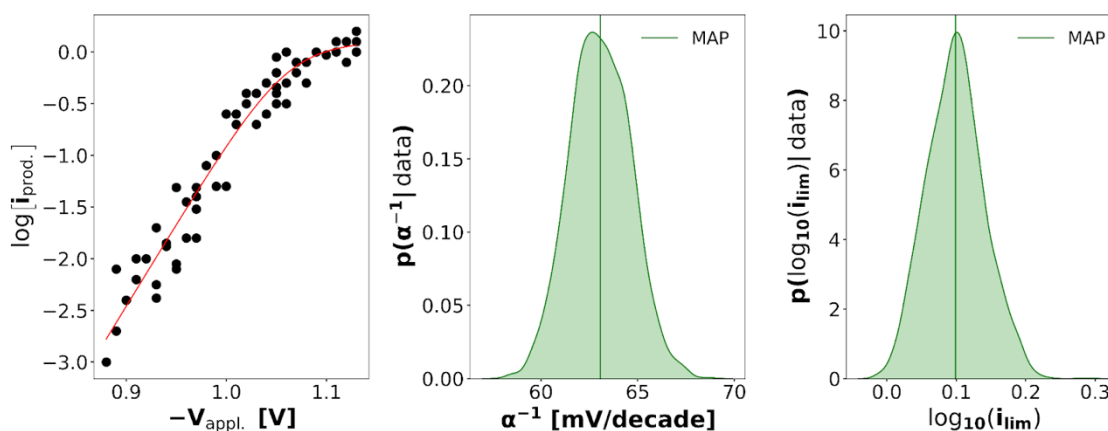


Figure S5.11. Bayesian analysis of the data from parallel flow H-Cell and mean *a posteriori* (MAP) fit are shown on left. Probability distributions for the slope and limiting current are shown with MAP drawn.

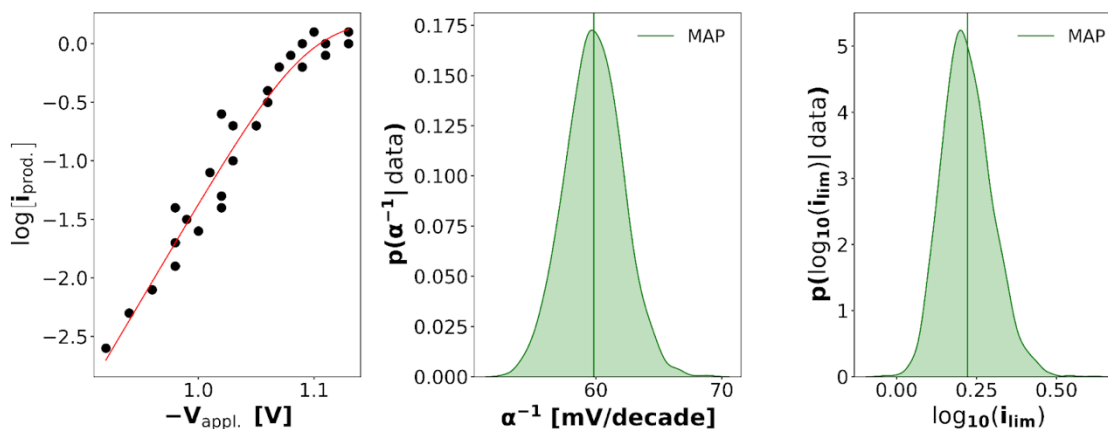


Figure S5.12. Bayesian analysis of the data from angled flow H-Cell and mean *a posteriori* (MAP) fit are shown on left. Probability distributions for the slope and limiting current are shown with MAP drawn.

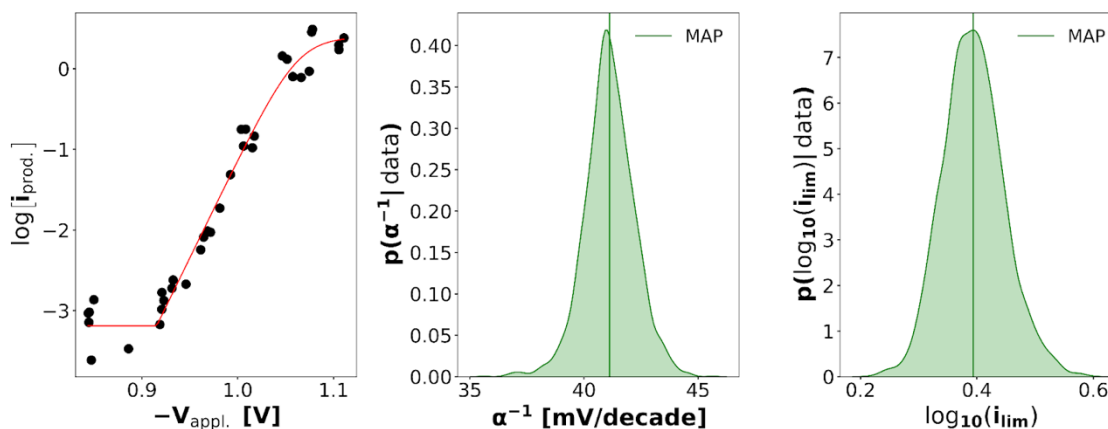


Figure S5.13. Bayesian analysis of the data from ANEC cell and mean *a posteriori* (MAP) fit are shown on left. Probability distributions for the slope and limiting current are shown with MAP drawn. Not shown is the probability distribution for the plateau at the bottom. This plateau is a simple “kink” in the system representing the lower detectability limit of the instruments.

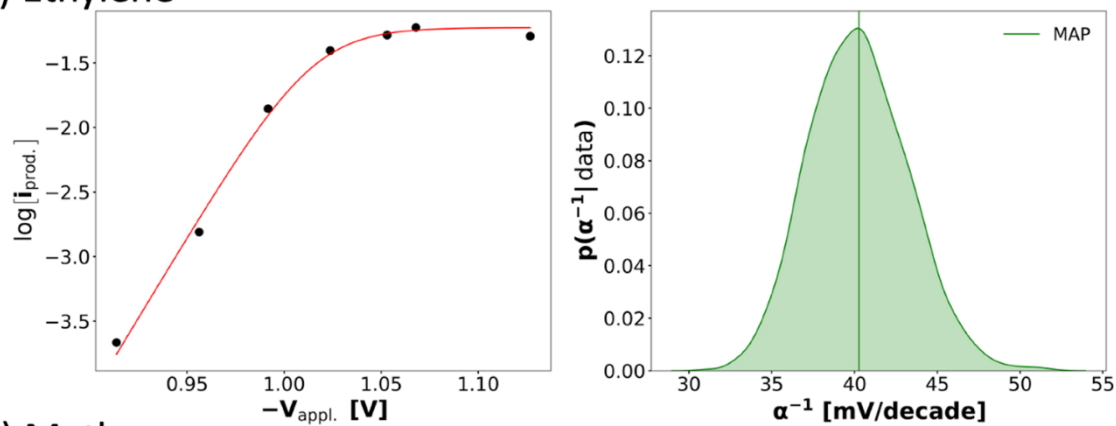
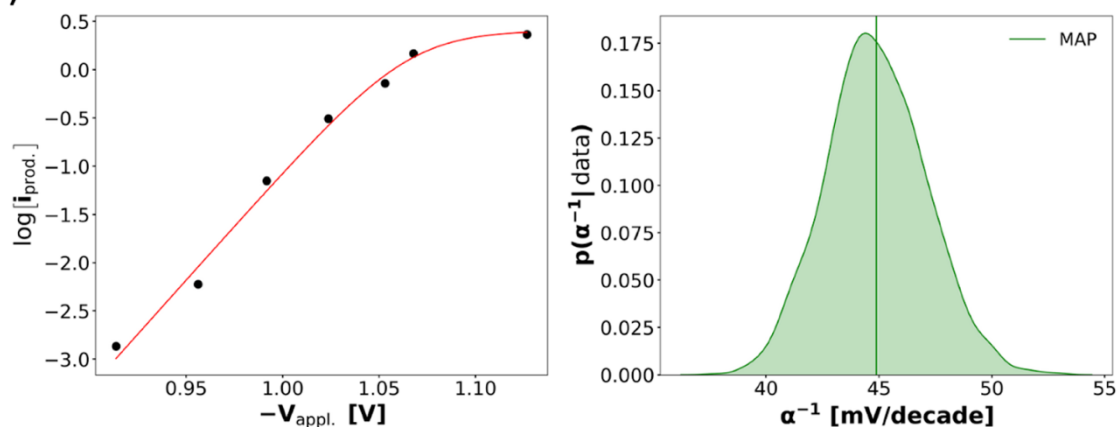
0.25 M KHCO₃ Bayesian Statistics Summary for Ethylene and Methane**a) Ethylene****b) Methane**

Figure S5.14: Tafel plots for a) ethylene and b) methane from ANEC with 0.25 M KHCO₃ with their mean *a posteriori* (MAP) fit shown on left. Probability distributions for the slope are shown with MAP drawn on the right.

Molecular Dynamics Discussion

All molecular dynamics calculations were performed using the Large-scale Atomic/Molecular Massively Parallel Simulator (LAMMPS) software.¹⁰ Valence (bond, angle, dihedral), electrostatic, and van-der-waals potentials were modeled by the Universal Force Field (UFF).¹¹ We began all simulations by a steepest descent minimization followed by a conjugate gradient minimization. The cell was then heated at constant volume (NVT ensemble) from 1 K to the desired temperature over the period of 10 ps via the Nose-Hoover thermostat. The cell was then maintained at the desired temperature (again NVT) for 2 ns to allow the system to reach equilibrium.

After 2 ns of constant-temperature NVT dynamics, the 2-Phase Thermodynamics (2PT) method was used to calculate CO diffusion coefficients (D_{CO}).¹² In essence, 2PT calculates the velocity autocorrelation function (VACF) and then integrates the VACF over time to yield D_{CO} . The VACF was integrated over a period of 20 ps in order to achieve proper convergence. For all cases, D_{CO} was averaged over 6 individual calculations to ensure adequate sampling.

Pure water systems included 282 water molecules and a single CO molecule. The volume was chosen to match the experimental density of pure water. Systems with additive featured 8 additive molecules, 200 waters, and a single CO molecule. Here the volume was kept the same as the system with no additive.

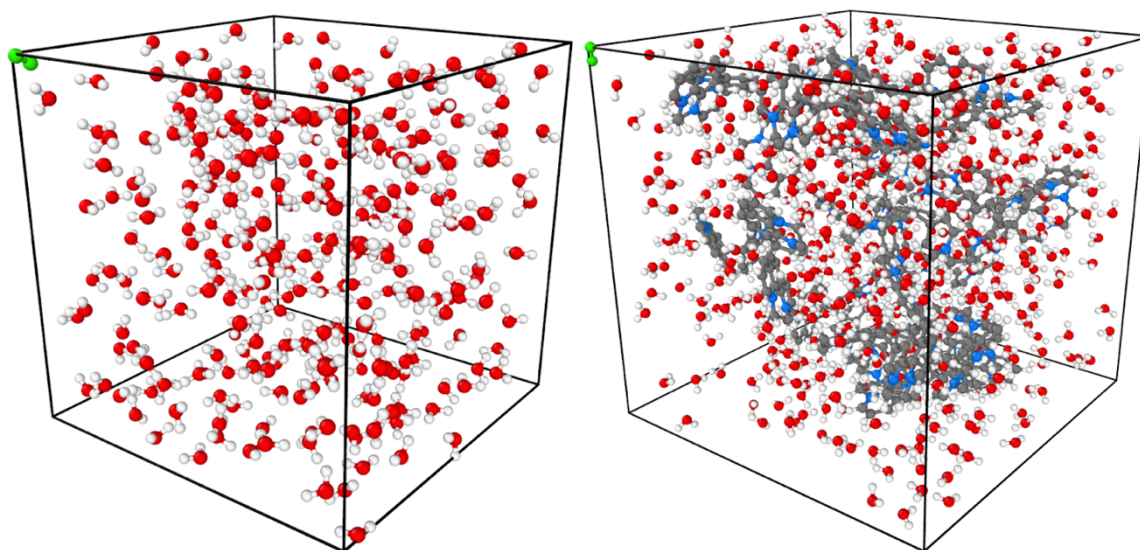


Figure S5.15: Simulation boxes for pure water (left) and additive (right) systems. White atoms are hydrogen, red are oxygen, grey are carbon, and blue are nitrogen. CO molecules are colored green for clarity.

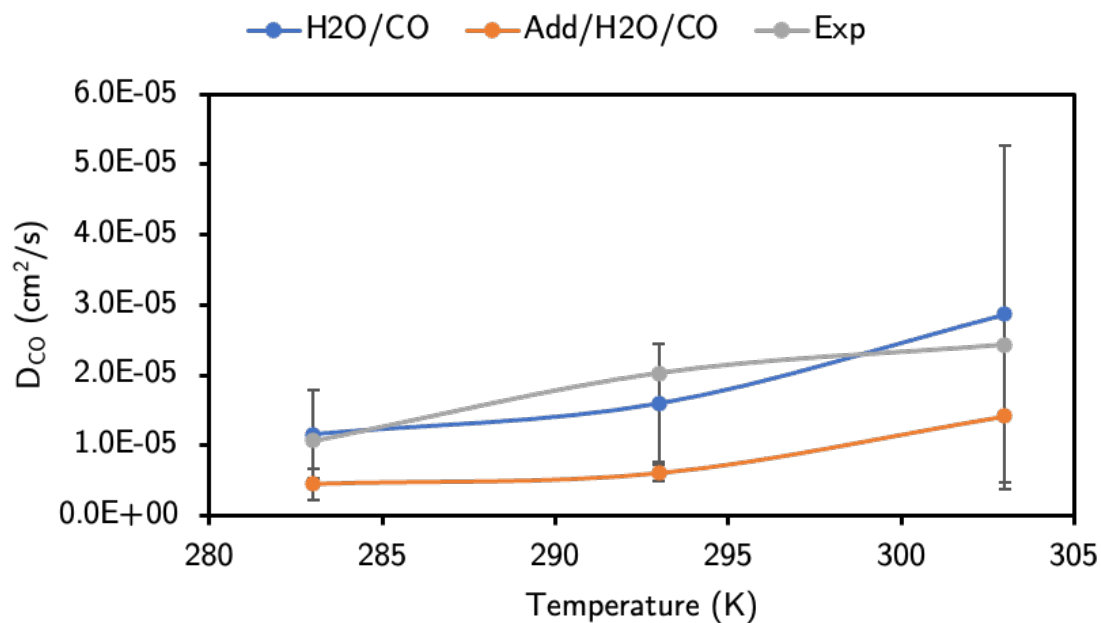


Figure S5.16: CO diffusion coefficients calculated at three temperatures (283, 293, 303) with and without the N,N' -ethylene-phenanthroline dimer (Add) present inside the box. The pure water calculations match the experimental reference, whereas the additive/water mixture shows a significant decrease in diffusion coefficient.

Table S5.2: All Faradaic efficiencies and currents

Cell	V	$\langle I \rangle$ (mA)	FE (%)								sum
			H ₂	CO	CH ₄	C ₂ H ₄	HCOOH	AcOOH	EtOH	1-PrOH	
ANEC	-0.84	-2.33	66.2	0	0	0	26.7	0.0	0.0	0.0	92.9
	-0.84	-2.40	63.1	0.6	0	0	28.6	0.0	0.0	0.0	92.3
	-0.84	-2.48	62.1	0.7	0	0	18.4	0.0	0.0	0.0	81.2
	-0.85	-2.26	59.4	2.4	0.1	0	15.4	0.0	0.0	0.0	77.3
	-0.85	-2.38	63.5	3.9	0	0	8.6	0.0	0.0	0.0	76.0
	-0.89	-2.89	92.3	5.7	0	0	20.5	0.0	0.0	0.0	118.5
	-0.92	-2.76	79.6	6.3	0	0	31.7	0.0	0.0	0.0	117.6
	-0.92	-3.47	59.6	2.2	0	0	30.1	0.0	0.0	0.0	91.9
	-0.92	-3.38	69	3.7	0	0	27.3	0.0	0.0	0.0	100.0
	-0.92	-3.48	56.3	3.2	0	0	31.1	0.0	0.0	0.0	90.6
	-0.93	-3.08	51	6.1	0.1	0	26.6	0.0	0.0	0.0	83.8
	-0.93	-3.04	47.3	7.4	0.1	0.1	31.3	0.0	0.0	0.0	86.2
	-0.95	-3.56	49.6	4.5	0.1	0	24.5	0.0	0.0	0.0	78.7
	-0.96	-3.09	64.3	8.2	0.2	0.2	29.0	0.0	0.0	0.0	101.9
	-0.96	-2.96	61.8	10.2	0.3	0.3	30.8	0.0	0.0	0.0	103.4
	-0.97	-3.22	60.1	9.1	0.3	0.3	37.5	0.0	0.0	0.0	107.3
	-0.97	-3.53	44.3	5.6	0.3	0.2	35.1	0.0	0.0	0.0	85.5
	-0.98	-3.10	47.4	10.3	0.6	0.6	36.5	0.0	0.0	0.0	95.4
	-0.99	-3.72	39	7.2	1.3	0.8	32.0	0.0	0.0	0.0	80.3
	-1.00	-4.34	33.4	12.2	4.1	3.3	39.8	0.0	1.4	0.7	94.9
	-1.01	-4.13	42.1	6.5	2.7	1.8	32.3	0.0	0.0	0.0	85.4
	-1.01	-3.94	42.7	6.4	4.5	2	34.0	0.0	0.0	0.9	90.5
	-1.02	-3.81	35.8	7.9	2.7	1.6	36.1	0.0	0.0	0.0	84.1
	-1.02	-3.72	37.2	11.9	3.9	1.9	18.3	0.0	5.3	1.8	80.2
	-1.05	-6.81	20.7	3.1	21.1	12	22.1	0.0	3.9	6.6	89.5
-1.05	-6.50	26.6	3.8	20.2	6.7	28.6	0.0	0.7	1.2	87.8	
-1.06	-6.42	26.8	10.5	12.4	6.7	29.7	0.0	0.0	2.5	88.6	
-1.07	-6.03	28.3	6.8	12.9	5.1	26.3	0.0	0.9	2.1	82.4	
-1.07	-5.64	28.4	10.8	16.5	4.8	13.7	0.0	6.0	1.6	81.8	

	-1.08	-9.94	15.1	1.9	28.7	14.9	14.2	0.0	4.4	5.8	85.0
	-1.08	-9.81	22.3	2	31.3	8.9	14.6	0.0	2.8	1.0	83.0
	-1.11	-8.76	23.2	8	19.7	7.7	20.7	0.0	0.0	3.0	82.3
	-1.11	-8.76	24.4	4.5	22.5	6.5	22.5	0.0	1.4	0.5	82.3
	-1.11	-8.52	27	9	28.3	6.2	23.4	0.0	1.2	2.5	97.6
ANEC 0.25 M KHCO₃	-0.78	-2.26	61.9	0.4	0	0	nd	nd	nd	nd	62.3
	-0.86	-3.22	62.8	0.6	0	0	nd	nd	nd	nd	63.4
	-0.91	-3.30	71.2	0.9	0	0	nd	nd	nd	nd	72.1
	-0.96	-3.97	63	1.4	0.2	0	nd	nd	nd	nd	64.6
	-0.99	-5.29	61.6	1.8	1.3	0.3	nd	nd	nd	nd	65.0
	-1.02	-6.92	63.5	1.7	4.5	0.6	nd	nd	nd	nd	70.3
	-1.05	-8.79	63.7	1.1	8.2	0.6	nd	nd	nd	nd	73.6
	-1.07	-11.98	64.1	0.6	12.3	0.5	nd	nd	nd	nd	77.5
	-1.13	-15.71	74.4	0.4	14.7	0.3	nd	nd	nd	nd	89.8
ANEC 1-Br₂	-0.75	-0.38	52.4	0	0	0	19.3	0.0	0.0	0.0	71.7
	-0.90	-0.81	22.6	7.6	1.3	5.1	34.1	0.0	0.0	0.0	70.7
	-0.90	-1.79	18.8	4.7	1.9	7	46.5	0.0	0.0	0.0	78.9
	-0.94	-0.96	16.9	8.1	0.3	7.8	nd	nd	nd	nd	33.1
	-0.83	-0.79	49.4	0.5	0	0	nd	nd	nd	nd	49.9
	-0.99	1.59	16.5	9.9	1.7	8.7	nd	nd	nd	nd	36.8
	-1.01	1.98	16	6.5	1.4	15.7	28.3	0.0	0.0	0.0	67.9
	-1.02	2.49	15.9	5.2	0.8	22	nd	nd	nd	nd	43.9
	-1.10	9.14	8.6	0.8	2.5	36.1	nd	nd	nd	nd	48.0
	-1.03	-2.71	19.6	6.2	3.8	19.7	nd	nd	nd	nd	49.3
	-1.08	-5.21	12.2	2.1	3.1	32.1	13.2	0.0	6.0	11.0	79.7
	-1.12	-7.92	10.1	0.9	4	35.9	17.0	0.0	6.4	2.7	77.0
	-1.15	-11.01	13.9	0.3	7.6	34	8.1	0.0	8.8	3.1	75.8
	-0.89	-0.63	27.1	24.8	0	2.6	5.9	2.2	10.1	11.7	84.3
	-0.97	-1.20	21.8	12.4	1.1	7.6	3.9	0.0	13.1	2.0	61.9
-1.04	-2.90	15.7	5.4	1.2	25.6	nd	nd	nd	nd	47.9	
-1.08	-5.55	10.9	1.3	1.4	34.6	nd	nd	nd	nd	48.2	
-1.10	-9.15	10.6	0.5	3.8	37.6	nd	nd	nd	nd	52.5	
-1.11	-8.58	10.2	0.8	3	33.8	2.8	2.5	11.1	7.0	71.2	

	-1.10	-8.89	11.3	0.8	3.6	32.8	1.1	2.4	11.4	6.1	69.4
H-Cell 1-Br₂	-1.19	-7.39	44.1	0.2	1.4	25.7	0.9	0.0	17.8	1.2	91.3
	-1.19	-7.43	40.4	0.2	0.2	28.5	1.0	0.0	19.9	1.1	91.2
	-1.19	-7.29	37.1	0.2	0.8	29.8	0.9	0.0	19.4	1.3	89.5
	-1.15	-6.31	22.9	0.5	0.5	40	1.8	0.0	21.6	2.0	89.3
	-1.15	-6.93	24.8	0.2	0.3	42.4	1.3	0.0	20.4	1.9	91.2
	-1.15	-5.80	27.9	0.5	0.7	36.7	1.5	0.0	20.1	1.6	89.0
	-1.07	-3.94	17.8	0.3	0	45.2	6.2	0.0	14.7	3.1	87.3
	-1.07	-3.53	13.6	1	0.1	45.6	6.1	0.0	15.4	3.8	85.5
	-1.07	-3.83	15.2	0.7	0	45.4	6.3	0.0	13.8	3.8	85.1
	-0.99	-1.26	21.8	5.6	0	27.9	21.3	0.0	0.0	0.0	76.6
	-0.99	-1.72	21.7	4.3	0	26.9	21.4	0.0	0.0	0.0	74.3
	-0.99	-1.73	21.4	4.2	0	25.8	22.6	0.0	0.0	0.0	74.0
	-0.89	-0.67	21.2	12.7	0	11.1	37.9	0.0	0.0	0.0	82.9
	-0.90	-0.54	21.4	15.6	0	10.7	35.3	0.0	0.0	0.0	83.0
	-0.90	-0.52	24.2	16.3	0	11.4	32.0	0.0	0.0	0.0	83.9
Sparged H-cell	-0.75	-0.49	61.8	11.5	0.1	0.4	19.2	0.0	0.0	0.0	93.0
	-0.82	-0.92	43.8	7.6	0.1	1.8	22.7	0.0	0.0	0.0	76.0
	-0.89	-1.34	37.7	8.7	0.7	3.6	24.6	0.0	0.0	0.0	75.3
	-0.96	-1.75	30.2	6.6	3	10.2	17.4	0.1	2.5	2.7	72.6
	-1.01	-3.42	25.4	4	17.4	18	10.7	0.2	5.6	4.0	85.4
	-1.05	-5.77	22.6	1.1	24.4	26	2.1	0.3	9.8	2.5	88.7
	-1.09	-9.41	22.2	0.6	29.6	21	1.4	0.2	9.2	2.1	86.3
	-1.14	-12.30	32.5	0.4	39.9	15.3	0.8	0.2	5.5	0.9	95.5
-1.17	-15.20	55.7	0.2	40.4	8.6	0.5	0.0	1.7	0.1	107.2	
Parallel H-cell	-0.88	-1.50	62.3	2.3	0	0.5	nd	nd	nd	nd	65.1
	-0.89	-1.50	62.2	2.7	0.5	0.7	nd	nd	nd	nd	66.1
	-0.89	-1.80	58.5	1.2	0.1	0.9	nd	nd	nd	nd	60.7
	-0.90	-1.60	54.5	2.9	0.2	1.5	nd	nd	nd	nd	59.1
	-0.90	-1.90	61.6	2.1	0.2	1.3	nd	nd	nd	nd	65.2
	-0.91	-1.50	51.2	2.8	0.7	2.4	nd	nd	nd	nd	57.1
	-0.91	-2.00	61.6	2.1	0.3	1.6	nd	nd	nd	nd	65.6
	-0.92	-2.10	56.6	2.4	0.5	2.4	nd	nd	nd	nd	61.9

Parallel H-cell	-0.93	-2.10	54.8	2.2	1	4.4	nd	nd	nd	nd	62.4
	-0.93	-1.73	64.4	6.9	0.3	1.8	nd	nd	nd	nd	73.4
	-0.93	-1.76	80.3	7.9	0.2	1.6	nd	nd	nd	nd	90.0
	-0.94	-1.73	69.3	8.6	0.8	1.7	nd	nd	nd	nd	80.4
	-0.94	-1.77	68.3	8	0.8	2.7	nd	nd	nd	nd	79.8
	-0.95	-2.40	56.7	4.9	0.3	2.8	nd	nd	nd	nd	64.7
	-0.95	-1.79	70.7	6.7	0.5	2.6	nd	nd	nd	nd	80.5
	-0.95	-1.90	74	8.2	2.6	6.3	nd	nd	nd	nd	91.1
	-0.96	-1.82	74	9.1	1.9	4.6	nd	nd	nd	nd	89.6
	-0.96	-2.40	60.7	5.8	0.6	3.1	nd	nd	nd	nd	70.2
	-0.97	-2.50	59.8	6	0.7	3	nd	nd	nd	nd	69.5
	-0.97	-2.20	47.1	5.1	1.7	6.7	nd	nd	nd	nd	60.6
	-0.97	-1.90	88.2	8.7	1.6	5	nd	nd	nd	nd	103.5
	-0.97	-2.23	65.1	6.5	2.2	5.5	nd	nd	nd	nd	79.3
	-0.98	-2.40	51.5	6	3.6	7.5	nd	nd	nd	nd	68.6
	-0.98	-2.10	46.3	5.8	3.6	9	nd	nd	nd	nd	64.7
	-0.98	-2.42	62.2	5.8	3.3	7.8	nd	nd	nd	nd	79.1
	-0.99	-2.00	54.5	5	2.6	4.9	nd	nd	nd	nd	67.0
	-0.99	-2.90	61.7	7.1	3.6	5	nd	nd	nd	nd	77.4
-1.00	-1.90	66.6	7.5	2.9	4.1	nd	nd	nd	nd	81.1	
-1.00	-3.90	88.6	1.5	7.1	4.7	nd	nd	nd	nd	101.9	
Parallel H-cell	-1.00	-2.70	52	2.9	8.6	10.7	nd	nd	nd	nd	74.2
	-1.01	-3.40	60.6	6.2	6.2	6.8	nd	nd	nd	nd	79.8
	-1.01	-2.80	45	2.8	8.7	10	nd	nd	nd	nd	66.5
	-1.02	-4.50	91.4	1.4	6.3	3.8	nd	nd	nd	nd	102.9
	-1.02	-3.90	63.2	5.3	9.3	7.9	nd	nd	nd	nd	85.7
	-1.03	-4.10	65.9	0.8	10.3	9.1	nd	nd	nd	nd	86.1
	-1.03	-3.10	58.5	6.3	5.9	7.4	nd	nd	nd	nd	78.1
	-1.04	-3.50	66.8	6.3	13.1	7.3	nd	nd	nd	nd	93.5
	-1.04	-3.10	60.5	6.9	8.8	5.8	nd	nd	nd	nd	82.0
	-1.04	-4.20	84.4	0.9	12.6	6.9	nd	nd	nd	nd	104.8
	-1.05	-6.80	66.4	1.6	5.8	10	nd	nd	nd	nd	83.8
-1.05	-4.10	55.6	4.1	8	7.6	nd	nd	nd	nd	75.3	

	-1.05	-4.30	55.2	3.3	14.6	6.8	nd	nd	nd	nd	79.9
	-1.05	-3.92	52	3.9	11.6	8.9	nd	nd	nd	nd	76.4
	-1.05	-5.77	45.8	1.3	15.6	13.4	nd	nd	nd	nd	76.1
	-1.05	-4.50	83.7	0.8	13.3	6.1	nd	nd	nd	nd	103.9
	-1.05	-4.80	74.4	0.6	11.9	5.5	nd	nd	nd	nd	92.4
	-1.06	-3.40	57.6	6.5	10.5	6.4	nd	nd	nd	nd	81.0
	-1.06	-4.60	43.8	1.8	10.5	10.6	nd	nd	nd	nd	66.7
	-1.06	-4.80	70.1	1.3	18.8	8.7	nd	nd	nd	nd	98.9
	-1.07	-4.10	62.6	5.1	13.8	6.8	nd	nd	nd	nd	88.3
	-1.07	-5.00	62.3	1.1	16.6	7.2	nd	nd	nd	nd	87.2
	-1.07	-5.20	53.8	0.6	16	12.3	nd	nd	nd	nd	82.7
	-1.08	-3.90	57.1	5.1	13.9	6.4	nd	nd	nd	nd	82.5
	-1.08	-6.40	84.2	0.5	12.8	5.6	nd	nd	nd	nd	103.1
	-1.09	-7.10	35.3	0.6	12.6	9.3	nd	nd	nd	nd	57.8
	-1.10	-6.06	46.1	0.8	15.5	11.3	nd	nd	nd	nd	73.7
	-1.11	-6.60	50.7	1.4	19.4	13.3	nd	nd	nd	nd	84.8
	-1.11	-6.09	52.7	2.5	16.6	6.1	nd	nd	nd	nd	77.9
	-1.12	-7.00	70.2	0.3	10.9	7.4	nd	nd	nd	nd	88.8
	-1.12	-6.60	55.3	1.2	19.9	13.4	nd	nd	nd	nd	89.8
	-1.13	-8.60	52.7	0.7	12.6	5.1	nd	nd	nd	nd	71.1
	-1.13	-8.10	51.8	0.8	17.3	14.4	nd	nd	nd	nd	84.3
	-1.13	-7.30	50.4	1	21.8	14.2	nd	nd	nd	nd	87.4
Angled H-cell	-0.92	-0.80	54.3	9.9	0.3	0.4	nd	nd	nd	nd	64.9
	-0.94	-0.90	48.3	11.2	0.5	0.8	nd	nd	nd	nd	60.8
	-0.96	-1.10	42.7	9.5	0.7	1.2	nd	nd	nd	nd	54.1
	-0.98	-2.30	59.4	8.9	0.5	1.3	nd	nd	nd	nd	70.1
	-0.98	-2.10	41.8	8.1	2.1	2.5	nd	nd	nd	nd	54.5
	-0.98	-1.20	49.7	11.2	1.5	2.9	nd	nd	nd	nd	65.3
	-0.99	-1.40	42.4	9.2	2.4	3.5	nd	nd	nd	nd	57.5
	-1.00	-2.50	64.9	9.9	1	1.7	nd	nd	nd	nd	77.5
	-1.01	-1.80	47.5	9.4	4.6	5.3	nd	nd	nd	nd	66.8
	-1.02	-2.60	32.3	5.4	8.6	9.4	nd	nd	nd	nd	55.7
	-1.02	-2.70	58.7	9.5	2	3.1	nd	nd	nd	nd	73.3

-1.02	-2.10	60.8	9.2	1.8	2.6	nd	nd	nd	nd	74.4
-1.03	-2.10	42.3	12.6	5	4	nd	nd	nd	nd	63.9
-1.03	-1.90	36.3	15.6	5.7	5	nd	nd	nd	nd	62.6
-1.03	-3.20	47.3	7.5	5.6	7.8	nd	nd	nd	nd	68.2
-1.05	-2.30	46.5	13	7.9	5	nd	nd	nd	nd	72.4
-1.05	-2.20	38.5	15.7	8.6	5.5	nd	nd	nd	nd	68.3
-1.06	-2.60	57.6	14.4	15.6	7.1	nd	nd	nd	nd	94.7
-1.06	-2.60	36.2	14.5	11.7	6.5	nd	nd	nd	nd	68.9
-1.06	-3.30	39.7	8.3	13.2	11.1	nd	nd	nd	nd	72.3
-1.07	-4.00	36.7	5.3	15.6	10.4	nd	nd	nd	nd	68.0
-1.07	-3.80	35.8	7	18.6	12.4	nd	nd	nd	nd	73.8
-1.08	-4.60	28.6	5.2	18.6	13	nd	nd	nd	nd	65.4
-1.09	-3.80	45.1	8.4	18.4	8.4	nd	nd	nd	nd	80.3
-1.09	-3.80	38.1	10.7	24.1	10.2	nd	nd	nd	nd	83.1
-1.10	-5.60	26.6	3.2	21.1	17.4	nd	nd	nd	nd	68.3
-1.11	-3.80	46.5	12.7	28.5	9.7	nd	nd	nd	nd	97.4
-1.11	-3.70	42.9	9.2	19.8	7.5	nd	nd	nd	nd	79.4
-1.13	-4.20	63.9	11.8	29.4	8.3	nd	nd	nd	nd	113.4
-1.13	-3.80	35.2	11.2	24.4	7.8	nd	nd	nd	nd	78.6

References

- (1) Lai, Y.; Jones, R. J. R.; Wang, Y.; Zhou, L.; Gregoire, J. M. Scanning Electrochemical Flow Cell with Online Mass Spectroscopy for Accelerated Screening of Carbon Dioxide Reduction Electrocatalysts. *ACS Comb. Sci.* **2019**, *21* (10), 692–704. <https://doi.org/10.1021/acscombsci.9b00130>.
- (2) Thevenon, A.; Rosas-Hernández, A.; Peters, J. C.; Agapie, T. In-Situ Nanostructuring and Stabilization of Polycrystalline Copper by an Organic Salt Additive Promotes Electrocatalytic CO₂ Reduction to Ethylene. *Angew. Chem. Int. Ed.* **2019**, *58* (47), 16952–16958. <https://doi.org/10.1002/anie.201907935>.

- (3) Poudyal, I.; Adhikari, N. P. Temperature Dependence of Diffusion Coefficient of Carbon Monoxide in Water: A Molecular Dynamics Study. *J. Mol. Liq.* **2014**, *194*, 77–84. <https://doi.org/10.1016/j.molliq.2014.01.004>.
- (4) Jones, R. J. R.; Wang, Y.; Lai, Y.; Shinde, A.; Gregoire, J. M. Reactor Design and Integration with Product Detection to Accelerate Screening of Electrocatalysts for Carbon Dioxide Reduction. *Rev. Sci. Instrum.* **2018**, *89* (12), 124102. <https://doi.org/10.1063/1.5049704>.
- (5) Kuhl, K. P.; Cave, E. R.; Abram, D. N.; Jaramillo, T. F. New Insights into the Electrochemical Reduction of Carbon Dioxide on Metallic Copper Surfaces. *Energy Environ. Sci.* **2012**, *5* (5), 7050–7059. <https://doi.org/10.1039/C2EE21234J>.
- (6) Lobaccaro, P.; Singh, M. R.; Clark, E. L.; Kwon, Y.; Bell, A. T.; Ager, J. W. Effects of Temperature and Gas–Liquid Mass Transfer on the Operation of Small Electrochemical Cells for the Quantitative Evaluation of CO₂ Reduction Electrocatalysts. *Phys. Chem. Chem. Phys.* **2016**, *18* (38), 26777–26785. <https://doi.org/10.1039/C6CP05287H>.
- (7) Clark, E. L.; Resasco, J.; Landers, A.; Lin, J.; Chung, L.-T.; Walton, A.; Hahn, C.; Jaramillo, T. F.; Bell, A. T. Standards and Protocols for Data Acquisition and Reporting for Studies of the Electrochemical Reduction of Carbon Dioxide. *ACS Catal.* **2018**, *8* (7), 6560–6570. <https://doi.org/10.1021/acscatal.8b01340>.
- (8) Asperti, S.; Hendrikx, R.; Gonzalez-Garcia, Y.; Kortlever, R. Benchmarking the Electrochemical CO₂ Reduction on Polycrystalline Copper Foils: The Importance of Microstructure Versus Applied Potential. *ChemCatChem* **2022**, *n/a* (n/a), e202200540. <https://doi.org/10.1002/cctc.202200540>.

- (9) Schreier, M.; Yoon, Y.; Jackson, M. N.; Surendranath, Y. Competition between H and CO for Active Sites Governs Copper-Mediated Electrosynthesis of Hydrocarbon Fuels. *Angew. Chem. Int. Ed.* **2018**, *57* (32), 10221–10225. <https://doi.org/10.1002/anie.201806051>.
- (10) Thompson, A. P.; Aktulga, H. M.; Berger, R.; Bolintineanu, D. S.; Brown, W. M.; Crozier, P. S.; in 't Veld, P. J.; Kohlmeyer, A.; Moore, S. G.; Nguyen, T. D.; Shan, R.; Stevens, M. J.; Tranchida, J.; Trott, C.; Plimpton, S. J. LAMMPS - a Flexible Simulation Tool for Particle-Based Materials Modeling at the Atomic, Meso, and Continuum Scales. *Comput. Phys. Commun.* **2022**, *271*, 108171. <https://doi.org/10.1016/j.cpc.2021.108171>.
- (11) Rappe, A. K.; Casewit, C. J.; Colwell, K. S.; Goddard, W. A.; Skiff, W. M. UFF, a Full Periodic Table Force Field for Molecular Mechanics and Molecular Dynamics Simulations. *J. Am. Chem. Soc.* **1992**, *114* (25), 10024–10035. <https://doi.org/10.1021/ja00051a040>.
- (12) Lin, S.-T.; Blanco, M.; Goddard, W. A. The Two-Phase Model for Calculating Thermodynamic Properties of Liquids from Molecular Dynamics: Validation for the Phase Diagram of Lennard-Jones Fluids. *J. Chem. Phys.* **2003**, *119* (22), 11792–11805. <https://doi.org/10.1063/1.1624057>.

Appendix 6

SUPPLEMENTARY INFORMATION FOR CHAPTER 6:
ELECTRODE SURFACE HEATING WITH ORGANIC FILMS
IMPROVES CO₂ REDUCTION KINETICS ON COPPER

In collaboration with Yungchieh Lai, Zachary J. Schiffer, and Virginia Canestraight.

Materials and Methods

All solvents and reagents were obtained from commercial sources and used as received, unless stated otherwise. Cu foils (99.999% Cu, 25 mm × 25 mm × 0.5 mm), potassium carbonate (99.995%), potassium ferricyanide ($\geq 99\%$), and potassium ferrocyanide hydrate (99.95%) were purchased from Sigma Aldrich. Carbon rods (99.999% C) were purchased from Strem Chemicals. Platinum foil (99.99% Pt, 25 mm × 25 mm × 0.05 mm) was purchased from Alfa Aesar. Natural abundance CO₂ (Research grade) was purchased from Airgas. Water was purified by a Nanopure Analytical Ultrapure Water System (Thermo Scientific) or a Milli-Q Advantage A10 Water Purification System (Millipore) with specific resistance of 18.2 MΩ·cm at 25 °C.

Prior to each use, copper foil was mechanically polished to a mirror-like finish using nanodiamond suspension (first 3 μm then 0.1 μm, Buehler) followed by rinsing in water and drying under a stream of nitrogen gas. The copper foil was then electropolished using a method similar to the one employed by Kuhl *et al.*: In a 85% phosphoric acid bath, +2.1 V versus a carbon rod counter electrode was applied to the Cu foil for 5 minutes and the foil was subsequently washed with copious amounts of ultra-pure water and dried under a stream of nitrogen gas. Prior to each use, platinum foil was washed with water and flame-annealed using a butane torch for 10 s. CO₂-saturated potassium bicarbonate electrolyte (KHCO₃, 0.1 M) was prepared by sparging an aqueous solution of potassium carbonate (K₂CO₃, 0.05 M) with CO₂ for at least 1 h prior to electrolysis.

Synthesis of Diphenyliodonium Triflate

The synthesis of diphenyliodonium triflate was performed as reported.¹ The as-synthesized compound was characterized by ¹H NMR in d₆-DMSO (400 MHz) δ (ppm): 8.26 (d, J = 7.0 Hz, 1H), 7.68 (t, J = 7.5 Hz, 1H), 7.54 (t, J = 7.8 Hz, 2H).

High throughput electrochemical testing

Prior to the electrolysis, the electrolyte (0.1 M KHCO₃, \geq 99.95% trace metals basis, Sigma Aldrich) with or without additives was purged with CO₂ (99.999%, Airgas) for at least 30 min. A bipolar membrane (BPM, Fumasep® FBM single film, Fumatech) was used to separate the working and counter electrodes. Platinum wire (99.9%, Sigma Aldrich) was used as the counter electrode. Electrolysis was carried out with a Gamry Reference 600TM potentiostat. All electrochemical data were collected using a Ag/AgCl reference electrode (LF2, Innovative Instruments) and converted to a reversible hydrogen electrode (RHE) scale using the measured solution pH of 6.8. All cells and all solution handling lines were purged with fresh electrolyte and CO₂ between electrolysis to avoid cross-contamination. The surface area of the counter electrodes were about 0.25 cm², while the working electrode surface areas were 0.32 cm². The “fast” flow rate of electrolyte was 150 μ L/s throughout the tests, and “slow” was 20 μ L/s. The electrode was heated using a Peltier element (Laird thermal) with a heat sink (by Digi Key) below it, which is controlled by TEC-1161-4A-VIN1-SCREW Meerstetter TEC controller. Prior to each refill/experiment, the surface of electrodes was preheated to the desired temperature. The electrolyte was not refilled into the cell until the software (TEC service software) indicated the temperature was stabilized.

Analytical and Electro-chemistry (HT-ANEC) is an analytical electrochemistry system previously published by our group to efficiently detect a wide range of CO₂R products.² At the end of each (photo)electrolysis, gaseous and liquid products were sampled by the robotic sample handling system (RSHS) and analyzed by GC (Thermo Scientific™ TRACE™ 1300) and HPLC (Thermo Scientific UltiMate 3000). Detailed product detection (method) can be found in previous publications.^{3,4} For any CO₂ reduction experiments with additives involved, the additives were pre-deposited at room temperature at the potential -1.2 V vs RHE for 7.5min.

COMSOL Modeling Information

The governing equations for laminar flow and heat transfer in fluids were solved in COMSOL Multiphysics 6.1, coupled by the nonisothermal flow interface. Buoyant effects were taken into account. The default solver configurations were used with a relative tolerance of 0.001. The modeling domain was discretized using an auto-generated extremely fine tetrahedral mesh with 2,020,386 elements. Inlet velocity boundary conditions were set to fully developed flow and matched to experimental flow rates. The outlet was set to 0 Pa to constrain fluid pressure. Inlet flow was set to room temperature and the electrode surface was set to experimental temperatures.

Parameter estimation for CO₂ reduction

We will follow the procedure of Limaye et al. for parameter estimation.⁵ Specifically, using Bayesian inference, we will generate distributions for parameters within a model given the

raw data. The model we use is the following model:

$$1/i = 1/i_{lim} + 1/i_{kinetic}$$

This model was used by Limaye et al. to represent mass transport limitations at high overpotentials, where i is the total current, i_{lim} is the transport-limited current, and $i_{kinetic}$ is the true kinetic current. For the kinetic model, we will use:

$$i_{kinetic} = Ae^{-E_a/RT + \alpha F\phi/RT}$$

$$\ln(i_{kinetic}) = \ln(A) - E_a/RT + \alpha F\phi/RT$$

This is the Butler-Volmer model with temperature dependence included. Here, E_a is the activation energy for the reaction, R is the ideal gas constant, T is the temperature, α is the transfer coefficient (the inverse of the Tafel slope, m_T), A is the prefactor of the Arrhenius rate constant expression, F is Faraday's constant, and ϕ is the applied potential versus RHE. Note that by construction, the potential is positive and higher potentials lead to higher currents. A few important notes about this expression. (1) the prefactor, A , represents the product of multiple prefactors, rate constants, and equilibrium constants in the case of a multi-step reaction where the rate-determining step is not the first electron transfer. (2) Similarly, the activation energy, E_a , is not the activation energy of rate-determining step, necessary, but instead represents a sum of all the Arrhenius expressions that go into the rate constant pre-factor, including the Gibbs free energies for equilibrium reactions before the rate-determining step. (3) the potential is shown as relative to RHE, but in practice could be shown as relative to any reference; the only thing that changes will be the exact value of the activation energy, modified by $\alpha\phi_{reference}$. Thus, the activation energy reported is actually a function of reference chosen for the system. In the case where the rate-determining step is

the first elementary reaction in a multi-step reaction, then the activation energy and the prefactor correspond to the expected values for an elementary step.

We can now modify the above expression with some math to get:

$$\ln(i) = \ln(i_{lim}) + \ln(i_{kinetic}) - \ln(i_{lim} + i_{kinetic})$$

$$\ln(i) = \ln(i_{lim}) + \ln(A) - E_a/RT + \alpha F\phi/RT - \ln(i_{lim} + Ae^{-E_a/RT + \alpha F\phi/RT})$$

Numerically, fitting this can cause problems, so instead we will fit a variation:

$$\begin{aligned} \ln(i_{kinetic}) - \ln(i_0) \\ = \ln(A) - E_a/RT + \alpha F\phi/RT - [\ln(A) - E_a/RT_0 + \alpha F\phi_0/RT_0] \end{aligned}$$

Essentially, we are now fitting a model where we have normalized the current by the “true” kinetic model. Of course, we do not have the “true” kinetic model, so we instead will use reference potential, temperature, and current from the experimental dataset. Our kinetic model becomes:

$$\ln(i_{kinetic}) - \ln(b) = -E_a/RT + \alpha F\phi/RT - [-E_a/RT_{0,exp} + \alpha F\phi_{0,exp}/RT_{0,exp}]$$

Here, b represents the *actual* kinetic current at the experimentally given reference potential and temperature indicated. Doing this removes some of the arbitrariness from the potential reference and gives physical meaning to the free parameter b instead of a pre-exponential factor A . Empirically, we found that this led to faster and more reproducible fitting with Monte Carlo sampling of the distributions (full parameter fits and distributions Figure S9).

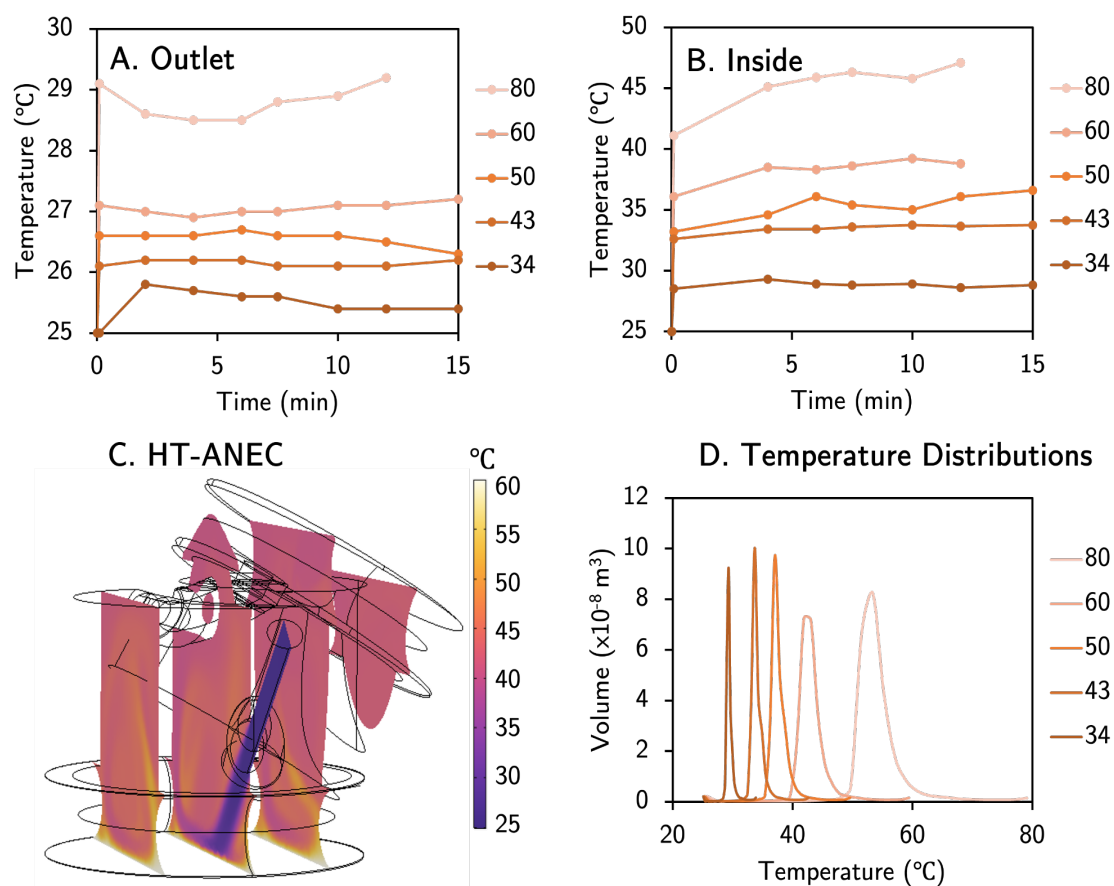


Figure S6.1: Electrolyte temperature profiles A) inside the cell compared to B) 3 cm past the outlet of the cell given variable surface heating temperatures. C) Cross-sectional COMSOL image of HT-ANEC with a flow rate of 150 $\mu\text{L/s}$ and SH=60 $^{\circ}\text{C}$ shows decent agreement with experimentally derived values, as shown in table S6.1, with variation in temperature shown in the histogram in D).

Table S6.1: Comparison of experimental and COMSOL internal temperatures. Δ corresponds to the difference between experimental and simulation temperatures. We expect the higher average temperature observed in our simulation is due to the cell not being perfectly insulating as it is in the model. Furthermore, the thermocouple is placed at the top of the cathodic chamber and will therefore read cooler temperatures than the average, which considers the electrolyte closest to the heated electrode.

Surface T	<Expt> internal T	Expt std dev	<COMSOL> internal	COMSOL std dev	Δ
25	25.0	0.0	25.0	0.0	0.0
34	28.4	0.3	29.5	0.9	-1.1
43	32.4	0.4	34.1	1.9	-1.7
50	34.0	1.2	37.8	2.6	-3.8
60	36.4	1.1	43.2	3.6	-6.8
80	42.3	2.1	53.9	5.6	-11.6

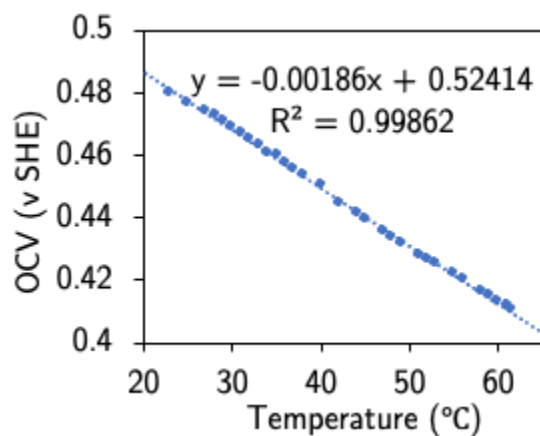


Figure S6.2: Calibration of OCV versus bulk temperature. Measurements in 0.5 M KCl with 5 mM $\text{K}_3\text{Fe}(\text{CN})_6$ and 5 mM $\text{K}_4\text{Fe}(\text{CN})_6$ using a platinum rotating disk electrode, with a platinum wire counter electrode, and a SCE reference electrode.

Table S6.2: Open Circuit Voltage (OCV) measurements in 0.5 M KCl with 5 mM $\text{K}_3\text{Fe}(\text{CN})_6$ and 5 mM $\text{K}_4\text{Fe}(\text{CN})_6$ shown in Figure 6.2. BH corresponds to projected values based on a linear regression of data points shown in figure S6.2. All slow/fast values are the average of two data points.

Set T	25	34	43	50	60
OCV_{BH}	0.478	0.461	0.444	0.431	0.413
$\langle \text{OCV}_{\text{fast}} \rangle$	0.482 ± 0.000	0.465 ± 0.006	0.452 ± 0.005	0.444 ± 0.007	0.420 ± 0.000
$\langle T_{\text{fast}} \rangle$	22.5 ± 0.2	31.9 ± 3.2	39.0 ± 2.6	43.2 ± 3.6	55.9 ± 0.0
$\langle \text{OCV}_{\text{slow}} \rangle$	0.483 ± 0.001	0.464 ± 0.006	0.450 ± 0.005	0.440 ± 0.005	0.413 ± 0.003
$\langle T_{\text{slow}} \rangle$	22.1 ± 0.5	32.3 ± 3.0	39.8 ± 2.6	45.5 ± 2.5	59.6 ± 1.4

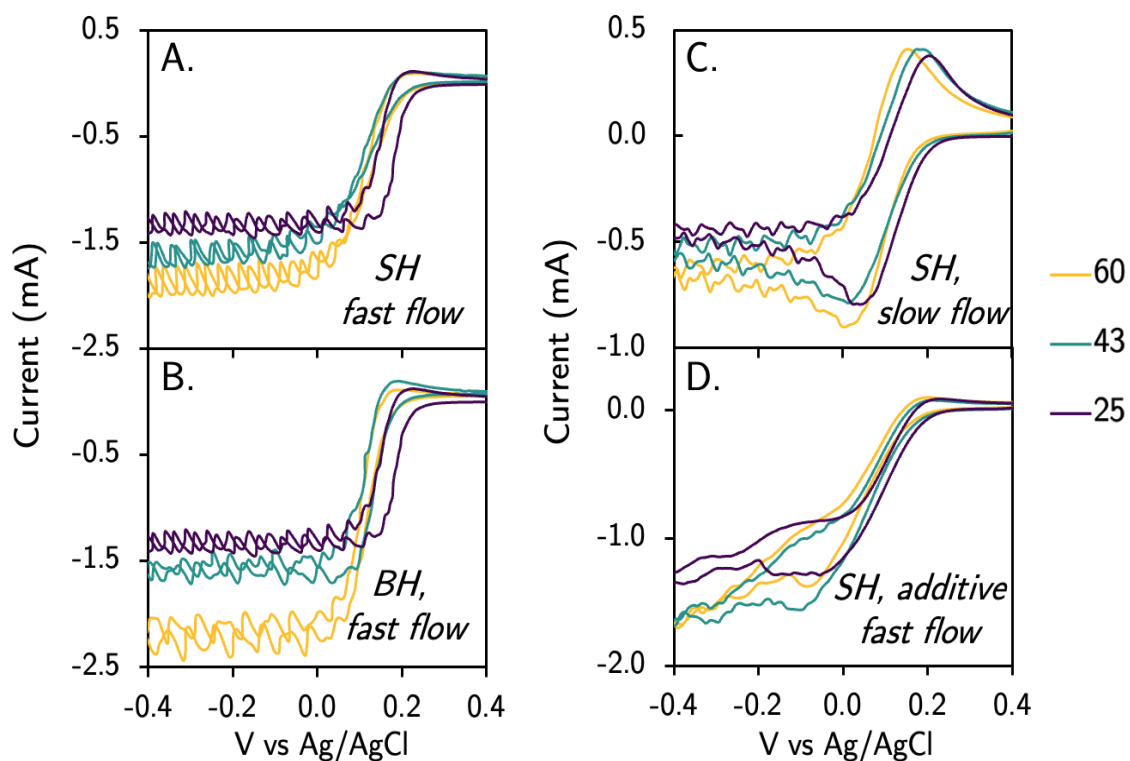


Figure S6.3: Zoomed out cyclic voltammograms (CVs) of A) surface heating with fast electrolyte recirculation, B) bulk heating with fast electrolyte recirculation, C) surface heating with slow electrolyte recirculation, and D) surface heating with fast electrolyte recirculation in the presence of a molecular film (deposited in the same way as otherwise referred to in the text). Cyclic voltammograms were performed with 10 mM $\text{K}_3\text{Fe}(\text{CN})_6$ in CO_2 -sparged 0.1 M KHCO_3 scanning at 100 mV/s from 0.5 V to -1 V vs Ag/AgCl with a gold working electrode, Pt counter electrode, and leakless Ag/AgCl reference electrode. CVs were performed to establish a mass transport limited regime for subsequent chronoamperometry experiments.

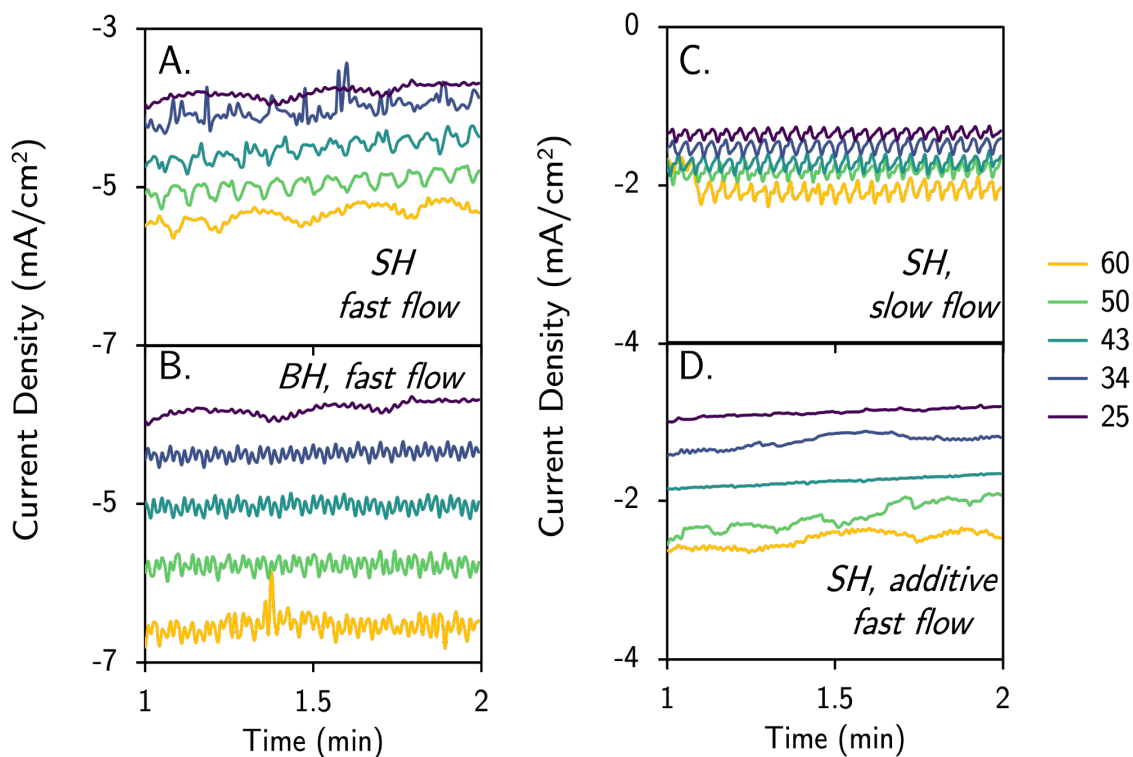


Figure S6.4: Chronoamperometry (CA) at -0.8 V vs Ag/AgCl for 2 minutes of A) surface heating with fast electrolyte recirculation, B) bulk heating with fast electrolyte recirculation, C) surface heating with slow electrolyte recirculation, and D) surface heating with fast electrolyte recirculation in the presence of a molecular film (deposited in the same way as otherwise referred to in the text). CAs were performed with 10 mM $K_3Fe(CN)_6$ in CO_2 -sparged 0.1 M $KHCO_3$ with a gold working electrode, Pt counter electrode, and leakless Ag/AgCl reference electrode. The average current across the second minute was used in subsequent boundary layer calculations. The significant decrease in activity with organic films may be due to the inhibition of the transfer of ferricyanide through the film.

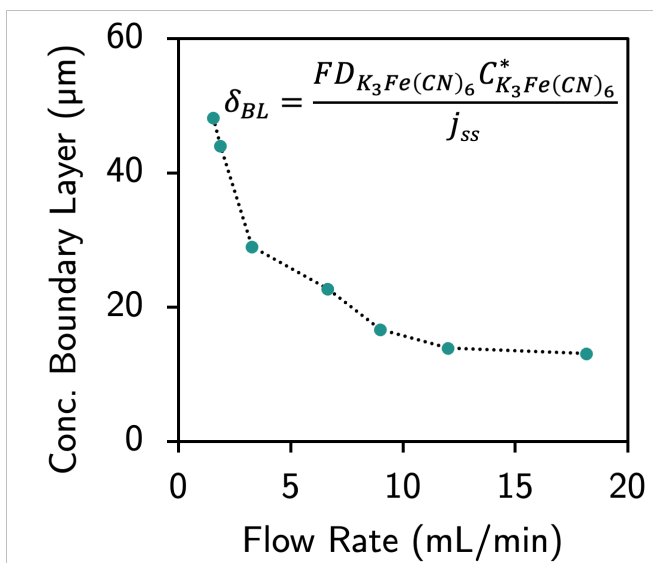


Figure S6.5: Concentration boundary layer versus electrolyte recirculation flow rate. These experiments were obtained according to section SI-4 from Clark et al.⁶ Briefly, a CV is initially performed to determine the mass transport limited regime, and then a potential is chosen for subsequent constant potential experiments to determine the boundary layer at different recirculation rates. The boundary layer was calculated using the inset equation, wherein $D_{K_3Fe(CN)_6}$ is the diffusivity of the ferricyanide ion at 25 °C ($0.72 \times 10^{-5} \text{ cm}^2 \text{ s}^{-1}$), $C^*[Fe(CN)_6^{3-}]$ is the concentration of ferricyanide ion in the bulk of the electrolyte (10 mM), and j_{ss} is the steady-state current density.

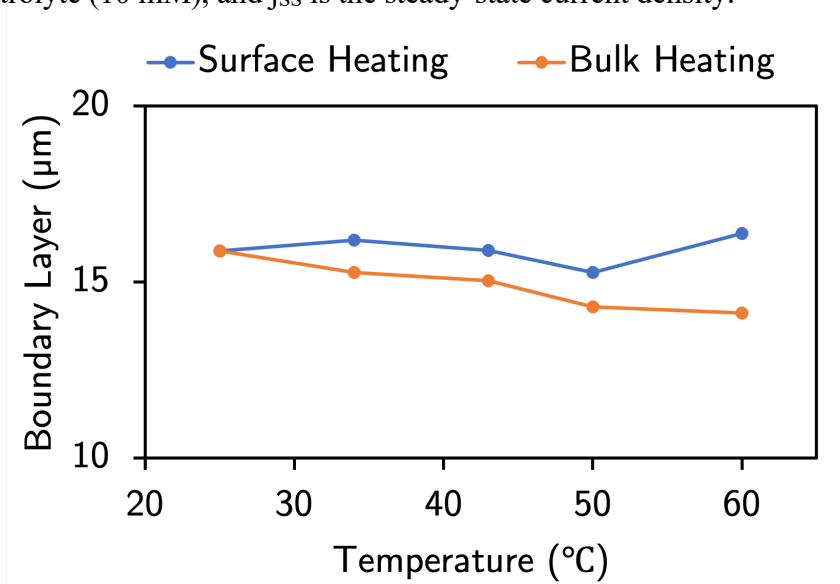


Figure S6.6: Calculated concentration boundary layer thickness at a 150 $\mu\text{L/s}$ flow rate using extrapolated diffusion coefficients and surface temperatures from Table S6.2.⁷

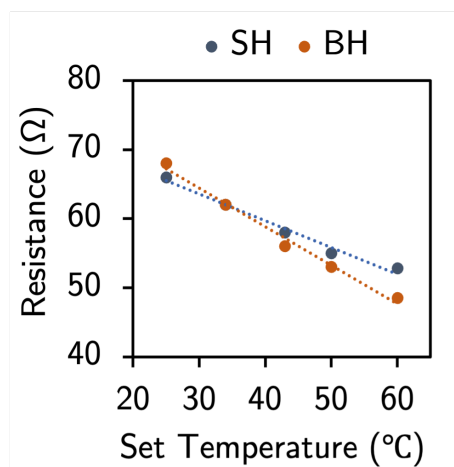


Figure S6.7: Temperature versus resistance plots of surface heated (SH) versus bulk heated (BH) electrolyte using 0.1 M KHCO_3 .

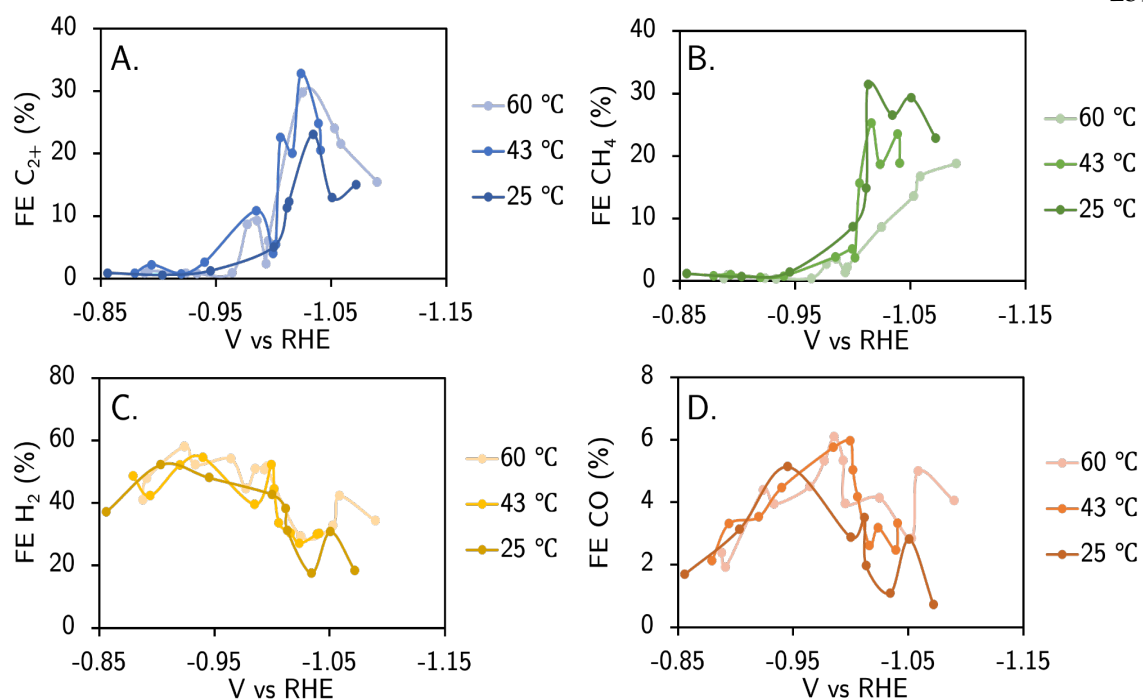


Figure S6.8: Plots of Faradaic efficiencies for polycrystalline Cu CO₂R at variable temperatures in 0.1 M KHCO₃. Each data point corresponds to an individual experiment.

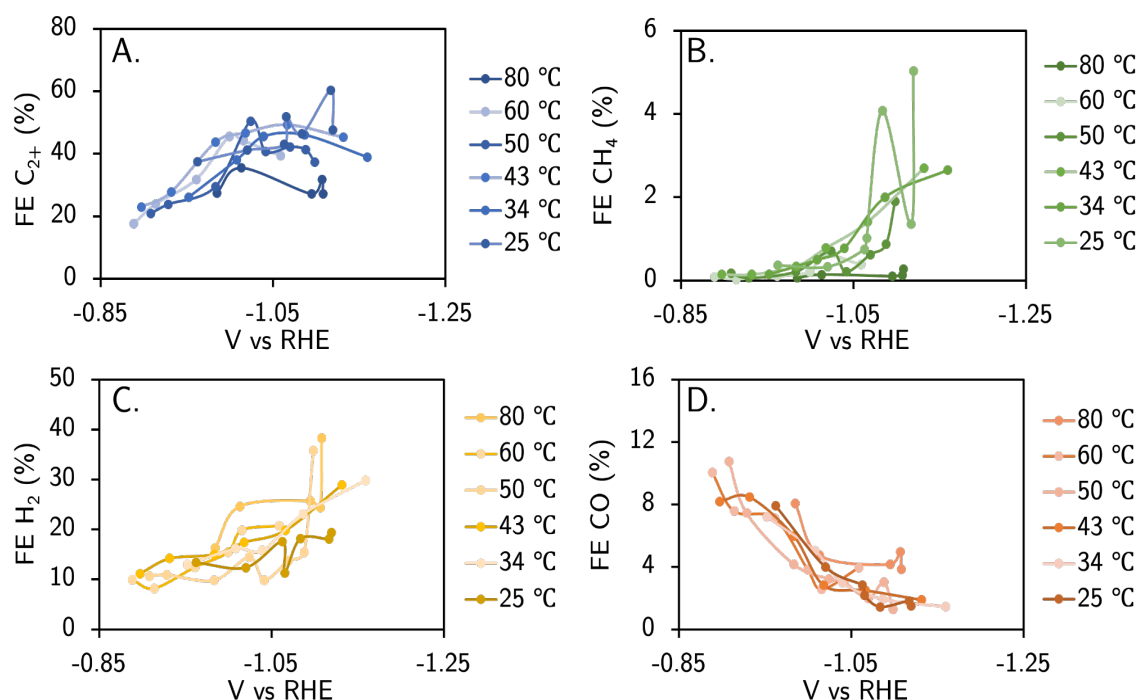


Figure S6.9: Plots of Faradaic efficiencies for organic-modified polycrystalline Cu CO₂R at variable temperatures in 0.1 M KHCO₃. Each data point corresponds to an individual experiment.

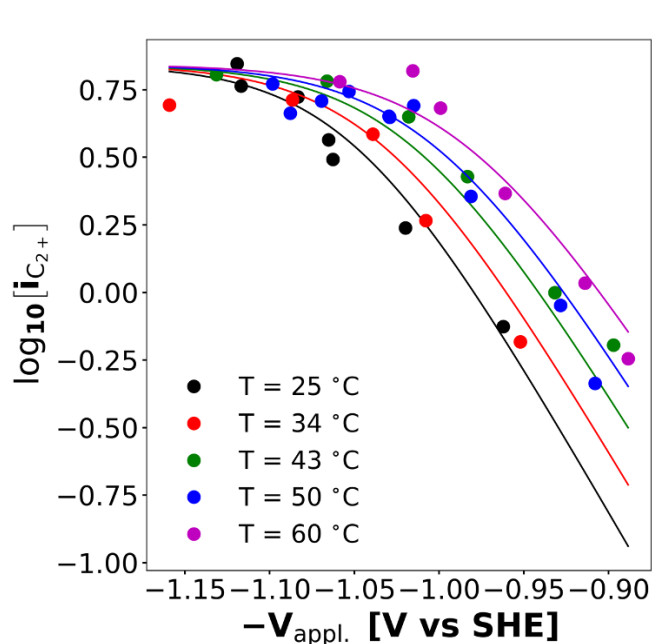


Figure S6.10: Fitting of experimental CO₂R data using Butler Volmer kinetics (Equation 6.2 in the main text and full model earlier in Appendix).

Table S6.3: Potentials, currents, temperatures, and Faradaic efficiencies of electrolyses reported herein.

T (°C)	[Add.] (mM)	V vs RHE	J total (mA/c m ²)	J total (mA/c m ²)							CHOO H	C ₂₊ Liq.	Total FE
				H ₂	CH ₄	CO	C ₂ H ₄	EtOH					
25	-	-0.86	-2.23	37.0	1.2	1.7	0.9	0.0	0.0	0.0	0.0	40.8	
25	-	-0.90	-2.36	52.2	0.7	3.1	0.6	0.0	0.0	0.0	0.0	56.6	
25	-	-0.95	-2.77	48.0	1.5	5.1	1.2	0.0	0.0	0.0	0.0	55.9	
25	-	-1.00	-5.06	42.6	8.7	2.9	3.4	0.0	0.0	1.7	59.2		
25	-	-1.01	-7.00	38.2	14.9	3.5	5.4	1.5	0.0	4.5	67.9		
25	-	-1.01	-13.25	31.1	31.4	2.0	7.0	1.5	0.7	3.8	77.4		
25	-	-1.03	-8.39	17.4	26.6	1.1	10.7	4.7	0.8	7.7	68.9		
25	-	-1.05	-10.10	30.7	29.4	2.8	6.5	1.6	0.5	4.8	76.3		
25	-	-1.07	-11.56	18.3	22.9	0.7	6.0	3.7	0.5	5.3	57.4		
25	10	-0.96	-1.99	13.4	0.4	7.9	16.8	20.7	0.0	0.0	59.2		
25	10	-1.02	-4.21	12.4	0.3	4.0	21.4	18.2	0.0	1.6	57.9		
25	10	-1.06	-7.22	17.6	0.7	2.8	31.6	10.9	0.0	0.5	64.2		
25	10	-1.07	-7.08	11.3	1.0	2.2	32.4	15.8	9.2	3.7	75.5		
25	10	-1.08	-11.39	18.1	4.1	1.4	25.8	19.2	0.0	1.4	70.1		
25	10	-1.12	-9.63	18.1	1.4	1.8	31.7	24.8	0.0	3.7	81.6		
25	10	-1.12	-14.76	19.3	5.0	1.5	28.5	17.8	0.0	1.3	73.5		
34	10	-0.95	-2.52	13.0	0.1	7.2	16.0	2.8	7.9	0.0	47.1		
34	10	-1.01	-4.84	16.2	0.5	5.0	21.5	7.2	14.8	4.4	69.6		
34	10	-1.04	-8.46	15.8	0.8	3.0	25.4	13.4	6.6	3.7	68.7		

34	10	-1.09	-11.22	23.1	2.0	1.9	27.5	15.3	3.0	1.3	74.1
34	10	-1.16	-12.66	29.8	2.7	1.5	23.2	13.0	2.1	1.3	73.5
43	-	-0.88	-4.18	48.5	0.9	2.1	0.8	0.0	28.2	0.0	80.5
43	-	-0.89	-3.31	42.2	1.1	3.3	1.4	0.0	42.3	0.8	91.1
43	-	-0.92	-4.74	52.0	0.6	3.5	0.7	0.0	24.5	0.0	81.4
43	-	-0.94	-3.55	54.5	0.8	4.5	1.5	0.0	42.4	1.1	104.7
43	-	-0.98	-5.34	39.5	3.8	5.8	4.2	0.7	29.4	5.9	89.3
43	-	-1.00	-5.96	52.1	5.1	6.0	4.0	0.0	33.4	0.0	100.7
43	-	-1.00	-5.81	44.4	3.7	5.0	4.2	0.0	29.5	1.2	88.2
43	-	-1.01	-11.50	33.6	15.7	4.2	10.4	2.2	9.0	10.0	85.0
43	-	-1.02	-16.81	30.3	25.3	2.6	10.9	2.0	9.8	7.1	88.0
43	-	-1.02	-10.44	27.0	18.7	3.2	16.0	4.7	14.3	12.2	96.0
43	-	-1.04	-15.46	29.9	23.5	2.5	12.9	3.4	21.1	8.6	101.9
43	-	-1.04	-12.40	30.1	18.9	3.3	9.5	2.9	19.4	8.2	92.3
43	10	-0.90	-2.78	11.2	0.1	8.2	9.3	3.2	20.8	2.2	55.1
43	10	-0.93	-3.59	14.2	0.1	8.5	13.8	4.1	13.1	1.4	55.3
43	10	-0.98	-6.14	15.0	0.3	6.0	24.0	7.3	13.2	6.5	72.2
43	10	-1.02	-9.57	17.4	0.8	2.8	26.8	13.8	6.1	3.3	71.0
43	10	-1.07	-12.29	19.9	1.4	2.5	27.4	15.9	4.1	3.5	74.7
43	10	-1.13	-14.12	28.9	2.7	1.9	27.1	14.9	1.6	1.4	78.5
50	10	-0.91	-2.21	10.7	0.2	10.8	13.1	5.3	19.4	2.5	61.8
50	10	-0.93	-3.77	10.9	0.1	7.5	13.1	5.8	12.2	4.9	54.4
50	10	-0.98	-7.57	19.1	0.1	7.5	17.6	7.8	11.9	4.5	68.7
50	10	-1.02	-11.79	24.0	0.2	4.4	21.5	12.9	6.7	7.3	77.1
50	10	-1.02	-9.25	14.4	0.7	3.2	26.6	16.9	6.7	7.0	68.8
50	10	-1.03	-10.89	21.3	0.2	4.9	21.0	12.6	7.3	7.3	74.4
50	10	-1.03	-10.86	22.3	0.1	4.9	21.8	13.3	7.7	6.2	76.4
50	10	-1.05	-12.54	21.1	0.2	4.0	25.4	13.5	3.6	5.4	73.1
50	10	-1.07	-12.12	13.8	0.6	2.0	20.5	16.9	5.9	4.8	64.5
50	10	-1.09	-11.16	15.5	0.9	3.0	20.4	14.3	7.4	6.7	60.7
50	10	-1.10	-15.86	35.8	1.9	1.3	20.0	14.2	1.9	3.1	78.2
60	-	-0.89	-3.95	40.9	0.4	2.4	0.9	0.0	0.0	0.0	44.6
60	-	-0.89	-3.73	47.8	1.0	1.9	1.2	0.0	0.0	0.0	51.9
60	-	-0.92	-4.85	58.0	0.5	4.4	0.9	0.0	0.0	0.0	63.8
60	-	-0.93	-4.24	52.2	0.4	3.9	0.8	0.0	0.0	0.0	57.3
60	-	-0.96	-5.46	54.1	0.4	4.5	0.9	0.0	0.0	0.0	59.9
60	-	-0.98	-6.23	44.6	2.7	5.3	3.9	1.2	0.3	3.6	61.6
60	-	-0.99	-7.28	50.8	3.6	6.1	4.1	0.7	0.6	4.5	70.4
60	-	-0.99	-6.78	50.7	1.4	5.3	2.4	0.0	0.0	0.0	59.8
60	-	-1.00	-6.67	51.4	2.2	4.0	2.9	0.0	0.0	3.1	63.6
60	-	-1.02	-11.14	29.3	8.6	4.1	13.4	3.9	1.6	12.6	73.4
60	-	-1.05	-15.73	32.7	13.6	2.8	11.0	3.0	1.3	10.0	74.5
60	-	-1.06	-12.18	42.2	16.7	5.0	12.3	1.7	0.7	7.6	86.2
60	-	-1.09	-13.38	34.3	18.8	4.0	9.4	1.6	0.2	4.5	72.8
60	10	-0.89	-3.24	10.0	0.1	10.0	9.3	4.2	18.1	4.2	55.8

60	10	-0.91	-4.53	8.2	0.0	7.6	9.9	5.8	5.0	8.2	44.7
60	10	-0.96	-7.31	12.4	0.1	7.1	20.2	6.4	8.6	5.3	60.1
60	10	-1.00	-10.56	15.4	0.2	3.8	23.6	15.1	8.0	6.8	73.0
60	10	-1.02	-14.96	19.8	0.6	2.6	22.2	16.0	4.3	6.0	71.6
60	10	-1.06	-15.32	20.7	0.4	4.0	21.7	12.5	3.9	5.1	68.3
80	10	-0.98	-8.57	16.3	0.1	8.1	13.9	5.9	9.0	7.6	60.8
80	10	-1.01	-13.88	24.6	0.1	4.7	19.6	10.4	5.8	5.6	70.8
80	10	-1.09	-15.24	25.7	0.1	4.2	13.3	8.5	12.7	5.4	69.8
80	10	-1.11	-14.36	24.3	0.1	5.0	16.5	9.0	5.1	6.2	66.2
80	10	-1.11	-17.98	38.3	0.3	3.9	15.3	8.6	4.7	3.3	74.3

References

- (1) Bielawski, M.; Olofsson, B. High-Yielding One-Pot Synthesis of Diaryliodonium Triflates from Arenes and Iodine or Aryl Iodides. *Chem. Commun.* **2007**, No. 24, 2521–2523. <https://doi.org/10.1039/B701864A>.
- (2) Jones, R. J. R.; Wang, Y.; Lai, Y.; Shinde, A.; Gregoire, J. M. Reactor Design and Integration with Product Detection to Accelerate Screening of Electrocatalysts for Carbon Dioxide Reduction. *Rev. Sci. Instrum.* **2018**, *89* (12), 124102. <https://doi.org/10.1063/1.5049704>.
- (3) Lai, Y.; Jones, R. J. R.; Wang, Y.; Zhou, L.; Richter, M. H.; Gregoire, J. The Sensitivity of Cu for Electrochemical Carbon Dioxide Reduction to Hydrocarbons as Revealed by High Throughput Experiments. *J. Mater. Chem. A* **2019**, *7* (47), 26785–26790. <https://doi.org/10.1039/C9TA10111J>.
- (4) Lai, Y.; Watkins, N. B.; Muzzillo, C.; Richter, M.; Kan, K.; Zhou, L.; Haber, J. A.; Zakutayev, A.; Peters, J. C.; Agapie, T.; Gregoire, J. M. Molecular Coatings Improve the Selectivity and Durability of CO₂ Reduction Chalcogenide Photocathodes. *ACS Energy Lett.* **2022**, *7* (3), 1195–1201. <https://doi.org/10.1021/acsenergylett.1c02762>.

- (5) Limaye, A. M.; Zeng, J. S.; Willard, A. P.; Manthiram, K. Bayesian Data Analysis Reveals No Preference for Cardinal Tafel Slopes in CO₂ Reduction Electrocatalysis. *Nat. Commun.* **2021**, *12* (1), 703. <https://doi.org/10.1038/s41467-021-20924-y>.
- (6) Clark, E. L.; Resasco, J.; Landers, A.; Lin, J.; Chung, L.-T.; Walton, A.; Hahn, C.; Jaramillo, T. F.; Bell, A. T. Standards and Protocols for Data Acquisition and Reporting for Studies of the Electrochemical Reduction of Carbon Dioxide. *ACS Catal.* **2018**, *8* (7), 6560–6570. <https://doi.org/10.1021/acscatal.8b01340>.
- (7) Arvía, A. J.; Marchiano, S. L.; Podestá, J. J. The Diffusion of Ferrocyanide and Ferricyanide Ions in Aqueous Solutions of Potassium Hydroxide. *Electrochimica Acta* **1967**, *12* (3), 259–266. [https://doi.org/10.1016/0013-4686\(67\)80004-5](https://doi.org/10.1016/0013-4686(67)80004-5).

Thanks for reading!